Masaryk University

Faculty of Science

Department of Theoretical Physics and Astrophysics

Doctoral Thesis

Study of multiple stellar systems

Jakub Kolář

Supervisor:
doc. RNDr. Miloslav Zejda, Ph.D.

Brno 2025

Bibliografický záznam

Autor:	Mgr. Jakub Kolář Přírodovědecká fakulta, Masarykova univerzita Ústav teoretické fyziky a astrofyziky
Název práce:	Studium vícenásobných hvězdných systémů
Studijní program:	Fyzika
Studijní plán:	Astrofyzika
Školitel:	doc. RNDr. Miloslav Zejda, Ph.D.
Akademický rok:	2024/2025
Počet stran:	IX + 120
Klíčová slova:	Dvojhvězdy, čtyřhvězdy, vícenásobné systémy, fotometrie, spektrální rozdělení energie, periodová analýza

Bibliographic Entry

Author:	Mgr. Jakub Kolář Faculty of Science, Masaryk University Department of Theoretical Physics and Astrophysics

Title of Thesis:	Study of multiple stellar systems
Degree Programme:	Physics
Study Plan:	Astrophysics
Supervisor:	doc. RNDr. Miloslav Zejda, Ph.D.
Academic Year:	2024/2025
Number of Pages:	IX + 120
Keywords:	Binaries, quadruples, multiple systems, photometry, spectral energy distribution, period analysis

Abstrakt

Práce se zabývá pozorováním a komplexní analýzou vícenásobných hvězdných systémů, se zaměřením na čtyřhvězdy v konfiguraci 2+2, kde oba hvězdné páry jsou zákrytové (tzv. dvojzákrytové systémy). Pro tento výzkum byla použita fotometrická pozorování z družice TESS, doplněná o dostupná měření z přehlídek a pozorování skupiny Squadra. Pro systém ASASSN-V J233336.79+615012.0 byla rovněž k dispozici spektroskopická data. U deseti vybraných soustav byla provedena podrobná analýza včetně modelování. $O-C$ analýza potvrdila u sedmi z nich gravitační působení mezi zákrytovými páry, zatímco v jednom případě byl identifikován blend dvou nesouvisejících dvojhvězd. Pro statistickou analýzu byl posbírán vzorek celkem 781 systémů. Rozdělení poměru vnitřních period odpovídá předpokládanému rovnoměrnému rozložení, přičemž výsledky ukazují na zvýšenou preferenci pro rezonanci 3:2. Parametr RUWE získaný z astrometrických měření družice Gaia, nevykazuje pro potvrzené čtyřhvězdy odchylku od statistiky celkového souboru. Statistická analýza se dále zaměřila na kompozitní teplotu systémů. Vzorek vykazuje zvýšený počet soustav s vysokou kompozitní teplotou, což je dáno zahrnutím objektů z Magellanových oblaků. Práce rovněž představuje další čtyřhvězdné kandidáty vhodné pro nadcházející výzkum.

Abstract

The thesis presents observations and a comprehensive analysis of multiple stellar systems, focusing on quadruples in the 2+2 configuration, where both stellar pairs are eclipsing (doubly eclipsing systems). This research uses photometric observations from the TESS satellite, supplemented by ground-based surveys and the Squadra observing group measurements. Spectroscopic data were additionally available for ASASSN-V J233336.79+615012.0. A detailed analysis and modelling were carried out for ten selected systems. The $O - C$ analysis confirmed the gravitational interaction between the pairs for seven systems, while one blend of two unrelated binaries was identified. A sample of 781 systems was collected for the statistical study. The inner period ratio distribution agrees with an assumed homogeneous distribution, with the results reveal a preference for the 3:2 resonance. The RUWE parameter from Gaia astrometry does not show statistically significant deviations for the confirmed quadruples compared to the overall sample. The composite system temperatures were investigated in the statistical analysis. The sample contains an enhanced number of systems with high composite temperature due to the objects from the Magellanic Clouds. The study also introduces additional candidates suitable for the follow-up research.

Acknowledgements

I would like to thank my supervisor, doc. RNDr. Miloslav Zejda, Ph.D., for his guidance and helpful advice throughout the study. I also thank my consultant doc. RNDr. Petr Zasche, Ph.D., for the valuable discussions on this project. I am also grateful to Bc. Sabina Pačková for proofreading the text and for her support. This research is part of the Squadra group, and I am thankful to all its members for their contributions, namely Mgr. Anna Richterková, RNDr. Jan Janík, Ph.D., Reinhold Fr. Auer Dipl. Ing., Ing. Petr Viewegh Ph.D., Ing. Radek Dřevěný, and Mgr. Milan Uhlár, Ph.D. I would also like to acknowledge prof. Gerald Handler, who supported me during my stay in Warsaw. Finally, I thank all co-authors and collaborators involved in the related publications.

Declaration

I hereby declare that I have prepared my doctoral thesis independently under the guidance of my supervisor, using the information sources cited in the thesis.

Brno 2025 . . . . . .

Jakub Kolář

Publication overview and author's contribution

The thesis is based on two manuscripts authored by Jakub Kolář (JK).

J. Kolář, S. Pačková, A. Richterková, M. Zejda, R. F. Auer, R. Dřevěný, J. Janík, M. Mašek, T. Merle, P. Ohlídal, T. Pribulla, M. Uhlár., P. Viewegh, J. Vyskočil. Study of doubly eclipsing quadruples: I. Methodology and results for ten Northern sky systems. Monthly Notices of the Royal Astronomical Society (prepared for submission), 2025.

JK analysed and modelled seven out of ten investigated objects, processed the photometric and SED data, and was the main contributor to the manuscript.

J. Kolář, M. Zejda, A. Richterková, P. Dvořák, R. F. Auer, Z. Henzl, R. Dřevěný, S. Pačková, and M. Uhlár. Period ratios and observation of noticeable resonance at 3: 2 for 2+2 quadruple systems. Monthly Notices of the Royal Astronomical Society, 538(2):1160–1166, 2025.

JK, under the guidance of the supervisor, prepared the data for the publication, created the simulations and data comparison, and was the main contributor to the manuscript.

Contents

Chapter 1

Multiple stellar systems

1.1 Binary stars

Multiple stellar systems consist of two or more components that are gravitationally bound and orbit their common centre of mass. We can observe different systems according to the stellar types and component numbers. In addition to binary stars, higher-order multiples (triples, quadruples, etc.) are observed. The current binary fraction (two or more components) varies significantly depending on the spectral types. Offner et al. (2023) (Figure 1.1) show that the binary fraction is almost 100 % for the O and B stars. On the other hand, the M star binary fraction is only about 30 %. A similar dependency is presented for higher-order multiples (triples and more).

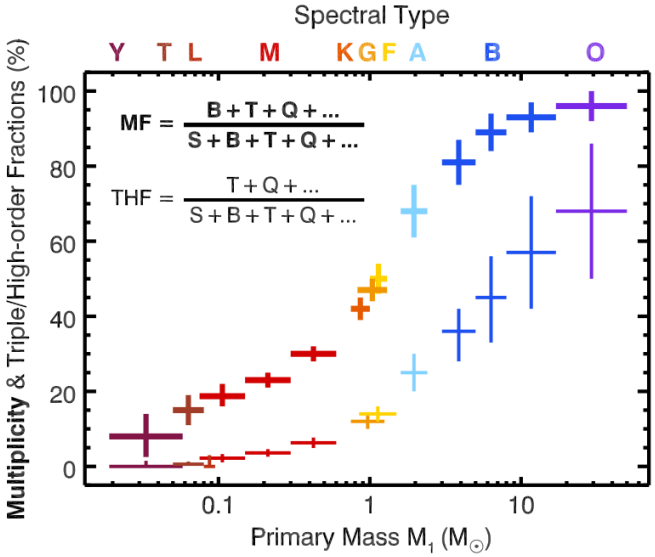

Figure 1.1: Multiplicity (MF) and triple/high-order (THF) fraction of brown dwarfs and main-sequence stars, adopted from Offner et al. (2023).

The binary system is the case with the lowest possible number of components. The stars (primary and secondary components) orbit around their common centre of mass following the third Kepler's law of motion:

$$\frac{(a_1 + a_2)^3}{P^2} = \frac{G\,(m_1 + m_2)}{4\,\pi^2}, \tag{1.1}$$

where $a_{1,2}$ are distances from the centre of mass, $m_{1,2}$ are the component masses, P denotes the orbital period, and G is the gravitational constant. Herein, the primary component is defined as the more luminous star. The orbits can be circular or elliptical with a non-zero eccentricity e parameter. The orbital velocities $v_{1,2}$ of the binary components could differ depending on the mass ratio q defined as:

$$q = \frac{m_2}{m_1} = \frac{a_1}{a_2}. \tag{1.2}$$

Wide binary systems consist of distant components that do not interact strongly with each other. With the consideration of long orbital periods in the order of decades or hundreds of years, astrometry is the most common observational technique for studying these systems. Spectroscopic observations of the spectral line wavelengths and radial velocities are also used to analyse and confirm the components' mutual motion (Kraus and Hillenbrand, 2009). Sometimes, it is possible to angularly resolve both components and measure their orbits visually (Hartkopf et al., 2001).

Close binary components interact with each other, resulting in mass transfer and q changes during their evolution. The mutual distances are typically comparable to the stars' dimensions. The typical orbital periods vary from hours to several days. The equipotential surfaces are defined around each star. The Roche potential Φ includes the gravitational interactions of the components and the centrifugal potential. The potential is defined as:

$$\Phi = -\frac{Gm_1}{r_1} - \frac{Gm_2}{r_2} - \frac{1}{2}\omega^2 r^2, \tag{1.3}$$

where $r_{1,2}$ are distances from each component to the studied point, r denotes the distance of the point from the centre of mass, and ω represents the angular velocity. Using the third Kepler's law, ω can be expressed as follows:

$$\omega = \frac{2\pi}{P} = \sqrt{\frac{G\left(m_1 + m_2\right)}{a^3}}. \tag{1.4}$$

Two equipotential surfaces that are connected through the L_1 Lagrangian equilibrium point are defined as the Roche lobes. The lobe size primarily depends on the star's mass ratio between the components (Budding and Demircan, 2022). At least one of the components fills its lobe entirely within the evolution. Using the filling degree of the Roche lobe, Kopal (1955) and Wilson (1979) made the classification of close binary systems (Figure 1.2). This classification works correctly for circular and eccentric orbits and cases with non-synchronous rotation (Wilson, 2001).

- *Detached*: Neither component fills its Roche lobe and does not reach the evolutionary stage for complete filling.
- *Semidetached*: One star already fills its Roche lobe, its volume and shape are limited by the Roche surface.
- *Double-contact*: Both binary components precisely fill their Roche lobes. However, they are not in physical contact (Wilson, 1979; Wilson and Twigg, 1980).
- *Overcontact*: The components' Roche lobes are overfilled, which can lead to a common envelope binary.

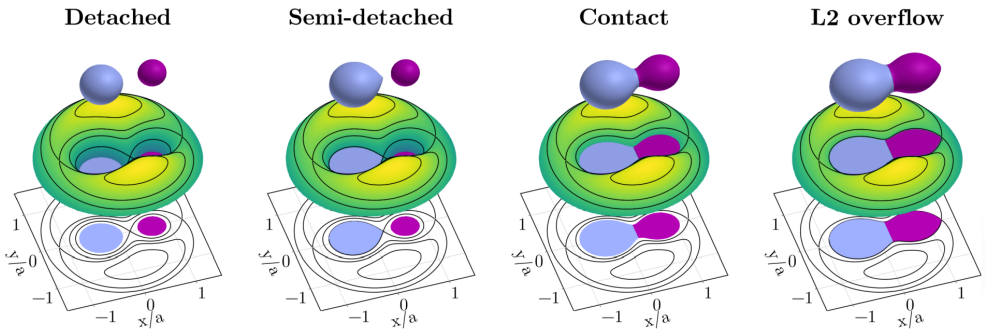

Figure 1.2: Binary types according to the Roche lobes filling, adopted from Marchant (2025).

The appropriate geometry of the binary star allows to observe periodic decreases in brightness. The general and well-known explanation of these changes is the propagation of the orbital motion when the stars eclipse each other during the periodic cycle. These objects are, thus, referred to as the *eclipsing binaries*. The variation period is equal to the orbital period. Hence, in one cycle, two brightness minima on the light curve, primary and secondary, are observed. For most cases, the primary minimum occurs when the primary (more luminous) component is eclipsed by the secondary one. A suitable geometry is necessary to observe the eclipses. The inclination angle i is defined as the angle between the normal to the orbital plane and the observer's line of sight. Using a notation $R_{1,2}$ for the components' radii and $a = a_1 + a_2$ for their mutual distance, the inclination value must be:

$$\sin\left(90^\circ - i\right) \geq \frac{R_1 + R_2}{a}, \tag{1.5}$$

to fulfill the condition for the eclipses (Hilditch, 2001). The probability of the eclipses increases with the shorter distances between the components. The inclination angle can be close to 90° for detached eclipsing systems (when $i = 90^\circ$, the orbital plane is coplanar with the plane of the line of sight). However, when the closer systems are discussed, the eclipses can occur for lower i values, i.e., 70° or smaller. The periodic brightness variations can be observed, nonetheless, without eclipses, for example, in the case of ellipsoidal binaries. Due to the non-spherical shape of the components, the surface area radiating towards the observer varies during the orbit, and the total brightness changes slightly.

The light curves are created from time series with time on the x-axis and magnitude or flux on the y-axis. Phase φ is plotted instead of time in a phase-folded light curve to see more clearly the brightness change. The phase is related to the orbital period P and the zero time M_0 (typically the time of the primary minimum) as follows:

$$\varphi = \mathrm{frac}\left(\frac{t - M_0}{P}\right). \tag{1.6}$$

The phase ranges between 0 to 1 (usually, the phase-folded light plots extend this interval for clarity). The epoch E represents the number of orbital cycles from the zero time M_0 (also referred to as the zero epoch):

$$E = \mathrm{floor}\left(\frac{t - M_0}{P}\right). \tag{1.7}$$

The eclipsing binary stars are divided into three main classes according to the light curve shape. These types are depicted in Figure 1.3. The classification does not precisely follow the morphological nature of the stars.

- *Algols (EA)*: Algol-like light curves usually have well-defined and narrow eclipses. The minima depths could be similar with almost identical components, or they can differ significantly in the case of different temperatures. The morphology types of these binaries are detached or semi-detached. The brightness outside the eclipses is constant or slightly varies due to other effects, i.e., reflection, accretion disk, and ellipsoidal shapes. The orbital period values are commonly long, several days or more (for non-degenerate systems).

- *β Lyr type (EB)*: The brightness varies continuously during the orbit cycle. The stars are tidally distorted into ellipsoidal shapes. The important sign for this type is the considerable difference between the depths of primary and secondary minima. This observation indicates the different effective temperatures (and radii) between the components. The components generally belong to early spectral types (B-A). The variation periods are primarily around 1 day or several days.

- *W UMa type (EW)*: The light curve shape continuously varies as in the previous case. However, the minima are almost identical with only minor differences. The components generally belong to spectral types F-G and later. These systems are classified as double contact or overcontact binaries with short orbital periods, typically less than 1 day.

A total velocity v of the studied object can be divided into radial v_r and tangential v_t parts, while it applies that $v^2 = v_\mathrm{t}^2 + v_\mathrm{r}^2$. The tangential velocity is analysed using astrometry and proper motion measurements. The velocity in the radial direction (toward or away from the observer) is derived from the wavelengths of the spectral lines. The Doppler effect causes a shift of the spectral lines relative to their rest wavelengths λ_0 for the stars with non-zero radial velocity. Thus, the spectral line can be found in the shifted measured wavelength λ. The radial velocity is then calculated using the general formula:

$$\frac{v_\mathrm{r}}{c} = \frac{\lambda - \lambda_0}{\lambda_0} = \frac{\Delta\lambda}{\lambda_0}, \tag{1.8}$$

where c is the speed of light. The redshift (spectral lines are shifted to the red edge of the spectrum) occurs when the object moves away from the observer with $v_\mathrm{r} > 0$. The blueshift is defined for the opposite situation ($v_\mathrm{r} < 0$).

In the case of spectroscopic binary, the spectral lines are shifted periodically. The wavelength and radial velocity variability are caused by the orbital motion of the components around their centre of mass. Moreover, the system can move with its systemic radial γ velocity. When only one component is detectable in the spectrum, the system is classified as a single-lined spectroscopic binary (SB1). In contrast, the spectrum of a double-lined spectroscopic binary (SB2) contains the spectral lines of both stars. In multiple systems, the lines of all system components could can be generally found (depending on the observational technique and components' luminosities). Then, these systems could be referred to as SB3, SB4, etc.

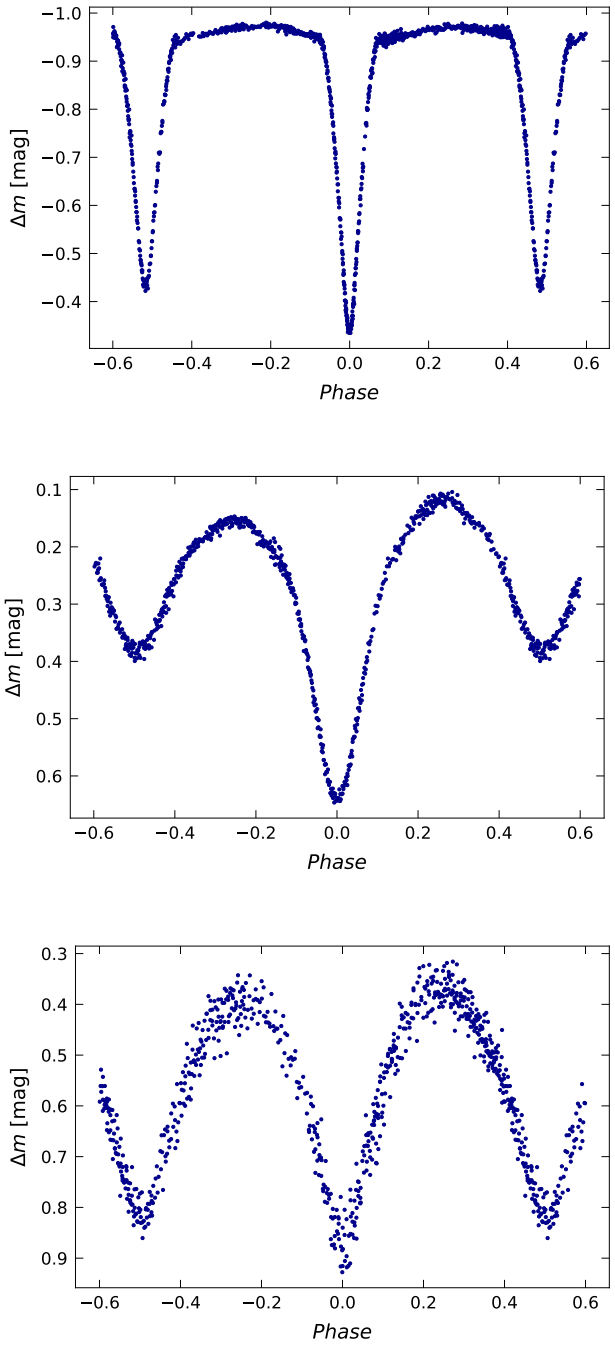

Figure 1.3: Eclipsing binary types according to the light curve shape, Algol type (CO Lac), β Lyr type (V474 Lac), and W UMa type (ATO J320.1286+51.7924). The example light curves were measured by Jakub Kolář and Miloslav Zejda at the observatories in Ždánice and Brno during the years from 2017 to 2022.

The radial velocity curve can be plotted as a time or phase-dependent function. The shape of the curve depends significantly on the system's geometry and mass ratio q between the components. Two sinusoidal variations during the orbital cycle are observed for a circular trajectory (Figure 1.4, for instance). Elliptical orbits and additional phenomena (multiple stars, exoplanets, spots, etc.) deform the shape of

the radial velocity curve. The second-order effects are also visible in the spectra, and can be modelled. The Rossiter-McLaughlin effect is caused by stellar rotation and occurs during the beginning and end of the eclipses when the parts of the star with different rotational velocities are eclipsed. This effect causes the distortions on the radial velocity curve around the eclipse phases (Figure 1.4).

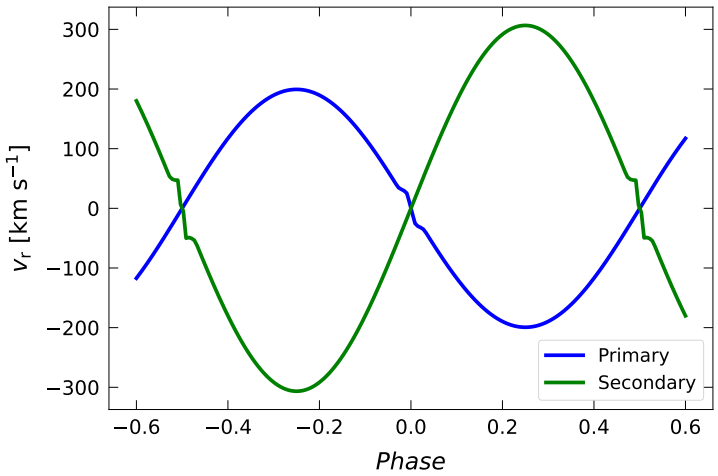

Figure 1.4: Synthetic radial velocity curve as a function of orbital phase, created in PHOEBE (version 0.32) software (Prša and Zwitter, 2005). The simulated binary consists of two main sequence components with the spectral types F9.5V and K9V for the primary and secondary star, respectively, with an orbital period of 1 day, inclination $i = 90°$, and mass ratio $q = 0.65$. The circular orbital trajectories and zero radial velocity for the centre of mass are assumed. The stellar parameters were adopted from Mamajek (2019), the simulation includes the Rossiter-McLaughlin effect.

The radial velocity curve of the SB2 system, serves to derive mass ratio q between the binary components. Using the velocity amplitudes K_1 and K_2 for primary and secondary stars, respectively, the q is given by:

$$q = \frac{m_2}{m_1} = \frac{K_1}{K_2}. \tag{1.9}$$

The mass ratio cannot be derived for the SB1 systems. It is possible to determine a mass function f_{m_2}, which defines the lowest possible mass of the secondary component, invisible in the spectra:

$$f_{m_2} = \frac{(m_2 \ \sin i)^3}{(m_1 + m_2)^2} \leq m_2. \tag{1.10}$$

Studying the spectra and spectral lines can lead to obtaining several essential parameters for the components and the system, i.e., effective temperatures, mass ratio, surface gravity, and systemic radial velocity of the centre of mass. The spectroscopic binary may also be identified as an eclipsing system, enabling a combination of spectroscopy and photometry.

Binary systems play a key role in stellar astrophysics. Various types of stars can be found in binaries systems, including the different spectral types and evolutionary

stages. A detailed analysis provides unique information about the stellar structure and evolution, and adds valuable general statistical knowledge. Measuring their variabilities using a combination of photometry, spectroscopy, and other methods can serve to derive the essential parameters (i.e., masses, radii, and distances) and also analyse the second-order effects (limb darkening, reflection effect, spots, etc.). The stellar mass is probably the most important parameter that could be acquired from the binary star study. It is generally not trivial to obtain the mass and binary stars present a precise method for calculations of this crucial parameter. The derivation of the minima timings and long-term period analysis could lead to a more detailed investigation of the system, such as mass transfer, apsidal motion, the presence of additional bodies, etc. The importance of binaries can be seen by studying larger and more complex objects such as multiple stellar systems, star clusters (Torres et al., 2018; Southworth et al., 2004), our Galaxy, and other galaxies, such as the Large (LMC) and Small (SMC) Magellanic Clouds. For instance, the distance to the LMC was derived by Pietrzyński et al. (2019) with 1 % precision using the analysis of eclipsing binaries.

1.2 Higher-order systems

Binary stars are applied in the structure of multiple stellar systems for a long-term stable solution (Tokovinin, 2021). The binarity levels can be observed in the multiple-star schemes (Figure 1.5, 1.6). A triple star consists of a close binary and a distant third component ($2 + 1$ hierarchy, Figure 1.5). The close inner binary creates a subsystem, where two binary components orbit their local centre of mass with the inner orbital period $P_{\rm in}$. On the higher binarity level, the inner binary orbits together with the additional third component around their common centre of mass with the outer period $P_{\rm out}$.

Two scenarios for a dynamically stable quadruple system: $2 + 2$ or $3 + 1$ (Figure 1.6) are possible. The $3 + 1$ configuration follows the previous case of the triple star and contains another fourth component with a larger distance. Hence, the outer orbit consists of the motion of the distant fourth star and the inner triple. In the $2 + 2$ quadruple system, two binaries orbit each other on the highest binarity level. The binaries are referred to as pair A and pair B, consisting of the primary (1) and secondary (2) components. Both binary stars have the inner orbital periods $P_{\rm A}$ and $P_{\rm B}$ for pairs A and B, respectively. Thus, the common outer orbital period is noted as $P_{\rm AB}$. Higher multiples are structured using the mentioned patterns and follow the binarity hierarchies (the pairs or the distant components).

As the number of components increases, the number of known hierarchical multiple systems decreases (Tokovinin, 2023; Offner et al., 2023). There are two main reasons to explain this phenomenon. Firstly, the decrease is a natural physical property. The systems with more components are less common due to the difficult creation process. In addition, multiple systems are more demanding to discover. Many selection effects are known, i.e., photometric precision, data cadence, and lack of spectroscopic observations (especially for faint stars). Multiple systems may sometimes fail to exhibit significant variability, particularly in terms of brightness changes. They could be non-eclipsing due to the system's geometry. Thus, the discovery is usually more challenging and requires different observing methods than only photometry.

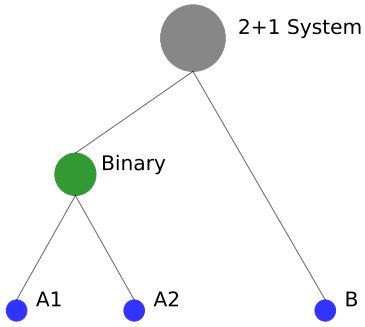

Figure 1.5: The schematic hierarchy of a triple system.

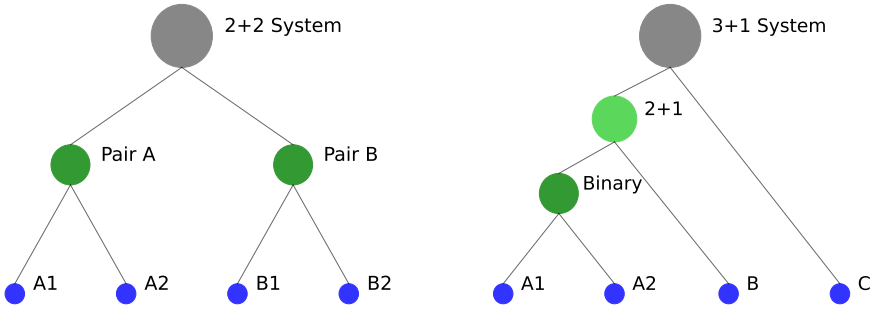

Figure 1.6: The schematic hierarchy of a quadruple system, left: 2+2 structure, right: 3+1 structure.

Quintuple eclipsing systems are known in several cases, e.g., HD 155448 in Schütz et al. (2011). Rappaport et al. (2016) comprehensively analysed two angularly separated eclipsing binaries in a quadruple system EPIC 212651213. The close star EPIC 212651234 is at the same distance as the EPIC 212651213. Moreover, radial velocities and proper motions of EPIC 212651213 are significantly similar to EPIC 212651234, indicating the systemic motion of a gravitationally bound (2+2)+1 quintuple star case. Lohr et al. (2015) studied a structured quintuple system 1SWASP J093010.78+533859.5 (V441+V442 UMa) containing the contact and detached eclipsing binaries and an additional star. Powell et al. (2021) comprehensively analysed the eclipsing sextuple system TIC 168789840, which consists of three gravitationally bound eclipsing pairs. A 2+2 quadruple star orbits around the global mass centre together with a more distant binary subsystem with an estimated outer period of around 2 000 years. Zasche et al. (2012) presented the 65 UMa system as a sextuple star with one eclipsing binary (known as DN UMa). In the Multiple Star Catalog by Tokovinin (2018), it is referred to as a septuple system. The instance of an octuple stellar system could be γ Cas (Hutter et al., 2021) with non-eclipsing components.

QZ Car is probably the highest multiple system consisting of nine components where at least a weak gravitational bound is still observable (Mayer et al., 2022; Brož

et al., 2022). This system contains one spectroscopic and one eclipsing binary. Multiples with around eight, nine, or more components (depending on the structure and stability) pass to more free objects with usually very low gravitational interactions, such as stellar associations, moving groups, and open clusters.

Binaries and multiple stars are formed in the giant molecular clouds. The collapse of the cloud starts due to a density turbulence of cold gas induced by several mechanisms, such as near supernova explosion, cloud collisions, etc. The clouds collapse inhomogeneously and fragment into smaller-scale structures called filaments. The fragmentation continues to create clumps and, later, the stellar cores (protostars) (Tokovinin, 2021).

Two main processes lead to the formation of the binary system: disk instability and core fragmentation. A massive dense disk is located around the protostar. The disk becomes unstable due to its high density, and the matter accumulates to form the secondary component (or possibly more stars). For the core (or filament) fragmentation scenario, two protostars interact with each other and create a gravitationally bound system. According to Offner et al. (2023), the length scale for this type of formation is typically around 0.1 pc. As a result, originally independent protostars can enter their orbits and become gravitationally bound.

Similar formation processes can also be observed for more component multiples. Tokovinin (2021) proposed five scenarios for forming multiple hierarchical systems: sequential and later disk instability, sequential core fragmentation, cloud collisions, and dynamical interactions. The known mechanisms from the binary formation and their combination are applied. The collisions and dynamical interactions are also noticeable. They can lead the independent protostars to mutual orbit and gravitational bond.

Significantly distant components in the multiple systems could evolve independently. Their common motion around the centre of mass occurs, but their mutual interactions and dynamical perturbations could be negligible if the hierarchical structure is long-term stable. For instance, the outer third component in the triple system only affects the inner binary when it is in close vicinity. The dynamical effects are not so strong for the circular trajectories and coplanar orbits. This geometry allows the systems to stay on the stable configuration. On the contrary, elliptical trajectories with the different inclinations tend to be dynamically unstable. The orbital period change, inclination and eccentricity variations, and other possible effects can play role.

1.3 2+2 quadruples

As mentioned above, the 2+2 hierarchical structure presents one possibility for a long-term stable solution for quadruple systems. Figure 1.7 depicts the mutual outer motion of both binaries around their common centre of mass. Each pair has its orbital velocity v_A and v_B. Equation 1.2 also applies to the case of a system with two binaries. The 2+2 quadruple is usually observed as one source of light. Both binary subsystems could be optically resolved when the angular distance is sufficiently large. Zasche et al. (2019) summarised the known pairs with the pair A and B angular resolution. Fezenko et al. (2022) found seven new 2+2 quadruple systems with typical angular resolution around several arcsec.

This hierarchy is approximately four times more frequent than the 3+1 configuration (Tokovinin, 2021). The natural representation for each arrangement is uncertain

due to many observational selection effects. The 2+2 structure is more photometrically observable because of the possible eclipses of one or both binaries. In the 3+1 case, the orbits would not have to meet the conditions for the eclipses, leading to the eclipses being rare and difficult to detect. Also, the outer periods for the distant third and fourth components could be very long (longer than our possible observing timescale). Thus, the outer eclipse could be missed during the observations. Other measurements (i.e., spectroscopy and astrometry) can also be generally used to detect quadruples. However, these methods are usually more time-consuming and have more constraints than photometry. For instance, photometric observations can identify and study faint quadruples, but current spectroscopic measurements are limited. For the 2+2 systems, the inclination condition for eclipses could be more easily fulfilled. The known orbital periods for each binary are relatively short (up to several days) in many cases. Therefore, the eclipses can lead to increased observational detection for the 2+2 systems.

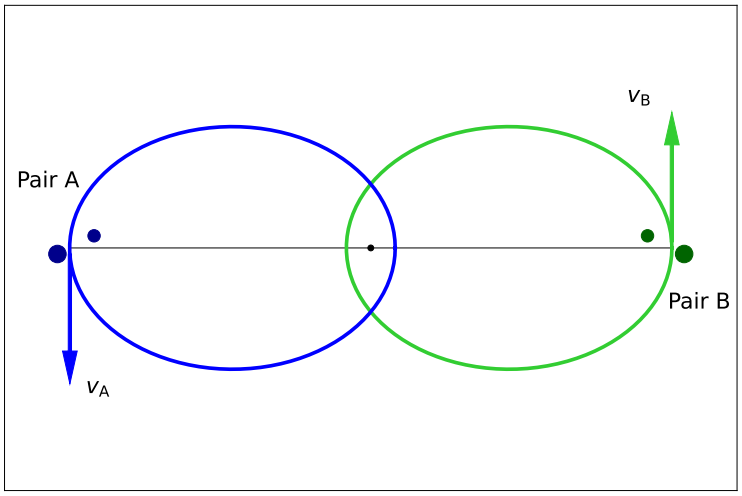

Figure 1.7: Structure of a 2+2 quadruple system.

When the system's geometry is suitable, we can observe both pairs as eclipsing binaries. These objects are generally known as *doubly eclipsing systems*. Therefore, the light curve shows two sources of periodic brightness variations. We can study these systems in greater detail due to both pairs' eclipses. Using a combination of mainly photometry, spectroscopy, and long-term monitoring, the parameters of the individual components can be derived. Moreover, the observations can confirm the gravitational interaction between the pairs with the outer orbit's parameters. Furthermore, these objects give a better understanding of the quadruples and other multiple stellar systems.

The 2+2 quadruples were initially discovered only sporadically without a systematic searching method. The first known and well-studied doubly eclipsing system is V994 Her (Lee et al., 2008). Zasche and Uhlař (2016) updated the data and stated that both eclipsing pairs have an apsidal motion visible in their $O-C$ diagrams (Chap-

ter 2). They also corrected the outer orbital period to the current value of 2.9 years. Vokrouhlický (2016) computed the secular variations for 2+2 quadruple systems. The paper used V994 Her as a numerical instance for these calculations. The essential assumption for the simulation is a proper knowledge of the orbital parameters. However, only a few systems nowadays have a comprehensive analysis that would make the secular variations meaningful. New research from Zasche et al. (2023a) describes the detection of other eclipses (pair C) from the TESS data and ground-based observations, deriving the system V994 Her as a sextuple star with three eclipsing binaries.

New candidates with two periods of brightness variations were found in the OGLE database (Pawlak et al., 2013, 2016). However, the first comprehensive research for searching the doubly eclipsing systems was done by Zasche et al. (2019), with a list of 146 candidates known at that time. Most of these systems were located in the LMC. The LMC overabundance was, however, caused by the selection effects of browsing the OGLE LMC data. In the following years, the TESS satellite has enabled a significant progress, and the number of 2+2 candidates has enhanced (Kostov et al., 2022, 2024; Zasche et al., 2022b). Other photometric data, i.e., the ZTF survey (Vaessen and van Roestel, 2024) and OGLE Bulge examination (Ádám et al., 2023), also contributed to bringing the total number of 2+2 candidates to around 1 000.

The precise population distribution in our Galaxy (and the LMC and SMC) of these systems is currently uncertain due to lack of a statistically significant dataset. However, the numbers are rapidly growing. With a large amount of available data, only a small fraction (fewer than 100) is nowadays confirmed as the quadruple system with two pairs. The vast majority is still referred to as the candidates. A frequency analysis should be done after excluding the blends and confirming the quadruple nature in the best case. On the contrary, the confirmation process is not trivial and requires very accurate measurements and a long observational timescale. The recent sample is too small for comprehensive statistics and general conclusions about the population frequency for these objects. There is presently no comprehensive theory explaining all formation and evolutionary processes. The formation mechanisms explained in Tokovinin (2021) are applied. However, the dominant mechanism for the 2+2 quadruples remains uncertain.

The unresolved open question of the long-term stability and possible preferred resonant states between the period ratio $R = \frac{P_{\rm A}}{P_{\rm B}}$ of the inner pairs was discussed in recent years. Zasche et al. (2019) made the inner period ratio distribution using their available sample and introduced some possible hints. The most discussed resonant ratios were 1:1, 2:1, and primarily 3:2. These values were described in Tremaine (2020) with the conditions of the resonant capture. However, too low number of known systems did not allow for observational evidence to be obtained at that time. The paper also discussed the properties of further period study and pointed out some observational hints. The current larger sample of the candidates allows to construct the period ratio distribution and also statistically analyse it. The indications for the higher 3:2 ratio frequency is noticed (Chapter 4). However, many other parameters are unknown. Some essential issues should be solved in time. Primarily, what is the frequency of the 2+2 quadruples and period ratio for each spectral type, what is the exact shape of the period ratio distribution and resonant state distribution in different evolutionary phases, is the Algol type dominant for the inner binaries and how much is biased by the selection effects, what is the blend ratio between the known candidates, etc. Answering these questions

properly and comprehensively is not trivial and observationally time-consuming. For instance, the outer orbital periods $P_{\rm AB}$ could last for decades or longer. One orbital cycle, or at least its majority, has to be detected and explained with certainty. The evolutionary state and all fundamental parameters (masses, radii, etc.) are known for only a few of the systems (Zasche et al., 2023a; Pejcha et al., 2022; Powell et al., 2025). Large amount of different types of data are usually missing for the faint stars, especially the spectroscopic observations are not commonly available for all the 2+2 candidates.

In recent years, quadruple stars with the 2+2 configuration have been on the rise. The number of newly detected candidates is still growing (Kostov et al., 2022, 2024; Zasche et al., 2022b), and their research state is improving with better observational techniques and analysis processes. For the reasons mentioned above, this unique class of astronomical objects represents an excellent laboratory for studying structures, evolution, and period properties of multiple stellar systems. This research mainly focuses on the observational and statistical analysis of the doubly eclipsing systems.

Chapter 2

Analysis methods

2.1 Photometric detection

The most common observing technique for detecting a doubly eclipsing candidate is photometry. This method presents a straightforward and relatively easy way to measure the additional brightness variations and recognise the eclipsing origin. Usually, one binary (typically noted as pair A) is already known. By a deeper analysis of its light curve from the photometric sources, other periodic brightness declines can be found (pair B). Confirming the additional signal as the eclipses and excluding other variability types is also necessary.

Several detection criteria need to be fulfilled. Amplitudes of both pairs (including primary and secondary minima) have to be sufficiently large than the scatter. All the eclipses need to be clearly identifiable in the data. Eclipse detection depends primarily on the system's composite brightness and the inner orbital period. The object must be well-measurable, and the observational technique should be selected according to its precision. The scatter usually depends on the brightness limits. The brightness-scatter dependency is illustrated in Figure 2.1 for the TESS sector 1 data. The orbital period of pair B could be a crucial parameter in the search for doubly eclipsing systems. The period values can be significantly long (several or dozens of days). Therefore, detecting these periodic variations can be challenging. However, very short periods (up to 1 day) also have several issues. The light curve type of these binaries is typically EW. These brightness variations can be confused with pulsations, stellar spots, and other similar light curve shapes.

The periods can be close to 1 day or its multiples and integer fractions in some cases. The eclipses are more challenging to capture due to the data sampling. The resonant period ratio between the pairs can cause misleading results regarding the amplitude and nature of the pair A light curve, potentially leading to the pair B changes being overlooked. The system ASASSN-V J101521.33-595651.9 consists of remarkably similar variable signals with almost the same periods (both around 0.69 days) and amplitudes. Specific shapes arise on the light curve under these conditions (Figure 2.2). The brightness variations appear identical within the measurement when investigating only one TESS sector. The change can be seen when comparing several sectors, obtaining observations over a longer timescale. This extreme case could cause the variations to be identified as different kinds of variations instead of eclipses. These situations

are most frequent for the EW binaries, where the light curve analysis alone could be uncertain.

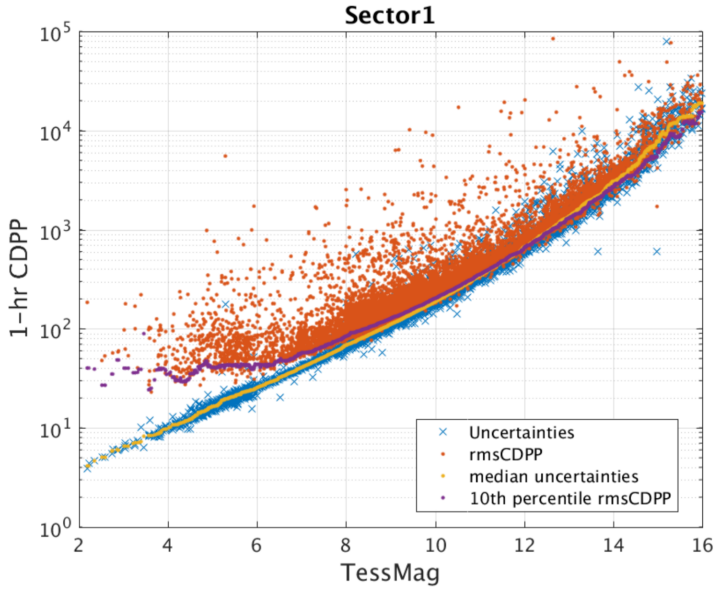

Figure 2.1: TESS photometric performance measured from sector 1, 1-hour combined differential photometric precision (CDPP), expressed in ppm (parts per million), adopted from TESS Observing technical details, tessgi.github.io/TessGiWebsite/observing-technical.html.

Significantly different combinations of inner periods and amplitudes of pair A and B can be observed. This can lead to many selection effects and misinterpretations. The orbital period could be well-derivable, but the amplitudes under the observational limits. The WISE J230200.8+405840 system serves as a good instance where pair A primary eclipse depth is above 0.10 mag in the TESS data, with the period value almost 1 day. The pair B, on the contrary, shows shorter periodic variations ($P_{\rm B} \approx 0.31$ days) but with significantly lower amplitudes of only 0.01 mag. Hence, a reliable data accuracy is difficult to obtain. The system is discussed in greater detail in Chapter 5. For some systems, the pair B variations are prominent, but the period is too long to be readily detected (e.g., TIC 79140936 in Kostov et al. (2022) with the period values of 3.5 days and nearly 31 days).

These conditions define the search process and the data usability. A single night observation is insufficient confirm the discovery of a new doubly eclipsing candidate. Continuos, high-quality data over a longer timescales are required. As the first step, photometric surveys are used for finding new objects that would be further analysed.

The potential blend with another binary in the close angular vicinity must be excluded. Additionally, long-term monitoring is one of the key methods to confirm the candidate as the 2+2 quadruple star, using primarily the $O-C$ diagrams (Section 2.4). Thus, several suitable photometric datasets should be combined to acquire as large a sample as possible. Ideally, new observations should be added as well. New kinds of variability are still being discovered. Without the comprehensive long-term study combining several observational sources, both multiplicity and additional phenomena

could not be discovered. The BG Ind system is one of the recently revisited quadruple stars (Borkovits et al., 2021) previously considered to be an eclipsing binary.

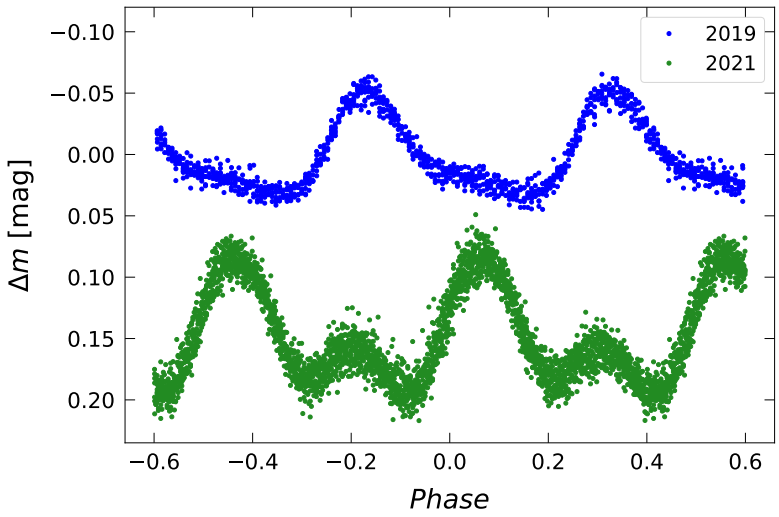

Figure 2.2: TESS phase-folded light curve of ASASSN-V J101521.33-595651.9, sector 10 from 2019 (upper part) and 36 from 2021 (lower part) obtained by differential photometry. The phase was calculated using the pair A ephemeris $P = 0.692710$ days and $M_0 = 2\,459\,281.364$ (HJD) (Chapter 4). The light curve shape stays almost the same within each sector, but changes over a long time, this course of variations is due to an almost identical signal B.

In recent years, the TESS satellite (Ricker et al., 2015) has allowed the study of new light curve phenomena and candidates for eclipsing multiples. Several new papers (e.g., Kostov et al. (2022, 2024); Zasche et al. (2022b)) have been published about the new on previously unknown systems. This survey is mainly used for bright stars (up to 12 mag). However, the data may still be usable for fainter stars up to 15 or 16 mag, if the variations are sufficiently large (at least 0.1 mag, e.g., Pačková (2024)). TESS is monitoring almost the whole sky, which is divided into sectors. The time span for one sector should be around 27 days, usually shorter due to instrumental matters. Moreover, the majority of observed stars have been measured multiple times.

The light curve continuity enables us to relatively easily detect other variations that do not follow the known eclipsing binary light changes. For example, Figure 2.3 shows the light curve of V1018 Cas as a time series and phase-folded. The additional pair B eclipses with lower amplitudes are visible in both cases. The first reliable pair B orbital period estimation can be done from the TESS light curve after disentangling the contributions of both pairs. The minima timings are derived from the disentangled light curves with high precision. Further study leads to a better determination of pair B period, although the TESS period analysis provides a significant first step.

The cadence of TESS data changes with the increasing sector numbers and target preferences. Some period values may be missed with these cadences. The observational precision also varies with this parameter, especially for fainter objects. The stars at the measurability limit are better observed with a lower cadence but longer exposure time,

allowing to obtain more reasonable data. With the shorter exposure, the precision of these systems is decreasing. New eclipsing stellar pairs with long orbital periods (with typical values of more than 20 days) could be overlooked when using only the TESS data. At most, one measured sector can only capture one eclipse. Generally, the TESS data should be combined for minima timings deriving and the period analysis. However, the number of measured sectors varies depending on the declination. Thus, TESS does not provide sufficient observations to catch the eclipses for these long-periodic pairs for certain parts of the sky, predominantly close to zero declination value. Various trends may be noted in the TESS data. The trend influence is a general issue for each photometric survey, but in it is primarily noticeable in the TESS light curves. The photometric data analysis and further study require detrending during the data processing.

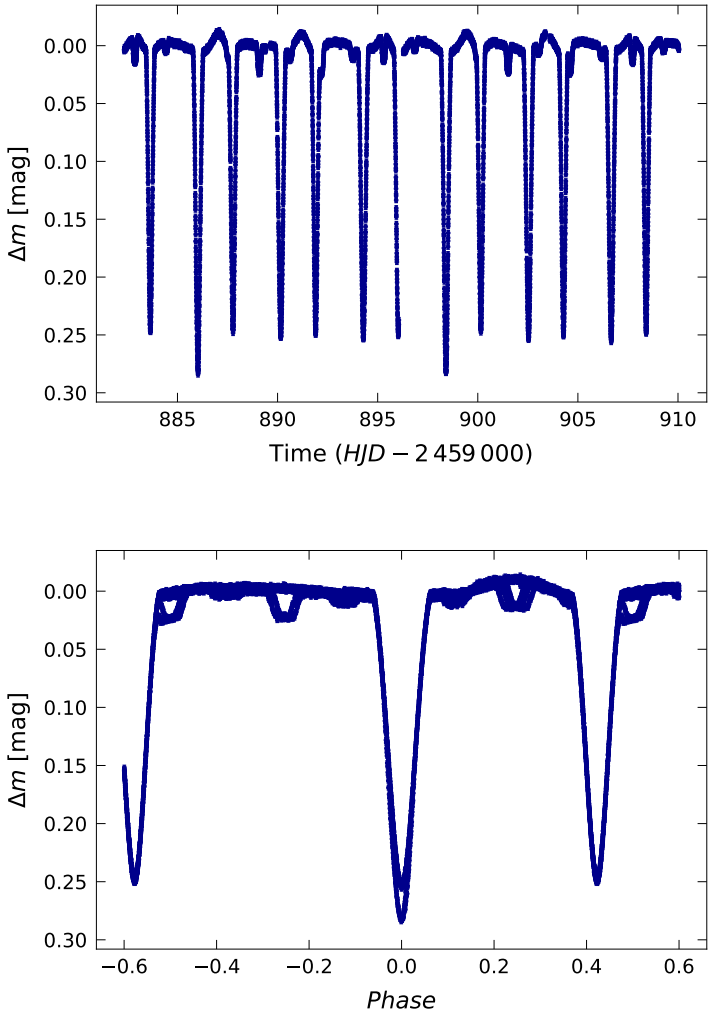

Figure 2.3: TESS detrended light curve of V1018 Cas (sector 58), time series (upper panel), and phase-folded curve according to pair A period $P_{\mathrm{A}} = 4.127745$ days adopted from Zasche et al. (2022b). Additional, significantly smaller brightness dimmings (pair B eclipses) are noticeable.

Despite high precision and good data cadence, TESS has a low angular resolution of 21 arcsec per pixel. This disadvantage arises significantly for the dense stellar fields. Figure 2.4 shows the TESS and DSS maps of the mentioned V1018 Cas (middle of the images). Two bright and well-resolved objects, HD 237050 and StRS 55, are visible together with the V1018 Cas. The DSS map shows other fainter stars close to the V1018 Cas that are only indicated in the TESS map. Even though they are fainter compared to the V1018 Cas, these stars still need to be considered during the analysis and excluded as a potential contaminating light. To conclude that two variable signals come from the same light source, the stellar catalogues and other data surveys need to be checked as a prerequisite. New photometric observations with high enough angular resolution and precision are the best way to identify the variation sources unquestionably. The nearest stars contaminate the studied object with the additional light. The eclipses are shallower because of the higher third light contribution, which must be included in physical models (Section 2.7).

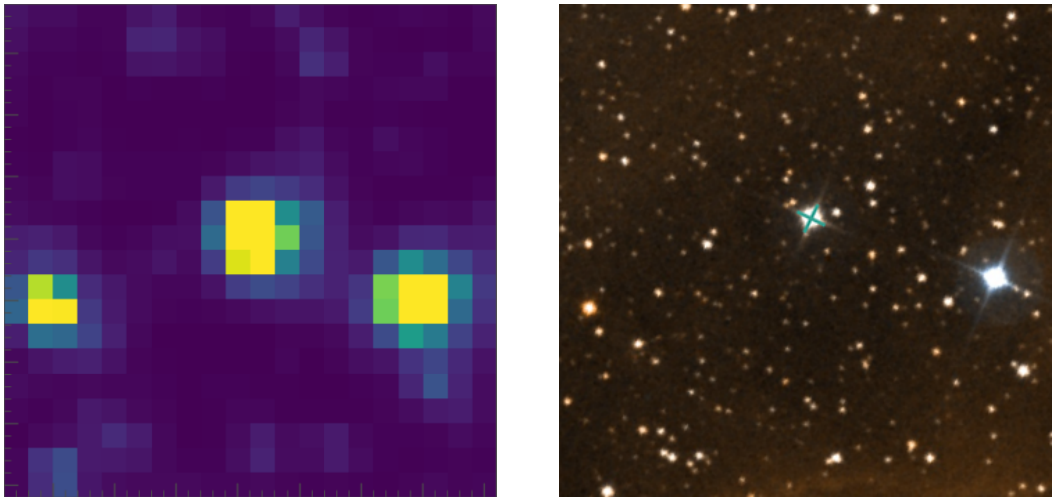

Figure 2.4: V1018 Cas and its vicinity with field of view FOV ≈ 7.1 arcmin, TESS map by Lightkurve Collaboration et al. (2018) (left panel), and DSS map (Lasker et al., 1996) (right panel), two bright stars, HD 237050 (the brighter and closer to V1018 Cas) and StRS 55, are noticeable in both maps.

Other, mostly ground-based, photometric surveys have substantially lower data cadence than the TESS light curves. On the other hand, the total observing timescale is usually longer. OGLE (Optical Gravitational Lensing Experiment) photometric survey (Pawlak et al., 2013, 2016; Soszyński et al., 2016) have been used in recent years to discover new doubly eclipsing candidates, especially in dense stellar environments, such as the Magellanic Clouds and the Galactic Bulge. Zasche et al. (2019) presented 146 known doubly eclipsing candidates up to date, with the vast majority of them located in the LMC. Nowadays, around 80 - 90 % of the known are in our Galaxy (Chapter 4) mainly due to the TESS data.

These time series generally have more regular and uniform data coverage over time than the TESS observations, which are divided into the sectors. The ground-based survey data can be phase-folded by knowing the pair A orbital period. Potential eclipses of the pair B are visible in this case as dimming that runs through the entire phase curve.

The time series of OGLE SMC-ECL-5925 and the phase-folded light curve according to pair A period, are shown in Figure 2.5. The pair B variations are then clearly identified in the residuals, which also allows for providing the basic period analysis to state the first estimate of the pair B inner period. The pair B visibility depends mainly on the system brightness, orbital period, and amplitude of light changes. The data cadence could also play a crucial role in detecting other possible variations in general. A number of pair B observations must be sufficient and individual measurements recognisable from the outliers. Inhomogeneities and more regular patterns in the phase curve can sometimes be observed when the pair B period is in resonance with the pair A.

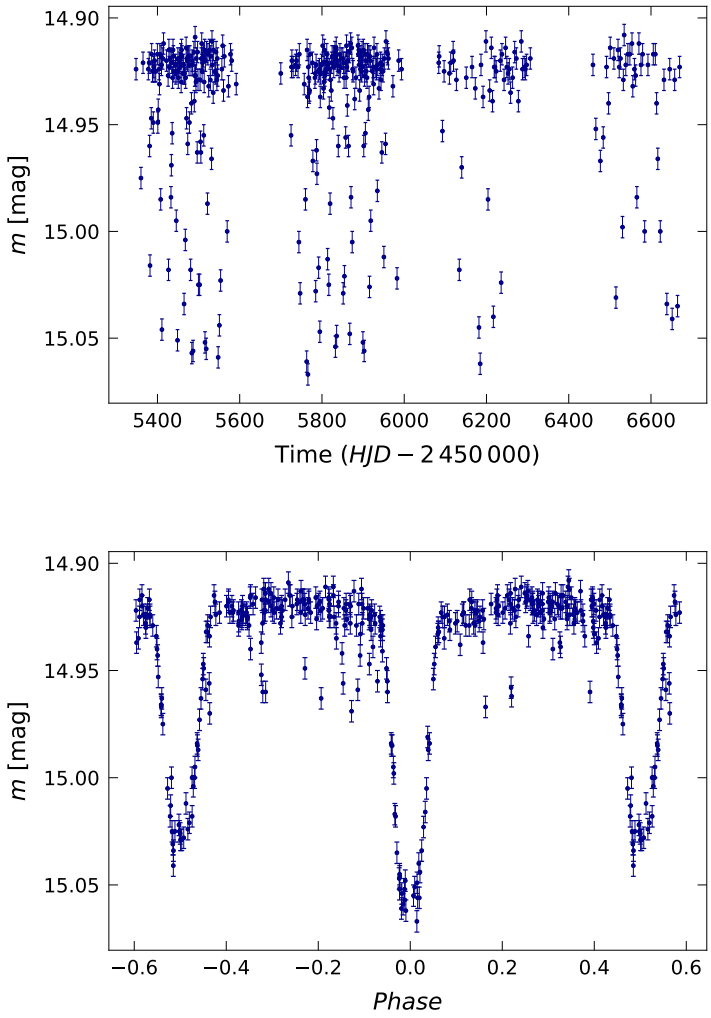

Figure 2.5: OGLE IV light curve of OGLE SMC-ECL-5925 in I band, upper panel: a time series, bottom panel: phase-folded light curve, the additional unphased eclipses are visible through the phase.

In most cases, photometric surveys, such as ZTF (Vaessen and van Roestel, 2024), ASAS-SN (Jayasinghe et al., 2019), and OGLE, have a higher angular resolution compared to the TESS satellite. However, the dense fields could still present an issue in correctly resolving the observed signals. The stars in their vicinity could contaminate them, potentially creating blends. Ádám et al. (2023) investigated the light curve

residuals of the known eclipsing binaries located in the Galactic Bulge observed by OGLE. They searched for the additional variability source after subtracting already known variations caused by eclipses, focusing mainly on the short periodic signals up to 1 day. They derived the period from the residuals and identified the variability type. A total number of 62 blends was excluded from their findings, and 246 new doubly eclipsing candidates were found. Zasche (2024) stated that 53 of these candidates are probably another blends. Additionally, the analysis in Ádám et al. (2023) reveals four new doubly eclipsing quadruples, where the 2+2 nature was proven by light time effect (LiTE) in the $O - C$ diagrams (more details in Section 2.4). This work is also important due to the EW systems with the short orbital periods, which are noticeably lacking in the doubly eclipsing candidate list.

Generally, the research should not rely on a single photometric data source. The use of more observations with different parameters (data cadence, observational time, photometric filter, etc.) to maximise the efforts to adequately prove other brightness variations is necessary. Studying the individual systems in more detail requires a comprehensive analysis to avoid the blends and suppress the selection effects. Additionally, the long-term monitoring is one of the key methods to confirm the candidate as a 2+2 quadruple star. Thus, several suitable photometric datasets should be combined to have as large a sample as possible. New own observations should also be added in the best case.

2.2 Light curves disentangling

The composite light curves must be disentangled into individual pairs. This step is essential for further analyses (predominantly deriving minima timings and accurate physical modelling). The iterative procedure, where the curves are alternately fitted by phenomenological or mathematical models, is a commonly used method of photometric data disentangling. The signal of one binary (A, for instance) is fitted and subtracted from the data as the first step. The residuals contain the pair B variations along with possible imperfections from pair A. Pair B is then fitted. The resulting pair B fit is used to subtract the pair B signal from the original data. Hence, the pair A light curve is obtained. This preliminary disentangling may not cover precisely all the light changes. It is necessary to repeat this procedure several times, depending on the light curve shape and the used models. The iterations are finished when the final residuals are unchanged within the scatter for both pairs.

SILICUPS (SImple LIght CUrve Processing System) software (Cagaš, 2017; Pejcha et al., 2022) enables the overview, maintenance, and analysis of photometric measurements. The phenomenological model function described in detail in Mikulášek (2015) is implemented in the software. The disentangling can be performed in the software using the function in the *Phased Curve Fit* tab. This process is typically finished after three or four iterations. Figure 2.6 shows the TESS phase curves of ASASSN-V J070838.27-171952.9 according to both inner orbital periods before and after the disentangling procedure using the SILICUPS software.

The mentioned model function is occasionally not suitable for the binaries with total eclipses. The resulting fit could not correspond in the phases around the brightness minimum, creating an additional trend. The sample of inaccurate total eclipse fitting

is shown in Appendices (Figure A.1). For these reasons, harmonic polynomials $H(\varphi)$ of degree n as a function of the phase φ are used to cover the parts with the total eclipses correctly:

$$H(\varphi) = a_0 + \sum_{i=1}^{n} \left[a_i \cdot \sin(2\pi i\varphi) + b_i \cdot \cos(2\pi i\varphi) \right]. \tag{2.1}$$

The polynomial degree should be selected according to the phase curve shape to cover adequately all the brightness variations. Generally, the n value could be large for the Algol-type binaries, especially where the brightness is constant outside the eclipses. The fitting was realised in Python using curve_fit from scipy.optimize package. This procedure helps primarily with the disentangling of the light curve containing total eclipses, but it can be commonly used for all types. Moreover, both methods, SILICUPS and harmonic polynomials model functions, can be combined to improve the final results. Other disentangling methods, e.g., the Fourier analysis, can also lead to disentangling the light curves. However, this thesis focuses primarily on the two mentioned methods, which provide reasonable results in most cases.

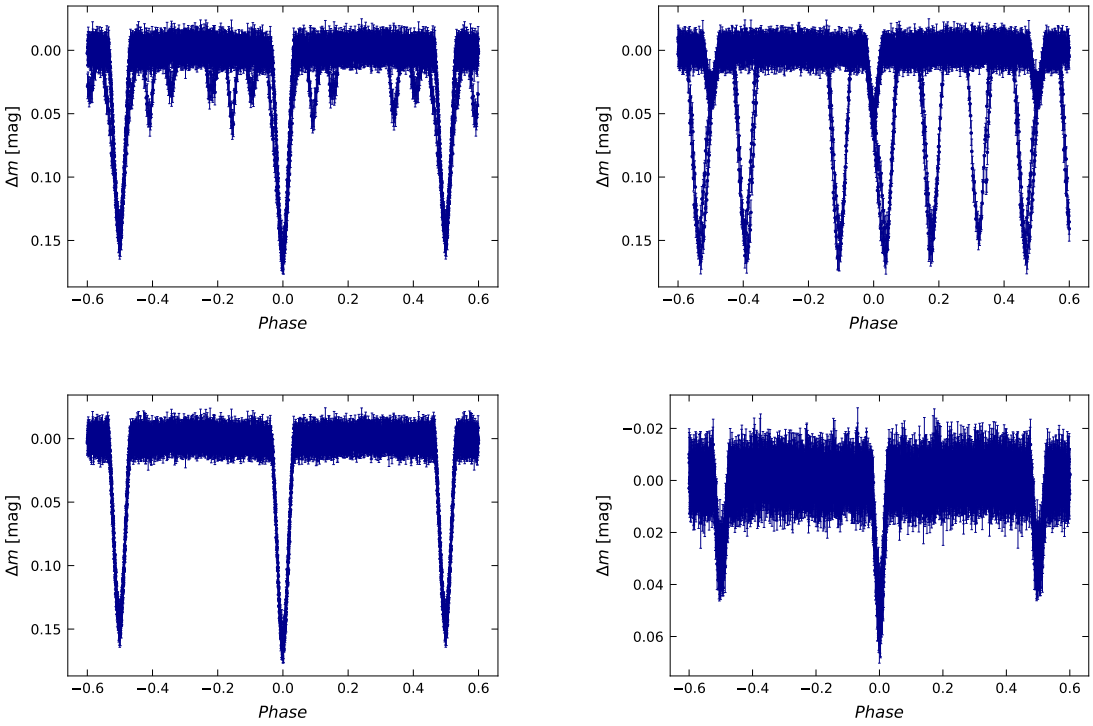

Figure 2.6: Phase-folded light curve of ASASSN-V J070838.27-171952.9 from the TESS satellite (sector 33), according to the known inner orbital periods $P_A = 4.300567$ days (left side) and $P_B = 3.767214$ days (right side) from Zasche et al. (2022b), original data (top), and disentangled light curves (bottom).

The photometric time series generally contain instrumental errors, outliers, and trends. Due to the continuous observations, the trend influences are mainly apparent in TESS and Kepler data (Ricker et al., 2015; Koch et al., 2010). However, all raw light

curves from various surveys could contain trends that affect the data. The trend effects have to be appropriately eliminated to provide a consistent and accurate research procedure. The automatic pipelines are not generally sufficient for all cases, and light curves should be assessed individually in every time series. The detrending process requires a good knowledge of the light variation course. After correctly subtracting the known brightness changes, only the trends should remain in the residuals. Then, the residuals with the trends are fitted by a suitable function and subtracted from the original light curves. There are several possibilities for choosing an accurate fitting method for detrending the data. The Chebyshev polynomials $P(x)$ of the n degree were used:

$$P(x) = \sum_{i=0}^{n} c_i \cdot T_i(x), \quad \text{where} \tag{2.2}$$

$$\begin{aligned} T_0(x) &= 1, \\ T_1(x) &= x, \\ T_i(x) &= 2x \cdot T_{i-1}(x) - T_{i-2}(x) \quad \text{for } i \geq 2. \end{aligned}$$

The Python package NumPy (specifically numpy.polynomial.Chebyshev.fit) was used. The script is already described by Pačková (2024) and Richterková (2025).

The doubly eclipsing stars are characterised by comprising two sources of eclipses. Therefore, the detrending is more difficult. Firstly, the light curves are disentangled by the process described above. The residuals after the disentangling should contain only the trend, which should be the same for both pairs. The fitted trend is subtracted from the raw data, and the disentangling is repeated using the iterative procedure. With the presence of the trends, the separated light curves could possibly contain slight deviations compared to the real variability after the first iteration. Thus, repeating disentangling and detrending is essential. The light curves are correctly disentangled, and the trend influences are maximally reduced when the residual curves stop changing and are the same for both pairs within the scatter. Figure 2.7 depicts the TESS light curve of ASASSN-V J222721.05+564425.3 before and after the detrending. Further light curve analysis containing minima timings derivation and physical modelling is possible when the detrending and disentangling processes are accomplished.

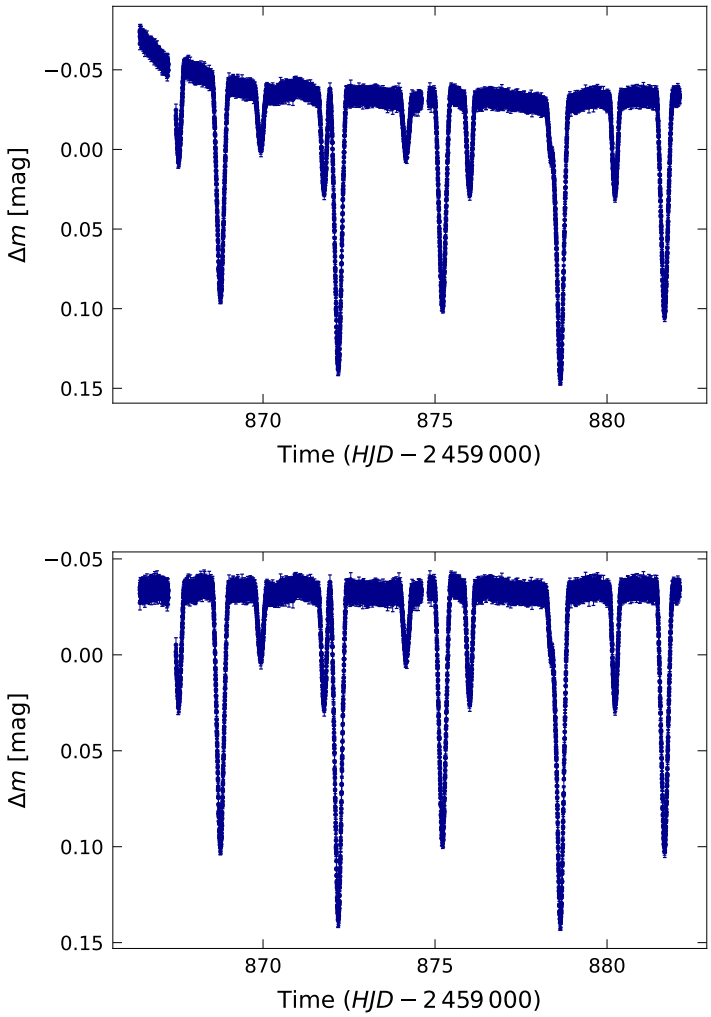

Figure 2.7: TESS light curve of ASASSN-V J222721.05+564425.3 (part of sector 57), top panel: original downloaded data, a relatively strong trend influence is readily apparent at the beginning of the time series, bottom panel: the same data after detrending.

2.3 Minima timings

One of the key methods for studying the periods of variable stars and detecting possible phenomena is the analysis of the $O - C$ diagrams (described in more detail in the following section). The diagram analysis generally includes the light curve extrema timings. The brightness minima are typical cases for the binary and multiple eclipsing stars. The observed minimum timings O are compared with the calculated (predicted) time C. Several different methods are used to obtain the observed timings, for instance, from Kwee and van Woerden (1956) in the past. However, using a specific method depends on many assumptions and data shapes. Sometimes, the correct result with realistic and trustworthy uncertainties is not achieved using inappropriate procedures. The data cadence, amount, quality, the eclipse duration and depth, the fact that the curves may not be symmetrical, etc., have to be considered.

The minima timings can be derived in the SILICUPS software (Pejcha et al., 2022). The fitting process uses the phenomenological function from Mikulášek (2015). The software allows for fitting the individual eclipses by manually setting the borders, between which the fit is performed. There is also an option to fit all the minima within the dataset. The P and M_0 parameters should be well-known together with the phase of the secondary minimum φ_s (assuming the zero phase φ_p for the primary one). The duration around every eclipse and the minimum number of points on the decreasing and increasing parts of the eclipse, need to be entered. These parameters, especially the durations, can be crucial in the fitting process, and it is recommended that the entire eclipse is covered. This method is less time-consuming and is mainly beneficial for continuous light curves with many observed eclipses, typically for TESS and Kepler data. There is an option to add the trend influence. However, it must be used with caution. The ideal case is to eliminate all instrumental influences during the detrending procedure. On the contrary, some light curve shapes can be strongly asymmetric, and the additional trend term in the fitting function could improve the fitting. It is always helpful to test how the minima timings are derived with and without the trend before considering this option.

The uncertainty estimation in SILICUPS is calculated using the bootstrapping statistical method. The bootstrap takes the same number of data points in the sample, some points are repeated, and some are missing (generally called resampling). The minimum timing is calculated using this new modified sample. The resampling and calculations are repeated, the SILICUPS error estimation contains 1 000 iterations (P. Cagaš, private communication). A histogram is created from these results to obtain the range of the error bar. The uncertainty value could generally vary when the estimation is repeated. The amplitudes of these variations are usually only minor fluctuations when using high-quality data with a large number of data points (around more than 100). The typical instance is the high cadence TESS sector. For the older datasets with significantly lower cadence (with only tens of points around the brightness minimum), the uncertainty value can vary significantly (sometimes several times in the extreme cases). It is important to correctly choose the borders on the light curve around the eclipse, if possible. The largest issues occur with short-periodic systems (when P is several hours) because the interval where the fit takes place has to be very short so as not to interfere with the next eclipse. The uncertainty should be primarily the higher value between the estimations in the case of significant changes. The estimation could lead to high uncertainty when the minimum lies close to the edges of the time series or the gap between data (mainly in TESS datasets). The timing should be derived manually to adapt the parameters rather than rely on the automatic fitting for all the minima.

Photometric ground-based surveys do not provide continuous measurements. The observations are usually composed into the dataset for a single season. The data points can have different cadences during this time. For instance, several photometric images of a specific object can be created in a few minutes, and other observations would be done after several days or weeks. It is not suitable to derive the minima timings from only a few points during one night. On the other hand, it is feasible to use all the seasonal data points and construct the phase-folded light curve.

According to the known ephemeris, the phase-folded data would suggest how the eclipse timings change in the observing time. The curve could be shifted against the

predicted model. The phase shift can then be fitted to align the data with the model light curve and calculate the $O - C$ value for the entire season. The data should be collected in the shortest time possible. However, all the brightness variations must be fully covered. The time O for one primary and one secondary minimum is obtained. Usually, these times are in the middle of the used photometric time series.

A simple Python code was created to derive the primary and secondary minima timings from the photometric surveys with non-continuous measurements. The inputs are based on the SILICUPS export files and fundamental parameters, but they can be generally obtained by other methods. The main data files that enter the code are the time series, phase-folded series, and residuals from the model light curve (phenomenological model function in SILICUPS). This modelling can be performed by merging several seasons to obtain more robust phase coverage (if possible, depending on the eclipse time variations). The other option is to use the well-known existing fit from TESS or own observations and modify it for the current survey (taking into account the differential magnitudes, and the phenomenological models are usually less complicated and relatively suitable for this modification). If these methods lead to insufficiently accurate results, harmonic polynomials or other similar functions can be used to achieve sufficient results. The outliers should be excluded from the data, as well as the two or more points with precisely the same time value (otherwise, the fitting will not work).

These files belong to every season, and the seasonal datasets used are fitted one by one. Additionally, period value, zero time epoch, and phase of the secondary minimum are essential to know. The orbital period does not change during the fitting process. It is recommended to keep one period value and adjust only the instantaneous zero time M_0, this change represents the actual physical variations within the fitting.

A model is created using the original residuals for each data point. The phase shift fitting moves with the whole phase-folded curve on the x-axis to find the smallest value for the sum of squares of the differences between data and model magnitude. The uncertainty estimation is done by bootstrapping using 1 000 iterations and the confidence interval of 95 %. The primary and secondary minima timings are then calculated from the phase shift fit described in the code below. The uncertainties for both minima timings are the same because the fitting includes all the data on the phase-folded curve. As mentioned, the time series used has the same value of the $O-C$ for all its data points. The main cause of this is that the phase-folded light curve and the fitting are done using all of these observations within the dataset (usually one observing season). Finer division is no longer possible because the light changes would not be adequately seen. The epoch in the middle of the time series is taken for the time O calculation and later construction of the $O - C$ diagram.

All the fitted and derived quantities can be printed, and optionally, the visualisation of the states before and after the fitting can be plotted (Figure A.3). A rough estimate of the instantaneous M_0 should be made as an initial state from which the fitting starts. The initial state slightly influences the uncertainties. The fitting is a reliable tool of the minima timings estimation from surveys. The apsidal motion or a combination of several effects can deform the light curve. These possible distortions should be considered individually for each season. It is necessary to derive the model light curve for the current time series and check the primary and secondary minima phases. The code can be used afterward, and all steps can be repeated iteratively if needed.

Script 2.1: Python code for deriving minima timings using photometric surveys.

```
#Data must not contain outliers
#Instantaneous M0 should be estimated for better fitting
#Two or more data points at precisely the same time cannot be used


#Packages import
import numpy as np
#import matplotlib.pyplot as plt #optional package for a
   visualization, depends on the user
import math
from math import *
import scipy
from scipy.interpolate import interp1d
from scipy.optimize import minimize


#Upload necessary data
#Ephemeris: period and instantaneous M0 (original M0, but shifted for
    the given time series for better fitting
#Phase of the secondary minimum for the given dataset (the primary
   minimum is always in phase 0)

P =
M0 =
phase_s =

#Time series
t, mag, err = np.loadtxt("path\\time_series.dat", unpack=True)

#Phase curve
phase, mag, err = np.loadtxt("path\\phase.dat", unpack=True)

#Residuals
t, mag_r, err = np.loadtxt("path\\residuals.dat", unpack=True)

model = mag-mag_r #model from SILICUPS
#-----------------------------------------------------------
#Fitting starts here


#Assuming these inputs:
#Phase: x-points, common for both sets
#Mag: first set (with phase that will be shifted)
#Model: second set (reference model, phase does not change here)
```

```
#The error function as a sum of squares: shifts the phase so that the
    sum of the squares of the errors is minimal
def error_by_shift(shift, phase, mag, model, model_phase, err):
    shifted_phase = phase + shift
    model_interp = interp1d(model_phase, model, bounds_error=False,
   fill_value="extrapolate")
    model_sampled = model_interp(shifted_phase)
    return np.sum(((mag - model_sampled) / err) ** 2)

#Phase shift fitting
result = minimize(
    error_by_shift,
    x0=0.0,
    args=(phase, mag, model, phase, err),
    method='L-BFGS-B',
    bounds=[(-0.1, 0.1)]
)
fitted_shift = result.x[0]

shifted_phase = phase + fitted_shift
model_interp = interp1d(phase, model, bounds_error=False, fill_value=
   "extrapolate")
model_sampled = model_interp(shifted_phase)


#Bootstrapping method for error of phase shift estimation
n_bootstrap = 1000 #Number of iterations
scale_factor = 1.0  #The error can be increased by the scale factor
   for more realistic estimation
boot_shifts = []


np.random.seed(100)


for _ in (range(n_bootstrap)):
    indices = np.random.choice(len(phase), size=len(phase), replace=
   True)
    phase_b = phase[indices]
    mag_b = mag[indices]
    err_b = err[indices]
    model_b = model[indices]

    mag_b_noisy = mag_b + np.random.normal(0, err_b * scale_factor)

    res = minimize(
        error_by_shift,
```

```
        x0=0.0,
        args=(phase_b, mag_b_noisy, model_b, phase_b, err_b),
        method='L-BFGS-B',
        bounds=[(-0.1, 0.1)]
    )
    boot_shifts.append(res.x[0])

boot_shifts = np.array(boot_shifts) #Array, mean, and standard
   deviation
mean_shift = np.mean(boot_shifts)
std_shift = np.std(boot_shifts)
ci_lower, ci_upper = np.percentile(boot_shifts, [2.5, 97.5]) #95 %
   confidence interval for phase shift


#Calculations of minima timings and uncertainties
t_middle = (np.max(t) + np.min(t)) / 2 #The epoch is derived for the
   middle of the time series
shift_t = -fitted_shift * P
E = np.floor((t_middle - M0) / P)
Cp = M0 + P * E
Op = shift_t + Cp #Primary minimum
Cs = M0 + P * (E + phase_s)
Os = shift_t + Cs #Secondary minimum
error_O = std_shift * P #Uncertainty is the same for both minima
   timings


#Visualization of the initial and final state can be added by
   matplotlib, optional, depends on the user by plotting the
   parameters phase with mag and phase with model (for the original
   state) and shifted_phase with mag and phase with model (the state
   after the fitting)


#Result list, can be set by the user
print("Results of the fitting")
print(f"Phase shift: {fitted_shift:.5f} ± {std_shift:.5f}")
print(f"Epoch: {E}")
print(f"Primary minimum: {Op:.4f} ± {error_O:.4f}")
print(f"Secondary minimum: {Os:.4f} ± {error_O:.4f}")
```

2.4 $O-C$ diagrams

The $O-C$ diagrams (also called eclipse time variations (ETV) in the case of eclipsing systems) represent a precise tool for studying period effects within the system. The observed O and calculated C times were introduced in the previous section. The observed minima timings are derived from the light curves using the suitable fitting methods described above. The C time is predicted to describe the period and the additional effects. The simplest case is a linear ephemeris. Assuming the constant period and the known zero epoch M_0, the next primary minimum time C is predicted as:

$$C = M_0 + PE, \tag{2.3}$$

where P and E are the orbital period and epoch, respectively. The $O-C$ diagram is a plot of the comparison between the observations and the predictions over time or epoch. The constant and correctly determined period shows no variations in the diagram. Therefore, all the points fluctuate around the zero value.

The inaccurate M_0 parameter causes the vertical shift. The $O-C$ diagram shows the shape of the oblique line if the orbital period is constant but inaccurately derived. The linear fitting and the C times recalculation with the new values can correct both M_0 and P parameters. The refinement leads to the line around the zero $O-C$.

The $O-C$ course can detect more complex phenomena over time. Non-linear models should describe the variations to study the effects adequately. A combination of multiple effects is also possible. Parabolic changes reveal a mass transfer between the components. The diagram shape indicates the period change (upward parabola for the period increase and downward parabola for the decrease). In the case of conservative mass transfer, total mass $m = m_1 + m_2$ and total angular momentum $\mathscr{L} = \mathscr{L}_1 + \mathscr{L}_2$ are conserved. These quantities are not constant in non-conservative mass transfer within the entire system. The basic description of these phenomena and the period change rate $\dot{P}$ is determined by a quadratic ephemeris:

$$C = M_0 + PE + QE^2, \qquad Q = \frac{P\dot{P}}{2}. \tag{2.4}$$

The apsidal motion is observed in some eccentric systems. The line of apsides changes periodically. The phenomenon is caused by the distortions in the components' internal structure. It can also occur due to relativistic effects or gravitational interactions with additional bodies (if present), which can affect the precession rate. The phases of primary and secondary eclipses vary with the apsidal motion period U. Two sine waves in the anti-phase are observed in the $O-C$ diagram. One cycle lasts typically several decades or longer (Hong et al., 2016; Švaříček et al., 2008).

Applying the $O-C$ analysis for the doubly eclipsing stars and multiples presents an important way to determine new knowledge of these systems. The study can reveal the gravitational bond between the pairs and their mutual outer orbit. Several different periodic phenomena can be observed on the $O-C$ due to the common orbit and gravitational interactions. The LiTE (Light Time Effect) is related to the system's geometry (Irwin, 1959; Mayer, 1990). The presence of the additional component influences the binary star, since the pair and the third body orbit their common centre of mass. The companion could be an additional star, a binary, or an exoplanet. More LiTE varia-

tions can exist simultaneously for the cases of multiple stellar or exoplanetary systems (e.g., TIC 9493888 (S1 Cam) in Chapter 3).

The true inner period of an eclipsing binary remains constant. However, the periodic sinusoidal variations caused by a third body are observed. When the binary is closer to the observer during the outer orbit, the light needs a shorter time to reach the detector. Thus, the eclipses will occur earlier with the negative $O-C$ value on the diagram. On the other hand, the second binary is more distant at that time. The light requires a longer time to be detected, which causes the positive $O-C$ against the zero value. This effect is repeated with the outer orbital period P_{AB} (generally noted as P_3 for the third body). Hence, the $O-C$ diagram shape is sinusoidal with the same variation course for primary and secondary minima. Assuming a coplanar outer orbit (outer orbit inclination $i_3 = 90°$), the mass function $f_m(m_3)$ can be derived as:

$$f_m(m_3) = \frac{(a_3 \sin i_3)^3}{P_3^2} = \frac{(m_3 \sin i_3)^3}{(m_1 + m_2 + m_3)^2}, \tag{2.5}$$

where the $m_{1,2,3}$ are the individual masses and a_3 the semi-major axis. The lower mass limit of the third body is estimated, providing a constraint between a stellar and an exoplanetary solution. However, the limit is typically underestimated.

The LiTE analysis is widely used for triple stars (Borkovits et al., 2016, 2022). Furthermore, it also serves well to confirm the quadruple nature of doubly eclipsing systems. The LiTE can be observed for both eclipsing binaries. Figure 2.8 shows the simulated situation of the doubly eclipsing quadruple with two equally massive pairs and an outer period of 10 years, assuming a circular orbit. The variations of both pairs must have the same outer period P_{AB} because the same periodic motion is observed. The shapes have to be strictly in anti-phase (as indicated in Figure 1.7). The masses of the binaries are generally different. With the mass and momentum conservation, the LiTE amplitudes A_{A} and A_{B} depend on the pairs' masses m_{A} and m_{B}. The mass ratio q_{AB} is then derived from LiTE amplitudes:

$$q_{\mathrm{AB}} = \frac{m_{\mathrm{A}}}{m_{\mathrm{B}}} = \frac{A_{\mathrm{B}}}{A_{\mathrm{A}}}. \tag{2.6}$$

Therefore, the LiTE analysis provides strong results because the mass ratio is derived only from the long-term photometry. LiTE could be accompanied by additional effects, most notably apsidal motion (e.g., Zasche et al. (2023b) and herein ASASSN-V J233336.79+615012.0 (S3 Cas) in Chapter 3).

The outer orbital periods can last for decades or hundreds of years. The confirmed quadruples with known or estimated outer orbit parameters are usually those with shorter periods, typically several years. However, the number of these well-described and comprehensively analysed systems is limited. Longer motions are usually beyond the current observational timescale.

Remarkably, there are quadruple systems with extremely short outer periods of less than a year. BU CMi, analysed by Pribulla et al. (2023), is the most compact case with an outer period of only 122 days. Powell et al. (2025) summarised the ten shortest outer periods (Table 1 therein), including two new compact systems, TIC 392229331 and 285853156. The periods are around 150 days long for both quadruples. Such binaries in these tight configurations cannot be formed in their current separation, but initially at a much wider distance. The formation and dynamical evolutionary

processes made the binaries go inward to the present observed state. All three orbits in each system (two inner binaries and one outer orbit) are almost coplanar. Interestingly, the eccentricities of the outer orbits are significantly high (more than 0.3). Powell et al. (2025) suggested that the primary formation process was the core fragmentation, followed by inward evolution (shortening the pairs' separation) due to the dynamical friction of the surrounding gas.

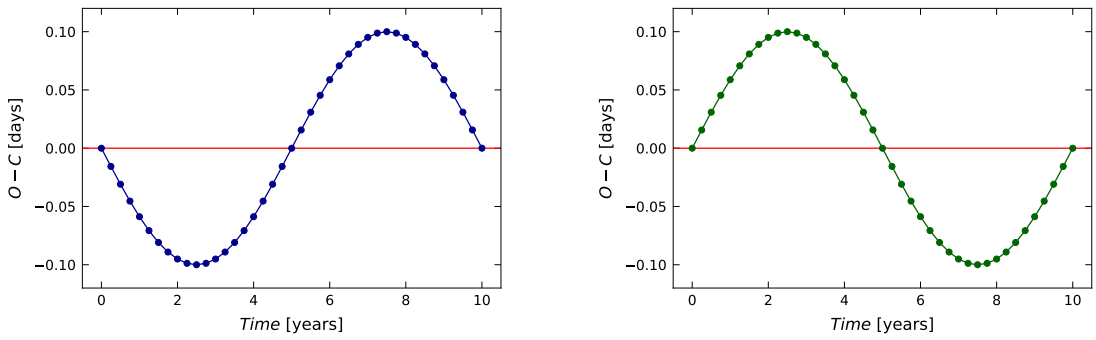

Figure 2.8: Simulated $O-C$ diagrams of the 2+2 quadruple system, assuming LiTE without further effects and a circular coplanar orbit. Both pairs have identical masses, the outer orbit period $P_{\mathrm{AB}} = 10$ years.

The dynamical effects are applied in multiple systems by the mutual interactions (tidal, gravitational, etc.) between the components (Borkovits, 2022). Here, two eclipsing binaries interact with each other. The $O-C$ description using only the geometric LiTE variations is not sufficient for these compact multiples. The dynamical effects have to be considered, especially for very compact structures. These interactions form a complex physical phenomenon. These periodic variations are measured primarily with the same outer period as LiTE. Two correlated sine waves are observed in the $O-C$ diagrams.

The dynamical effects can dominate the $O-C$ variations for remarkably short outer periods. The LiTE is observed to be more significant in the quadruple systems with their outer orbital cycles several years long. Rowden et al. (2020) derived the outer period for TIC 278956474 to 860 days (2.36 years). The strict LiTE variations are noticeable in the $O-C$ diagrams with no apparent signs of dynamical perturbations. Zasche et al. (2019) made a graph with the outer periods and the ratio between LiTE and dynamical amplitudes (Figure 1 therein). With the typical P_{AB} values of several years, LiTE amplitudes are higher in orders of magnitude. A similar case is probable for the ASASSN-V J000432.60+632605.0 (S1 Cas) system (more details are provided in Chapter 3). The dynamical effects are possibly not negligible in these systems, but their influence is minor.

2.5 Spectral energy distribution

The spectral energy distribution (SED) is the flux density as a function of wavelength λ or frequency ν. This thesis uses the wavelength in Angströms [Å] on the x-axis and

the flux density per unit wavelength F_λ in erg/s/cm^2/Å on the y-axis. Both axes are on logarithmic scales. The SED of stars and multiple systems can be investigated as blackbody radiation. However, this approximation presents only the first step. Considering the stellar atmosphere templates, for instance, the widely used Castelli and Kurucz (2003) models, is more appropriate to describe the radiation reliably.

The SED analysis examines the object using the multi-band photometry. Each filter does not create monochromatic radiation but has a defined wavelength range. The flux density is generally time-dependent for the variable stars. The observations taken during or out of the eclipses can differ. Therefore, each data point should contain the precise information on the wavelength range and time of observation. The observed flux is affected by the extinction, whose influence must be eliminated before the SED analysis.

The main result of the SED fitting is the effective temperature, and further, the surface gravity $\log g$, and the metallicity. All the components contribute to the total flux in an unresolved binary star or multiple system. Figure 2.9 depicts the composite SED of TIC 219006972 and the individual components, adopted from Kostov et al. (2023). The final SED output is a composite temperature of the entire system. The SED presents a valuable temperature estimation tool when comprehensive spectroscopic data to model the individual components are lacking. The estimated fitting value serves as the maximum limit for the components. This constraint should be used with caution and considering the other parameters. The light curve shape, in more bands ideally, can reveal the temperature ratio estimation between the components. When the primary and secondary eclipse depths differ significantly, the primary star dominates the system, and its temperature is higher compared to the others. The temperatures are relatively equal when the primary and secondary eclipses are identical.

The components can deform the composite SED shape. They can enlarge the flux in the specific bands, which only a single object would not cause. This overall composition could affect the final SED fitting. Using the composite temperatures has the limitations defined by the mentioned factors. Several surveys provide temperature measurements using different methods. Gaia DR3 (Gaia Collaboration, 2023) is one of the most common. However, the automatic pipelines could overlook important details and provide misleading outputs. For instance, the surrounding stars could influence the measurements, and the observations during the eclipses would change the colour index. For these reasons, the SED modelling provides an independent composite temperature source that takes into account the individual properties instead of the automated fitting. Chapter 3 compares the SED temperatures with Gaia, TESS (Stassun et al., 2019), and StarHorse (Anders et al., 2019) catalogues. The mentioned issues involve the binaries and multiple stars in general. The quantities derived from the SED are essential for advanced research. The fitting results should be the standard initial parameters that should be available in catalogues in the near future.

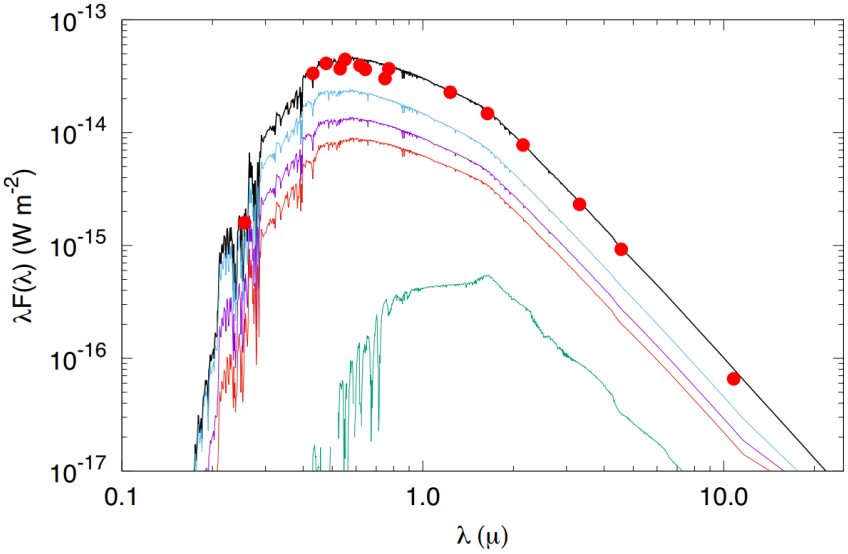

Figure 2.9: The SED of the TIC 219006972 quadruple, adopted from Kostov et al. (2023). The red dots represent the observations and the black line the composite SED, the colourful lines show the individual stars.

2.6 Spectral analysis

Spectroscopic observations provide an enhancement to photometric measurements, enabling the analysis of stellar atmospheres and radial motions. Essential spectral parameters are the resolving power (or resolution) R and signal-to-noise ratio S/N. The resolving power $R = \frac{\lambda}{\Delta\lambda}$ states the ratio between the observed wavelength λ and the smallest wavelength difference $\Delta\lambda$ that can still be distinguished. The typical R values usually range between 10^3 and 10^5. Higher resolution enables to study of the line profiles in greater detail. The signal-to-noise ratio $\mathrm{S/N} = \frac{S}{\sigma}$ expresses the mean signal S in relation to the standard deviation σ of the noise. A minimal value of $\mathrm{S/N} \approx 50$ is generally required for radial velocity measuring.

Spectral analysis plays a crucial role in the research of multiple stars. A quadruple system comprises four stars in total. Thus, the spectral lines of all four components can be theoretically visible. The lines of the individual components differ in several parameters (e.g., in depth, width, and central wavelength). The precise line positions vary with the radial motions of the individual stars. The system moves as a whole, which could cause the spectral lines to be systematically Doppler-shifted due to its non-zero systemic radial velocity γ. Both pairs orbit with the outer orbital period P_{AB} around the common centre of mass with their radial velocities $v_{\mathrm{A,B}}$. Furthermore, the components orbit within each pair with their inner periods. The inner motion is the shortest within the system. It causes the most considerable variations in spectral line positions in the short term. On the other hand, the outer orbit requires long-term observations to be properly detected.

The combined line shifts are observed as a result of all the mentioned phenomena. The first view of the spectra could be ambiguous. The spectral lines would appear deformed or split. In some cases, the shifts could create a merge. For instance, pair A can merge with lines of pair B at some specific observational time. Thus, the spectral

analysis is generally not trivial and requires measurements at the different orbital phases for both binaries.

The radial velocities are measurable adequately when the spectral lines are correctly identified and disentangled. Firstly, the inner motion of each pair should be detected. The spectroscopic measurements should ideally cover the entire orbital cycle for both binaries. The orbital inner periods must be known precisely to construct the phase-folded radial velocity curves. The accurate $P_{\rm A}$ and $P_{\rm B}$ values are primarily derived from photometry. The phase predictions can then be calculated. It is advantageous in the beginning to measure the system with specific phases to better recognise the inner orbital motions. For instance, the pair A eclipses can be observed, expecting practically zero radial velocities and negligible shifts for this binary. In this case, the spectrum contains a constant contribution of pair A. At the same time, the orbit of pair B produces its line shifts. The pair B spectral lines would then be identified. The same observations should also be made for pair A.

The outer mutual motion is defined as a long-term effect on the radial velocity curves. The radial velocities of both pairs move against each other over time, creating the periodic variations with the outer orbital period. The system is spectroscopically confirmed as a quadruple if the outer orbital motion is detected. The radial velocity amplitudes $K_{\rm A}$ and $K_{\rm B}$ give the mass ratio $q_{\rm AB}$ between the pairs:

$$q_{\rm AB} = \frac{m_{\rm A}}{m_{\rm B}} = \frac{K_{\rm B}}{K_{\rm A}}. \tag{2.7}$$

Measuring the spectra during the eclipses of both binaries could be a helpful tool to measure their velocities on the outer orbit. The outer motion is measured within the long timescale with the known inner radial velocity curves.

The spectral lines must be disentangled to calculate the radial velocities. The most common approaches to disentangling are Fourier-based methods and cross-correlation (CCF) with template spectra. The CCF compares observed spectra with synthetic templates to identify similarities. Torres et al. (2017) presented the radial velocity curves for V482 Per. The system is unique with well-measured inner orbit radial velocities of both binaries (Figure 2.10) and their outer motion (Figure 2.11). The individual spectra were disentangled by the cross-correlation. Another possibility is using a Gaussian process method described comprehensively by Czekala et al. (2017). The main principle of this method is to recover the individual spectra and the radial velocities without using the fixed templates. The Doppler shifts are fitted for all assumed components. The method assumes a time-stationary spectrum without strong spectral variability (e.g., spots and flares). Using this method benefits from better fitting the data with a lower S/N ratio, because it relies on more flexible principles than the line templates. A Gaussian process (Czekala et al., 2017) was used to disentangle the ASASSN-V J233336.79+615012.0 (S3 Cas) spectra in Chapter 3. The composite Hα lines and modelled He I 5876 lines are shown in Appendices (Figures A.7 and A.6).

A comprehensive quadruple system study requires a large dataset of high-quality spectroscopic observations. Ideally, the spectra must have sufficient resolving power to measure all four components. These constraints allow the complex analysis of bright systems. The exposure time could be the limiting factor for short-period pairs. If the exposure time is too long, it may cover a significant fraction of the orbital cycle. In this case, the spectral lines appear smeared, and the resulting information can be limited.

If the time is longer than approximately 5 % of the orbital period, the spectrum can be blurred significantly (J. Janík, private communication). This issue arises primarily for the fainter objects that require a long exposure time. The specific observational criteria depend on observing conditions and the used technique.

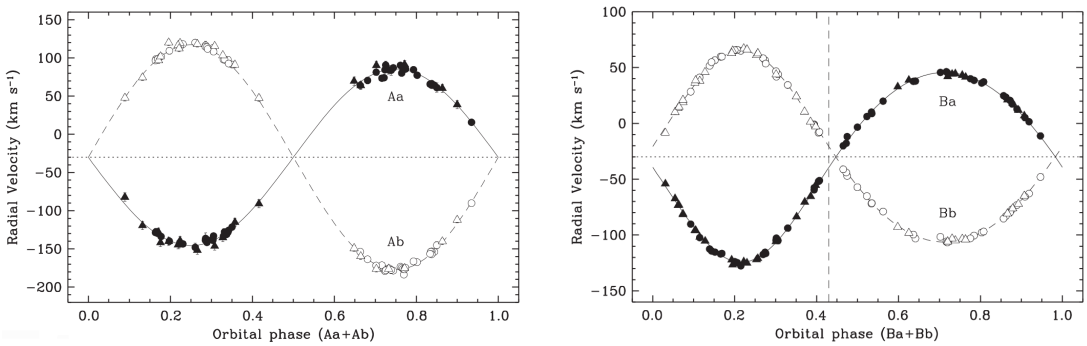

Figure 2.10: Radial velocity curves of the quadruple system V482 Per for inner binaries, pair A with a 2.4-day period (left) and pair B with a 6-day period (right), the radial velocities are corrected for the outer motion, adopted and modified from Torres et al. (2017).

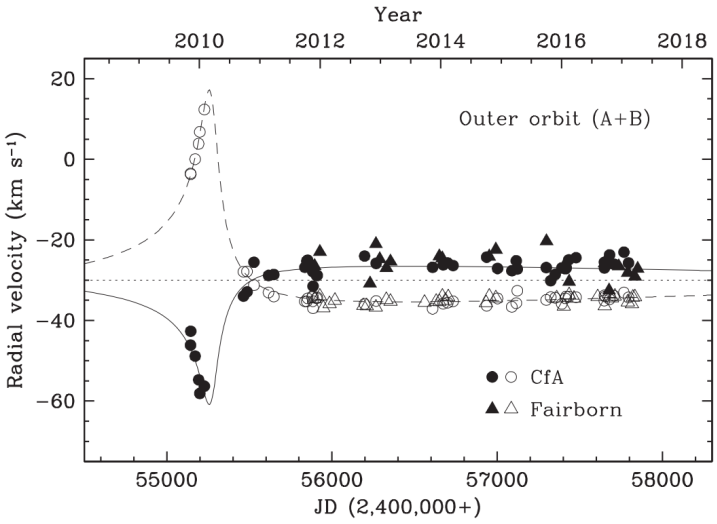

Figure 2.11: Radial velocity curve of the outer motion of two pairs for V482 Per, the inner orbit influence is subtracted to see clearly the outer motion with the period of 16.67 years, the orbit shows significant eccentricity, adopted from Torres et al. (2017).

2.7 Modelling

The physical modelling of the 2+2 eclipsing quadruple systems involves several different data types. Combining all the measurements over a long timescale is essential to obtain comprehensive results. The photometric observations represent the main source of information in most cases. Light curve modelling can provide the first step to a complex analysis. The $O-C$ diagrams constructed from the minima timings can

reveal the quadruple nature of the studied system and derive the orbital parameters. The composite temperature can be acquired from the SED fitting. The relative depths of the eclipses allow for an estimation of the individual stellar temperatures. If the radial velocities are available from the spectroscopic observations, the radial velocity curves can be modelled along with the light curves. It is suitable to use more robust models for dynamical systems with short outer periods (e.g., Pribulla et al. (2023) and Borkovits et al. (2021)). For LiTE dominant configurations, both pairs can be analysed separately (Chapter 3 herein or Zasche et al. (2022a)).

The light curves are detrended and disentangled before the modelling. The amplitudes of the eclipses are mutually influenced. Thus, the third light parameter is generally assumed to be high. The initial values could be set to 50 % for both pairs, depending on the individual systems. The third light sum should theoretically be 100 %. However, this value is higher in practice. The reason is the additional light contamination. This increase could indicate another stellar component within the system. On the other hand, the argument alone is not sufficient to assert this possibility. The main source of the additional light is from nearby stars that are not related to the system, especially in the TESS data. Unsurprisingly, the sum of the third light from TESS can exceed 100 %. Therefore, the results of the third light from TESS and other higher-resolution observations generally differ.

PHOEBE (PHysics Of Eclipsing BinariEs) software, version 0.32 (Prša and Zwitter, 2005), was used to model the light curves. The package is based on the Wilson-Devinney code (Wilson and Devinney, 1971). Two possible fitting methods, differential corrections and Nelder-Mead simplex, are available. The output is a physical binary model. In other words, it is essential to calculate the physically consistent parameters according to the known information. In contrast to phenomenological models, the final parameters should be the same for the light curves in different bands. Furthermore, a possible light curve asymmetry, deformation, and other influences should be physically explained.

The fitting process requires an initial set of parameters. The main inputs are the linear ephemeris values (P and M_0), estimated effective temperatures T_1 and T_2, the first approximation for radius ratio R_1/R_2 and mass ratio q, surface coefficients (albedo α and gravity brightening β), and the third light l_3. The orbital elements from the $O-C$ modelling, primarily an eccentricity e and argument of periastron ω, can also be added (if known). The ephemeris and temperature of the primary star are commonly fixed throughout the fitting. In most cases, the synchronicity component parameters F_1 and F_2 are set to 1, meaning the rotation period coincides with the orbital period. The initial third light value can be set to 50 %, and later treated as a free parameter. The limb darkening coefficients are gradually fitted with improved accuracy of the effective temperature. The surface coefficients are primarily set to constant nominal values during the fitting. They can be fitted in the end to improve the final model.

Deriving the photometric mass ratio q is usually not trivial. Several indirect methods can provide a sufficient q value estimation. The q-search method evaluates the models with different mass ratios and seeks the optimal solution with the minimal cost function value (minimal residuals). The step size and precise values can be adaptively refined as the solution approaches convergence. Kouzuma (2023) introduced a new method of photometric mass ratio estimation for overcontact binaries. The procedure uses the third derivative of the light curve and specific time intervals. This approach

was tested using the systems with known spectroscopic mass ratios, and gives a typical, realistic uncertainty of approximately 0.1.

Graczyk (2003) stated the formulas for mass ratio calculating using the PHOEBE bolometric magnitudes M_{bol1} and M_{bol2} and luminosities L_1 and L_2:

$$\log L_1 - \log L_2 = \frac{M_{\mathrm{bol2}} - M_{\mathrm{bol1}}}{2.5}\,, \tag{2.8}$$

$$\log q = \frac{\log L_2 - \log L_1}{3.664}\,. \tag{2.9}$$

The light curve is modelled with the fixed initial q parameter. The equations 2.8 and 2.9 are then applied to refine the mass ratio. The process is repeated until the q parameter remains unchanged within the uncertainty. The method is adequate primarily for the semidetached and contact systems.

The PHOEBE fitting and light curve plotting are shown in Appendices in Figures A.4 and A.5. The sample modelling is shown for the pair A of ASASSN-V J000432.60+632605.0 (S1 Cas) system, described in more detail in the following Chapter. The radial velocity modelling is also possible in PHOEBE. Using the photometric and spectroscopic data simultaneously, the software can acquire other essential parameters, mainly the radii, semi-major axis, and enhanced mass ratio value. However, the spectroscopic measurements are not widely available for most of faint 2+2 candidates, and the modelling relies mainly on photometry.

Chapter 3

Study of doubly eclipsing quadruples: I. Methodology and results for ten Northern sky systems

Jakub Kolář,[1] Sabina Pačková,[1] Anna Richterková,[1,2] Miloslav Zejda,[1] Reinhold Friedrich Auer,[3] Radek Dřevěný,[3] Jan Janík,[1] Martin Mašek,[3,4] Thibault Merle,[5,6] Prokop Ohlídal,[1] Theodor Pribulla,[7] Milan Uhlár,[8] Petr Viewegh,[9] and Jakub Vyskočil[1]

[1]Department of Theoretical Physics and Astrophysics, Faculty of Science, Masaryk University, Kotlářská 2, CZ-611 37 Brno, Czech Republic
[2]Prostějov Observatory, Museum and Gallery in Prostějov, Kolářovy sady 3348, CZ-798 11 Prostějov, Czech Republic
[3]Variable Star and Exoplanet Section of the Czech Astronomical Society, Fričova 298, CZ-251 65, Ondřejov, Czech Republic
[4]FZU - Institute of Physics of the Czech Academy of Sciences, Na Slovance 1999/2, CZ-182 21, Praha, Czech Republic
[5]BLU-ULB, Institut d'Astronomie et d'Astrophysique, Université Libre de Bruxelles, CP 226, Bvd du Triomphe, BE-1050 Brussels, Belgium
[6]Royal Observatory of Belgium, Avenue Circulaire 3, BE-1180 Brussels, Belgium
[7]Astronomical Institute of the Slovak Academy of Sciences, Tatranská Lomnica, SK-059 60 Vysoké Tatry, Slovakia
[8]Ďáblice Observatory, Pod Hvězdárnou 768, CZ-182 00 Praha 8, Czech Republic
[9]Brno University of Technology, Institute of Physical Engineering, Technická 2, CZ-616 69 Brno, Czech Republic

Prepared manuscript to submit to Monthly Notices of the Royal Astronomical Society (MNRAS), 2025.

Abstract

Doubly eclipsing quadruple systems provide an excellent opportunity to analyse multiple stellar systems and their evolutionary processes. However, their fundamental parameters and multiplicity have been derived in only a few cases. We conducted new observations and studied ten doubly eclipsing 2+2 candidates in the Northern sky. The new ground-based measurements were combined with TESS and archival data from available additional surveys (ASAS-SN, ZTF, and SuperWASP). We detrended and disentangled the light curves to derive precise minima timings. Further modelling was made using the PHOEBE 0.32 software package. Orbital period $O-C$ analysis revealed seven candidates as newly confirmed quadruple systems. We identified ASASSN-V J020003.56+452605.2 as a blend of two independent binaries. The spectral analysis was carried out for ASASSN-V J233336.79+615012.0, and all four components and their radial velocities were measured. Notably, TIC 9493888 was confirmed as a quadruple system, and the $O-C$ variations suggest the presence of a fifth component, another star, or an exoplanetary object.

3.1 Introduction

Doubly eclipsing quadruple systems represent one of the new rapidly growing research fields of stellar astrophysics in the era of modern photometric surveys and satellites. They are unique astrophysical laboratories for studying multiple systems' properties and evolution. The 2+2 structure containing two inner binaries offers the unique opportunity to detect new candidates through eclipses. Hundreds of new doubly eclipsing systems were identified in our Galaxy using TESS (Ricker et al., 2015) light curves (Kostov et al., 2022, 2024; Zasche et al., 2022b) and Zwicky Transient Facility (ZTF) (Vaessen and van Roestel, 2024). Other candidates were found in the Large and Small Magellanic Cloud (LMC and SMC) and the Galactic Bulge by the OGLE III and IV surveys (Pawlak et al., 2013, 2016; Zasche et al., 2019; Ádám et al., 2023). Nowadays, the total number of known 2+2 candidates is around 1 000.

We denote both eclipsing binaries as pair A (usually the first detected) and pair B. Both binaries have their inner orbital periods $P_{\rm A}$ and $P_{\rm B}$. Besides the inner motion, both pairs are gravitationally bound and orbit their common centre of mass with the outer $P_{\rm AB}$ period. The outer periods are usually several years or decades long. Long-term monitoring of the minima timings can be used to confirm the quadruple nature. With the analysis of the $O-C$ diagrams (sometimes referred to as eclipse time variations) for both inner pairs, the mutual motion is detected through the light time effect (LiTE). However, there are known cases with very short outer periods of around a year or shorter where the dynamical effects in the system play a significant role and dominate over LiTE (e.g., Kostov et al. (2021); Pribulla et al. (2023)).

Yet only a small fraction of the doubly eclipsing candidates are confirmed quadruple systems. The open question of inner period ratio preferences and possibly more stable resonant states is still not answered adequately. More stellar multiples, i.e., triples, quintuples, sextuples, etc., are also found. Furthermore, binary structures are also applied in these multiple type configurations (Powell et al., 2021). This fact makes the doubly eclipsing quadruples even more important because their structure and evolution can be applied to study other multiples. For these reasons, studying the individual

doubly eclipsing systems more comprehensively and combining several available observing techniques is essential.

Photometric observations present a relatively straightforward method for the initial study of these systems. Satellite data and ground-based observations, provide us with a wide timescale to confirm the gravitational bond between the inner binaries. It is important to have as accurate data as possible and continue to observe the known objects. Another essential step is to add more data types, including spectroscopy. The analysis should also consider spectral energy distribution (SED), astrometry, and interferometry.

This paper presents a comprehensive study of ten doubly eclipsing 2+2 quadruple candidates in the Northern sky. This research is conducted by the Squadra group, made up of academics, students, citizen scientists, and collaborators. We introduce our methodology in this first part of the paper series. Photometry, SED, spectroscopy, and long-term observations are the main cornerstones of this analysis. The study of S3 Cas (ASASSN-V J233336.79+615012.0) is described as a sample example. Then, we show the results for the individual systems. We can conclude seven systems as confirmed quadruples, including one candidate, S1 Cam (TIC 9493888), for a quintuple star, or a quadruple with an exoplanet.

3.2 Observation and Data Collecting

3.2.1 Studied Objects

We selected suitable candidates from Zasche et al. (2019); Zasche et al. (2022b) and Kostov et al. (2022) to assemble new ground-based observations. The criteria were selected according to the available telescopes. The typical brightnesses were in the range of 11 - 15 mag in V band. The period values vary between a few hours and several days. Finally, the amplitudes of all four eclipses must be sufficiently visible in our data and in at least some of the other surveys used. The last condition sets a constraint of the minimal amplitude values between 10 mmag and 40 mmag, depending on the specific telescope and local conditions. The 2+2 candidates studied in this paper are listed in Table 3.1. The text uses working names, consisting of the constellation abbreviation and a serial number, for better clarity and readability. The basic orbital parameters are summarised in Table 3.2.

3.2.2 TESS

TESS light curves were acquired using the Python package Lightkurve (Lightkurve Collaboration et al., 2018). First, the background noise was subtracted, and the fluxes were normalised and converted to differential magnitudes. The original datasets contain a variable signal of both binaries. Hence, further analysis requires the light curves to be disentangled into individual pairs. The disentangling process was done using the SILICUPS software (Cagaš, 2017; Pejcha et al., 2022). This method is based on the phenomenological light curve fitting by template function from Mikulášek (2015), which is iteratively repeated. One binary was modelled initially, and its contribution was subtracted to obtain the second one, and vice versa. The disentangling usually

requires a few iteration steps. The harmonic polynomials were additionally used for the cases of total eclipses, where the SILICUPS fitting did not reach high accuracy.

Data were detrended simultaneously with the disentangling. Chebyshev polynomials of n degree were used. The TESS sectors were divided into smaller parts to better cover the instrumental errors and trends. The polynomial degree n was individually considered and set usually up to the value 10. After the successful disentangling and detrending procedures, the residuals for both eclipsing pairs were the same, with only potentially negligible fluctuations.

3.2.3 New Observations

Follow-up ground-based observations contain primarily photometry. The measurements were carried out in different bands according to the equipment. The frames were processed using standard corrections and calibrations, including composite master dark and flat-field frames. The differential aperture photometry was used to obtain the final data, which was subsequently analysed. Suitable comparison and check stars were chosen based on angular vicinity, similar brightness, and spectral type. These steps were made using software C-Munipack 2.1 (Motl, 2011) and SIPS 4.2 (Pejcha et al., 2022). The following instruments were used for the new photometric measurements:

i. ASA 800 + G4-16000 and C5A-150M, Ždánice, Czech Republic,

ii. Newton 600 + G4-16000, Brno, Czech Republic,

iii. D400 + G2-0400, Prostějov, Czech Republic,

iv. NWT 200 + G2-1600, Veverská Bítýška, Czech Republic,

v. NWT 200 + CMOS C2 7000A, Znojmo, Czech Republic,

vi. CARL ZEISS 200 + QHY 294 Pro Mono, Jirny, Czech Republic,

vii. SCT 250 + MII G2-1000BI, FRAM-CTA-N, La Palma.

We focus on one specific system, S3 Cas, to acquire new spectroscopic observations. We preferred to collect a large amount of data for one object and analyse the spectral dataset in greater detail, rather than measure only a few spectra for several objects. This candidate is one of the brightest in our sample, making it suitable for our purposes. Another three telescopes were used to gather new spectroscopic data:

viii. MUSICOS (MUlti-SIte COntinuous Spectroscopy) spectrograph at Skalnaté Pleso Observatory, Slovakia, with a resolving power $R \approx 38\,000$,

ix. HERMES (High-Efficiency and high-Resolution Mercator Echelle Spectrograph) spectrograph at La Palma, Spain, $R \approx 86\,000$,

x. OES (Ondřejov Echelle Spectrograph) on the 2-m Perek telescope, Astronomical Institute of the Czech Academy of Sciences in Ondřejov, Czech Republic, a resolution $R \approx 40\,000$.

Table 3.1: List of studied doubly eclipsing systems, the V magnitude was stated by Zacharias et al. (2013), RA and DEC are in Eq. 2000.

Name	Working Name	RA [°]	DEC [°]	V [mag]
ASASSN-V J000432.60+632605.0	S1 Cas	1.13583	63.43473	12.332
ASASSN-V J020003.56+452605.2	S1 And	30.01481	45.43476	11.982
TIC 9493888	S1 Cam	69.51021	55.73152	13.143
ASASSN-V J081048.48+133402.0	S1 Cnc	122.70200	13.56722	13.643
ZTF J194856.47+360309.2	S5 Cyg	297.23533	36.05257	15.160
Brh V154	S1 Vul	301.67721	24.98909	13.013[a]
GSC 02693-00926	S1 Cyg	306.68275	35.34167	11.923
NSVS 5871089	S3 Cyg	313.10229	38.17175	11.100
ZTF J205229.71+473345.9	S6 Cyg	313.12383	47.56276	13.838
ASASSN-V J233336.79+615012.0	S3 Cas	353.40329	61.83668	11.146

a: Zacharias et al. (2015).

The spectroscopic data were processed, calibrated, and normalised by standard procedures. Hα emission line was observed within all three datasets (the Hα sample spectrum is available online). The HERMES and MUSICOS spectra were disentangled using Gaussian process fitting implemented in MATLAB. The spectrum of each component was modelled as a Gaussian process across all observing epochs. The individual spectral lines were Doppler-shifted, and the radial velocities were measured. The composite spectrum was obtained as the sum of the four realised models. The method is described by Czekala et al. (2017). The disentangling and radial velocity measuring were made for He I 5876 and 6678 lines. The sample fits are available online.

3.2.4 Other surveys

Besides the new observations and the TESS light curves, we processed the available data from the surveys ASAS-SN (Kochanek et al., 2017; Jayasinghe et al., 2019), ZTF (Vaessen and van Roestel, 2024), and SuperWASP (SWASP) (Pollacco et al., 2006; Smith and WASP Consortium, 2014) as well. The data were divided into smaller parts according to the observing seasons, and the light curves were disentangled by using the same methods described above.

3.3 S3 Cas Analysis

3.3.1 $O-C$ diagrams

Minima timings were determined using the SILICUPS software by *Fit minimum* tool. applied an automated fitting process of fitting all the minima in the dataset for TESS and our new light curves. The derived results were then manually inspected.

The other survey data were using a different method. Since they do not have continuous time series, the minima timings cannot be fitted directly. We took the smaller datasets, usually according to observational seasons, where we can still manage the disentangling to see the light curves of both pairs clearly. The phase-folded light curves and the phase shift estimation were then used to acquire the $O-C$ value from

Table 3.2: Orbital parameters of the studied doubly eclipsing candidates (inner orbital period P and zero epoch M_0 for each pair.

Name	P_A [days]	M_{0A} [HJD]	P_B [days]	M_{0B} [HJD]
S1 Cas	1.0979165	2458772.2905	0.9944755	2458772.360
S1 And	2.889838	2458793.973	0.5891595	2458806.9617
S1 Cam	2.0989969	2458816.2345	2.706232	2458818.6891
S1 Cnc	2.122729	2457283.1503	4.013354	2459245.0095
S5 Cyg	0.6414049	2458687.6353	0.8664298	2458700.1961
S1 Vul	0.554947	2459430.422	1.94456111	2459439.461
S1 Cyg	1.3504470	2459421.845	1.0992030	2457600.805
S3 Cyg	0.7480267	2459440.8646	0.53787	2459426.562
S6 Cyg	1.9223369	2458728.427	1.153058	2458715.6435
S3 Cas	3.34301	2458975.462	1.266711	2458799.7349

the set. The estimation was done by phase shift fitting in Python and in SILICUPS by changing the M_0 epoch.

The $O-C$ diagrams of both pairs were constructed and examined by the OCFit software (Gajdoš and Parimucha, 2019). The S3 Cas $O-C$ diagrams are shown in Figure 3.1. This system contains measurements from the ASAS-SN survey (additionally with TESS and our data). The pair A is affected by apsidal motion with period U incomparably longer than the overall observing time. The vertical shift between the primary and secondary minima timings is changing over time. However, the precise apsidal motion model is currently unable to be obtained. Furthermore, the $O-C$ variations reveal the presence of the LiTE effect with a 7-year orbital period (see Table 3.4). On the other hand, the pair B variations behave differently from the pair A case. The non-linear changes are noticeable, but without a clearly detectable nature. The possible interpretation would be a combination of several effects that would require more observational time to specify precisely.

Additional wave-like variations were detected in TESS data in the residuals. The SILICUPS period search stated the period value to 0.93631 days, combining the available TESS sectors. This variation was subtracted, and hence, its influence for the minima timings precision is negligible. Due to the low amplitude of only 0.04 mag, this variation is seen only in TESS. The S3 Cas angular vicinity is unclear and contains several stars as light contamination sources. Gaia DR3 2015579193692265216 intervene to TESS and slightly to our data. The other two stars, Gaia DR3 2015579193692272000 and Gaia DR3 2015579365490951680, were only in the TESS aperture. None of these, and other more distant objects, is known as the variable star with the corresponding 0.9-day period. Since these variations are not observed in other data, it is impossible to tell which object they belong to.

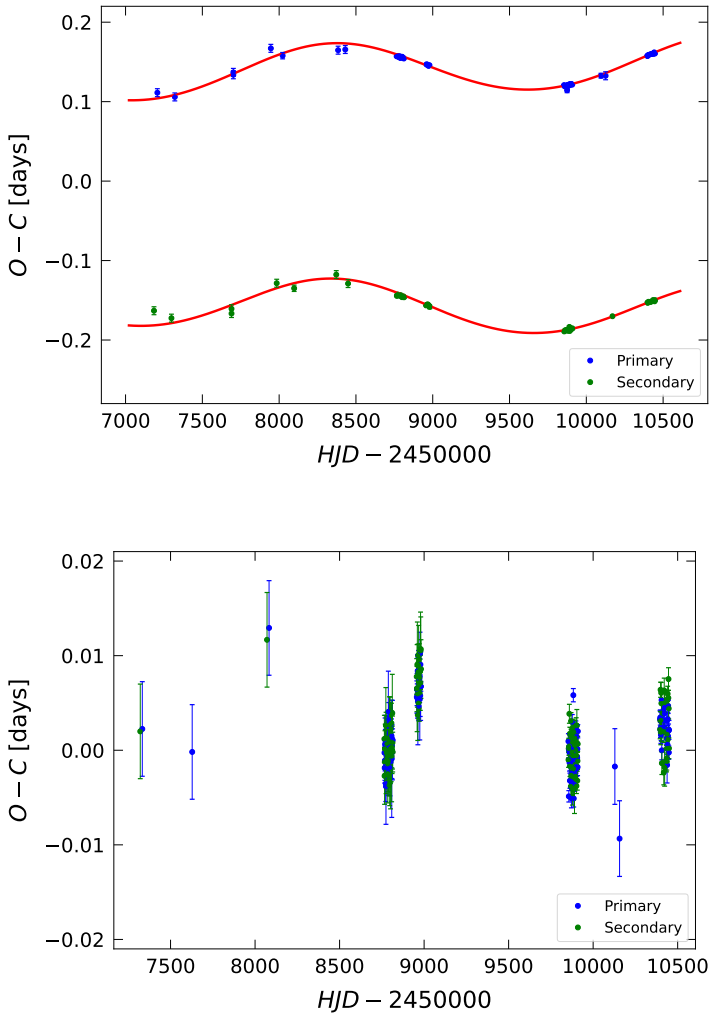

Figure 3.1: $O-C$ diagrams of S3 Cas, upper panel: pair A with a combination of LiTE and apsidal motion model, bottom panel: pair B.

3.3.2 SED

The spectral energy distribution (SED) was constructed and fitted using the VOSA (VO Sed Analyzer) tool (Bayo et al., 2008). The flux measurements were retrieved from the VOSA database. The observed fluxes were corrected for extinction parameter $A_V = 1.48 \pm 0.05$ mag. The extinction values were stated using Green et al. (2019). The extinction strongly depends on distance. The Gaia DR3 (Gaia Collaboration, 2023) or DR2 (Gaia Collaboration, 2018) distances (or parallaxes) were taken for consistent methodology and results. The SED fit for S3 Cas is depicted in Figure 3.2. The resulting SED temperature means the composite value for the whole system. All four components are reflected in the SED and the fit. Hence, the resulting temperature shows the maximum limit for the components, not indicating the individual star temperatures. The composite temperature for S3 Cas is 7 500 K (Table 3.3) with an estimated uncertainty of 200 K from the VOSA fitting. The SED gives us constraints on the maximum temperature limit.

Table 3.3: Composite temperatures (in K) of the analysed objects (S1 And was not included in further analysis), SED fitting, Gaia DR3 or DR2 (Gaia Collaboration, 2023, 2018), TESS input catalogue (Stassun et al., 2019), and StarHorse catalogue (Anders et al., 2019).

System	SED	Gaia	TESS	StarHorse
S1 Cas	8 300	7 200[b]	8 200	9 500
S1 Cam	5 500	5 300[a]	5 100	6 200
S1 Cnc	6 300	6 300[a]	6 400	6 300
S5 Cyg	6 500	6 400[b]	x	x
S1 Vul	5 500	6 300[a]	x	x
S1 Cyg	7 500	5 400[a]	6 300	8 600
S3 Cyg	9 000	6 600[b]	6 800	6 700
S6 Cyg	5 500	5 100[b]	x	x
S3 Cas	7 500	5 900[a]	8 000	6 900

a: Gaia DR3, b: Gaia DR2

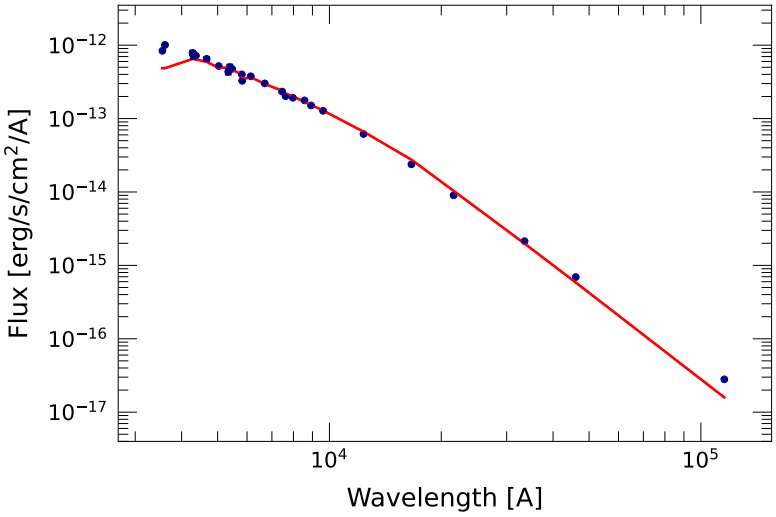

Figure 3.2: The SED of S3 Cas, fitting from VOSA.

3.3.3 Physical modelling

We performed the physical light curves modelling of both pairs. The calculations were made using the PHOEBE software, version 0.32 (Prša and Zwitter, 2005), described for S3 Cas in greater detail. Pair A eclipses dominate the system (Figure 3.3). For this reason, we assumed larger temperatures and radii for pair A than for pair B. The third light values were set initially to 50 % and left as a free parameter during the fitting. The TESS sector 78 and our new data in the R band were modelled.

Both pairs' light curve models were depicted in Figure 3.3, and the fundamental parameters are summarised in Table 3.5. The sum of the third light is 125 % for TESS and 114 % for our observations in R. These values correspond with the assumed prediction of the third light increase due to the stars in the system's vicinity. The

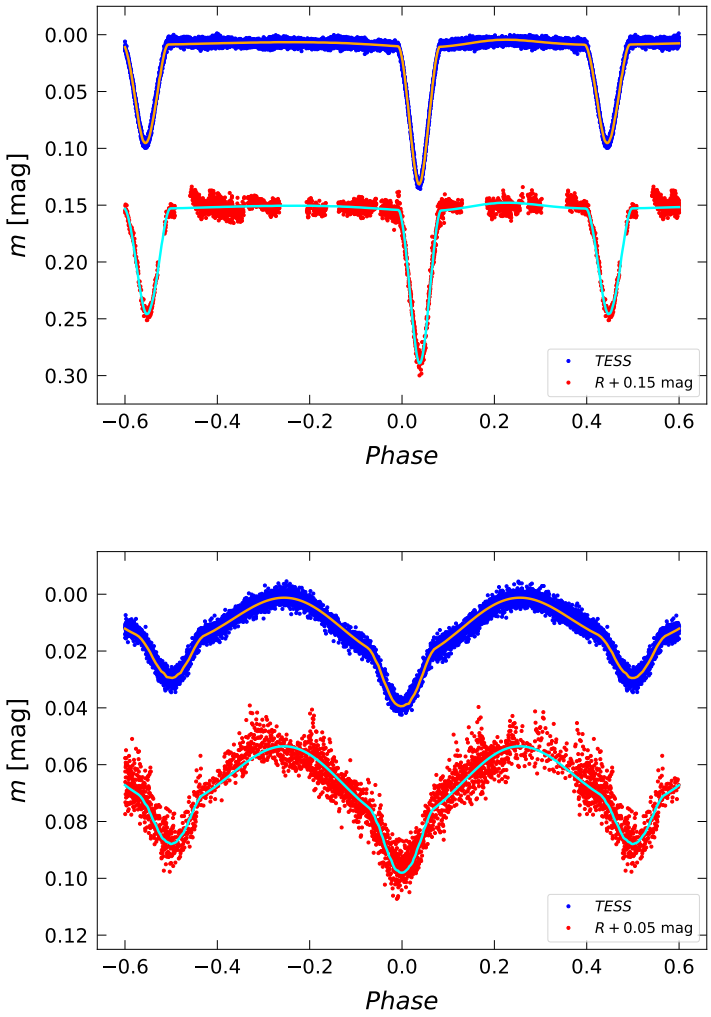

Figure 3.3: S3 Cas light curves, data and PHOEBE model, upper panel: pair A, bottom panel: pair B.

TESS data were influenced more significantly by the surrounding objects. The non-zero eccentricity value of pair A agrees with the $O - C$ diagram.

The disentangled radial velocities are shown in Figure 3.4. The graphs contain HERMES and MUSICOS data. The OES spectra did not contain all the components, and the disentangling was unsuccessful. The current phase coverage of the radial velocity curves does not allow us to provide a consistent and reliable fit to support the photometric observations. Nevertheless, the S3 Cas system is suitable for follow-up spectroscopic observations to enhance the essential parameters and the outer orbit.

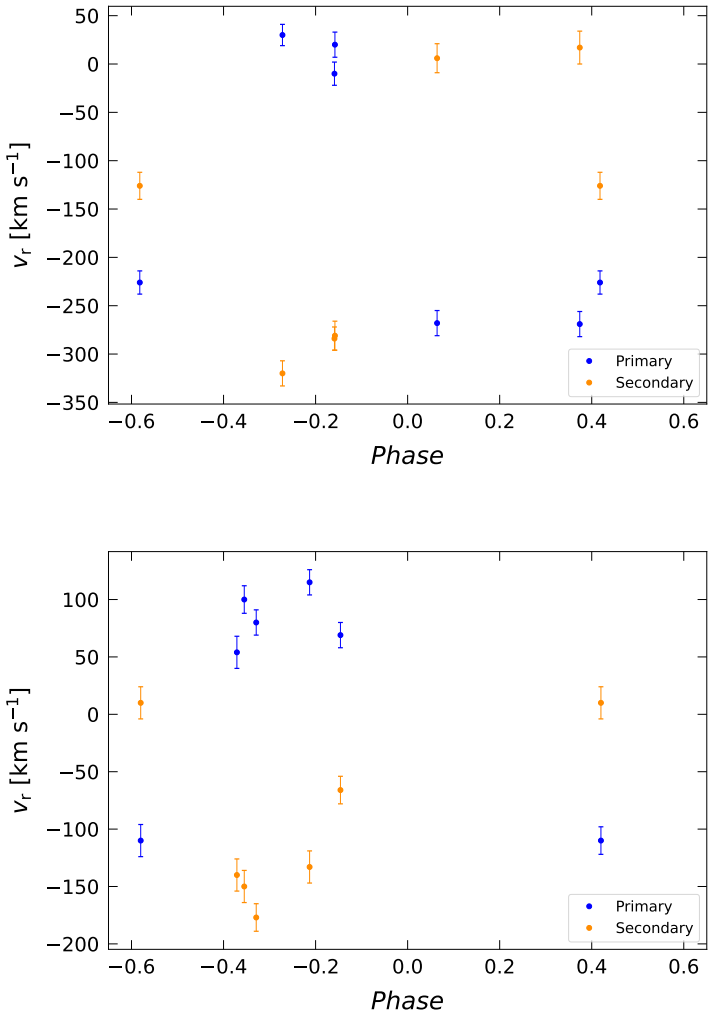

Figure 3.4: S3 Cas: phased radial velocities according to period for pair A (upper panel) and B (bottom panel).

3.4 Other objects

We made the same methodology procedures described in detail for the S3 Cas system for other examined candidates. This section presents the most important results and remarks on each. The SED composite temperatures are listed in Table 3.3. The SED fits are available online. There is also a comparison with the temperature values from Gaia DR3 (if available) or DR2 (Gaia Collaboration, 2023, 2018), TESS input catalogue (Stassun et al., 2019), and StarHorse catalogue (Anders et al., 2019). The physical parameters from PHOEBE with typical uncertainty values are summarised in Table 3.5 (last column).

Table 3.4: Results for LiTE parameters from the OCFit fitting with their uncertainties: outer period, orbit projection (semi-major axis times sine of the inclination angle), eccentricity, time of periastron passage, and argument of periastron according to each pair.

	S3 Cas		S1 Cas			S1 Cnc			S6 Cyg			1 Cam				
	Pair A	δ	Pair A	Pair B	δ	Pair A	Pair B	δ	Pair A	Pair B	δ	Pair A	Pair B	δ	Second LiTE	δ
P_{AB} [years]	7.0	0.4	6.0	6.1	0.4	11.7	11.7	0.6	14	14	2	33	34	5	7.6	0.6
$a_3 \sin i_3$ [au]	5.6	0.5	1.1	1.3	0.4	0.7	0.8	0.3	1.2	1.1	0.6	5	4	1	0.5	0.3
e_3	0.05	0.05	0.08	0.03	0.05	0.40	0.42	0.05	0.0	0.0	0.1	0.1	0.0	0.1	0.08	0.05
M_{03} [HJD]	2 458 300	400	2 458 400	2 458 400	400	2 459 400	2 459 400	500	2 456 100	2 456 100	900	2 457 800	2 458 200	900	2 458 900	400
ω_3 [°]	80	20	320	150	10	340	150	20	50	220	30	40	250	30	210	20

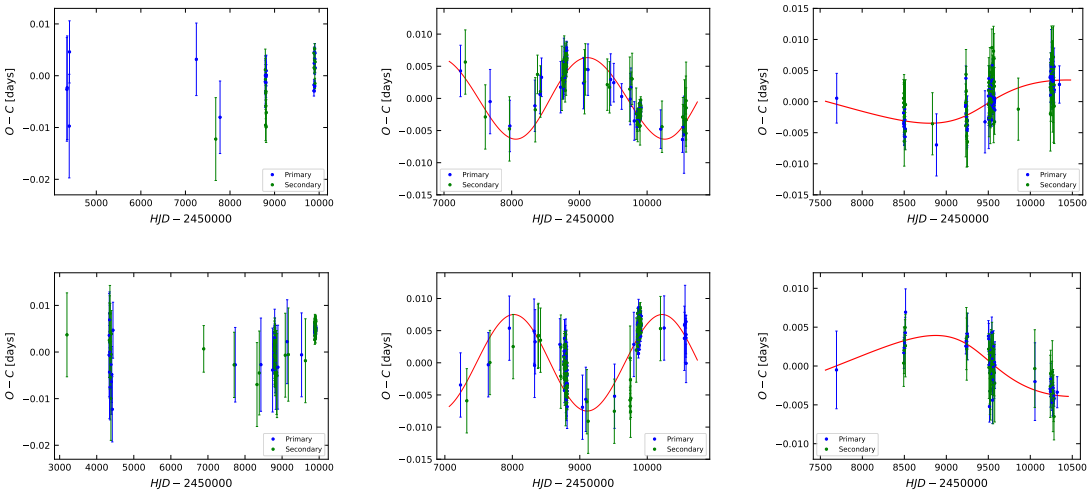

Figure 3.5: The $O-C$ diagrams, from left: S1 And, S1 Cas, and S1 Cnc, upper panel: pairs A, bottom panel: pairs B.

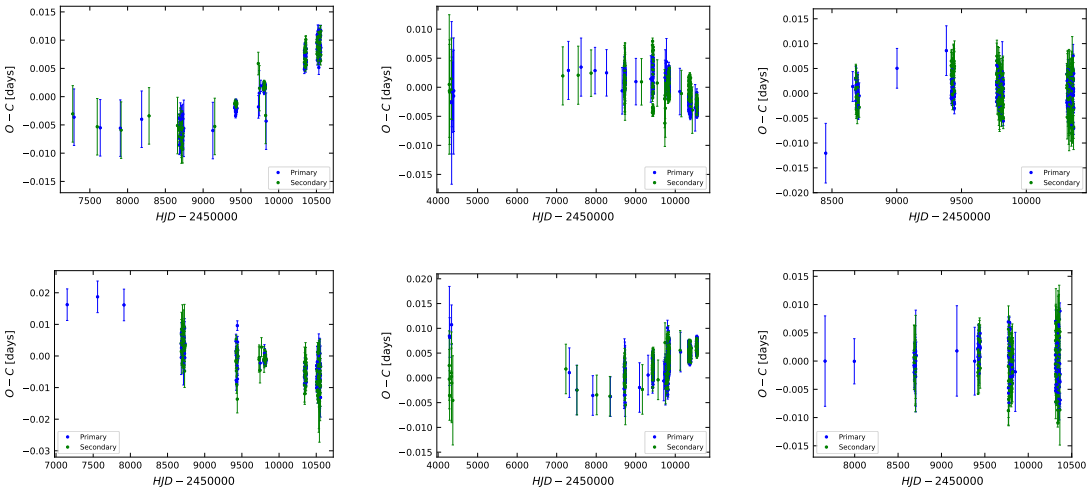

Figure 3.6: The $O-C$ diagrams, from left: S1 Cyg, S3 Cyg, and S5 Cyg, upper panel: pairs A, bottom panel: pairs B.

Table 3.5: Light curve parameters for each pair derived from PHOEBE modelling with typical uncertainty values: effective temperatures, radius ratio, inclination, mass ratio, eccentricity, and third light.

	S3 Cas		S1 Cas		S1 Cnc	S1 Cyg		S3 Cyg		S5 Cyg		S6 Cyg		S1 Vul		S1 Cam		
Pair A	TESS	R	TESS	*Clear*	TESS	TESS	V, R	TESS	V, R	TESS	V, R	TESS	V, R	TESS	V, R	TESS	R	δ
T_1 [K]	7 000	7 000	7 500	7 500	6 000	6 400	6 400	5 900	5 900	6 300	6 400	5 100	5 100	5 300	5 300	5 000	5 000	fixed
T_2 [K]	6 700	6 700	5 600	5 700	4 100	6 400	6 300	4 500	4 600	4 300	4 200	3 600	3 500	5 300	5 300	4 700	4 750	100
R_1/R_2	1.07	1.04	1.33	1.35	2.68	1.00	1.02	1.88	1.74	1.74	1.55	1.19	1.13	1.98	1.76	1.13	1.08	0.02
i [$\circ$]	80.3	80.0	88.2	88.1	81.9	79.1	76.2	87.7	87.9	73.0	81.0	84.0	85.0	78.2	79.2	84.6	84.7	0.3
q	0.91	0.92	0.50	0.49	0.40	1.00	1.00	0.23	0.23	0.46	0.47	0.62	0.64	0.21	0.26	0.90	0.90	0.05
e	0.15	0.15	0.00	0.00	0.00	0.00	0.00	0.00	0.00	0.01	0.00	0.01	0.00	0.00	0.00	0.00	0.00	0.02
l_3 [%]	53	49	46	46	49	62	52	42	41	49	49	49	49	69	38	47	46	2
Pair B	TESS	R	TESS	*Clear*	TESS	TESS	V, R	TESS	V, R	TESS	V, R	TESS	V, R	TESS	V, R	TESS	R	δ
T_1 [K]	6 000	6 000	5 600	5 600	5 900	5 500	5 500	4 800	4 800	6 000	6 000	4 900	4 900	5 300	5 300	4 800	4 800	fixed
T_2 [K]	5 300	5 500	5 300	5 300	4 400	5 250	5 300	4 600	4 700	4 200	4 500	4 000	4 100	4 300	4 500	4 700	4 750	100
R_1/R_2	1.11	1.07	1.11	1.30	1.39	1.14	1.15	1.16	1.12	1.33	1.31	2.21	2.12	1.14	1.25	1.05	1.04	0.02
i [$\circ$]	61.9	61.8	79.4	79.8	81.8	69.1	68.6	60.7	60.8	72.0	80.0	71.0	68.0	79.1	79.8	84.3	85.2	0.3
q	0.92	0.92	0.89	0.88	0.70	0.70	0.70	0.80	0.78	0.57	0.63	0.51	0.59	0.80	0.78	0.94	0.95	0.05
e	0.00	0.00	0.00	0.00	0.00	0.01	0.02	0.00	0.00	0.00	0.02	0.00	0.00	0.00	0.00	0.00	0.00	0.02
l_3 [%]	72	65	75	74	52	68	64	59	59	51	52	52	52	60	48	50	53	2

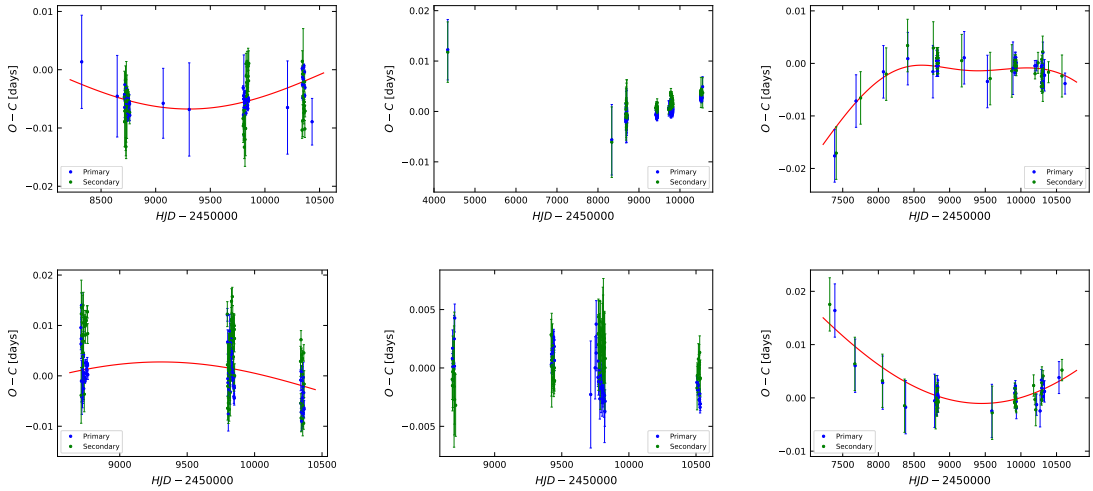

Figure 3.7: The $O-C$ diagrams, from left: S6 Cyg, S1 Vul, and S1 Cam, upper panel: pairs A, bottom panel: pairs B.

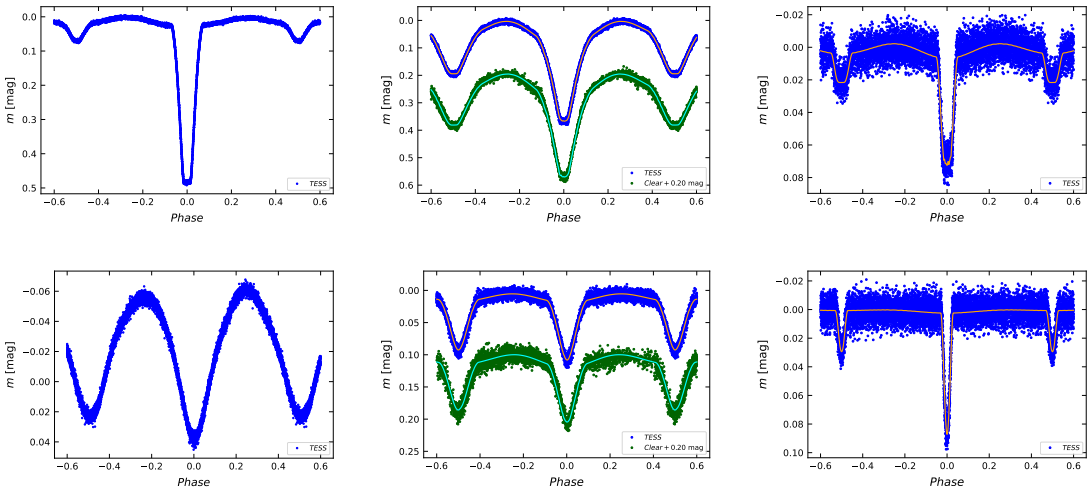

Figure 3.8: The light curves and PHOEBE models, from left: S1 And (only the light curves), S1 Cas, and S1 Cnc.

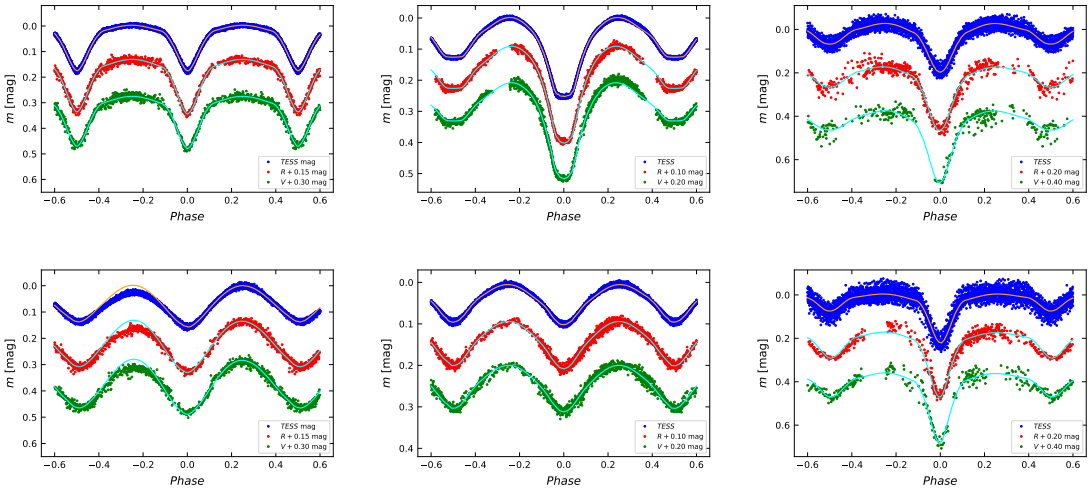

Figure 3.9: The light curves and PHOEBE models, from left: S1 Cyg, S3 Cyg, and S5 Cyg.

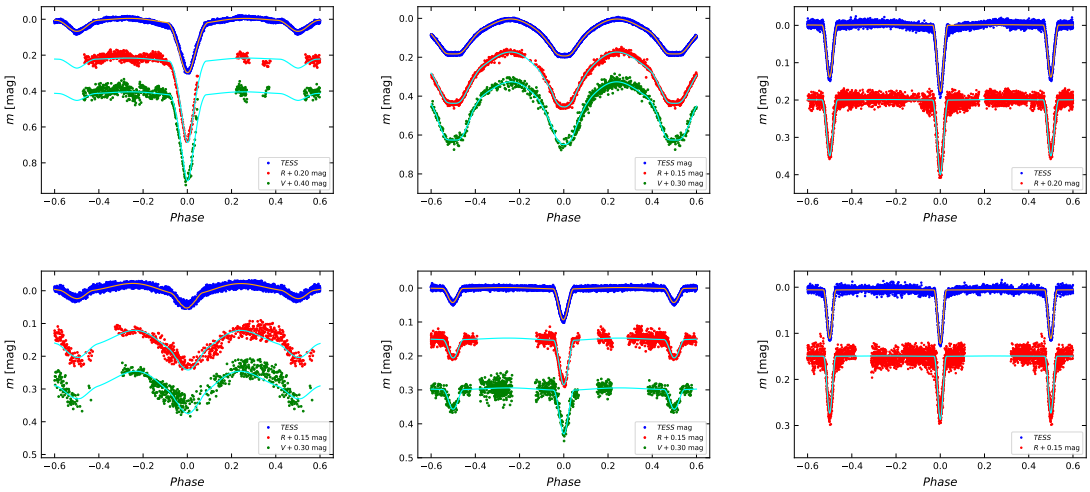

Figure 3.10: The light curves and PHOEBE models, from left: S6 Cyg, S1 Vul, and S1 Cam.

3.4.1 S1 And

Pair A primary minimum dominates in the light curve with the brightness decrease of almost 0.5 mag in TESS (Figure 3.8, left panels). The pair B curve shows the O'Connell effect with the different maxima brightness levels, indicating a surface activity. The $O-C$ diagram of pair B (Figure 3.5, bottom left panel) indicates possible non-linear variations, particularly in the newest region. On the other hand, pair A has a significant scatter with no evidence of any potential variations. Due to all the collected data, predominantly TESS and SuperWASP, the time range for S1 And observations is 15 years. However, the $O-C$ variations still do not present proper indications of the mutual motion.

Upon thorough analysis of the new observations and catalogues scanning, we found that both pairs are angularly resolved eclipsing binaries. Pair A is Gaia DR3 355800111620808576 on the coordinates 30.01709 and 45.43419. In contrast, pair B is documented as ZTF J020003.55+452605.2 (or Gaia DR3 355800111620283904) with the coordinates 30.01481 45.43476 (the original coordinates of the system from Table 3.1). Moreover, these two eclipsing binaries are heavily blended in TESS data with other close stars. We can optically resolve them using the Gaia catalogue and new data from the Ždánice observatory (Figure 3.11). The distances of the pairs differ according to the Gaia DR3 (Gaia Collaboration, 2023) catalogue. We can conclude this system to be a blend of two independent binary stars with consideration of pair A distance of 2 300 pc and pair B 1 400 pc. Thus, this candidate is probably not a 2+2 system, and we have not provided further analysis.

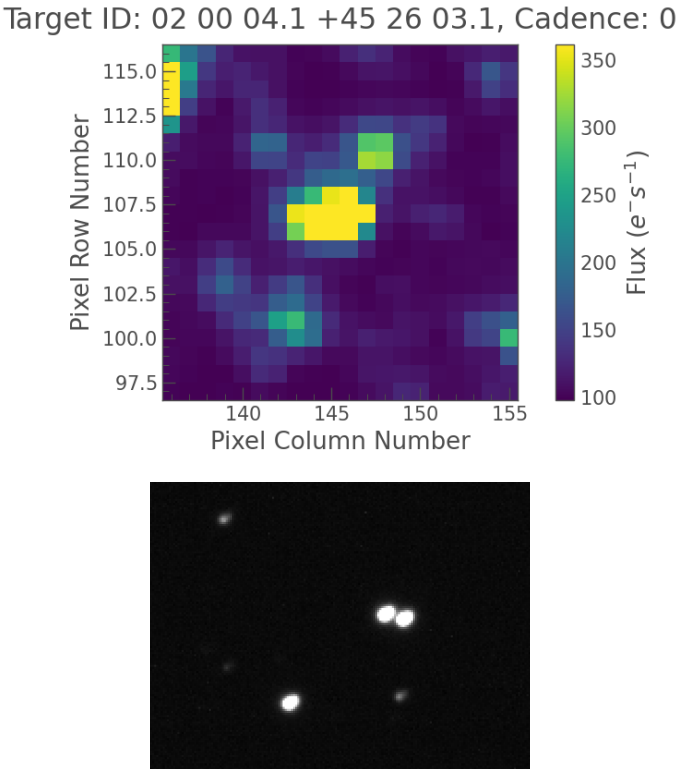

Figure 3.11: The maps of the S1 And system, upper panel: TESS with a field of view FOV ≈ 7.1 arcmin, both pairs and another star in close vicinity, Gaia DR3 355800077260542976, are merged to one large light source (the structure in the middle of the TESS map). Bottom panel: Ždánice observatory (R band), FOV ≈ 1.8 arcmin, the pairs, and the third star are distinguished.

3.4.2 S1 Cas

The $O - C$ variations (Figure 3.5, middle panels) of S1 Cas reveal the sinusoidal changes of both pairs that are opposite. Therefore, the system is confirmed quadruple with an outer period of around 6 years. With the observing time exceeding one orbital cycle, the outer period would be derived with certainty. Slight deviations are visible in some parts of the diagram (still within the uncertainty range). They could have appeared due to the lower accuracy of these measurements. The outer period is in order of several years. Therefore, the dynamical effects could explain these deviations with an additional minor influence. Nevertheless, it is not suitable to model these effects from the current observational sample.

The light curves of S1 Cas pairs are depicted in Figure 3.8 (middle panels). The pair B light curve shape with almost identical primary and secondary eclipses reveals the similarity between its components. On the contrary, pair A light curve contains a prominent primary eclipse. The SED fitting gives the composite temperature of 8 300 K. It indicates that the components should be primarily convective, with the exception of pair A primary star, in which the radiative envelope is assumed. The final PHOEBE parameters (Table 3.5) from TESS and new measurements in *Clear* show the expected values according to the light curve shapes.

There are relatively large l_3 values with a total luminosity of around 120 %. Gaia DR3 4315833321025328 64 can be found close to the examined quadruple. There could be a small light contamination in TESS data that indicates a larger l_3 parameter in TESS compared with the observations in *Clear*, done with better angular resolution. Interestingly, the third light values for both data sources are similar. Hence, the angular surroundings would not contribute significantly. The third light increase could mean another component in the system (or the independent star in the same direction with no possibility to distinguish).

3.4.3 S1 Cnc

The $O - C$ analysis of S1 Cnc confirms the gravitational bond between the eclipsing pairs. The outer orbits are eccentric (Figure 3.5, right panels) with a relatively high eccentricity value of 0.40. The common outer motion occurs with a period of almost 12 years. However, the available data do not cover one complete cycle. The LiTE dominates in the system, and no dynamical effects are visible.

All four components should be convective according to the SED fitting (6 300 K for the resulting composite temperature). The S1 Cnc vicinity does not contain any potential source of additional light. Our observations are not complete for both light curve models. Nevertheless, we measured and derived new minima timings. For these reasons, the TESS light curves were used for the physical modelling. The primary eclipses for both pairs are the most significant compared to much shallower secondary ones (Figure 3.8, right panels). The sum of the third light (Table 3.5) corresponds to 100 % of the luminosity within the errors.

3.4.4 S1 Cyg

Minima timings are well-derivable primarily for pair A. It was not possible to extract much suitable data with sufficient precision for the pair B. The non-linear variations in the $O - C$ diagrams (Figure 3.6, left panels) are noticeable, especially for pair A. The overall changes of pair B are higher than for pair A, which indicates a lower mass for the B binary. It is, hence, assumed that S1 Cyg consists of two eclipsing binaries. The outer orbit cannot be fitted due to the long P_{AB} period. The period value should be longer than 30 years concerning the current $O - C$ diagrams shape, assuming that the observed variations are roughly a quarter of the period or less.

The SED indicates a composite temperature of 7 500 K, near the limit between radiative and convective stars. The individual component temperatures are lower than the fitted composite value. Thus, we expect the components as convective. The angular vicinity is contaminated, Gaia DR3 2056435121634062848, partly by the TESS data. On the other hand, our new light curves contain the signal without this contamination. Therefore, it can be expected that the third light is higher for the TESS data than for our observations.

The light curves and PHOEBE models are depicted in Figure 3.9, left panels. The sum of the third light is 130 % and 116 % for both TESS and our data, respectively. As expected, the third light differs between these two datasets.

The pair A components are practically identical. The stars are also relatively similar for pair B. The O'Connell effect is visible on the pair B light curves with a slight

brightness decrease around the phase of 0.7. The effect does not have the strongest influence precisely on the brightness maximum, but before it.

The presence of the stellar spots is a general explanation of this phenomenon. The spots could cause the non-zero eccentricity value, which is still very small but not negligible in our model. The basic estimated models with one cool spot on the primary component could describe the O'Connell effect with a zero eccentricity value. Without any detailed information about the spot parameters, such as numbers, radii, and location, available, our model was done with no fitted spots.

3.4.5 S3 Cyg

The $O - C$ diagrams of the S3 Cyg system reveal the antiphase variations in the newest data (Figure 3.6, middle panels). The course of these changes has some slight differences. Moreover, the ASAS-SN minima timings in V tend to have a potential additional variation. The system seems to be a quadruple star with the gravitational bond confirmed via long-term photometry. However, the precise orbital parameters and final explanation for all possible $O - C$ variations require more data from the longer timescale. Therefore, our conclusions make this object a possible target for future monitoring.

The precise distance value for S3 Cyg is uncertain. Gaia DR3 (Gaia Collaboration, 2023) data do not contain any information about the distances or parallax. The Gaia DR2 (Gaia Collaboration, 2018) stated the parallax value with enormously large uncertainties, giving the distance of $1\,900 \pm 2\,200$ pc. The distance corresponds with Bailer-Jones et al. (2018), which is, on the other hand, based on the Gaia DR2 data. Anders et al. (2019) published the distance around 1 000 pc. This distance discrepancy and high uncertainty lead to unreliable extinction and SED fitting results. The extinction in this sky area depends strongly on the distance, according to Green et al. (2019). The most significant influence is between 500 pc and 5 000 pc, giving A_V in the range of 0.05 mag and 1.67 mag.

We used the Gaia DR2 distance as an approximated estimation. The SED fitting derived the composite temperature of 9 000 K. However, the resulting temperature is in large discrepancy with the other available sources (Table 3.3), where the temperature values are surprisingly consistent, between 6 600 K and 6 800 K. Therefore, these values were preferred over SED, which can be significantly biased by the inaccurate input parameters. The light curve models (Figure 3.9, middle panels) show the dominant pair A primary component and very the similar other three stars. The pair A light curve contains slight deviations against the model between the phases 0.2 and 0.4, indicating a possible surface activity.

3.4.6 S5 Cyg

This system is the faintest in our sample with 15 mag in the V band. Fortunately, it was still possible to obtain TESS light curves of both pairs due to their relatively deep eclipses (Figure 3.9, right panels). Unfortunately, only the primary minima timings were determined from ASAS-SN dataset. The pair A $O - C$ diagram (Figure 3.6, upper right panel) shows a non-linear change for older data. This course is seen even when using only the TESS minima timings, where the first sector used differs from the

others. Pair B (Figure 3.6, bottom right panel) does not show any variations, compared to pair A, and the period appears to be constant.

Stassun et al. (2019) state the distance of 1 700 pc. Without any available distance in Gaia DR2 and DR3, we took this value as a sufficient estimation. The composite temperature is 6 500 K according to the SED fit, which corresponds well with the Gaia DR2 temperature parameter (Table 3.3). Two pairs are similar, consisting of convective stars. The inner period ratio is close to the resonant state 4:3 (Table 3.2). This system is potentially interesting from an evolutionary perspective due to the resonance, similarities between the pairs, and short orbital periods. However, the outer orbit has not been proven yet.

3.4.7 S6 Cyg

S6 Cyg, like the previous case, is relatively faint (13.8 mag in V). The $O-C$ diagrams (Figure 3.7, left panels) indicate the mutual outer orbit. The simple LiTE fit was done. However, the results cannot be significantly precise because the outer orbit is not fully covered. The LiTE model reveals that the outer period should be longer than 13 years. Only the TESS data were suitable for pair B minima timings derivation. The vertical shifts between primary and secondary minima are noticed, indicating a possible apsidal motion.

Figure 3.10 (left panels) depicts the light curves and their model. All four components are convective according to the composite temperature of 5 500 K from the SED model. The deepest eclipse is observed in pair A primary minimum. There are slight differences between TESS and our data. The TESS observations are more reliable because of the complete phase coverage and lower scatter.

3.4.8 S1 Vul

Figure 3.7 (middle panels) depicts the $O-C$ diagrams for both S1 Vul binaries. Pair A indicates parabolic or sinusoidal variations. However, this non-linear assumption relies primarily on the oldest observations from SWASP. These two derived primary and secondary minima timings were obtained using the same methods as the other measurements, with no fitting issues. Moreover, the SWASP light curve is significantly phase shifted compared to other data, only at a glance, which states that the $O-C$ value should be different. Therefore, we can conclude that the non-linear variations are realistic. The pair A is probably a contact binary with a common envelope. The $O-C$ data can already be fitted by a consistent parabolic fit, but there is no clear evidence that the change really follows this variation course. There is also a slight vertical shift between primary and secondary minima that the mass transfer and contact between the components could cause. Pair B, on the contrary, does not show any significant changes. The SWASP data cannot be used for the pair B minima timings derivation because the pair B eclipses are not visible in this dataset. Although this system is characterised by the inner period ratio close to the 7:2 resonant state, the mutual orbit is not proven by the $O-C$.

The pair A models (Figure 3.10, middle panels for pair A and B) conclude that the components' temperatures are practically the same. On the other hand, there are considerable differences between the radii. The light curve fits, hence, state a possible

common envelope system. The third light values differ significantly. The TESS data give the sum of 119 %. On the other hand, using our V and R data we derived lower results with only 86 %. These data give a larger pair A amplitude, which causes the main third light decrease. The mass ratio q was derived using the q-search method. There is a slight difference between our data and TESS observations. The datasets could differ because of the S1 Vul vicinity. Gaia DR3 1833941590778469760 and Gaia DR3 1833929835438488576 can contaminate the TESS observations and may cause the additional third light increase. In our ground-based data, the total light is less than 100 %. One explanation could be the hange in the composite temperature, the SED and Gaia results give two relatively different values. This third light discrepancy should be explained in future work by adding observations in more photometric filters, spectroscopy, and SED revision.

3.4.9 S1 Cam

The S1 Cam system shows the antiphase variations in the $O-C$ diagrams of both pairs (Figure 3.7, right panels). The quadruple nature is, hence, proven. However, the outer orbital period is significantly long. The fitted model (Table 3.4) gives an estimated LiTE P_{AB} value of 33 years. This result could not be precise. On the other hand, the diagrams depict that the outer period should be at least 20 years or more.

Pair A contains an additional sinusoidal variation with a period of less than 8 years. This is much shorter than the outer motion period. Therefore, there is another possible component, a star or an exoplanet. According to the variation amplitudes, the fifth body can probably be less massive than the other four components. The physical model does not provide any significant additional light, the third light sum is around 100 % within the uncertainty. This may prefer the exoplanet solution. However, the precise nature of the potential fifth body needs to be discussed more in the future with new $O-C$ and other available data. The $O-C$ diagram of pair A in Figure 3.7 contains both variations. The influence of the shorter changes is not observed with certainty for pair B. Thus, the second LiTE fit was added only for the pair A $O-C$ diagram.

Both pairs' light curves (Figure 3.10, right panels) resemble each other. All four components are convective stars with the temperature range between 4 700 K and 5 000 K. With no obvious source of light contamination, the TESS and R third light values are the same within the uncertainty.

3.5 Discussion

The observed SED represents the combined flux of all four stellar components. Therefore, each star could contribute to the overall SED shape differently. The flux maxima are generally at different wavelengths, depending on their temperatures. A significantly cooler component could enlarge the flux at longer wavelengths. On the other hand, one hot dominating star reshapes the SED fit to a higher composite temperature. The hot stars also require more data for short-wavelength bands. The resulting inferred flux fitting then represents the maximum temperature estimation.

Despite these issues, we use all available photometric bands to construct the SED. This multi-band modelling allows us to derive a more robust temperature estimate than relying only on the catalogue automated pipeline outputs. The near objects in

the angular vicinity could influence the results in dense stellar fields. Additionally, the measurements were made at different times. The observations made during the eclipses could affect the colour indices and total brightness. We can minimise these effects by combining photometric measurements from various times and sources.

We compare the composite temperatures from our SED fitting to those from large surveys, Gaia, TESS, and StarHorse (Table 3.3). The comparison reveals both consistencies and systematic discrepancies that highlight the strengths and limitations of each method in the general context of multiple stellar systems.

The S1 Cnc results are in significant agreement for all investigated sources. The system's light is probably not perturbed by any surrounding stars. Both binaries are similar and consist of cool components. Furthermore, the periods are relatively long, and the eclipses take only a small part of the phase-folded light curves. Hence, substantial distortions do not affect the temperature derivations. The four modelled S1 Cam components (the fifth component's nature is currently unclear) show noticeably similar temperatures between 4 700 K and 5 000 K. As in the previous case, the sky field is clear of any potential contamination sources. It is then possible to expect no obvious distortions in the measurements.

S5 Cyg and S6 Cyg temperatures agree with Gaia DR2. Unfortunately, other investigated catalogue values are not available. S1 Cas, S3 Cas, and S1 Cyg behave similarly. The mean Gaia, TESS, and StarHorse values are practically identical to the SED fitting. However, the output parameters are broadly scattered, mainly for S1 Cyg. We can conclude that using one specific source for the temperature could lead to extremely varied results.

The SED fitting of S1 Vul does not follow the Gaia observations. The other two catalogues do not contain the temperature information. This discrepancy could be explained by the pair A common envelope structure, Gaia bias, or possibly different extinction for the SED modelling. The common envelope and biased SED outputs could have created the third light discrepancy.

The S3 Cyg catalogue and composite temperatures were found to be consistent. However, the SED fitting is systematically shifted compared to other data. As mentioned, the distance and extinction parameters are inaccurate, and the resulting values are biased. For these reasons, we preferred other sources instead of the SED.

We have detected several cases where the SED fitting confirms the composite temperature values derived by different methods. On the contrary, remarkable inconsistencies are visible in some systems, which could lead to significantly different conclusions. In this paper, we study specific individual objects. However, we suggest making this comparison for all multiple candidates to provide robust statistics of the catalogue composite temperature consistency and credibility.

The outer orbital periods can last for several decades. With our observational timescales of usually several years, depending on the specific system, the outer orbit parameters cannot always be fitted with high precision (Table 3.4). The S6 Cyg and S1 Cam $O - C$ models are primarily the suggestions of the outer orbit. However, the fits give us constraints on the minimal outer period value. For S1 Cyg and S3 Cyg, the outer motion could last several decades without significant constraints from our current data. The apsidal motion of S3 Cas pair A is a similar case. The variations between primary and secondary minima are visible but cannot fit properly due to the long apsidal motion period.

S1 Cas, S1 Cnc, S3 Cas pair A, and additional LiTE for S1 Cam models provide the fundamental outer orbit parameters with higher certainty. The S1 Cnc orbit shows a high eccentricity of 0.40. The 12-year orbital cycle is not observed in its entirety. The data coverage enhancement is planned for the ongoing research. There is a slight increase of radius ratio between the S1 Cnc pair A components. We fitted only the TESS light curves because our data are incomplete due to the long inner periods. The follow-up multi-band observations would improve the model.

3.6 Summary

We present an analysis of ten doubly eclipsing systems in the Northern sky. Within the Squadra observing project, we made new photometric and spectroscopic measurements and combined them with ASAS-SN, ZTF, SuperWASP, and TESS datasets. Our research methods contain primarily long-term photometry that allows us to construct the $O-C$ diagrams for individual pairs within each system. Seven systems are considered as the 2+2 quadruples among the ten studied candidates. S1 And (ASASSN-V J020003.56+452605.2) was excluded from the candidate list as a probable blend. The detrended and disentangled light curves were modelled using the PHOEBE software (0.32). Using the SED fitting, we calculated the composite effective temperature for each candidate. The SED fit provides us with consistent and reliable results for most cases. We have shown that the fitting without optimal distance and extinction parameters could create significant differences between the models. The radial velocities of all four S3 Cas (ASASSN-V J233336.79+615012.0) components were obtained from our spectral analysis, and the emission of the Hα line was confirmed. The $O-C$ analysis of S1 Cam (TIC 9493888) provides evidence of the mutual motion and outer orbit between its pairs. Furthermore, the additional LiTE variations suggest the presence of the fifth component. The nature of this object could be stellar or exoplanetary.

Acknowledgements

JK was partly supported by the project MUNI/A/1503/2024. TP acknowledges support from the Slovak Research and Development Agency – contract No. APVV-20-0148 and the VEGA grant of the Slovak Academy of Sciences No. 2/0031/22. This work is supported by MEYS (Czech Republic) under the projects Czech Republic MEYS LM2023032, LM2023047, and CZ.02.01.01/00/22_008/0004632.

Based on data from the Perek telescope at the Astronomical Institute of the Czech Academy of Sciences in Ondřejov. We would like to thank all the observers for their efforts. This publication makes use of VOSA, developed under the Spanish Virtual Observatory (https://svo.cab.inta-csic.es) project.

Data Availability

The data underlying this article will be shared on reasonable request to the corresponding author.

Chapter 4

Period ratios and observation of noticeable resonance at 3:2 for 2+2 quadruple systems

Jakub Kolář,[1] Miloslav Zejda,[1] Anna Richterková,[1,2] Petr Dvořák,[3] Reinhold Friedrich Auer,[4] Zbyněk Henzl,[4] Radek Dřevěný,[4] Sabina Pačková,[1] and Milan Uhlár[5]

[1]Department of Theoretical Physics and Astrophysics, Faculty of Science, Masaryk University, Kotlářská 2, 611 37 Brno, Czech Republic
[2]Prostějov Observatory, Museum and Gallery in Prostějov, Kolářovy sady 3348, Prostějov, Czech republic
[3]Brno University of Technology, Institute of Physical Engineering, Technická 2, 616 69 Brno, Czech Republic
[4]Variable Star and Exoplanet Section of the Czech Astronomical Society, Vsetínská 78, CZ-757 01 Valašské Meziříčí, Czech Republic
[5]Ďáblice Observatory, Pod Hvězdárnou 768, 182 00 Ďáblice, Czech Republic

Published in Monthly Notices of the Royal Astronomical Society (MNRAS), Volume 538, Issue 2, April 2025, Pages 1160–1166.

Abstract

Quadruple stellar systems with two mutually orbiting eclipsing pairs (2+2 quadruples) are currently of great scientific interest because they offer a unique opportunity to determine the physical parameters of their constituent stars with high precision. In this study, we enlarge their numbers and present an analysis of the orbital periods and their ratios for a sample of 781 quadruple candidates with a 2+2 structure. Moreover, we compare the observed distribution of period ratios to a simulated prediction based on a uniform distribution of inner periods. We find a preference for a 3:2 resonance between the inner orbital periods, while the 1:1, 4:3, and 5:3 resonances do not deviate

significantly from the predicted distribution model. Higher resonant values are on a slight decline, probably due to a lack of data. These results, derived from the largest statistical ensemble of 2+2 quadruples to date, provide evidence for the hypothesis that gravitational interactions between the star pairs can preferentially lead to a 3:2 resonance during their evolution.

4.1 Introduction

Stars are categorised into single stars, binaries, or higher-order multiple systems. Binary and high-order fraction increases for more massive objects (Offner et al., 2023). Usually, we observe multiple stellar systems in stable configurations. In the case of four component systems, two possible hierarchical structures exist. The first possibility is a 3+1 configuration, a triple star with an additional distant component. The 2+2 system consists of two binary pairs, A and B (Figure 4.1), which orbit together around their common centre of mass. More known quadruples exist in the 2+2 configuration than in the 3+1 (Tokovinin, 2014, 2023), because their geometry sometimes allows both pairs to be eclipsing binaries. Therefore, this object class is often referred to as a doubly eclipsing system. In fact, 2+2 quadruples, especially those containing Algol-like systems, enable us to obtain the physical parameters of individual stars and a deeper understanding of the evolution of these higher-order multiple systems.

Zasche et al. (2019) first introduced the general statistics for 2+2 doubly eclipsing and non-eclipsing systems and increased their numbers. Photometric surveys, satellites, and ground-based observations represent a powerful tool for detecting and calculating the pair's mutual motion around their common centre of mass. Using the $O-C$ diagrams (also known as eclipse time variations ETV), we can study the doubly eclipsing star on a long timescale and detect the light time travel effect (LiTE) for both pairs. The LiTE periods of the binaries have to be the same. However, the $O-C$ variations are in antiphase. The LiTE amplitudes $A_{\rm A}$ and $A_{\rm B}$ can be different but in most cases they are similar. The amplitude ratio gives us the mass ratio $q_{\rm AB}$ between both binary pairs

$$q_{\rm AB} = \frac{m_{\rm A}}{m_{\rm B}} = \frac{A_{\rm B}}{A_{\rm A}}, \tag{4.1}$$

where $m_{\rm A}$ and $m_{\rm B}$ are the corresponding binary masses. Deriving the mass ratio is one of the main parameters of the quadruple stars research. Moreover, we can obtain the following parameters from the light curve analysis, such as relative radii or surface temperatures, and thus, it is fully desirable to obtain as large a database of these 2+2 quadruples as possible.

Nowadays, the number of doubly eclipsing candidates has started growing rapidly (Kostov et al., 2022; Zasche et al., 2022b), especially with TESS (Ricker et al., 2015) and other photometric surveys. However, only a few candidates (60 systems in our used sample) are confirmed 2+2 quadruple stars with at least estimated orbital parameters for their common outer orbit. The first statistics of 146 2+2 systems and their candidates were done by Zasche et al. (2019). They defined the period ratio $R = \frac{P_{\rm A}}{P_{\rm B}}$, where $P_{\rm A}$ and $P_{\rm B}$ are inner periods for binary pairs A and B, respectively. The period ratio distribution indicated some interesting possibilities for resonant capture: The increase around 1:1 resonance surroundings was noticeable together with 3:2 resonant ratio

overabundance. On the other hand, another first-order orbital resonance of 2:1 was in decline.

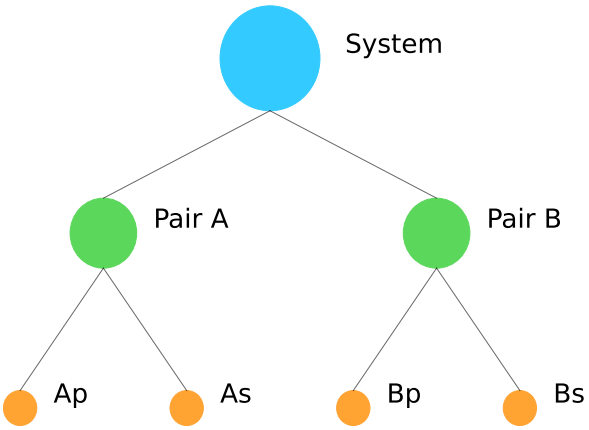

Figure 4.1: Structure of 2+2 quadruple system with used notation, each pair contains primary (p) and secondary (s) component.

Breiter and Vokrouhlický (2018) studied the dynamics of the 1:1 resonance case. Their calculations stated that the 1:1 resonant capture was improbable and not highly expected. They also suggested to expand their work and to add the cases of 2:1 and 3:2 resonances. Tremaine (2020) described the conditions for resonant capture of 2:1 and 3:2 and discussed which period ratios are near or directly at the resonance. He also analysed and compared the results with the period ratio distribution from Zasche et al. (2019) and pointed out issues of systems near 1:1 resonance but not generally at the precise resonant value. Interestingly, decreased density in the 2:1 ratio was observed instead of the expected enhancement. Only two systems were at the 3:2 resonance, and the other six were in its surroundings. However, these datasets still need to be larger to provide specific results. Tremaine (2020) presented essential questions at the end of the paper, i.e., what is the exact shape of the period ratio distribution, how far from the given ratio can we still consider a resonance, and what the statistics look like for each spectral type. We open up and add one more fundamental question to which there is currently no known answer: What this distribution would look like for systems in different evolutionary states? More 2+2 candidates with well-described inner orbital periods are needed for proper analysis and statistics. Enhancing the confirmed candidate numbers is also essential to improve the current research state.

In this paper, we comprehensively analyse the periods and resonances of currently available systems of 2+2 quadruples and their candidates. Moreover, we present newly detected candidates and additional used data. For the acquired data, we describe the general period statistics through observations and show the period ratio distribution and resonance statistics. Our results are evidence to specify the systems' closeness to resonant values at 3:2 and, therefore, resolve the issues suggested by Tremaine (2020). This work can be used to compare theoretical models and the observations in the planned paper mentioned by Breiter and Vokrouhlický (2018).

4.2 Data collecting

4.2.1 Small Magellanic Cloud

We searched for new doubly eclipsing quadruple candidates. We selected the OGLE photometric survey (Pawlak et al., 2013, 2016). Zasche et al. (2019) already inspected the light curves of the Large Magellanic Cloud (LMC). However, the Small Magellanic Cloud (SMC) was still not carefully and adequately searched for new candidates. We decided to manually inspect the phase-folded light curves of known eclipsing binaries (pair A in our notation) in the OGLE database, looking for the detection of additional periodic variations corresponding to another eclipsing pair (B). Our criteria were system brightness constraints (up to 20 mag in I filter), a reasonable orbital period value of the known pair (our period range was set to 0.5 - 20 days), and a sufficient variations' amplitude 0.08 mag for pair A primary minimum. The 0.5 days minimum limit allows us to detect the additional brightness changes due to eclipses and distinguish between other possible variability causes. Our maximum period limit was set so that the brightness changes could be well measured against further surveys and ground-based observations. The amplitudes of both pairs had to be clearly visible through the scatter, which depended on the brightness. Thus, our typical brightness values were between 13 and 17 mag.

On the phase-folded light curve (according to pair A period) we could easily see other brightness decreases that are not phase-folded with a known pair A period. Usually, these eclipses go through the whole phase curve as random brightness dimming (Figure 4.2 upper panel). We could see some kind of regularity if the binary pairs are in resonance.

It was necessary to check every phase curve visually to prevent instrumental error influences and false positive signals. A common issue was that the pair A orbital period in OGLE was half or twice the real value. This factor could lead to a strange phase curve shape, but it is usually well recognizable (the secondary minimum misses or the eclipses are repeating during one falsely determined cycle). The orbital period was also determined inaccurately in some cases, or there were other effects such as period change or apsidal motion. We could not clearly state the situation for eclipsing systems where the other possible pair B changes were lost in the noise (below ~ 0.01 mag), and sometimes, we detected outliers that were probably caused by instrumental faults. For some candidates, we were not able to detect the additional period. The cause could be a lack of data points or also not obvious outliers that do not have a physical origin. Another case of false positives was when the other signal had a different nature than the eclipses, typically pulsations, rotation effects, or unclear causes. We did not include these systems in our analysis.

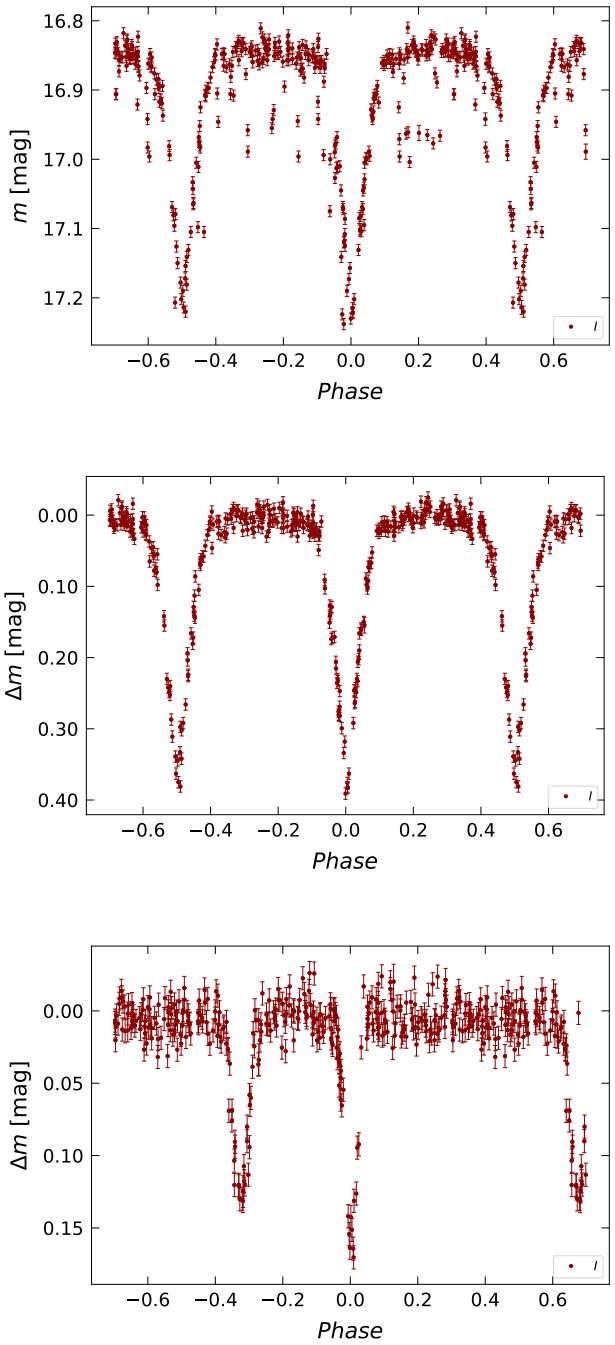

Figure 4.2: Phase-folded light curve of OGLE SMC-ECL-6093 in I filter from OGLE IV data according to known OGLE pair A period (upper panel), additional unphased dimming represent the second binary pair (B), disentangled pair A phase-folded light curve (middle panel), and disentangled pair B phase-folded light curve (lower panel). The light curves disentangling was made with SILICUPS software (more details in follow-up work Kolář et al. (in preparation)).

The suspicious systems were further analysed using light curve disentangling in SILICUPS software (Cagaš, 2017). Phenomenological models from Mikulášek (2015) were used for modelling the known pair A. After pair A subtraction, unphased pair

Table 4.1: The studied 2+2 candidates and their parameters: name, coordinates (J2000), location, confirmed quadruple, both inner orbital periods, period ratio, resonance occurrence, resonance closeness, reference (source), RUWE number with composite effective temperature from Gaia DR3 (Gaia Collaboration, 2023) (if available), and additional note. Every source contains information about the number of the contributed candidates. The full table is available online.

Name	RA [°]	DEC [°]	Loc.	Conf.	P_A [days]	P_B [days]	R	Res.	C [%]	Ref.	RUWE	T_{eff} [K]	Note
TIC 418699570	0.486195	63.106782	Gal	0	1.6737	4.2703	2.55141	x	x	12	28.908		
WISE J000246.4+695224	0.693290	69.873550	Gal	0	0.2893554	35.6614	123.24429	x	x	9	20.545	5887.2	
ASASSN-V J000432.60+632605.0	1.135830	63.434730	Gal	1	1.097909	0.994421	1.10407	x	x	9, 15			
Gaia DR3 386474080852740992	1.461502	44.447714	Gal	0	2.599973	0.114405	22.72604	x	x	13	0.986	7368.2	
Gaia DR3 384686137507666944	2.702797	43.426465	Gal	0	0.561156	0.30431	1.84403	x	x	13	1.034	6525.1	
ZTF J001301.21+660356.8	3.255080	66.065800	Gal	0	1.3770888	3.9170333	2.84443	x	x	15	1.399	6539.8	
TIC 201310151	4.111881	-58.141759	Gal	0	5.538208	8.485997	1.53226	x	x	6	6.746	5660.2	
TIC 407060024	5.393878	66.226673	Gal	0	1.8569	5.8375	3.14368	x	x	12	1.151	6899.5	

1: Pawlak et al. (2013), (15); 2: Fedurco and Parimucha (2018), (1); 3: Zasche et al. (2019), (149); 4: Kounkel et al. (2021), (1); 5: Fezenko et al. (2022), (7); 6: Kostov et al. (2022), (84); 7: Southworth (2022), (1); 8: Zasche et al. (2022a), (4); 9: Zasche et al. (2022b), (110); 10: Tokovinin (2023), (55); 11: Zasche et al. (2023b), (7); 12: Kostov et al. (2024), (95); 13: Vaessen and van Roestel (2024), (192); 14: Zasche et al. (2024), (5); 15: This paper, (90).

B remains. We searched for its orbital period, and in some cases, the period was easily found by our estimations. After excluding false positive cases, we have found eight new doubly eclipsing candidates: OGLE SMC-ECL-1086 (with OGLE SMC-ECL-1087 as the possible pair B), 2417, 2541, 4569, 4595, 5925, 8061, and 8098. Two other systems studied by Zasche et al. (2024) were also independently found in our searching. We consider that P_B of OGLE SMC-ECL-2339 is half the value mentioned in paper above (1.69788 days). From the $O-C$ variations (Kolář et al. (in preparation)), we could state that OGLE SMC-ECL-6093 is probably a new confirmed quadruple system (also confirmed in Zasche et al. (2024)). Detailed information about objects, especially their periods, are listed in Table 4.1.

4.2.2 TESS

Another main source of our search was the Transiting Exoplanet Survey Satellite (TESS) (Ricker et al., 2015). Due to its continuous measurements for a period of 27 days for each sector and very high precision, it is an excellent tool for detecting new periodic variations that could not possibly be seen or detected by other surveys. For the reasons stated above, we could detect binary pairs with brightness changes to 0.01 mag (depending on the total system brightness and current sector) and orbital periods with sometimes even more than 10 or 15 days with the careful combination of more TESS sectors. The light curves were disentangled using SILICUPS software with the same process as in the previous subsection.

The disadvantage of TESS images is the low angular resolution. Thus, we had to deal with possible blends and false positive candidates. We checked the candidates pixel by pixel and used ground-based photometric surveys to identify the blends (follow-up observations would be the other helpful method, but it was not feasible due to the large total candidates number). Some of these targets were already published in Zasche et al. (2022b). Here, we introduce new doubly eclipsing systems without duplicity with other available mentioned sources.

4.2.3 Additional data

We took additional quadruple candidates available in the literature. We used data from Kostov et al. (2022, 2024), Zasche et al. (2019); Zasche et al. (2022a,b, 2023b, 2024), Vaessen and van Roestel (2024), Pawlak et al. (2013), Southworth (2022), Kounkel et al. (2021), Fedurco and Parimucha (2018), Fezenko et al. (2022), and Tokovinin (2023) together with our new candidates' parameters for the analysis.

For our purposes of period analysis, we selected the following system criteria: both inner periods have to be known for every object, the period lengths are a maximum of hundreds of days (usually several days), and also already known blends were discarded. Based on these parameters, our sample consists of 781 systems in total, mostly in our Galaxy and a small amount in the LMC and the SMC (Figure 4.3).

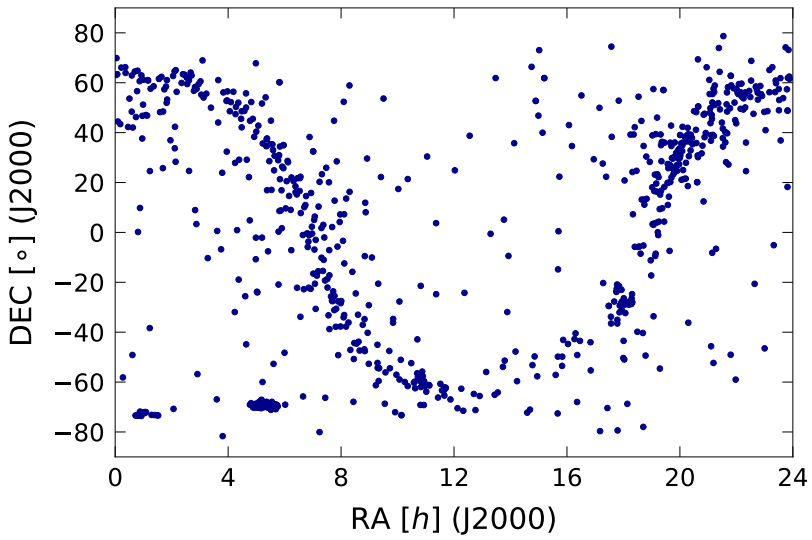

Figure 4.3: Sky distribution of analysed quadruple candidates.

4.3 Analysis

4.3.1 Period ratio distribution

We investigated the known inner periods' relations in every given system. We calculated the period ratio R:

$$R = \frac{P_{\mathrm{A}}}{P_{\mathrm{B}}}. \tag{4.2}$$

Period values were ordered to be $R \geq 1$ (longer period divided by shorter one). We made this sorting to get a uniform order. The pair naming, A or B, has no physical significance; pair A is usually the first detected binary. The detection depends also on brightness amplitudes, observation sampling, etc.

The period ratio distribution was plotted in the histogram in Figure 4.4. The data show a decline with increasing R value with small deviations. We calculated the model prediction of the R distribution and compared it with the used dataset. We assumed

two uniform distributions for the inner periods P_A and P_B in the range between 0.2 and 20 days. The lower limit of the range can be set to 0.2 days because these are simulated data and we do not have observational constraints. We took two period values and calculated their ratio R. We repeated the procedure for 781 systems to get the same amount as the data sample. By this method we obtained one simulated period ratio distribution. We generated 500 000 simulations to derive the average model distribution. We plotted this model as our prediction together with the data histogram. Using the Kolmogorov-Smirnov (K-S) test, there is a high probability of 93 % that data and model statistically correlate (the comparison was made to the maximum value of $R = 5$ as in the histogram in Figure 4.4, because higher R values had too few known systems). We could still see some minor differences, probably caused by a lack of data.

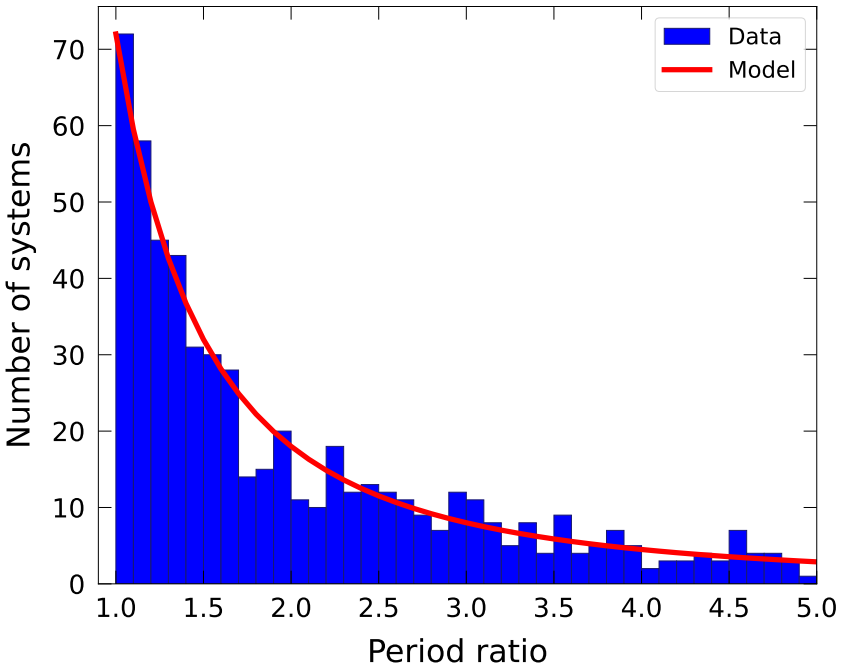

Figure 4.4: Period ratio distribution, data together with the computed model prediction.

4.3.2 Resonant values

The relatively large sample of the candidates allows us to investigate resonant ratios in more detail. First, we had to choose which resonant values could be reliable and have sufficient data for analysis. We decided to study the smallest integers and half-integers and added the nearest third values. Thus, the studied resonances were 1:1, 4:3, 3:2, 5:3, 2:1, 5:2, 3:1, 7:2, and 4:1. Higher values had no sufficient coverage in the sample. We aimed primarily for the most discussed resonances, 1:1, 3:2, and 2:1, which could have, according to previous literature, some kinds of deviation compared with the predicted expectations.

Another crucial parameter is the condition under which R goes into some of the mentioned resonant ratio. We defined the closeness C to the resonance, represented by the following equation, and two closeness vicinity ranges

$$C = \left[\frac{P_{\mathrm{A}}}{P_{\mathrm{B}}} : \mathrm{Resonance} \right] - 1. \tag{4.3}$$

The critical role of the C vicinity range was to have sufficient system numbers to detect some possible phenomena (overabundance/decrease). On the other hand, too wide a range is not suitable because the possible deviations disappear in the scatter of the wide vicinity. We defined the shorter range of resonance vicinity as $C < 1$ % to fulfill the condition of having large enough systems. We took double the range with $C < 2$ % for comparison. We considered systems that fit within these intervals for the selected resonance values to be close to the given resonance. The vicinity limits for both ranges are shown in Table 4.3.

We tested the properties of the resonant values. For each C range (1 % and 2 %), we plotted the resonance diagrams (Figure 4.5 and 4.6) using our data together with the simulated model. The data and model comparison is also shown in Table 4.4. The model predicts how many systems we should detect for every resonance. The model uncertainty is ± 1 for every resonant ratio. Resonance comparison diagrams indicate some interesting behavior.

Table 4.3: The vicinity resonance limits for both used ranges, 1:1 resonance has both minimum values one according to period ratio definition as the lowest possible limit.

Resonance	$C < 2$ %		$C < 1$ %	
	R_{min}	R_{max}	R_{min}	R_{max}
1:1	1.000	1.020	1.000	1.010
4:3	1.307	1.360	1.320	1.347
3:2	1.470	1.530	1.485	1.515
5:3	1.633	1.700	1.650	1.683
2:1	1.960	2.040	1.980	2.020
5:2	2.450	2.550	2.475	2.525
3:1	2.940	3.060	2.970	3.030
7:2	3.430	3.570	3.465	3.535
4:1	3.920	4.080	3.960	4.040

i. The 1:1 resonance corresponds very well with the assumed prediction, with no significant differences. The number of systems is not large compared to the following resonances, because the C ranges are the smallest for 1:1 resonance (depending on the C definition as the fraction between the R ratio and the given resonance).

ii. Resonant values 4:3 and 5:3 are in agreement with the model. There is only a negligible deviation for 4:3 in the case of $C < 1$ %.

iii. We can observe an overabundance for the 3:2 resonant ratio. This excess is the most significant within our sample for both C ranges.

Table 4.4: The number of systems with the given resonance for the data and model prediction.

Resonance	$C < 2$ %		$C < 1$ %	
	Data	Model	Data	Model
1:1	15	15	9	7
4:3	23	24	10	13
3:2	27	21	16	11
5:3	17	19	9	9
2:1	12	16	6	8
5:2	9	13	3	7
3:1	13	10	2	6
7:2	7	9	5	5
4:1	4	8	2	4

iv. 2:1 and 5:2 indicate a slight decline compared with the assumed model.

v. The 3:1 and 7:2 ratios show slight changes between the C ranges. There are only two systems close to the 3:1 resonance with $C < 1$ %, the 7:2 deviations are less significant.

vi. There is a small decrease in the 4:1 resonant ratio. However, 4:1 is the least represented element in the analysis and could be crucially influenced by selection effects.

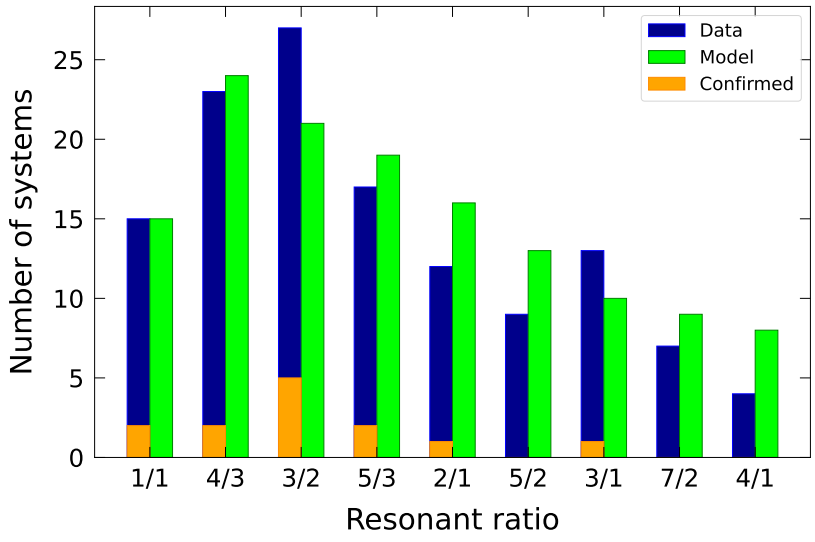

Figure 4.5: Resonance comparison diagram between data and model with $C < 2$ %, together with marked confirmed quadruples.

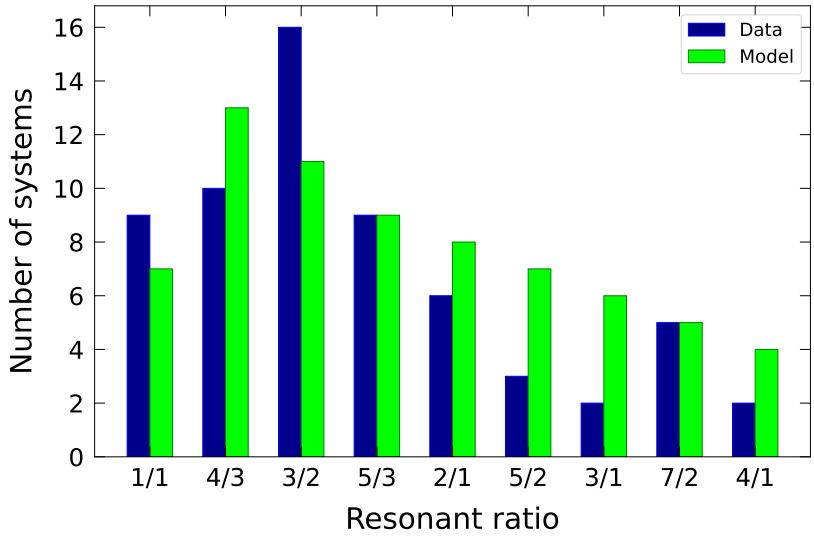

Figure 4.6: Resonance comparison diagram between data and model with $C < 1$ %, the confirmed quadruples are not marked in this plot because of lack of data.

4.3.3 Confirmed quadruple systems

Long-term monitoring of the selected candidates led to the confirmation of mutual motion around the common centre of mass. The outer period P_{AB} and other orbit parameters are usually challenging to derive. There are only a few well-described 2+2 system outer orbits (i.e., Zasche et al. (2019); Zasche et al. (2022a, 2024)) with short orbital outer periods (in order of years). We can consider the system as confirmed when we can see non-linear changes for both binaries in the $O-C$ diagrams that correspond to each other. The $O-C$ variations can lead to confirmation even though the LiTE is covered partially. We included these cases in our analysis as sufficient confirmation of the quadruple nature.

Only 60 (7.5 %) indisputably confirmed 2+2 quadruples are known in our sample. This small percentage is caused mainly by the orbital outer periods, which are usually very long (compared to the inner periods and the available observing time). There are 13 quadruples close to the resonances for $C < 2$ % and 6 for $C < 1$ %. Statistical calculations of the period ratio R and the resonances were not possible from such a small number.

4.3.4 Galaxies

We investigated the sky positions of the studied candidates (Figure 4.3). The vast majority of objects are located in our Galaxy, and only 12 % are in LMC and SMC. Systems' distribution in the Galaxy follows primarily the position of the galactic plane. We found 107 systems close to the resonance for $C < 2$ % and 52 for $C < 1$ %. The LMC and SMC contain 22 systems for $C < 2$ % and 10 for $C < 1$ %. We observe mostly more luminous stars in the Magellanic Clouds. Thus, statistics could be biased (towards more luminous stars).

4.4 Discussion

Our sample contains mostly Algol-type binary stars. Usually, at least one of the inner periods is long, around 1 day or more. 27 % of the inner periods were shorter than 1 day. Selection effects strongly influence the candidates' detection. Quadruples with longer periods (several days) are significantly more prevalent in photometric surveys, and light curve disentangling is usually easier. Algol-type binaries are thus preferred in our sample. Therefore, the distribution between Algol, β Lyr, and W UMa type binary stars could not be covered. We suggest searching for new candidates with inner orbital periods of up to 1 day to provide these statistics.

The used dataset consists of various literature sources and our new objects. Thus, periods precision is not uniform. The most accurately derived periods' precision is in the order of 0.01 s. Furthermore, the sample includes data of lower precision, about several seconds and even several minutes or hours for the extreme cases. The period ratio R accuracy also varied, depending on the quality of the measured inner periods. In most cases, especially for the statistically sufficiently covered part between ratios 1 and 5, the periods belonged to the better-defined group. Larger R could sometimes have poorer accuracy, because longer inner periods may not always be determined precisely.

The period ratio distribution (Figure 4.4) shows that the used data mainly correspond to the model prediction. Zasche et al. (2019) described this distribution for 146 candidates and discussed the deviations against their model. There were primarily three of the most significant phenomena: an increase of the 3:2 resonance, a decline between the ratio 1.2 and 1.5, and a minor dip around the 2:1 resonant ratio. Most of the deviations disappeared using the current numbers of 781 candidates compared with the simulation. A 3:2 increase and a potential 2:1 decline are visible during resonance analysis, where we used shorter C ranges of the vicinity than the histogram bins. We do not observe the dip between the 1.2 and 1.5 values. There are two slight decreases between 1.7 and 1.9 and 2.0 and 2.2. The exact explanation of this phenomenon is not clear yet. The reasons could be data fluctuations and bin width influences in the histogram.

The data and model agreement for the 1:1 ratio (Figure 4.5 and 4.6) shows that there is no clear preference for long-term stay in this resonance, it occurs here within the expected state. The same is observed for the 4:3 and 5:3 resonant ratios. The 3:2 overabundance was first detected by Zasche et al. (2019) and was discussed as a potential long-term stable solution. This ratio has the largest increase in our data sample. However, this difference is prevalent in only several systems. The given deviations indicate a possible preference for the 3:2 state as the long-term stable option. A precise analysis with certain conclusions would require more data than is currently available.

The 2:1 ratio has a slight decrease that almost disappears within the C range up to 1 %. Interestingly, a similar decline is also observed for the 5:2 resonance. The 3:1 and 7:2 ratios are not sufficiently covered to state specific properties and they vary between the two C ranges. The 3:1 overabundance for $C < 2$ % changed for $C < 1$ % to have only two known systems. On the other hand, the 7:2 resonance has a decline for $C < 2$ % and is in good agreement for $C < 1$ %. As we stated in Section 3.2, the selection effects could be extremely strong for the 4:1 ratio. The R value is relatively large, and the longer inner period could be hard to detect even for the TESS satellite

and other surveys. Overall, the larger R values comprise too small an amount of data to draw clear conclusions.

Fabrycky et al. (2014) studied features of first-order resonant period ratios for multi-transiting exoplanet candidates in KEPLER data. They analysed the first-order resonance offset from all the planetary pair candidates. There are practically no systems within the ratio between 1.00 and 1.25. Nevertheless, our sample contains 162 2+2 candidates within this R range. Thus, we can observe first-order resonant values like 6:5, 7:6, 8:7, etc., that could contain misleading results. The configuration of multi-transiting exoplanet systems is significantly different than in the 2+2 quadruple. For these reasons, this method is not suitable for multiple stellar objects.

There is a relatively small representation close to the 3:2 resonance for the systems with one or both inner periods up to 1 day. We can see only three binaries (11 %) with a longer inner period and five binaries (19 %) with a shorter one close to the 3:2 ratio within $C < 2$ %. It is the least represented case out of the mentioned resonances. The 1:1 value has five binaries (33 %) for both cases, with longer and shorter inner periods. Interestingly, the 4:3 ratio has the largest sample of the resonances within the inner period values up to 1 day, eight binaries (35 %) for the longer periods and nine (39 %) for the shorter ones. The 5:3 ratio has three binaries (18 %) for both categories. We see here the largest sample of the periods up to 1 day for the 4:3 resonance and the smallest one for the 3:2 resonance, the ratio with the largest overabundance compared to the used model. Thus, most 3:2 candidates (more than expected) have their inner periods longer than 1 day.

13 of 60 confirmed 2+2 systems are close to the studied resonant values within $C < 2$ %. The relative coverage is similar to the whole sample of candidates, but in absolute numbers there are only a few systems to state any properties. Most of the confirmed candidates have relatively short outer periods P_{AB}. Thus, the binaries should be close to each other. We suggest a question of whether the dynamical interactions between the binary pairs could lead to breaking their resonant state. We can observe (i.e., Kostov et al. (2021, 2023)) that dynamical effects can be stronger than LiTE for very close quadruple stars with short outer periods. On the contrary, very wide binaries could evolve independently and possibly not create and stay in the resonant ratio.

The possible resonance could be broken by another scenario. Each binary evolves within its subsystem. Mass transfer plays a key role during the evolution process of close binaries, and the inner orbital period changes. Thus, the resonant ratio can be potentially disturbed by the inner evolution of one or both pairs. The eccentric orbits could also contribute to the resonance breaking. However, there are no observational evidences for these suggestions within the used dataset.

4.5 Summary

In summary, we assembled the largest sample of available 2+2 quadruple candidates up to date, and we complemented it with our newly discovered doubly eclipsing systems into a comprehensive analysis of inner orbital periods and period ratios, comprising a sample of 781 systems. Most analysed objects are located in our Galaxy following the galactic plane (Figure 4.3). The remaining candidates are in the LMC and SMC. We

determined the inner period ratio R distribution (Figure 4.4) and compared it with the simulated prediction, assuming a uniform period distribution. Using two vicinity ranges for the chosen resonant values, we created resonance comparison diagrams (Figure 4.5 and 4.6) for our data and model. The majority of the observing ratios corresponded well with the prediction model. However, we observed the preference resonance at 3:2, which is also supported by previous studies. On the other hand, the ratios at 1:1, 4:3, and 5:3 show a remarkably close match with the prediction, and therefore, there are no signs of preference for these resonant values. A slight decline compared to the model can be seen for the 2:1 ratio, similar to the 5:2 resonance. The higher examined resonances have too few systems to state their properties. Interestingly, the 3:2 ratio has most of the inner periods longer than 1 day, more than we could expect from the studied sample. Further searching and analysis of a larger sample of 2+2 candidates (in the order of thousands of systems) will show us more period and resonance features. For future work, we plan to observe the sets of candidates to confirm their quadruple nature and exclude the blends.

Acknowledgements

The authors thank T. Plšek for helpful discussions, S. N. de Villiers for the text suggestions and comments, and the anonymous referee for the review and analysis of this paper. JK was partly supported by the project MUNI/A/1419/2023.

Data Availability

The data underlying this article are available in the article.

Chapter 5

Additional statistics and systems

5.1 Resonance vicinity

The sample statistics used in Chapter 4 are expanded here with additional elements. Previously, two resonance ranges were considered, $C < 1$ % and $C < 2$ %, to obtain two samples for comparison. Above the 2 % limit, the period ratios are too far from the precise ratio value to be assessed as the resonance. The 3:2 resonance overabundance against the prediction was noticed. The possible preferences for some resonant states lead to the systems' inner periods going closer to the exact resonant ratio (unless the ratio is changed by inner binary evolution, another body influence, and other possible effects). Thus, the systems in the larger resonant vicinity should be underabundant because they tend to go and lock in the resonance. This vicinity decline should be observed if the dataset is large enough to reveal the resonant overabundance. In other words, higher C values could contain fewer systems than expected using the homogeneous period distribution. This assumption may not be observed significantly. Many selection effects and phenomena generally influence the statistics. However, it is still possible to detect the strongest period ratio properties.

In this section, the statistics of the period ratio in the resonance vicinity are presented. The same resonances were examined as in Chapter 4. The closeness C range between 2 % and 3 % was analysed. Table 5.1 shows the ratio R limits for each resonant value in these intervals. A comparison between the observed data and the simulated models was carried out. The detailed results of this comparison are summarised in Figure 5.1 (bottom panel) and Table 5.2. Despite the small-number statistics, some remarkable properties have been discovered.

i. The data of the 1:1 vicinity show a slight increase.

ii. A decrease is observed for the 4:3, 3:2, 5:3, and 2:1 ratios, with the 3:2 resonance showing the largest difference compared to the model.

iii. Interestingly, the 5:2 ratio vicinity is overabundant, which is in high contrast against the resonance diagram with $C < 1$ % (Figure 5.1, bottom panel), only three systems are known.

iv. The remaining studied ratios, 7:2 and 4:1, are in good agreement with the simulated prediction.

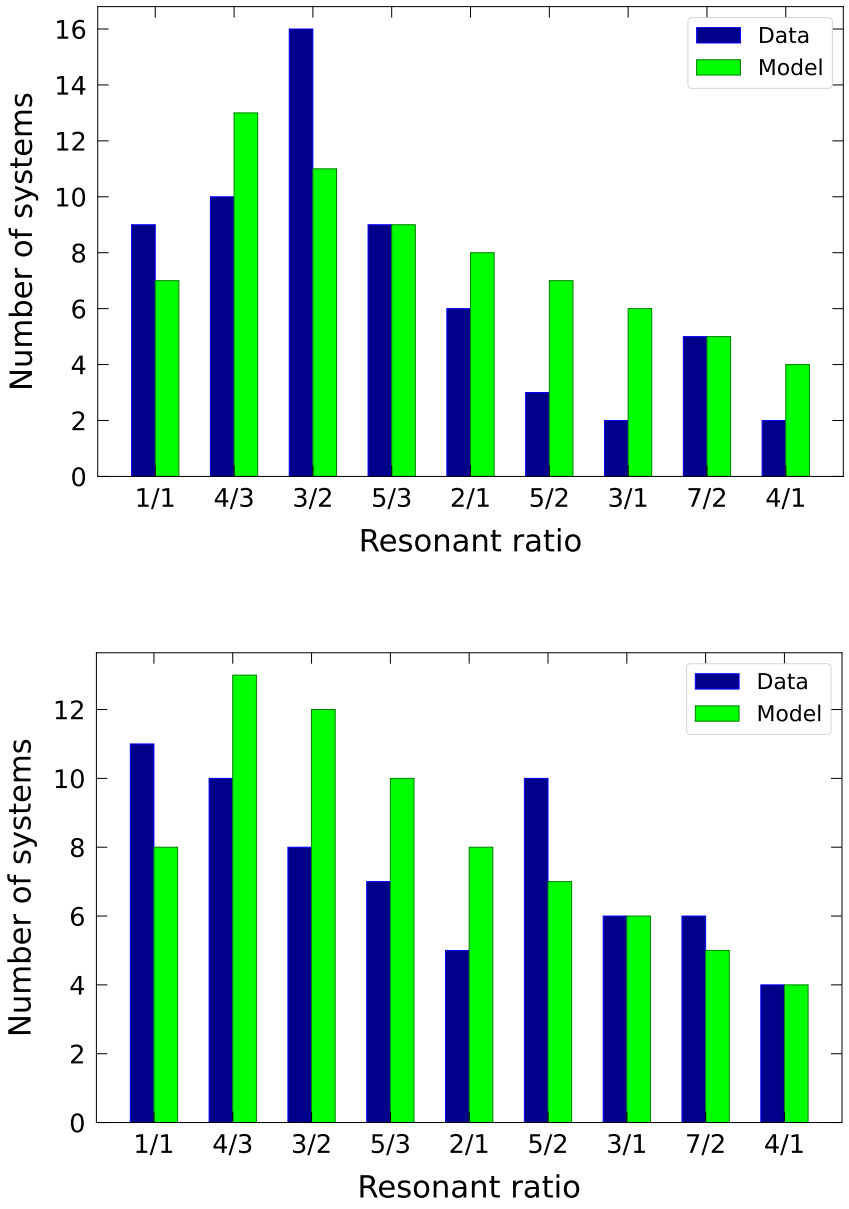

Figure 5.1: Resonance comparison diagrams, upper panel: the resonances with $C < 1\,\%$ (this graph reproduces Figure 4.6 for ease of comparison), bottom panel: diagram for the resonance vicinity with the C range of 2 - 3 %.

Table 5.1: The used vicinity ranges for $C = 2$ - 3 %.

Resonance	Lower interval		Higher interval	
	$R_{\min}$	$R_{\max}$	$R_{\min}$	$R_{\max}$
1:1	-	-	1.020	1.030
4:3	1.293	1.307	1.360	1.373
3:2	1.455	1.470	1.530	1.545
5:3	1.617	1.633	1.700	1.717
2:1	1.940	1.960	2.040	2.060
5:2	2.425	2.450	2.550	2.575
3:1	2.910	2.940	3.060	3.090
7:2	3.395	3.430	3.570	3.605
4:1	3.880	3.920	4.080	4.120

Table 5.2: The number of systems in the resonance within $C < 1$ % and resonant vicinity ($C = 2$ - 3 %), observations and predicted model.

Resonance	$C < 1$ %		$C = 2$ - 3 %	
	Data	Model	Data	Model
1:1	9	7	11	8
4:3	10	13	10	13
3:2	16	11	8	12
5:3	9	9	7	10
2:1	6	8	5	8
5:2	3	7	10	7
3:1	2	6	6	6
7:2	5	5	6	5
4:1	2	4	4	4

The data-model comparison was made for the resonance closeness C up to 1 % and the resonant vicinity between 2 % and 3 %. Both of these ranges are equally wide and thus suitable for comparison. The diagram in Figure 5.2 shows the residuals (differences between data and model numbers) for both diagrams from Figure 5.1 and reveals the behavior of the resonant states and their vicinity. As mentioned in Chapter 4, the 3:2 resonance exhibits the largest overabundance in the sample. Additionally, the resonance vicinity shows a decrease in the number of systems. This decline is the most significant compared to other resonances. The systems appear to be accumulated in the resonant ratio and at the same time are missing in its wider vicinity. These statistics provide the evidence that the 3:2 resonance fulfills the assumption of vicinity underabundance for the preferred stable resonant state.

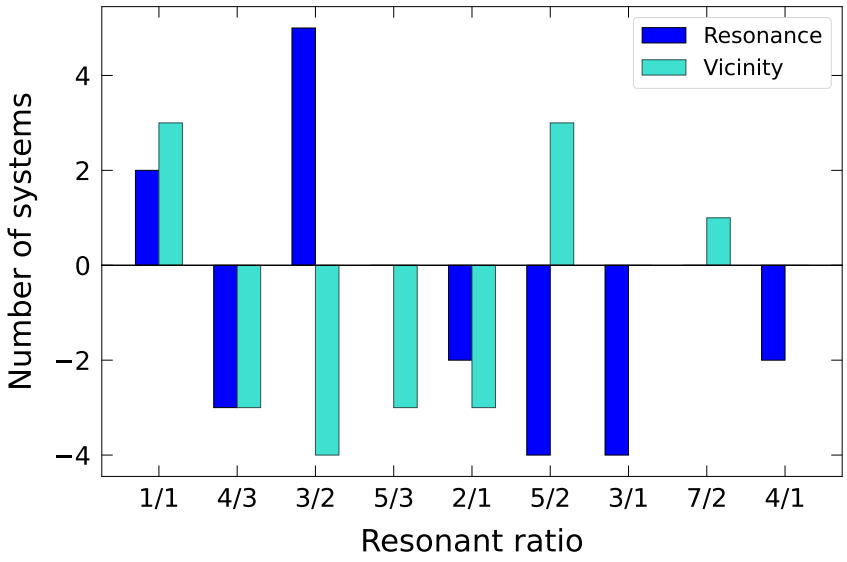

Figure 5.2: Residuals (data numbers against the simulated model values) for the resonant diagrams shown in Figure 5.1. The most significant differences are shown for the 3:2 resonance, where the resonance peak is at maximum and the vicinity peak at minimum compared with other examined ratios.

Figures 5.1 and 5.2 reveal the observational confirmation of the 3:2 resonance as a possible long-term stable configuration. However, this stability may be affected by secular changes (studied, for instance, in Vokrouhlický (2016) for V994 Her). The presence of other components could significantly influence the system's mutual configuration. The resonant state can also be perturbed by the inner binary evolution due to the mass transfer. These considerations should be taken into account.

For these reasons, the objects in the resonant vicinity were inspected, focusing on the 3:2 resonance. Table 5.3 summarises the systems within the closeness range of 2 - 3 % for this period ratio. Eight systems in total fulfill this C condition. Interestingly, all of them are located in our Galaxy. The inner periods are usually longer than 1 day, as for systems in the 3:2 resonance. Only one candidate among these eight, OGLE BLG-ECL-277539, has both inner periods shorten than 1 day. The EB and EW candidates would be great targets for future work for the complex dynamical study. The mass transfer and other effects could possibly disrupt the resonant state.

Two systems within this dataset are confirmed multiples, OGLE BLG-ECL-088871 and V994 Her. The V994 Her star is a system showing a complicated structure with three eclipsing binaries (Zasche et al., 2023a) with apsidal motion. The outer orbital period between A and B pairs is relatively short, only 1 062 days. Zasche et al. (2023a) calculated the time required for the evolution from the 3:2 resonance to the current state using the Tremaine (2020) results. This time is significantly longer than the estimated age of V994 Her, making it improbable that the pairs A and B were in the precise 3:2 resonant ratio.

A complex orbital study, including LiTE, short time-scale dynamical effects, and the secular period changes should be conducted for all the systems in the 3:2 resonance and its vicinity. The question about the precise resonant properties would be then more

feasible. However, most of these systems are not yet confirmed as the 2+2 quadruples. Firstly, long-term observations and further data collecting are necessary to detect the mutual orbits and other interactions, enabling more comprehensive research.

Table 5.3: Eight systems with the inner period ratio in the 3:2 resonant vicinity with $C = 2$ - 3 %, name, coordinates in J2000, confirmation of the quadruple nature, inner orbital periods, light curve (LC) types for each binary, and period ratio R.

Name	RA [°]	DEC [°]	Conf.	P_A [days]	LC type A	P_B [days]	LC type B	R
TIC 201310151	4.111881	-58.141759	0	5.538208	EA	8.485997	EA	1.53226
ASASSN-V J124203.23-644513.2	190.513460	-64.753650	0	2.0725413	EA	1.4122993	EA/EB	1.46749
OGLE BLG-ECL-088871	266.248670	-23.712610	1	3.8779159	EA	5.6508216	EA	1.45718
OGLE BLG-ECL-277539	270.900470	-28.128210	0	0.3753292	EW	0.5779823	EB/EA	1.53993
V994 Her	276.941220	24.697410	1	2.0832658	EA	1.4200395	EA	1.46705
ZTF J194331.02+255254.0	295.879290	25.881670	0	1.3572871	EA	2.0934434	EA	1.54237
Gaia DR3 1862347439319475072	309.435623	30.852742	0	0.920364	EA	1.417808	EA	1.54049
Gaia DR3 2010769070836151424	351.050509	59.819433	0	1.312382	EA	0.89549	EA	1.46555

Table 5.4: The list of the system with the 3:2 resonant ratio within the C parameter up to 2 %, the table structure is the same as for the Table 4.1, resonance, reference, and note columns are excluded for clarity.

Name	RA [°]	DEC [°]	Loc.	Conf.	P_A [days]	P_B [days]	R	C [%]	RUWE	T_{eff} [K]
OGLE SMC-ECL-1076	11.648210	-73.240780	SMC	0	6.40349	4.30215	1.48844	0.77	1.158	9993.2
OGLE SMC-ECL-1086	11.666710	-73.521600	SMC	0	3.3209	2.18068	1.52287	1.52	1.120	7999.7
OGLE SMC-ECL-5015	16.335960	-72.062250	SMC	0	1.15616	0.76283	1.51562	1.04	1.044	24039.2
Gaia DR3 330442487264141952	29.369827	36.938288	Gal	0	3.201325	2.165996	1.47799	1.47	1.008	5132.5
OGLE LMC-ECL-03611	74.251610	-69.511930	LMC	0	2.119573	1.39688	1.51736	1.16	0.872	16213.3
OGLE LMC-ECL-10429	78.429360	-69.310260	LMC	0	5.3666155	3.5779357	1.49992	0.01	0.887	23997.0
OGLE LMC-ECL-21569	84.743300	-69.076450	LMC	1	2.9328514	1.9815435	1.48008	1.33	0.889	
OGLE LMC-ECL-22148	85.123960	-70.083310	LMC	0	2.7147783	1.8267531	1.48612	0.93	1.005	9967.0
OGLE LMC-ECL-23000	85.654350	-69.070080	LMC	1	1.8998605	1.2455112	1.52537	1.69	3.296	24457.8
CzeV343	87.100050	30.950990	Gal	0	1.209364	0.806869	1.49884	0.08	1.617	10793.3
TIC 78333248	88.730875	26.354792	Gal	0	11.3808	7.552	1.50699	0.47	0.986	
CzeV1640	91.826630	28.123640	Gal	0	0.842581	0.554234	1.52026	1.35		
Gaia DR3 3112366227355971584	103.057739	-1.125556	Gal	0	0.948312	0.632336	1.4997	0.02	1.817	8401.1
CRTS J065302.9+381408	103.262700	38.235700	Gal	1	1.8664	1.24652	1.49729	0.18	1.052	6586.8
TIC 237816747	104.490886	2.292214	Gal	0	6.7663	4.4813	1.5099	0.66	1.039	
ASASSN-V J071131.63-153341.3	107.881790	-15.561460	Gal	0	2.611144	1.7289645	1.51024	0.68	1.622	9488.4
TIC 144475902	121.339546	-34.049985	Gal	0	3.4287	2.2991	1.49132	0.58	1.020	
TIC 414969157	141.176162	22.200757	Gal	0	6.928951	4.630508	1.49637	0.24	2.022	4935.4
TIC 459400252	162.552438	-56.449916	Gal	0	8.4146	5.5037	1.5289	1.93	1.195	6669.4
OGLE BLG-ECL-145467	268.023280	-29.328730	Gal	1	4.9097045	3.3049105	1.48558	0.96	0.970	8008.8
Gaia DR3 1834469768675202560	298.530047	24.682368	Gal	0	4.353022	2.881026	1.51093	0.73	1.460	8483.8
V0346 Sge	300.871983	21.086656	Gal	0	0.4662684	0.3092951	1.50752	0.50	6.154	
TIC 278352276	307.503640	48.607056	Gal	1	18.810761	12.403102	1.51662	1.11	0.845	
TIC 273919067	316.241965	43.796242	Gal	0	3.1915	2.1394	1.49177	0.55	3.601	
TIC 414026507	336.837717	56.740362	Gal	0	6.455288	4.229981	1.52608	1.74	2.093	17953.0
CzeV1645	350.883830	60.886940	Gal	0	1.6594636	1.0944876	1.5162	1.08		
TIC 417752064	356.147418	74.173107	Gal	0	15.0798	10.0118	1.5062	0.41	8.158	6938.0

5.2 RUWE

Angularly unresolved binaries or multiples can affect the Gaia astrometric measurements. Gaia Renormalised Unit Weight Error (RUWE) is a reliable indicator for quality assessment of the single-star astrometric solution (Gaia Collaboration, 2023; Castro-Ginard et al., 2024). This parameter can reveal the presence of unresolved stellar components when the single star solution does not unambiguously correspond. The RUWE number is computed from the astrometric chi-square value χ^2, number of observations n (suitable in the quality), and function $\mu_0(G, BP-RP)$ for renormalisation depending on G brightness and Gaia colour index:

$$\mathrm{RUWE} = \frac{\sqrt{\frac{\chi^2}{(n-5)}}}{\mu_0(G, BP-RP)}, \qquad n > 5. \tag{5.1}$$

Factor 5 refers to the five parameters from the astrometric model (right ascension, declination, proper motion in both coordinates, and parallax). A RUWE limit of 1.4, as recommended by Lindegren et al. (2018)) and used in (Castro-Ginard et al., 2024; Guo et al., 2025), is considered the threshold for a reliable single star model. Values above this limit may indicate a possible multiplicity.

721 objects (92 %) from the examined dataset of 781 systems contain the Gaia DR3 RUWE information. Hence, almost all of the 2+2 candidates are included in further analysis. Figure 5.3 shows the RUWE cumulative distribution within the sample. The right panel of Figure 5.3 focuses in more detail on the region around the 1.4 threshold. The RUWE range is surprisingly large, from a minimum of 0.843 to an extreme maximum of 59.61. A total of 427 systems (59 %) have the RUWE under the 1.4 threshold. There are no preferences in the RUWE numbers for the systems with the 3:2 resonance (up to $C < 2$ %), with with 15 out of 25 systems with available RUWE falling below the threshold.

RUWE can only be considered as an indicative parameter of possible multiplicity, but not as direct evidence for a quadruple star confirmation. It shows that some systems have significantly high values of this parameter, exceeding 10 and reaching almost 60 at the maximum. There are 67 systems with the RUWE of 10 or greater. However, only 4 of them are confirmed 2+2 quadruples. Moreover, the highest RUWE number within the confirmed systems is 26.331, which is still not the highest measured value. The candidates with the largest RUWE (from 30 to 60) are not confirmed. These systems represent a promising sample of candidates for future astrometric and other studies. Blends and other possible contaminations can affect these objects, especially in very dense stellar fields. Therefore, careful analysis is required to rule out such effects.

Of the amount of 60 confirmed 2+2 quadruple systems, 56 of them have derived RUWE parameter. As stated previously, RUWE = 26.331 is the maximum value for this class. However, there are 35 confirmed systems with the RUWE number below the 1.4 limit. Moreover, 16 of these do not exceed 1. The number of confirmed systems is currently low compared with the total number of candidates. Nevertheless, more than a half of them fall under the RUWE limit for a sufficient single-star solution. This ratio agrees with the entire sample without observed deviations.

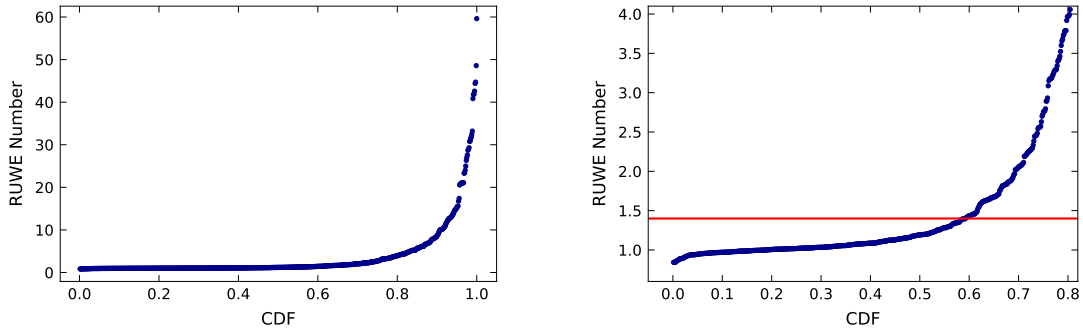

Figure 5.3: Cumulative distribution function (CDF) of RUWE parameter, the CDF is plotted on the x-axis and RUWE on the y-axis to better see how the RUWE increases, left panel: all the systems, right panel: more detailed view on the RUWE single star limit and its surroundings, RUWE = 1.4 is marked by the solid red line.

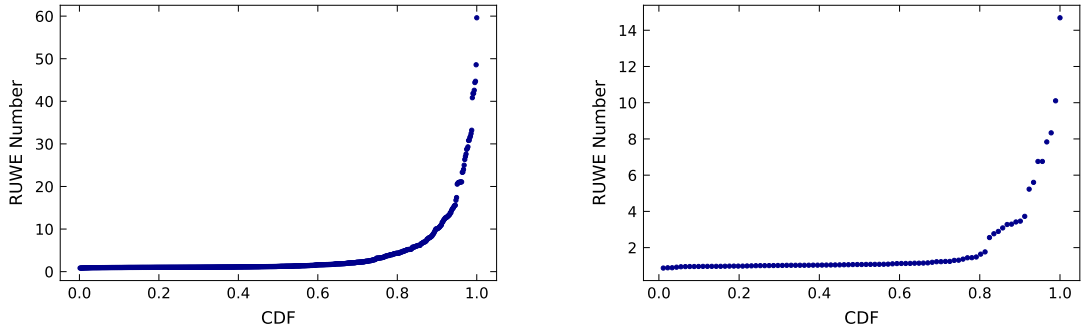

Figure 5.4: Cumulative distribution function (CDF) of RUWE according to the galaxies, left panel: our Galaxy, right panel: the Magellanic Clouds, most values are in the Galaxy (almost 95 % while there are only a few in the LMC and SMC).

Figure 5.4 depicts the same as the previous graphs, but for our Galaxy and the Magellanic Clouds separately. The cumulative distribution for the Galaxy is practically identical to the left panel of Figure 5.3 because most of the systems with the RUWE number (almost 95 %) come from the Galaxy. Interestingly, the LMC and SMC solutions do not contain large values compared to our Galaxy. The largest RUWE value for the Magellanic Clouds is 14.688, and 76 % of the systems fall below the 1.4 threshold.

RUWE is not well suited for very dense stellar fields where the systematic deviations in astrometric measurements occur. The central regions of the LMC and SMC can exhibit a systematically increased RUWE parameter due to the high field density. Therefore, the RUWE deviations depend on sky position of the examined object. (Castro-Ginard et al., 2024). One of the main parameters of the astrometric model is also parallax. However, the parallax measurements are generally less precise for the larger distances and the proper motion. Therefore, the LMC and SMC solutions can be distorted toward smaller values (except for the central regions). More precise astrometry over a much longer timescale is required for objects outside our Galaxy to obtain a more reliable RUWE parameter. This analysis concludes that the RUWE

parameter can serve well for the galactic candidates as the first hint of the multiple nature. However, it is currently not a suitable indicator for the Magellanic Clouds. It is important to note that this parameter does not mean that the given object consists of multiple components, as a large number of confirmed 2+2 quadruples have significantly low RUWE parameter.

5.3 Temperatures

Only 534 (68 %) systems have an effective temperature T from Gaia DR3 (Gaia Collaboration, 2023) available. Unlike RUWE, which is available for most systems, the temperature statistics may be biased due to the lack of all data. Systems without RUWE also do not have temperature information. The listed values are the composite temperatures of all the components together. This can result in significantly misleading conclusions about the system and the individual components. The stars can be divided into radiative and convective using the known effective temperature using with a limit of 7 000 K. However, only the composite parameters are commonly available for multiple systems. For instance, a quadruple star can have one dominant hot component above 7 000 K, while the other three components can have significantly lower temperatures. The composite temperature can show a higher value than most stars have. It is necessary to know more details about the systems, mainly the multi-band photometric observations, from which the eclipses are observed, and spectroscopic measurements, to better determine the individual parameters. A key factor is also the precise time of the observations. The colour index changes with time because of the eclipses. Hence, the derived temperature value is influenced by this time-dependent variation. With the currently available knowledge, one should not rely on only one parameter, but enlarge the possible data amount. If the temperatures are not sufficiently derived from the spectra, the SED fitting should be taken into account together with the light curves and other measurements (Chapter 3). The Gaia and SED temperatures do not generally coincide, and considering all parameters together is essential for precise modelling.

Firstly, the distribution of the composite temperatures was investigated. The temperature histogram is shown in Figure 5.5 with a binning step of 500 K. Two peak bins are located within the T range of 5 500 K and 6 500 K. There are 273 systems with temperatures lower than the 7 000 K and 261 systems above this limit. Therefore, the number of hot and cool systems according to the Gaia DR3 temperatures is almost identical. However, it is not trivial to state how many hot or cool stars each system actually contains using only this value.

The spectral type distribution was done with respect to the system location (our Galaxy and the Magellanic Clouds). Of the 534 objects with Gaia temperatures, 457 are in the Galaxy and 77 are in the LMC and SMC. The spectral type was stated by the Gaia composite temperature. Table 5.5 summarises the system numbers using this classification. Figure 5.6 provides a graphical representation of this distribution. The B and F spectral classes are the most represented. On the contrary, O and M stars are missing in Gaia data. Despite their smaller numbers, the Magellanic Clouds introduce a large bias into the statistics, even though significantly fewer of them exist. Almost all LMC and SMC candidates (63 out of 77) are B-type systems according to the composite temperature. This large increase in B-type stars is relatively expected,

as the brighter and hotter stars are primarily observed from these galaxies and can be studied in greater detail. It is, therefore, necessary to divide the spectral types with respect to the precise location. Our Galaxy contains only 70 (15 %) B-type systems.

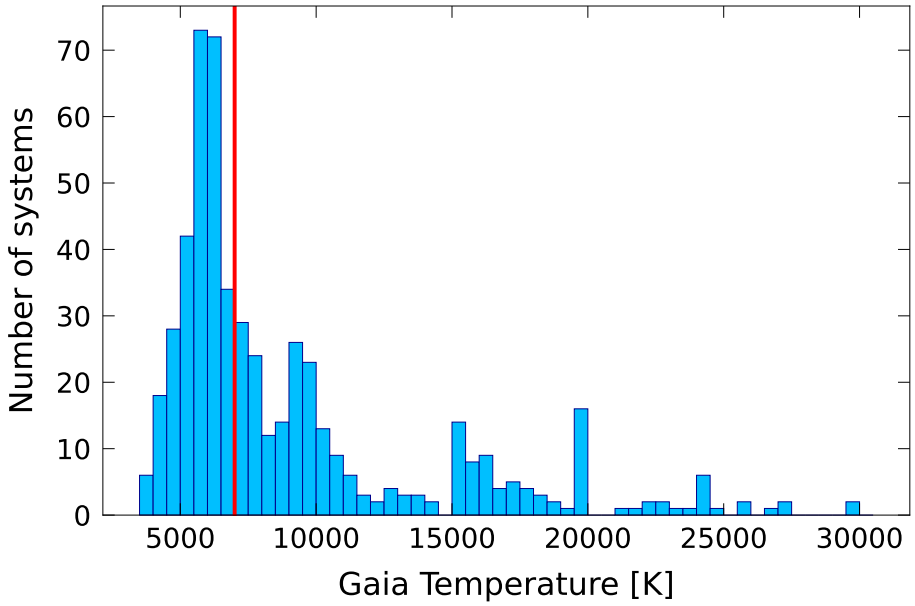

Figure 5.5: The Gaia composite temperature distribution (the bin width is 500 K), the red vertical line shows the $T = 7\,000$ K limit between radiative and convective stars.

The most significant 3:2 resonance was also inspected according to the composite temperature. Within 27 systems in this resonant state up to $C < 2$ % (Table 5.4), 18 have Gaia temperature information (11 systems in our Galaxy and 7 in the Magellanic Clouds). There should be approximately equal numbers of radiative and convective systems with respect to the whole sample statistics. On the contrary, the numbers differ from the expected values. There are 13 systems (72 %) that belong to hot types and 5 (28 %) to cool types. A binomial test between these numbers and expectations gives the p-value of 0.048. This is statistically significant compared to the assumption of equal representation, but still not conclusive.

Table 5.5: The system numbers dependency on the spectral type, in total number, our Galaxy, and the Magellanic Clouds, according to Gaia DR3 composite temperatures.

Spectral type	Total	Gal	LMC + SMC
O	0	0	0
B	133	70	63
A	99	91	8
F	135	131	4
G	115	113	2
K	52	52	0
M	0	0	0

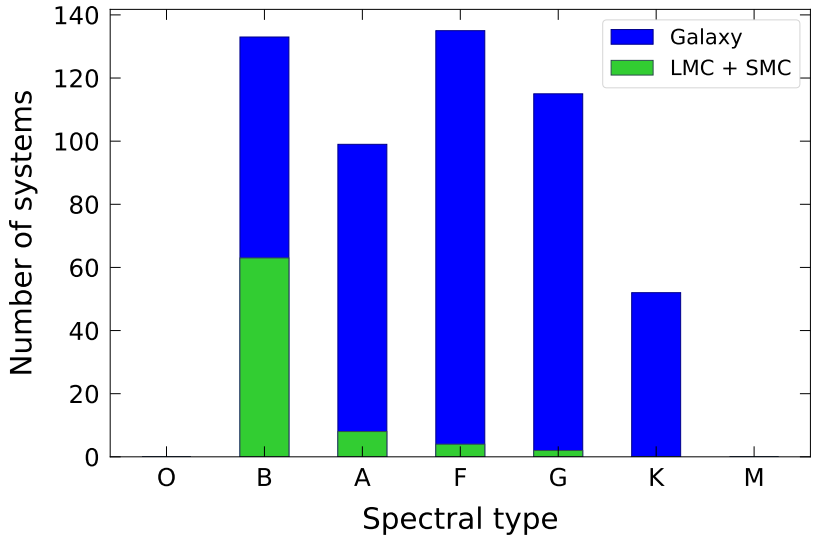

Figure 5.6: The spectral type distribution of studied systems, the type was determined from the Gaia composite temperature, the Galaxy and Magellanic Clouds systems are distinguished, an enormous LMC and SMC bias for B stars is seen due to the LMC and SMC observational selection effects of preference for hot stars.

Zasche et al. (2023b) showed an increase in the 3:2 resonance together with its wide vicinity for hot stars. This work enlarges the total numbers and provides a sharper limit within the closeness $C < 2$ % around the 3:2 resonance. Under these conditions, the statistics yield valuable insights, even with small numbers. This new result cannot be interpreted as strong proof that the 3:2 quadruples are preferably hot stars because of a small sample. However, it suggests that the particular property is already statistically significant and could be proven in the future with a larger dataset. Generally, the 3:2 resonance is observed more frequently with periods longer than 1 day. A possible preference of this resonant state is observed for hotter systems. This dependency is not surprising, as hotter binaries generally have longer periods than cooler systems due to their larger radii.

5.4 Additional systems

This section presents additional 2+2 candidates and the preliminary results of their analysis. The TESS light curves were disentangled using the methods described in Chapter 2. The minima timings in the disentangled and detrended light curves were primarily derived using the SILICUPS fitting. The $O - C$ diagrams were constructed in the OCFit software.

5.4.1 ZTF J212128.80+514855.6 (S4 Cyg)

The doubly eclipsing quadruple candidate ZTF J212128.80+514855.6 was discovered by Zasche et al. (2022b). The $O - C$ diagrams (Figure 5.7) are relatively noisy with higher uncertainties of the minima timings. The precision was probably affected by

long eclipses of the pair A and low amplitudes of the pair B. The period analysis enhanced the ephemeris to $P_{\mathrm{A}} = 2.195303(2)$ days, $M_{0\mathrm{A}} = 2\,458\,719.400(1)$ (HJD), $P_{\mathrm{B}} = 1.628122(1)$ days, $M_{0\mathrm{B}} = 2\,458\,746.2363(6)$ (HJD). New inner period ratio $R = 1.3483$ gives the closeness value of 1.13 %. Figure 5.8 depicts the TESS disentangled light curves. Pair A seems to be a potential contact binary with a slight O'Connell effect. The Pair B amplitudes are low compared to the Pair A eclipses.

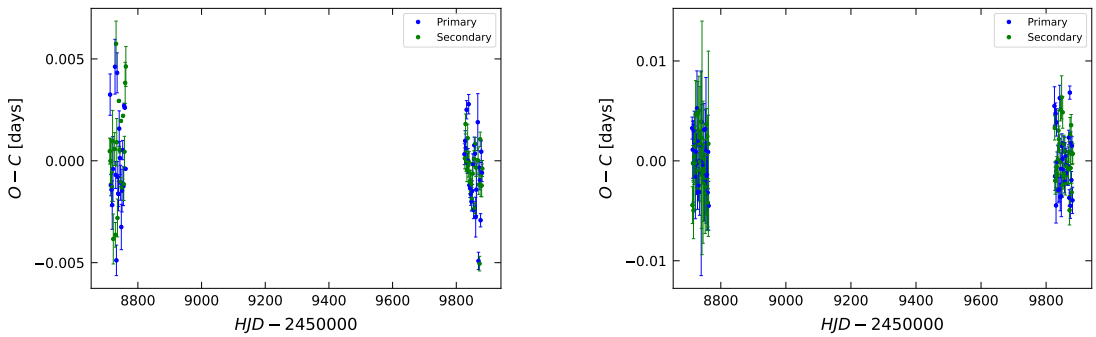

Figure 5.7: The $O - C$ diagrams of S4 Cyg, left panel: pair A, right panel: pair B.

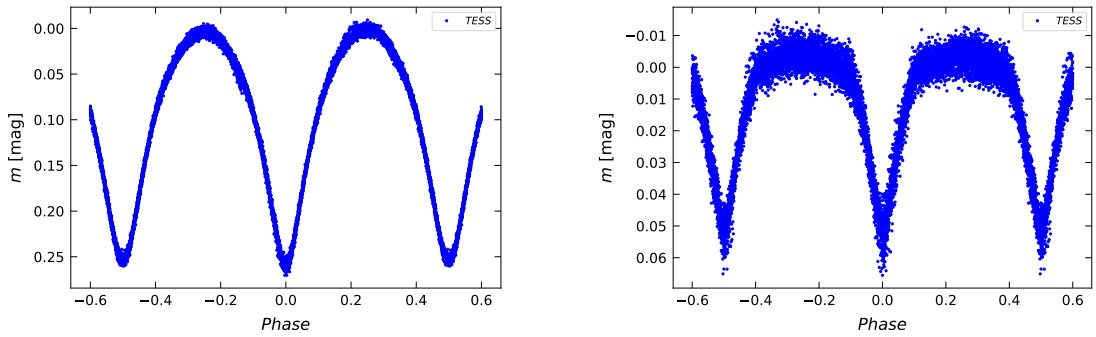

Figure 5.8: The disentangled light curves of S4 Cyg, left panel:pair A, right panel: pair B.

5.4.2 V1018 Cas (S5 Cas)

The S5 Cas system is a relatively bright object (10.2 mag in V band according to Zacharias et al. (2013)). The system was first described by Kostov et al. (2022). With the TESS minima timings, the $O - C$ diagrams (Figure 5.9) were constructed. The pair A $O - C$ variations show an apsidal motion with a significantly long period and large amplitudes (the measured $O - C$ difference between the primary and secondary minima is more than 8 hours). A possible sign of the apsidal motion is visible in the pair B $O - C$ diagram. The ephemeris was improved for each binary. The new values are 4.127745(6) days and 2 458 821.085(3) (HJD) for pair A and 3.107388(4) days and 2 458 820.148(2) (HJD) for pair B. The inner period ratio of 1.3284 is significantly

close to $C = 0.37$ % to the 4:3 resonance, making this system important for further analysis. Its brightness also offers the possibility to add spectroscopic observations.

The light curves of S5 Cas system (Figure 5.10) significantly differ. Pair A dominates the system with similarly deep eclipses. High eccentricity is observed from the eclipse phases. The eccentricity effects are primarily visible in the phase range of 0.2 and 0.3. This deformation could not be fitted correctly in the SILICUPS software, and the harmonic polynomials were used. The pair B eclipses are enormously shallower compared to pair A. An additional wave-like variation is observed in the pair B light curve. The period of this variation agrees with the binary orbital period, which suggests a possible surface activity.

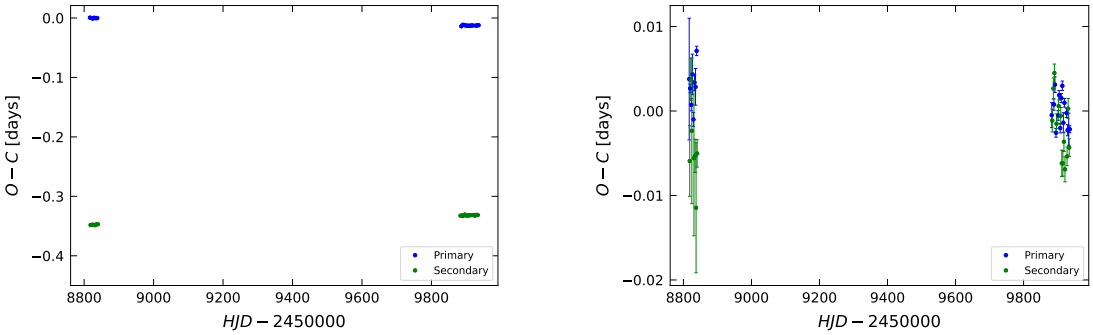

Figure 5.9: The $O - C$ diagrams of S5 Cas, left panel: pair A, right panel: pair B.

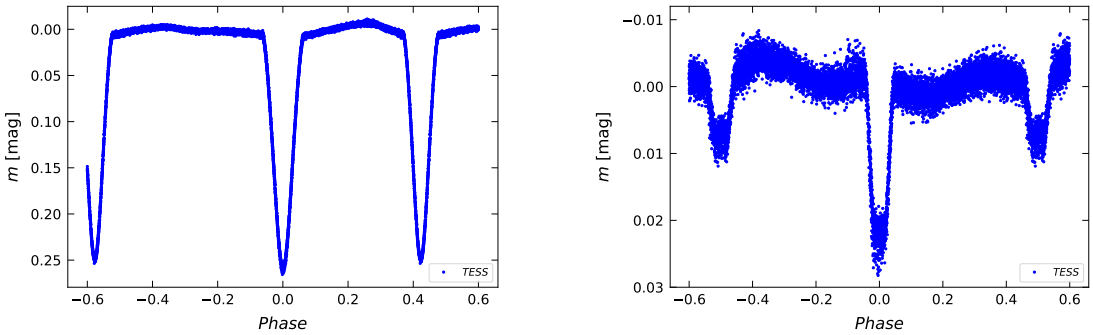

Figure 5.10: The disentangled light curves of S5 Cas, left panel:pair A, right panel: pair B.

5.4.3 GSC 03275-00703 (S7 Cas)

Kostov et al. (2022) firstly introduced the system GSC 03275-00703 as a 2+2 candidate. The $O-C$ analysis using multiple TESS sectors revealed new corrected period values: $P_{\mathrm{A}} = 2.4925056(2)$ days, $M_{0\mathrm{A}} = 2\,458\,766.5396(3)$ (HJD), $P_{\mathrm{B}} = 4.742380(1)$ days, $M_{0\mathrm{B}} = 2\,458\,766.200(3)$ (HJD). The $O-C$ diagrams (Figure 5.11) are constant within the TESS observing timescale. The minima timing derivation was more accurate for

higher cadence measurements (the right regions of both diagrams show significantly lower uncertainties).

The TESS light curves of inner binaries (Figure 5.12) are similar. Both pairs are detached systems without notable interactions. The period of pair B is relatively long, about 4.75 days. It is close to a three-quarter day value, which could introduce a systematic bias in ground-based observations. In addition, the pair A period is almost precisely 2.5 days (close to a half-day value). For these reasons, the system is difficult to observe in practice for ground-based telescopes and requires carefully scheduled observations.

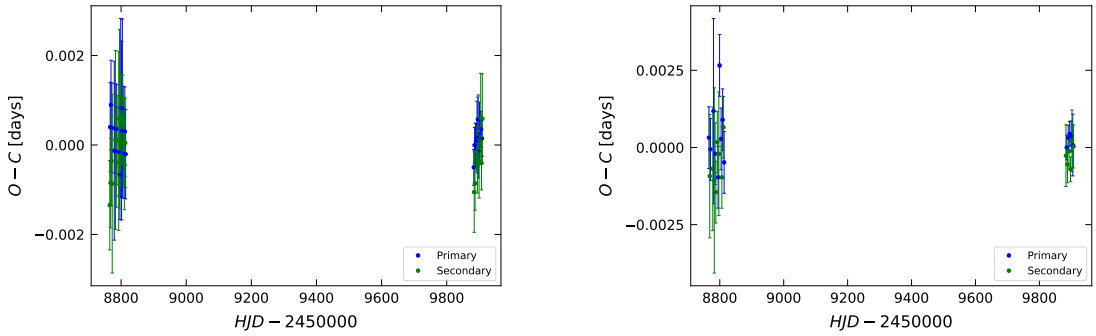

Figure 5.11: The $O - C$ diagrams of S7 Cas, left panel: pair A, right panel: pair B.

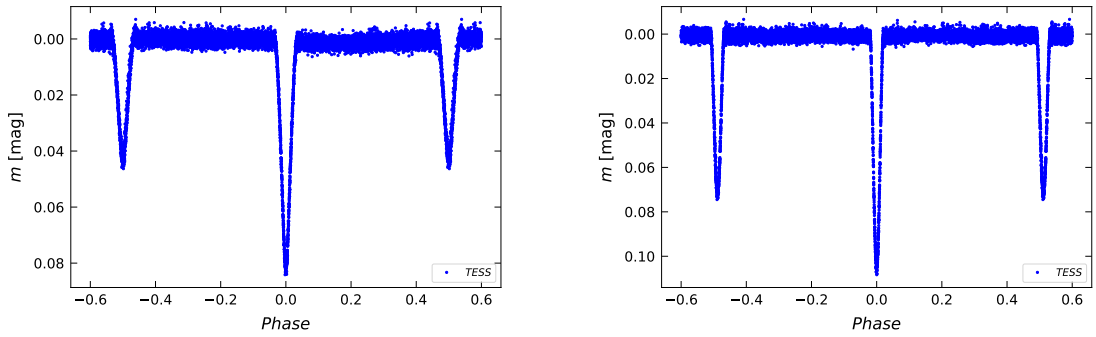

Figure 5.12: The disentangled light curves of S7 Cas, left panel:pair A, right panel: pair B.

5.4.4 ATO J223.4251+52.7158 (S2 Boo)

ATO J223.4251+52.7158 was introduced by Kostov et al. (2022) and later in Vaessen and van Roestel (2024). The $O - C$ diagrams were constructed with the following ephemeris: $P_{\mathrm{A}} = 1.350249(2)$ days, $M_{0\mathrm{A}} = 2\,458\,744.720(2)$ (HJD), $P_{\mathrm{B}} = 1.488497(3)$ days, $M_{0\mathrm{B}} = 2\,458\,739.159(2)$ (HJD). Preliminary TESS results indicate possible nonlinear variations (Figure 5.13) for both binaries. However, the current observing time is short for clear conclusions. The light curves are shown in Figure 5.14. Slight ellip-

soidal variations are apparent, primarily for pair A. The pair B light curve contains an asymmetry in the parts out of the eclipses.

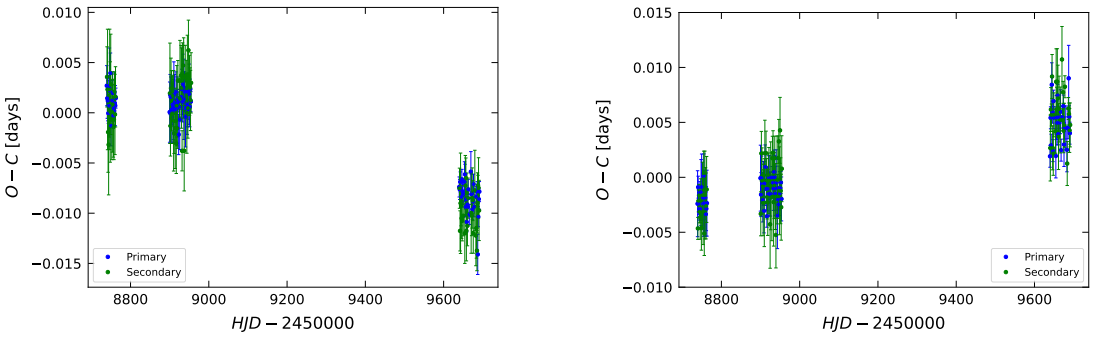

Figure 5.13: The $O - C$ diagrams of S2 Boo, left panel: pair A, right panel: pair B.

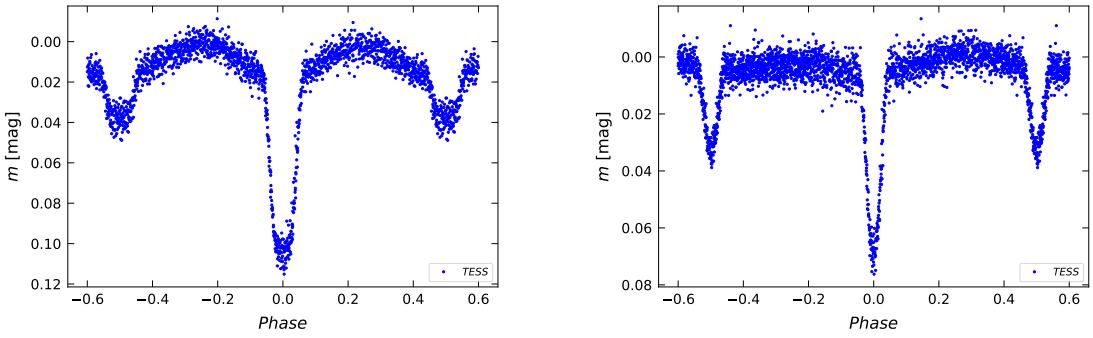

Figure 5.14: The disentangled light curves of S2 Boo, left panel:pair A, right panel: pair B.

Discussion

In recent years, several hundred new multiple system candidates have been discovered. Most of the candidates were already known as eclipsing binaries. With the better observing technique, smaller light changes are identified and analysed. The continuous datasets, such as TESS measurements, are helpful in detecting relatively long periods of more than several days. On the other hand, many selection effects could lead to significantly biased results. The blends of independent objects are the general issue, most evident in dense stellar fields. A very careful analysis of the angular vicinity is required for the correct blend identification (e.g., Ádám et al. (2023) and Zasche (2024)). The TESS light curves can be strongly contaminated by the nearby stars due to the low angular resolution (21 arcsec per pixel) of the TESS equipment. The possibility of blending could be relatively high in these cases. Using other data sources with more precise angular resolution is essential to conclude the system as a multiply eclipsing candidate. However, the an unresolved blend option is still possible.

The histogram plots of the inner period ratio R were used in Chapters 3 and 5. Bins can generally distort the results. For the specific bin widths, false dependency could be created. The period ratio distribution in Figure 4.4 was made with a bin of 0.1 for optimal visualisation. However, narrower ranges are needed when studying the individual resonances. The closeness parameter C was defined to take into account the specific width around the precise resonant value. The resonant properties could be misinterpreted in the R histogram containing all possible ratios. For instance, using the 0.1 bin width, split the 3:2 resonance into two columns, between 1.4 - 1.5 and 1.5 - 1.6. Therefore, taking the resonant ratio in the centre of the range and going symmetrically from this value is essential. The period ratio distribution was compared to the simulated prediction. In this case, the distribution was studied as a large statistical sample that included all the analysed values, not only the numbers in one individual bin. The maximum studied R ratio value was stated to be 5 because high period ratios contain too few systems to provide a sufficient sample.

The resonant state could be disturbed by the inner binary evolution or the dynamical and secular effects within the system. More stable solutions are preferred for binaries with longer periods and circular orbits. The systems in the 3:2 resonance have the inner periods longer than 1 day more frequently than the complete data sample. This resonant state shows the preference compared to other investigated ratios. This result was obtained for both stated C ranges. On the other hand, the resonance vicinity shows the opposite. The decrease in data for the wide C region is modest, but it is the largest among the resonances. Almost 800 quadruple candidates were collected for the statistics. However, the numbers for each resonance are relatively small. The results are sufficient to see the 3:2 preference. There are also indications for some other resonant values, a slight 2:1 decline or an increase for the 5:2 vicinity. It is important to

enlarge the number of 2+2 candidates to at least double the current value to provide more robust statistics and period ratio properties.

Most of the collected systems have the RUWE information available. Hence, the statistics were carried out on a relatively large sample of 721 objects. Around 59 % of the systems are within the range for a good astrometric solution for a single star. The RUWE values are reduced for the Magellanic Clouds. The main reasons can be the large distance of these galaxies, along with the small brightness of the objects.

High values of the RUWE parameter with the extreme cases of RUWE > 10 are observed. Despite this parameter, most of these systems are not confirmed quadruples. In contrast, more than half of the confirmed systems have their RUWE number under the 1.4 value. This distribution significantly agrees with the entire sample statistics. Moreover, several cases with significantly low RUWE values are known for the confirmed systems. Most of these are located in our Galaxy, where the distances are well-measurable by Gaia compared to the Magellanic Clouds. The confirmed systems have usually short orbital outer periods in order of years or decades. The astrometric solution could discover at least slight deviations caused by the outer orbit. However, no increase was observed for the known 2+2 quadruples. Some observational biases could affect the results, mainly the small brightness of the object and the density of the stellar field.

Generally, this parameter must be considered with caution. It is not a suitable multiplicity indicator for the Magellanic Clouds. Furthermore, multiple systems in our Galaxy contain this parameter within the single star solution. The primary RUWE function for examined candidates is only a suggestion, which proposes additional investigation.

The effective composite temperatures from the Gaia DR3 catalogue were examined. Only 68 % of the studied objects have this information available. The statistics reveal the observational bias due to hot stars in the Magellanic Clouds. These objects are more preferred for detection than systems with low temperatures. The spectral type distribution was made from the Gaia composite temperatures. Interestingly, there are no known doubly eclipsing candidates of O and M type. Generally, the composite temperature estimation is influenced by the effective temperatures of individual components. Since these are extreme classes, the selection effects could reduce their numbers.

A slight preference for high effective temperatures is detected for the systems with the 3:2 resonance. The inner periods of this resonant state are typically longer than 1 day, usually several days. These two properties can connect because the hot systems have relatively long orbital periods. This study can conclude the 3:2 resonant state as a possible, more stable solution in the 2+2 configuration. An increase in high composite temperatures is observed for this resonance. However, the precise statistical properties require a large sample of systems.

The composite temperature plays a crucial role in the light curve modelling. The automated catalogue pipelines could lead to misinterpretation. It is essential to know more parameters than only one catalogue value, such as the light curve shape, minima depths, angular vicinity of the studied system, the precise distance, and extinction. The SED fitting provides reliable results when the extinction is known precisely.

The third light could be one of the most problematic parameters during the physical modelling. The TESS low angular resolution is also reflected in the third light

fitting. The light contamination can be relatively large in some cases, giving the sum of the third light more than, for instance, 120 %. This parameter can differ significantly for observations with higher angular resolution. Theoretically, the fitted sum of the third light should always be at least 100 % within uncertainties. High-resolution spectroscopic and photometric observations would reduce the light contamination and improve the models.

Conclusions

This thesis focuses on doubly eclipsing 2+2 quadruple stellar systems. Such systems consist of two eclipsing binaries orbiting a common centre of mass. The main achievements of this study include photometric observations, confirmation of the outer orbit of new quadruple candidates, and the analysis of their statistical properties.

The data from the TESS satellite are the initial source of light curve shape and orbital period for both inner binaries within the system. However, many selection effects and issues must be considered. The low angular resolution sometimes leads to signal contamination with other light sources. Additional ground-based surveys (ASAS-SN, ZTF, and SWASP) and new photometric measurements were used in this study to enhance the datasets and exclude the potential blends. Moreover, the outer periods can be significantly longer than the TESS observing timescale. Therefore, the outer orbit confirmation requires long-term monitoring of the individual candidates.

The data generally contain a trend, which could affect the light curves, especially for low-amplitude binaries. A detrending process was carried out using the Python script and Chebyshev polynomials. The composite light curves must be disentangled into individual inner binaries before further analysis. The iterative procedure using the SILICUPS software phenomenological modelling was made as a primary method. Harmonic polynomials were used in the case of binaries with total eclipse, fitted in Python.

The minima timings were derived primarily in SILICUPS. This fitting was suitable for continuous data. The Python code was created for the case of ground-based photometric surveys. The code uses known phenomenological models of phase-folded light curves. The entire curve is phase-shifted according to the model, and the minima timings are derived from the phase shift. This approach is primarily focused on non-continuous measurements where the other processes are not substantial to use. The mutual motion caused by the outer orbit can be discovered by variations in minima timings using the $O-C$ diagrams. The light time effect (LiTE), suggesting a quadruple nature, should be visible in the diagram of each pair.

The spectral energy distribution (SED) allows for the composite temperature of the system to be obtained. This parameter provides the upper limit for the components, from which the individual temperatures can be estimated. Adding the spectroscopic observations can lead to measuring the radial velocities of all four stars within the system and discovering the outer orbit. The mentioned data types provide a complex source of information for comprehensive physical modelling.

Ten systems in the Northern sky were comprehensively analysed. Seven candidates were confirmed as doubly eclipsing quadruples using the $O-C$ diagrams constructed with the OCFit software. The outer orbit parameters were obtained for these with the relatively short outer periods. Furthermore, the system TIC 9493888 (S1 Cam) sug-

gests the presence of an additional fifth component. ASASSN-V J020003.56+452605.2 (S1 And) is, with high probability, a blend of two eclipsing pairs without mutual interaction. The radial velocity curves were measured for the individual components of ASASSN-V J233336.79+615012.0 (S3 Cas). The TESS and new data light curves were modelled in PHOEBE 0.32, allowing derivation of the essential parameters, i.e., effective temperatures, radius ratio, inclination, mass ratio, and third light. The third light parameter was generally different for TESS and new data, primarily due to the light contamination in the TESS field. The SED composite temperatures were compared with Gaia, TESS, and StarHorse catalogues. In some cases, the composite temperatures differ significantly. The usage of the individual temperature source could influence the final physical model.

Period statistical analysis was carried out on the sample of 781 systems. The inner period ratio R distribution was compared with the simulated prediction assuming a homogenous distribution between 0.2 and 20 days. Using the Kolmogorov-Smirnov (K-S) test, both data and simulations are in significant agreement. The resonant ratios were investigated. The closeness parameter C was defined for each examined resonance. The data were compared with simulations for two closeness/C ranges, up to 1 % and 2 %. The 3:2 resonant ratio was detected in the highest overabundance of the used values. Furthermore, the vicinity of this resonant state (C = 2 - 3 %) shows a decline. This comparison suggests that the systems preferentially occupy the 3:2 resonant state. Despite the statistics of small numbers, these main results are evident.

The analysis of Gaia Renormalised Unit Weight Error (RUWE) was made for the collected sample. A high RUWE value could indicate multiplicity for the studied object. On the other hand, this parameter cannot be considered as proof of additional components in the system. More than half of the already confirmed quadruples have the RUWE number in the range of a single object astrometric solution. The study of Gaia composite temperatures reveals an increased fraction of hot systems. However, the significant influence of the Magellanic Clouds was observed. A slight increase in hot temperatures was noticed for the systems in the 3:2 resonance.

The research introduces additional candidates for further observations. The preliminary $O - C$ analysis of ATO J223.4251+52.7158 (S2 Boo) indicates non-linear variations, making this system a potential target for follow-up research.

Bibliography

R. Z. Ádám, T. Hajdu, A. Bódi, R. Hajdu, T. Szklenár, and L. Molnár. Variable stars in the residual light curves of OGLE-IV eclipsing binaries towards the Galactic Bulge. A&A, 674:A170, June 2023. doi: 10.1051/0004-6361/202346006.

F. Anders, A. Khalatyan, C. Chiappini, A. B. Queiroz, B. X. Santiago, C. Jordi, L. Girardi, A. G. A. Brown, G. Matijevic, G. Monari, T. Cantat-Gaudin, M. Weiler, S. Khan, A. Miglio, I. Carrillo, M. Romero-Gomez, I. Minchev, R. S. de Jong, T. Antoja, P. Ramos, M. Steinmetz, and H. Enke. VizieR Online Data Catalog: StarHorse, Gaia DR2 photo-astrometric distances (Anders+, 2019). VizieR On-line Data Catalog: I/349. Originally published in: 2019A&A...628A..94A, Sept. 2019.

C. A. L. Bailer-Jones, J. Rybizki, M. Fouesneau, G. Mantelet, and R. Andrae. Estimating Distance from Parallaxes. IV. Distances to 1.33 Billion Stars in Gaia Data Release 2. AJ, 156(2):58, Aug. 2018. doi: 10.3847/1538-3881/aacb21.

A. Bayo, C. Rodrigo, D. Barrado Y Navascués, E. Solano, R. Gutiérrez, M. Morales-Calderón, and F. Allard. VOSA: virtual observatory SED analyzer. An application to the Collinder 69 open cluster. A&A, 492(1):277–287, Dec. 2008. doi: 10.1051/0004-6361:200810395.

T. Borkovits. Eclipsing Binaries in Dynamically Interacting Close, Multiple Systems. *Galaxies*, 10(1):9, Jan. 2022. doi: 10.3390/galaxies10010009.

T. Borkovits, T. Hajdu, J. Sztakovics, S. Rappaport, A. Levine, I. B. Bíró, and P. Klagyivik. A comprehensive study of the Kepler triples via eclipse timing. MNRAS, 455(4):4136–4165, Feb. 2016. doi: 10.1093/mnras/stv2530.

T. Borkovits, S. A. Rappaport, P. F. L. Maxted, I. Terentev, M. Omohundro, R. Gagliano, T. Jacobs, M. H. Kristiansen, D. LaCourse, H. M. Schwengeler, A. Vanderburg, and M. G. Blackford. BG Ind: the nearest doubly eclipsing, compact hierarchical quadruple system. MNRAS, 503(3):3759–3774, May 2021. doi: 10.1093/mnras/stab621.

T. Borkovits, T. Mitnyan, S. A. Rappaport, T. Pribulla, B. P. Powell, V. B. Kostov, I. B. Bíró, I. Csányi, Z. Garai, B. L. Gary, T. G. Kaye, R. Komžík, I. Terentev, M. Omohundro, R. Gagliano, T. Jacobs, M. H. Kristiansen, D. LaCourse, H. M. Schwengeler, D. Czavalinga, B. Seli, C. X. Huang, A. Pál, A. Vanderburg, J. E. Rodriguez, and D. J. Stevens. Triply eclipsing triple stars in the northern TESS fields: TICs 193993801, 388459317, and 52041148. MNRAS, 510(1):1352–1374, Feb. 2022. doi: 10.1093/mnras/stab3397.

S. Breiter and D. Vokrouhlický. Resonant dynamics of gravitationally bound pair of binaries: the case of 1:1 resonance. MNRAS, 475(4):5215–5230, Apr. 2018. doi: 10.1093/mnras/sty132.

M. Brož, P. Harmanec, P. Zasche, R. Catalan-Hurtado, B. N. Barlow, W. Frondorf, M. Wolf, H. Drechsel, R. Chini, A. Nasseri, J. Labadie-Bartz, G. W. Christie, W. S. G. Walker, M. Blackford, D. Blane, A. A. Henden, T. Bohlsen, H. Božić, and J. Jonák. Towards a consistent model of the hot quadruple system HD 93206 = QZ Carinæ. II. N-body model. A&A, 666:A24, Oct. 2022. doi: 10.1051/0004-6361/202243596.

E. Budding and O. Demircan. *A Guide to Close Binary Systems*. CRC Press, 2022.

P. Cagaš. Variable Stars in the Field of V729 Aql. *Open European Journal on Variable Stars*, 180:8, Apr. 2017.

F. Castelli and R. L. Kurucz. New Grids of ATLAS9 Model Atmospheres. In N. Piskunov, W. W. Weiss, and D. F. Gray, editors, *Modelling of Stellar Atmospheres*, volume 210 of *IAU Symposium*, page A20, Jan. 2003. doi: 10.48550/arXiv.astro-ph/0405087.

A. Castro-Ginard, Z. Penoyre, A. R. Casey, A. G. A. Brown, V. Belokurov, T. Cantat-Gaudin, R. Drimmel, M. Fouesneau, S. Khanna, E. P. Kurbatov, A. M. Price-Whelan, H.-W. Rix, and R. L. Smart. Gaia DR3 detectability of unresolved binary systems. A&A, 688:A1, Aug. 2024. doi: 10.1051/0004-6361/202450172.

I. Czekala, K. S. Mandel, S. M. Andrews, J. A. Dittmann, S. K. Ghosh, B. T. Montet, and E. R. Newton. Disentangling Time-series Spectra with Gaussian Processes: Applications to Radial Velocity Analysis. ApJ, 840(1):49, May 2017. doi: 10.3847/1538-4357/aa6aab.

D. C. Fabrycky, J. J. Lissauer, D. Ragozzine, J. F. Rowe, J. H. Steffen, E. Agol, T. Barclay, N. Batalha, W. Borucki, D. R. Ciardi, E. B. Ford, T. N. Gautier, J. C. Geary, M. J. Holman, J. M. Jenkins, J. Li, R. C. Morehead, R. L. Morris, A. Shporer, J. C. Smith, M. Still, and J. Van Cleve. Architecture of Kepler's Multi-transiting Systems. II. New Investigations with Twice as Many Candidates. ApJ, 790(2):146, Aug. 2014. doi: 10.1088/0004-637X/790/2/146.

M. Fedurco and Š. Parimucha. Double eclipsing binary system KIC 3832716. Ap&SS, 363(12):267, Dec. 2018. doi: 10.1007/s10509-018-3487-7.

G. B. Fezenko, H.-C. Hwang, and N. L. Zakamska. Enhancement of double-close-binary quadruples. MNRAS, 511(3):3881–3894, Apr. 2022. doi: 10.1093/mnras/stac309.

Gaia Collaboration. Gaia Data Release 2. Summary of the contents and survey properties. A&A, 616:A1, Aug. 2018. doi: 10.1051/0004-6361/201833051.

Gaia Collaboration. Gaia Data Release 3. Summary of the content and survey properties. A&A, 674:A1, June 2023. doi: 10.1051/0004-6361/202243940.

P. Gajdoš and Š. Parimucha. New tool with GUI for fitting O-C diagrams. *Open European Journal on Variable Stars*, 197:71, Apr. 2019.

D. Graczyk. Light-curve solutions for bright detached eclipsing binaries in the Small Magellanic Cloud: absolute dimensions and distance indicators. MNRAS, 342(4): 1334–1348, July 2003. doi: 10.1046/j.1365-8711.2003.06636.x.

G. M. Green, E. Schlafly, C. Zucker, J. S. Speagle, and D. Finkbeiner. A 3D Dust Map Based on Gaia, Pan-STARRS 1, and 2MASS. ApJ, 887(1):93, Dec. 2019. doi: 10.3847/1538-4357/ab5362.

D. Guo, L. Kaper, A. G. A. Brown, J. H. J. de Bruijne, and E. Zari. The Gaia DR2 census of the Scorpius OB2 association based on kinematic modeling. A&A, 696: A119, Apr. 2025. doi: 10.1051/0004-6361/202244011.

W. I. Hartkopf, B. D. Mason, and C. E. Worley. The 2001 US Naval Observatory Double Star CD-ROM. II. The Fifth Catalog of Orbits of Visual Binary Stars. AJ, 122(6):3472–3479, Dec. 2001. doi: 10.1086/323921.

R. W. Hilditch. *An introduction to close binary stars*. Cambridge University Press, 2001.

K. Hong, J. W. Lee, S.-L. Kim, J.-R. Koo, and C.-U. Lee. Apsidal motions of 90 eccentric binary systems in the Small Magellanic Cloud. MNRAS, 460(1):650–663, July 2016. doi: 10.1093/mnras/stw955.

D. J. Hutter, C. Tycner, R. T. Zavala, J. A. Benson, C. A. Hummel, and H. Zirm. Surveying the Bright Stars by Optical Interferometry. III. A Magnitude-limited Multiplicity Survey of Classical Be Stars. ApJS, 257(2):69, Dec. 2021. doi: 10.3847/1538-4365/ac23cb.

J. B. Irwin. Standard light-time curves. AJ, 64:149, May 1959. doi: 10.1086/107913.

T. Jayasinghe, K. Z. Stanek, C. S. Kochanek, B. J. Shappee, T. W. S. Holoien, T. A. Thompson, J. L. Prieto, S. Dong, M. Pawlak, O. Pejcha, J. V. Shields, G. Pojmanski, S. Otero, C. A. Britt, and D. Will. The ASAS-SN catalogue of variable stars - II. Uniform classification of 412 000 known variables. MNRAS, 486(2):1907–1943, June 2019. doi: 10.1093/mnras/stz844.

D. G. Koch, W. J. Borucki, G. Basri, N. M. Batalha, T. M. Brown, D. Caldwell, J. Christensen-Dalsgaard, W. D. Cochran, E. DeVore, E. W. Dunham, T. N. Gautier, III, J. C. Geary, R. L. Gilliland, A. Gould, J. Jenkins, Y. Kondo, D. W. Latham, J. J. Lissauer, G. Marcy, D. Monet, D. Sasselov, A. Boss, D. Brownlee, J. Caldwell, A. K. Dupree, S. B. Howell, H. Kjeldsen, S. Meibom, D. Morrison, T. Owen, H. Reitsema, J. Tarter, S. T. Bryson, J. L. Dotson, P. Gazis, M. R. Haas, J. Kolodziejczak, J. F. Rowe, J. E. Van Cleve, C. Allen, H. Chandrasekaran, B. D. Clarke, J. Li, E. V. Quintana, P. Tenenbaum, J. D. Twicken, and H. Wu. Kepler Mission Design, Realized Photometric Performance, and Early Science. ApJ, 713(2):L79–L86, Apr. 2010. doi: 10.1088/2041-8205/713/2/L79.

C. S. Kochanek, B. J. Shappee, K. Z. Stanek, T. W. S. Holoien, T. A. Thompson, J. L. Prieto, S. Dong, J. V. Shields, D. Will, C. Britt, D. Perzanowski, and G. Pojmański. The All-Sky Automated Survey for Supernovae (ASAS-SN) Light Curve Server v1.0. PASP, 129(980):104502, Oct. 2017. doi: 10.1088/1538-3873/aa80d9.

Z. Kopal. The classification of close binary systems. *Annales d'Astrophysique*, 18:379, Jan. 1955.

V. B. Kostov, B. P. Powell, G. Torres, T. Borkovits, S. A. Rappaport, A. Tokovinin, P. Zasche, D. Anderson, T. Barclay, P. Berlind, P. Brown, M. L. Calkins, K. A. Collins, K. I. Collins, D. M. Conti, G. A. Esquerdo, C. Hellier, E. L. N. Jensen, J. Kamler, E. Kruse, D. W. Latham, M. Mašek, F. Murgas, G. Olmschenk, J. A. Orosz, A. Pál, E. Palle, R. P. Schwarz, C. Stockdale, D. Tamayo, R. Uhlař, W. F. Welsh, and R. West. TIC 454140642: A Compact, Coplanar, Quadruple-lined Quadruple Star System Consisting of Two Eclipsing Binaries. ApJ, 917(2):93, Aug. 2021. doi: 10.3847/1538-4357/ac04ad.

V. B. Kostov, B. P. Powell, S. A. Rappaport, T. Borkovits, R. Gagliano, T. L. Jacobs, M. H. Kristiansen, D. M. LaCourse, M. Omohundro, J. Orosz, A. R. Schmitt, H. M. Schwengeler, I. A. Terentev, G. Torres, T. Barclay, A. H. Friedman, E. Kruse, G. Olmschenk, A. Vanderburg, and W. Welsh. Ninety-seven Eclipsing Quadruple Star Candidates Discovered in TESS Full-frame Images. ApJS, 259(2):66, Apr. 2022. doi: 10.3847/1538-4365/ac5458.

V. B. Kostov, T. Borkovits, S. A. Rappaport, B. P. Powell, A. Pál, T. L. Jacobs, R. Gagliano, M. H. Kristiansen, D. M. LaCourse, M. Moe, M. Omohundro, A. R. Schmitt, H. M. Schwengeler, I. A. Terentev, and A. Vanderburg. TIC 219006972: a compact, coplanar quadruple star system consisting of two eclipsing binaries with an outer period of 168 d. MNRAS, 522(1):90–101, June 2023. doi: 10.1093/mnras/stad941.

V. B. Kostov, B. P. Powell, S. A. Rappaport, T. Borkovits, R. Gagliano, T. L. Jacobsy, R. Jayaraman, M. H. Kristiansen, D. M. LaCourse, T. Mitnyan, M. Omohundro, J. Orosz, A. Pál, A. R. Schmitt, H. M. Schwengeler, I. A. Terentev, G. Torres, T. Barclay, A. Vanderburg, and W. Welsh. 101 eclipsing quadruple star candidates discovered in TESS full frame images. MNRAS, 527(2):3995–4017, Jan. 2024. doi: 10.1093/mnras/stad2947.

M. Kounkel, K. R. Covey, K. G. Stassun, A. M. Price-Whelan, J. Holtzman, D. Chojnowski, P. Longa-Peña, C. G. Román-Zúñiga, J. Hernandez, J. Serna, C. Badenes, N. De Lee, S. Majewski, G. S. Stringfellow, K. M. Kratter, M. Moe, P. M. Frinchaboy, R. L. Beaton, J. G. Fernández-Trincado, S. Mahadevan, D. Minniti, T. C. Beers, D. P. Schneider, R. Barba, J. R. Brownstein, D. A. García-Hernández, K. Pan, and D. Bizyaev. Double-lined Spectroscopic Binaries in the APOGEE DR16 and DR17 Data. AJ, 162(5):184, Nov. 2021. doi: 10.3847/1538-3881/ac1798.

S. Kouzuma. Mass Ratio Estimates for Overcontact Binaries Using the Derivatives of Light Curves. ApJ, 958(1):84, Nov. 2023. doi: 10.3847/1538-4357/ad03e1.

A. L. Kraus and L. A. Hillenbrand. Unusually Wide Binaries: Are They Wide or Unusual? ApJ, 703(2):1511–1530, Oct. 2009. doi: 10.1088/0004-637X/703/2/1511.

K. K. Kwee and H. van Woerden. A method for computing accurately the epoch of minimum of an eclipsing variable. Bull. Astron. Inst. Netherlands, 12:327, May 1956.

B. Lasker, J. Doggett, B. McLean, et al. The second generation digitized sky survey. In *ASP Conf. Ser*, volume 101, page 88, 1996.

C. U. Lee, S. L. Kim, J. W. Lee, C. H. Kim, Y. B. Jeon, H. I. Kim, J. N. Yoon, and A. Humphrey. V994 Herculis: the multiple system with a quadruple-lined spectrum and a double eclipsing feature. MNRAS, 389(4):1630–1636, Oct. 2008. doi: 10.1111/j.1365-2966.2008.13708.x.

Lightkurve Collaboration, J. V. d. M. Cardoso, C. Hedges, M. Gully-Santiago, N. Saunders, A. M. Cody, T. Barclay, O. Hall, S. Sagear, E. Turtelboom, J. Zhang, A. Tzanidakis, K. Mighell, J. Coughlin, K. Bell, Z. Berta-Thompson, P. Williams, J. Dotson, and G. Barentsen. Lightkurve: Kepler and TESS time series analysis in Python. Astrophysics Source Code Library, record ascl:1812.013, Dec. 2018.

L. Lindegren, J. Hernández, A. Bombrun, S. Klioner, U. Bastian, M. Ramos-Lerate, A. de Torres, H. Steidelmüller, C. Stephenson, D. Hobbs, U. Lammers, M. Biermann, R. Geyer, T. Hilger, D. Michalik, U. Stampa, P. J. McMillan, J. Castañeda, M. Clotet, G. Comoretto, M. Davidson, C. Fabricius, G. Gracia, N. C. Hambly, A. Hutton, A. Mora, J. Portell, F. van Leeuwen, U. Abbas, A. Abreu, M. Altmann, A. Andrei, E. Anglada, L. Balaguer-Núñez, C. Barache, U. Becciani, S. Bertone, L. Bianchi, S. Bouquillon, G. Bourda, T. Brüsemeister, B. Bucciarelli, D. Busonero, R. Buzzi, R. Cancelliere, T. Carlucci, P. Charlot, N. Cheek, M. Crosta, C. Crowley, J. de Bruijne, F. de Felice, R. Drimmel, P. Esquej, A. Fienga, E. Fraile, M. Gai, N. Garralda, J. J. González-Vidal, R. Guerra, M. Hauser, W. Hofmann, B. Holl, S. Jordan, M. G. Lattanzi, H. Lenhardt, S. Liao, E. Licata, T. Lister, W. Löffler, J. Marchant, J. M. Martin-Fleitas, R. Messineo, F. Mignard, R. Morbidelli, E. Poggio, A. Riva, N. Rowell, E. Salguero, M. Sarasso, E. Sciacca, H. Siddiqui, R. L. Smart, A. Spagna, I. Steele, F. Taris, J. Torra, A. van Elteren, W. van Reeven, and A. Vecchiato. Gaia Data Release 2. The astrometric solution. A&A, 616:A2, Aug. 2018. doi: 10.1051/0004-6361/201832727.

M. E. Lohr, A. J. Norton, E. Gillen, R. Busuttil, U. C. Kolb, S. Aigrain, A. McQuillan, S. T. Hodgkin, and E. González. The doubly eclipsing quintuple low-mass star system 1SWASP J093010.78+533859.5. A&A, 578:A103, June 2015. doi: 10.1051/0004-6361/201525973.

E. Mamajek. A modern mean dwarf stellar color and effective temperature sequence. *URl: http://www. pas. rochester. edu/˜ emamajek/EEM_ dwarf_ UBVIJHK_ colors_ Teff. txt*, 2019.

P. Marchant. Evolution of binary stars. *arXiv preprint arXiv:2503.16099*, 2025.

P. Mayer. Eclipsing Binaries with Light-time Effect. *Bulletin of the Astronomical Institutes of Czechoslovakia*, 41:231, July 1990.

P. Mayer, P. Harmanec, P. Zasche, M. Brož, R. Catalan-Hurtado, B. N. Barlow, W. Frondorf, M. Wolf, H. Drechsel, R. Chini, A. Nasseri, A. Pigulski, J. Labadie-Bartz, G. W. Christie, W. S. G. Walker, M. Blackford, D. Blane, A. A. Henden, T. Bohlsen, H. Božić, and J. Jonák. Towards a consistent model of the hot quadruple system HD 93206 = QZ Carinæ. I. Observations and their initial analyses. A&A, 666:A23, Oct. 2022. doi: 10.1051/0004-6361/202142108.

Z. Mikulášek. Phenomenological modelling of eclipsing system light curves. A&A, 584: A8, Dec. 2015. doi: 10.1051/0004-6361/201425244.

D. Motl. Muniwin v2.1, 2011. URL http://c-munipack.sourceforge.net/.

S. S. R. Offner, M. Moe, K. M. Kratter, S. I. Sadavoy, E. L. N. Jensen, and J. J. Tobin. The Origin and Evolution of Multiple Star Systems. In S. Inutsuka, Y. Aikawa, T. Muto, K. Tomida, and M. Tamura, editors, *Protostars and Planets VII*, volume 534 of *Astronomical Society of the Pacific Conference Series*, page 275, July 2023. doi: 10.48550/arXiv.2203.10066.

S. Pačková. Fotometrická analỳza vícenásobně zákrytovỳch systém. 2024. URL https://is.muni.cz/th/k04bo/.

M. Pawlak, D. Graczyk, I. Soszyński, P. Pietrukowicz, R. Poleski, A. Udalski, M. K. Szymański, M. Kubiak, G. Pietrzyński, Ł. Wyrzykowski, K. Ulaczyk, S. Kozłowski, and J. Skowron. Eclipsing Binary Stars in the OGLE-III Fields of the Small Magellanic Cloud. Acta Astron., 63(3):323–338, Sept. 2013. doi: 10.48550/arXiv.1310.3272.

M. Pawlak, I. Soszyński, A. Udalski, M. K. Szymański, Ł. Wyrzykowski, K. Ulaczyk, R. Poleski, P. Pietrukowicz, S. Kozłowski, D. M. Skowron, J. Skowron, P. Mróz, and A. Hamanowicz. The OGLE Collection of Variable Stars. Eclipsing Binaries in the Magellanic System. Acta Astron., 66(4):421–432, Dec. 2016. doi: 10.48550/arXiv.1612.06394.

O. Pejcha, P. Cagaš, C. Landri, M. M. Fausnaugh, G. De Rosa, J. L. Prieto, Z. Henzl, and M. Pešta. The complex dynamical past and future of double eclipsing binary CzeV343: Misaligned orbits and period resonance. A&A, 667:A53, Nov. 2022. doi: 10.1051/0004-6361/202244335.

G. Pietrzyński, D. Graczyk, A. Gallenne, W. Gieren, I. B. Thompson, B. Pilecki, P. Karczmarek, M. Górski, K. Suchomska, M. Taormina, B. Zgirski, P. Wielgórski, Z. Kołaczkowski, P. Konorski, S. Villanova, N. Nardetto, P. Kervella, F. Bresolin, R. P. Kudritzki, J. Storm, R. Smolec, and W. Narloch. A distance to the Large Magellanic Cloud that is precise to one per cent. Nature, 567(7747):200–203, Mar. 2019. doi: 10.1038/s41586-019-0999-4.

D. L. Pollacco, I. Skillen, A. Collier Cameron, D. J. Christian, C. Hellier, J. Irwin, T. A. Lister, R. A. Street, R. G. West, D. R. Anderson, W. I. Clarkson, H. Deeg, B. Enoch, A. Evans, A. Fitzsimmons, C. A. Haswell, S. Hodgkin, K. Horne, S. R. Kane, F. P. Keenan, P. F. L. Maxted, A. J. Norton, J. Osborne, N. R. Parley, R. S. I. Ryans, B. Smalley, P. J. Wheatley, and D. M. Wilson. The wasp project and the superwasp cameras. PASP, 118(848):1407–1418, Oct. 2006. doi: 10.1086/508556.

B. P. Powell, V. B. Kostov, S. A. Rappaport, T. Borkovits, P. Zasche, A. Tokovinin, E. Kruse, D. W. Latham, B. T. Montet, E. L. Jensen, et al. Tic 168789840: A sextuply eclipsing sextuple star system. *The Astronomical Journal*, 161(4):162, 2021.

B. P. Powell, G. Torres, V. B. Kostov, T. Borkovits, S. A. Rappaport, M. Moe, D. W. Latham, T. L. Jacobs, R. Gagliano, M. H. K. Kristiansen, M. Omohundro, H. M. Schwengeler, D. M. LaCourse, I. A. Terentev, and A. R. Schmitt. The Discovery of Two Quadruple Star Systems with the Second and Third Shortest Outer Periods. ApJ, 985(2):213, June 2025. doi: 10.3847/1538-4357/adcece.

T. Pribulla, T. Borkovits, R. Jayaraman, S. Rappaport, T. Mitnyan, P. Zasche, R. Komžík, A. Pál, R. Uhlař, M. Mašek, Z. Henzl, I. B. Bíró, I. Csányi, R. Stuik, M. H. Kristiansen, H. M. Schwengeler, R. Gagliano, T. L. Jacobs, M. Omohundro, V. Kostov, B. P. Powell, I. A. Terentev, A. Vanderburg, D. LaCourse, J. E. Rodriguez, G. Bakos, Z. Csubry, and J. Hartman. BU Canis Minoris - the most compact known flat doubly eclipsing quadruple system. MNRAS, 524(3):4220–4238, Sept. 2023. doi: 10.1093/mnras/stad2015.

A. Prša and T. Zwitter. A Computational Guide to Physics of Eclipsing Binaries. I. Demonstrations and Perspectives. ApJ, 628(1):426–438, July 2005. doi: 10.1086/430591.

S. Rappaport, H. Lehmann, B. Kalomeni, T. Borkovits, D. Latham, A. Bieryla, H. Ngo, D. Mawet, S. Howell, E. Horch, T. L. Jacobs, D. LaCourse, Á. Sódor, A. Vanderburg, and K. Pavlovski. A quintuple star system containing two eclipsing binaries. MNRAS, 462(2):1812–1825, Oct. 2016. doi: 10.1093/mnras/stw1745.

A. Richterková. Studium vícenásobných hvězdných systémů. 2025. URL https://is.muni.cz/th/npg5a/.

G. R. Ricker, J. N. Winn, R. Vanderspek, D. W. Latham, G. Á. Bakos, J. L. Bean, Z. K. Berta-Thompson, T. M. Brown, L. Buchhave, N. R. Butler, R. P. Butler, W. J. Chaplin, D. Charbonneau, J. Christensen-Dalsgaard, M. Clampin, D. Deming, J. Doty, N. De Lee, C. Dressing, E. W. Dunham, M. Endl, F. Fressin, J. Ge, T. Henning, M. J. Holman, A. W. Howard, S. Ida, J. M. Jenkins, G. Jernigan, J. A. Johnson, L. Kaltenegger, N. Kawai, H. Kjeldsen, G. Laughlin, A. M. Levine, D. Lin, J. J. Lissauer, P. MacQueen, G. Marcy, P. R. McCullough, T. D. Morton, N. Narita, M. Paegert, E. Palle, F. Pepe, J. Pepper, A. Quirrenbach, S. A. Rinehart, D. Sasselov, B. Sato, S. Seager, A. Sozzetti, K. G. Stassun, P. Sullivan, A. Szentgyorgyi, G. Torres, S. Udry, and J. Villasenor. Transiting Exoplanet Survey Satellite (TESS). *Journal of Astronomical Telescopes, Instruments, and Systems*, 1:014003, Jan. 2015. doi: 10.1117/1.JATIS.1.1.014003.

P. Rowden, T. Borkovits, J. M. Jenkins, K. G. Stassun, J. D. Twicken, E. R. Newton, C. Ziegler, C. Hellier, A. G. Soto, E. C. Matthews, U. Kolb, G. R. Ricker, R. Vanderspek, D. W. Latham, S. Seager, J. N. Winn, L. G. Bouma, C. Briceño, D. Charbonneau, W. Fong, A. Glidden, N. M. Guerrero, N. Law, A. W. Mann, M. E. Rose, J. Schlieder, P. Tenenbaum, and E. B. Ting. TIC 278956474: Two Close Binaries in One Young Quadruple System Identified by TESS. AJ, 160(2):76, Aug. 2020. doi: 10.3847/1538-3881/ab9d20.

O. Schütz, G. Meeus, A. Carmona, A. Juhász, and M. F. Sterzik. The young B-star quintuple system HD 155448. A&A, 533:A54, Sept. 2011. doi: 10.1051/0004-6361/201016396.

A. M. S. Smith and WASP Consortium. The SuperWASP exoplanet transit survey. *Contributions of the Astronomical Observatory Skalnate Pleso*, 43(3):500–512, Mar. 2014.

I. Soszyński, M. Pawlak, P. Pietrukowicz, A. Udalski, M. K. Szymański, Ł. Wyrzykowski, K. Ulaczyk, R. Poleski, S. Kozłowski, D. M. Skowron, J. Skowron, P. Mróz, and A. Hamanowicz. The OGLE Collection of Variable Stars. Over 450 000 Eclipsing and Ellipsoidal Binary Systems Toward the Galactic Bulge. Acta Astron., 66(4):405–420, Dec. 2016. doi: 10.48550/arXiv.1701.03105.

J. Southworth. Rediscussion of eclipsing binaries. Paper 8: The doubly-eclipsing quadruple star system V498 Cygni. *The Observatory*, 142:54–68, Apr. 2022. doi: 10.48550/arXiv.2201.02516.

J. Southworth, P. F. L. Maxted, and B. Smalley. Eclipsing binaries in open clusters - I. V615 Per and V618 Per in h Persei. MNRAS, 349(2):547–559, Apr. 2004. doi: 10.1111/j.1365-2966.2004.07520.x.

K. G. Stassun, R. J. Oelkers, M. Paegert, G. Torres, J. Pepper, N. De Lee, K. Collins, D. W. Latham, P. S. Muirhead, J. Chittidi, B. Rojas-Ayala, S. W. Fleming, M. E. Rose, P. Tenenbaum, E. B. Ting, S. R. Kane, T. Barclay, J. L. Bean, C. E. Brassuer, D. Charbonneau, J. Ge, J. J. Lissauer, A. W. Mann, B. McLean, S. Mullally, N. Narita, P. Plavchan, G. R. Ricker, D. Sasselov, S. Seager, S. Sharma, B. Shiao, A. Sozzetti, D. Stello, R. Vanderspek, G. Wallace, and J. N. Winn. The Revised TESS Input Catalog and Candidate Target List. AJ, 158(4):138, Oct. 2019. doi: 10.3847/1538-3881/ab3467.

A. Tokovinin. From Binaries to Multiples. II. Hierarchical Multiplicity of F and G Dwarfs. AJ, 147(4):87, Apr. 2014. doi: 10.1088/0004-6256/147/4/87.

A. Tokovinin. The Updated Multiple Star Catalog. ApJS, 235(1):6, Mar. 2018. doi: 10.3847/1538-4365/aaa1a5.

A. Tokovinin. Architecture of Hierarchical Stellar Systems and Their Formation. *Universe*, 7(9):352, Sept. 2021. doi: 10.3390/universe7090352.

A. Tokovinin. VizieR Online Data Catalog: Spectro. orbits of subsystems in multiple stars X (Tokovinin, 2023). VizieR On-line Data Catalog: J/AJ/165/220. Originally published in: 2023AJ....165..220T, Oct. 2023.

G. Torres, C. H. Sandberg Lacy, F. C. Fekel, M. Wolf, and M. W. Muterspaugh. The Quadruple-lined, Doubly Eclipsing System V482 Persei. ApJ, 846(2):115, Sept. 2017. doi: 10.3847/1538-4357/aa8633.

G. Torres, J. L. Curtis, A. Vanderburg, A. L. Kraus, and A. Rizzuto. Eclipsing Binaries in the Open Cluster Ruprecht 147. I. EPIC 219394517. ApJ, 866(1):67, Oct. 2018. doi: 10.3847/1538-4357/aadca8.

S. Tremaine. Resonant capture in quadruple stellar systems. MNRAS, 493(4):5583–5595, Apr. 2020. doi: 10.1093/mnras/staa643.

T. Vaessen and J. van Roestel. A systematic search for double eclipsing binaries in Zwicky Transient Facility data. A&A, 682:A164, Feb. 2024. doi: 10.1051/0004-6361/202348451.

D. Vokrouhlický. Secular dynamics of gravitationally bound pair of binaries. MNRAS, 461(4):3964–3975, Oct. 2016. doi: 10.1093/mnras/stw1596.

P. Švaříček, M. Wolf, A. Claret, L. Kotková, L. Brát, L. Šmelcer, and M. Zejda. Rapid apsidal motion in eccentric eclipsing binaries: OX Cassiopeia, PV Cassiopeia, and CO Lacertae. A&A, 477(2):615–620, Jan. 2008. doi: 10.1051/0004-6361:20078022.

R. E. Wilson. Eccentric orbit generalization and simultaneous solution of binary star light and velocity curves. ApJ, 234:1054–1066, Dec. 1979. doi: 10.1086/157588.

R. E. Wilson. Binary Star Morphology and the Name Overcontact. *Information Bulletin on Variable Stars*, 5076:1, May 2001.

R. E. Wilson and E. J. Devinney. Realization of Accurate Close-Binary Light Curves: Application to MR Cygni. ApJ, 166:605, June 1971. doi: 10.1086/150986.

R. E. Wilson and L. W. Twigg. On the Existence of Double-Contact Binaries. In M. J. Plavec, D. M. Popper, and R. K. Ulrich, editors, *Close Binary Stars: Observations and Interpretation*, volume 88 of *IAU Symposium*, page 263, Jan. 1980.

N. Zacharias, C. T. Finch, T. M. Girard, A. Henden, J. L. Bartlett, D. G. Monet, and M. I. Zacharias. The Fourth US Naval Observatory CCD Astrograph Catalog (UCAC4). AJ, 145(2):44, Feb. 2013. doi: 10.1088/0004-6256/145/2/44.

N. Zacharias, C. Finch, J. Subasavage, G. Bredthauer, C. Crockett, M. Divittorio, E. Ferguson, F. Harris, H. Harris, A. Henden, C. Kilian, J. Munn, T. Rafferty, A. Rhodes, M. Schultheiss, T. Tilleman, and G. Wieder. The First U.S. Naval Observatory Robotic Astrometric Telescope Catalog. AJ, 150(4):101, Oct. 2015. doi: 10.1088/0004-6256/150/4/101.

P. Zasche. Comment on Ádám et al. (2023): Large fraction of already known systems reported. A&A, 688:A41, Aug. 2024. doi: 10.1051/0004-6361/202450463.

P. Zasche and R. Uhlař. Updated study of the quintuple system V994 Herculis. A&A, 588:A121, Apr. 2016. doi: 10.1051/0004-6361/201628153.

P. Zasche, R. Uhlář, M. Šlechta, M. Wolf, P. Harmanec, J. A. Nemravová, and D. Korčáková. Unique sextuple system: 65 Ursae Majoris. A&A, 542:A78, June 2012. doi: 10.1051/0004-6361/201219134.

P. Zasche, D. Vokrouhlickỳ, M. Wolf, H. Kučáková, J. Kára, R. Uhlař, M. Mašek, Z. Henzl, and P. Cagaš. Doubly eclipsing systems. *Astronomy & Astrophysics*, 630: A128, 2019.

P. Zasche, Z. Henzl, and J. Kára. The first study of four doubly eclipsing systems. A&A, 659:A8, Mar. 2022a. doi: 10.1051/0004-6361/202142771.

P. Zasche, Z. Henzl, and M. Mašek. Multiply eclipsing candidates from the TESS satellite. A&A, 664:A96, Aug. 2022b. doi: 10.1051/0004-6361/202243723.

P. Zasche, T. Borkovits, R. Jayaraman, S. A. Rappaport, M. Brož, D. Vokrouhlický, I. B. Bíró, T. Hegedüs, Z. T. Kiss, R. Uhlař, H. M. Schwengeler, A. Pál, M. Mašek, S. B. Howell, S. Dallaporta, U. Munari, R. Gagliano, T. Jacobs, M. H. Kristiansen, D. LaCourse, M. Omohundro, I. Terentev, A. Vanderburg, Z. Henzl, B. P. Powell, and V. B. Kostov. V994 Herculis: a unique triply eclipsing sextuple star system. MNRAS, 520(2):3127–3142, Apr. 2023a. doi: 10.1093/mnras/stad328.

P. Zasche, Z. Henzl, M. Mašek, R. Uhlař, J. Kára, J. Merc, and H. Kučáková. Detection of seven 2+2 doubly eclipsing quadruple systems. A&A, 675:A113, July 2023b. doi: 10.1051/0004-6361/202346848.

P. Zasche, Z. Henzl, J. Merc, J. Kára, and H. Kučáková. Eight new 2+2 doubly eclipsing quadruple systems detected. A&A, 687:A6, July 2024. doi: 10.1051/0004-6361/202450400.

Appendices

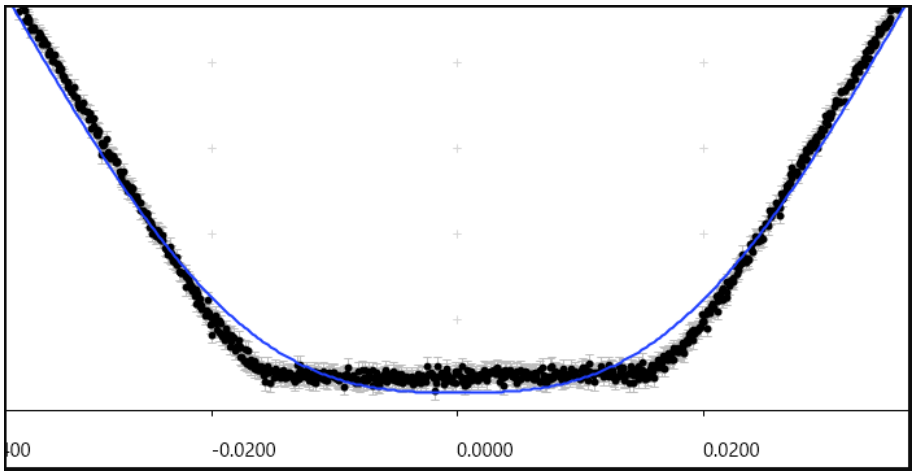

Figure A.1: ASASSN-V J020003.56+452605.2 (S1 And) primary eclipse fitting in the SILICUPS software, TESS light curve, part of sector 58. A total eclipse is not fitted adequately, and the additional trend would be created in the residuals.

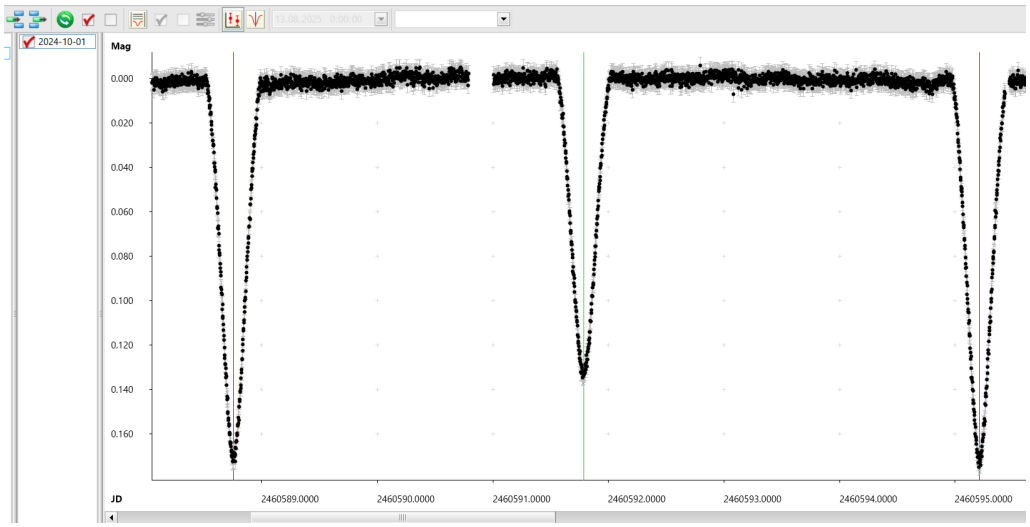

Figure A.2: ASASSN-V J222721.05+564425.3 (S1 Lac) minima timings calculations in the SILICUPS software, TESS light curve, part of sector 84.

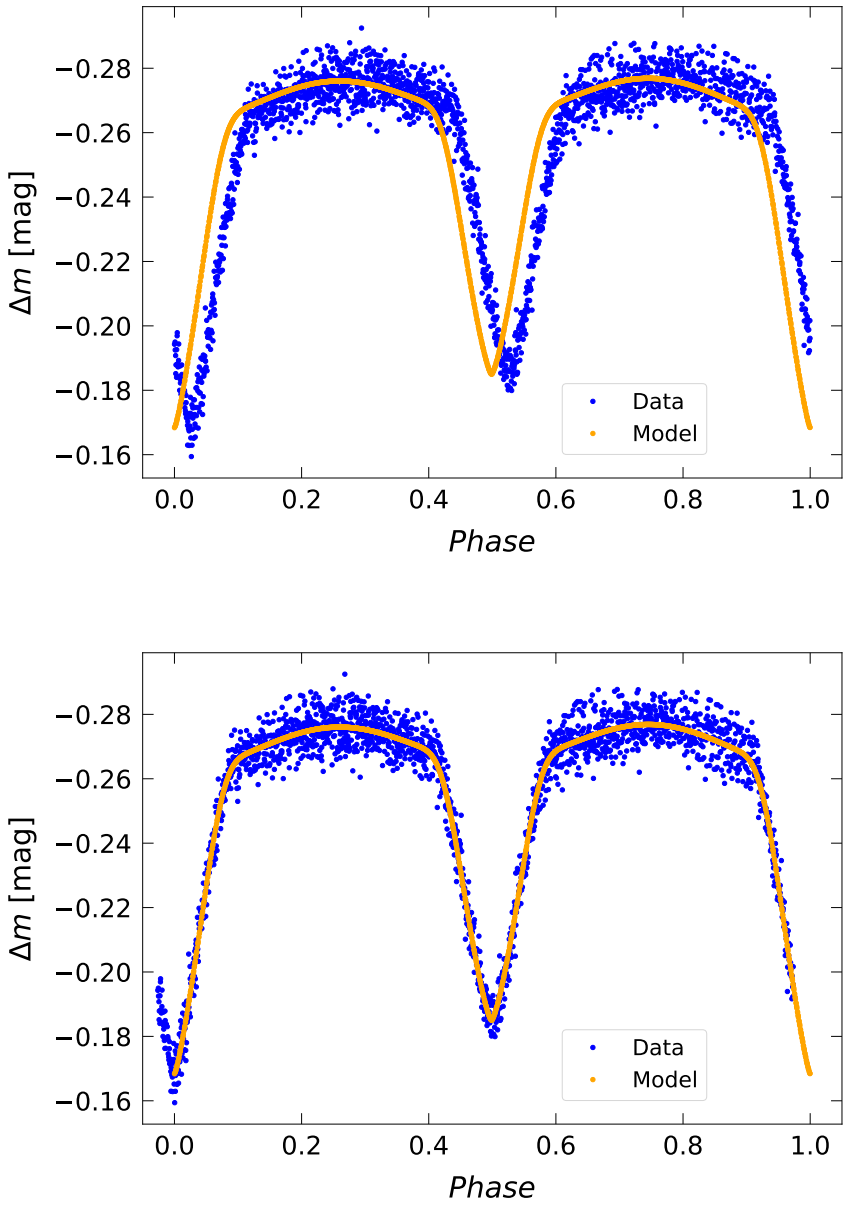

Figure A.3: Minima timings derivation from the script 2.1, part of the TESS sector 77 for ASASSN-V J000432.60+632605.0 (S1 Cas), pair B, upper panel: before the fitting process, bottom panel: after the fitting when the data are phase-shifted. It is recommended to state the initial values of the instantaneous M_0 time by a rough estimation to have a small phase shift, and use the survey data where the continuous time series are missing. The minima timings from the TESS should be derived directly. These data are mainly illustrative to show the script's function and purpose.

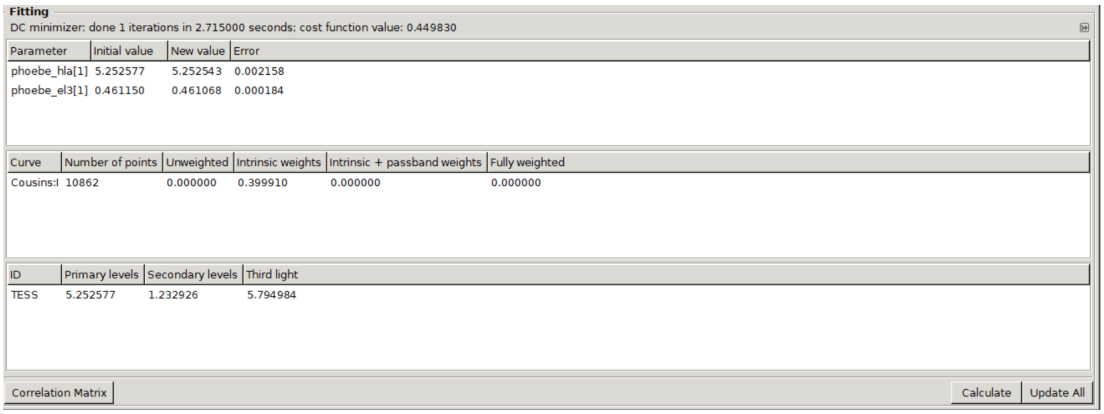

Figure A.4: PHOEBE *Fitting* tab, pair A third light and luminsosity level modelling of ASASSN-V J000432.60+632605.0 (S1 Cas).

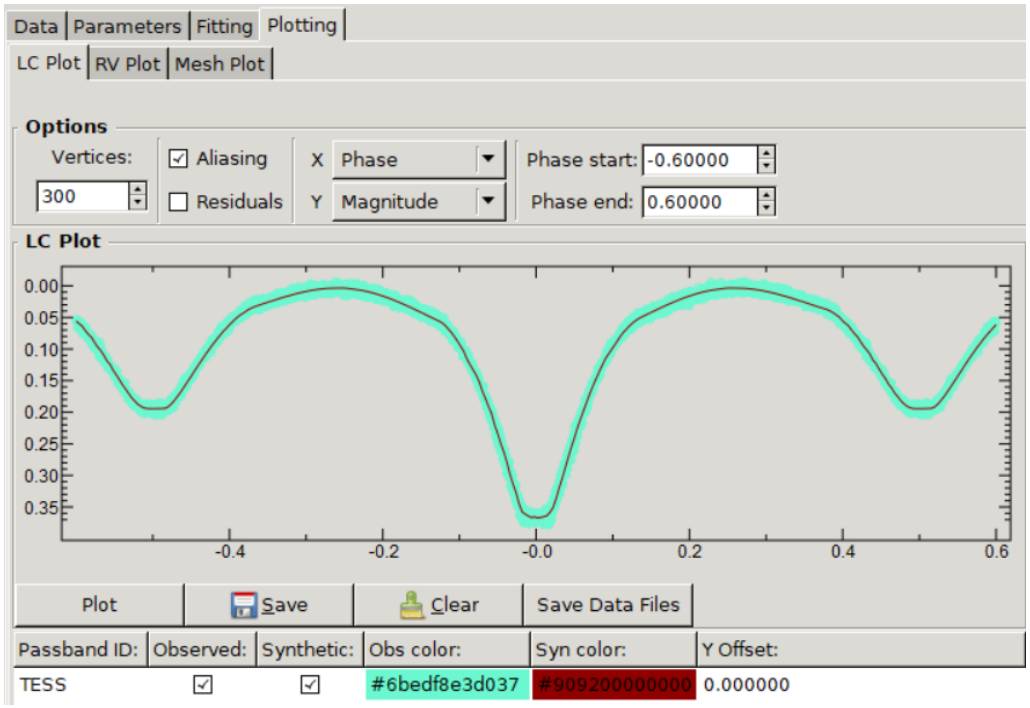

Figure A.5: Light curve plot of pair A of ASASSN-V J000432.60+632605.0 (S1 Cas) in PHOEBE.

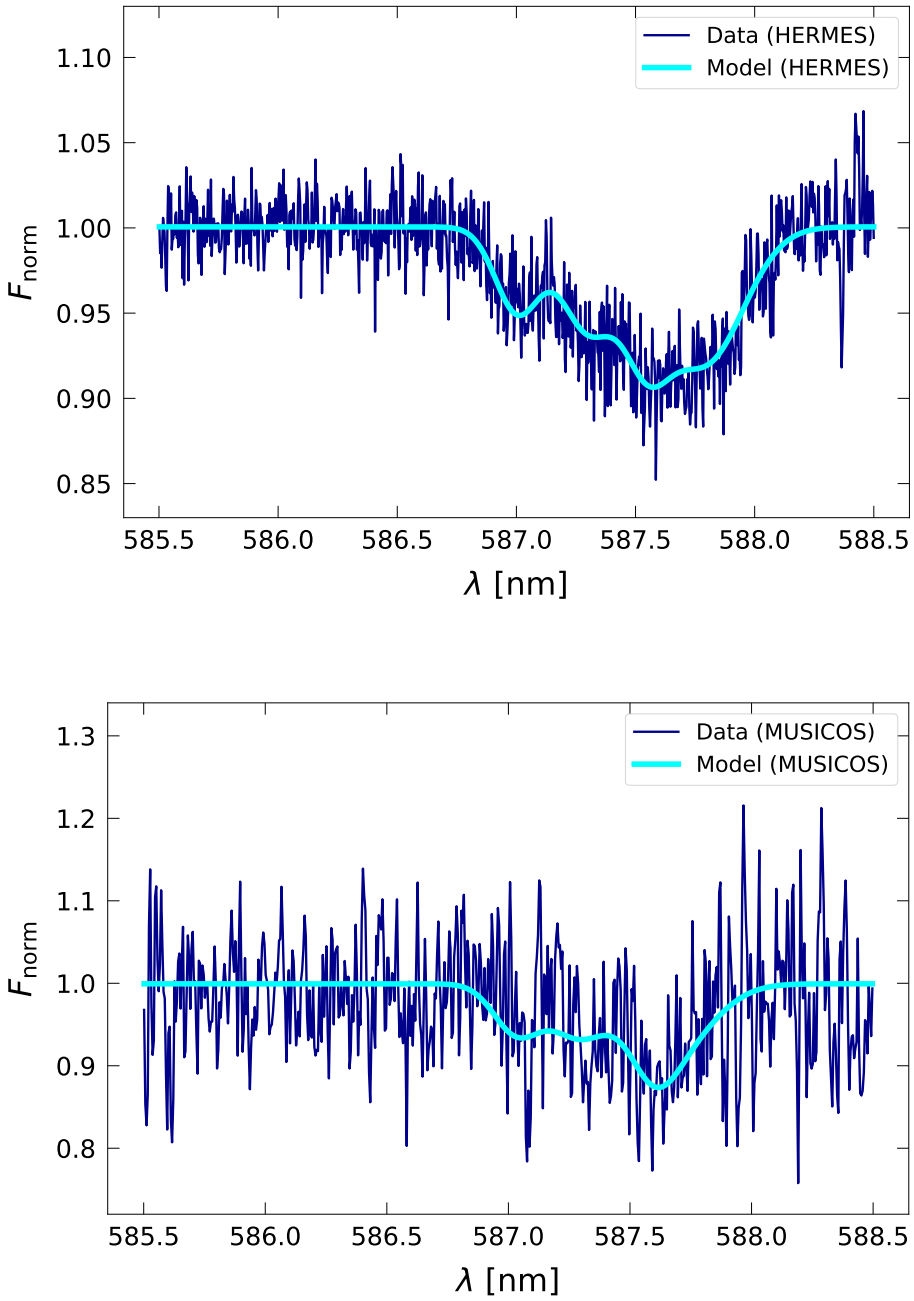

Figure A.6: He I 5876 spectral line of ASASSN-V J233336.79+615012.0 (S3 Cas), upper panel: Hermes observation, bottom panel: MUSICOS observation.

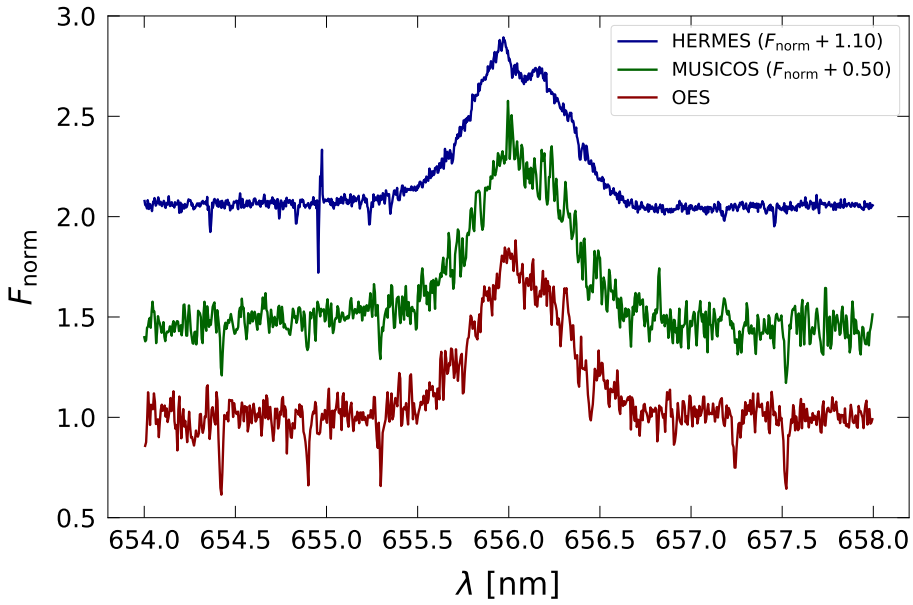

Figure A.7: Hα line observations of ASASSN-V J233336.79+615012.0 (S3 Cas), the spectral line splitting is observed, primarily for the HERMES observations (the flux is rescaled by a factor of 10).

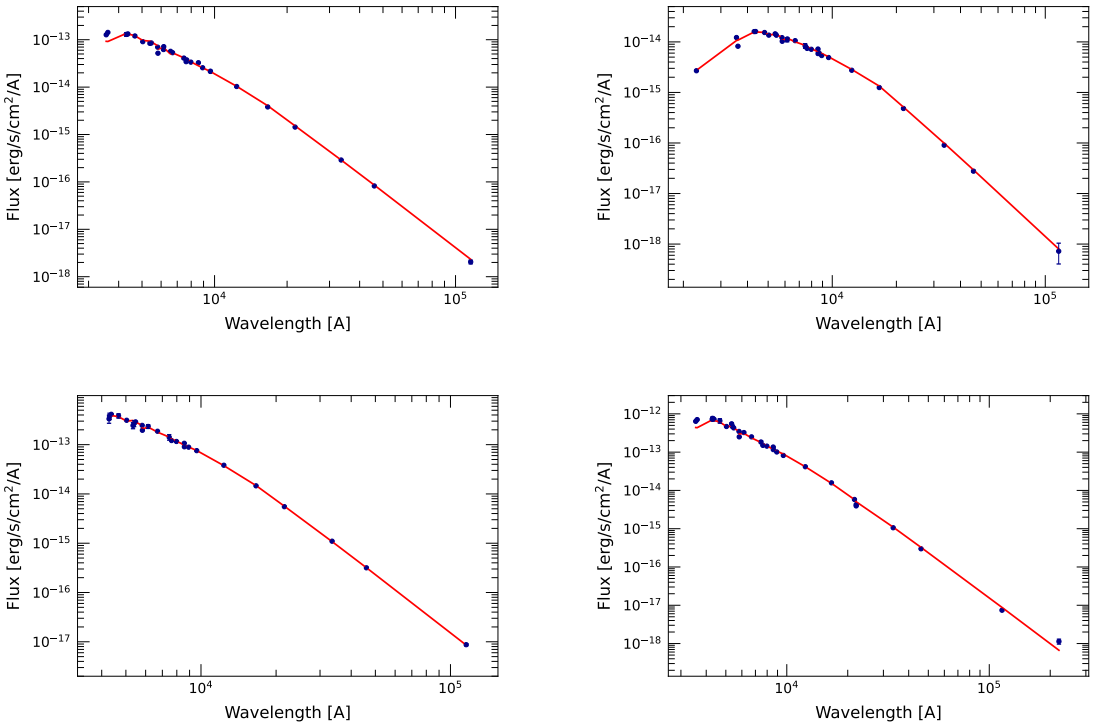

Figure A.8: The SED from VOSA, upper left: S1 Cas, upper right: S1 Cnc, bottom left: S1 Cyg, bottom right: S3 Cyg.

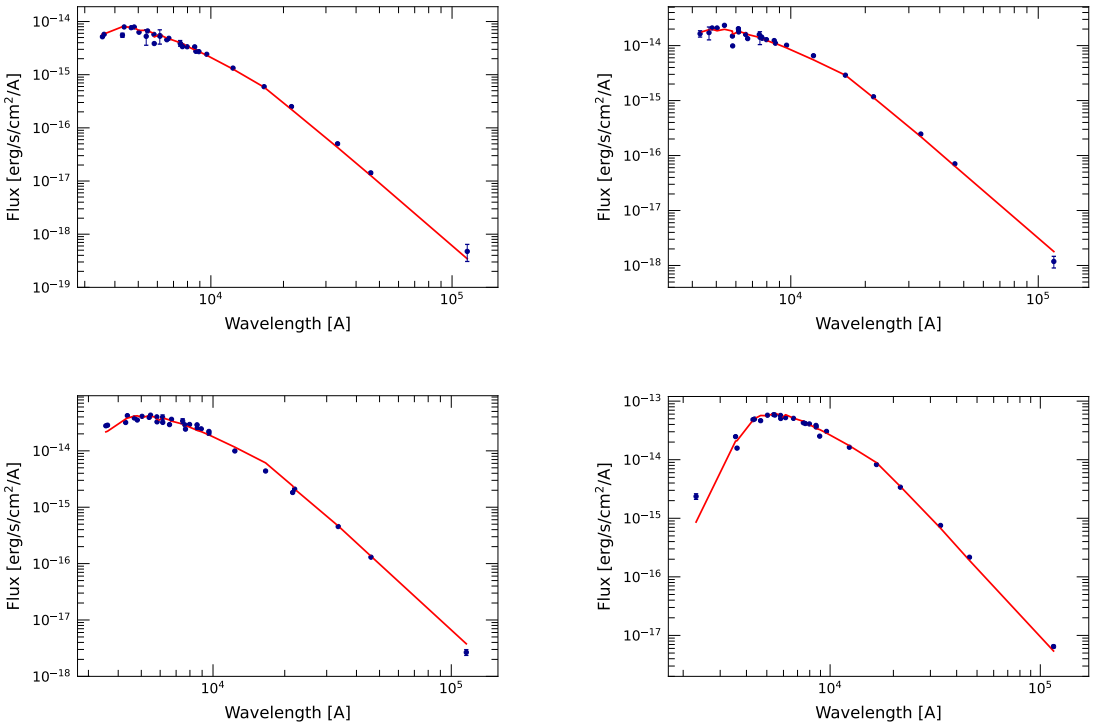

Figure A.9: The SED from VOSA, upper left: S5 Cyg, upper right: S6 Cyg, bottom left: S1 Vul, bottom right: S1 Cam.

Table A.1: The full Table 4.1, the Note column is excluded.

Name	RA [°]	DEC [°]	Loc.	Conf.	P_A [days]	P_B [days]	R	Res.	C [%]	Ref.	RUWE	T_{eff} [K]
TIC 418699570	0.486195	63.106782	Gal	0	1.6737	4.2703	2.55141	x	x	12	28.908	
WISE J000246.4+695224	0.693290	69.873550	Gal	0	0.2893554	35.6614	123.24429	x	x	9	20.545	5887.2
ASASSN-V J000432.60+632605.0	1.135830	63.434730	Gal	1	1.097909	0.994421	1.10407	x	x	9, 15		
Gaia DR3 386474080852740992	1.461502	44.447714	Gal	0	2.599973	0.114405	22.72604	x	x	13	0.986	7368.2
Gaia DR3 384686137507666944	2.702797	43.426465	Gal	0	0.561156	0.30431	1.84403	x	x	13	1.034	6525.1
ZTF J001301.21+660356.8	3.255080	66.065800	Gal	0	1.3770888	3.9170333	2.84443	x	x	15	1.399	6539.8
TIC 201310151	4.111881	-58.141759	Gal	0	5.538208	8.485997	1.53226	x	x	6	6.746	5660.2
TIC 407060024	5.393878	66.226673	Gal	0	1.8569	5.8375	3.14368	x	x	12	1.151	6899.5
Gaia DR3 431071367690614016	5.530266	63.915121	Gal	0	1.993434	2.83458	1.42196	x	x	13	1.024	4758.3
GSC 02791-00763	6.850710	42.275420	Gal	0	0.3023338	22.6636661	74.9624	x	x	15	1.351	6157.2
TIC 202664216	7.575510	53.642415	Gal	0	1.9919	4.0076	2.01195	2:1	0.60	12	1.390	4754.7
Gaia DR3 390942874067575936	8.806599	48.418240	Gal	0	0.254808	100.03476	392.58877	x	x	13	0.952	5479.3
TIC 283940788	8.851436	62.901596	Gal	0	0.876867	8.167894	9.31486	x	x	6	2.260	
TIC 156016697	9.158236	-49.132325	Gal	0	3.7418	22.1432	5.91779	x	x	10		
TIC 191283915	9.375472	42.038605	Gal	0	5.4814	10.5971	1.93328	x	x	12	0.998	5485.8
TIC 284806955	10.407757	64.480380	Gal	0	1.8872	2.4575	1.30219	x	x	12	4.359	16651.3
OGLE SMC-ECL-0629	10.795370	-73.394690	SMC	0	3.95327	244.79804	61.92292	x	x	1, 3	1.067	5748.6
TIC 191463077	11.046933	46.235557	Gal	0	4.7183	6.3892	1.35413	4:3	1.56	10	1.251	6307.4
OGLE SMC-ECL-1076	11.648210	-73.240780	SMC	0	6.40349	4.30215	1.48844	3:2	0.77	1, 3	1.158	9993.2
WISE J004636.0+563744	11.650190	56.629060	Gal	0	0.4788537	0.3555189	1.34691	4:3	1.02	15	41.836	
OGLE SMC-ECL-1086	11.666710	-73.521600	SMC	0	2.18068	3.3209	1.52287	3:2	1.52	15	1.120	7999.7
TIC 284814380	11.863676	64.818018	Gal	0	4.079268	4.986977	1.22252	x	x	6	0.908	
EPIC 220204960	12.136030	0.171804	Gal	0	13.2735	14.4158	1.08606	x	x	3	1.018	6044.9
OGLE SMC-ECL-1758	12.480100	-73.280920	SMC	0	0.92917	3.73518	4.01991	4:1	0.50	1, 3, 8	1.147	19233.0

Table A.1 (continued)

Name	RA [°]	DEC [°]	Loc.	Conf.	P_A [days]	P_B [days]	R	Res.	C [%]	Ref.	RUWE	T_{eff} [K]
OGLE SMC-ECL-2036	12.767860	-72.794130	SMC	0	1.25371	21.75096	17.34928	x	x	1, 3	0.979	17312.8
OGLE SMC-ECL-2141	12.852430	-72.671050	SMC	0	0.56554	1.2733	2.25148	x	x	1, 3	1.483	24112.7
OGLE SMC-ECL-2208	12.915410	-73.312590	SMC	0	5.72602	2.61777	2.18737	x	x	1, 3	3.087	19991.9
Gaia DR3 4272966111372504 32	13.007138	60.631402	Gal	0	1.39752	1.233086	1.13335	x	x	13	0.941	9014.7
OGLE SMC-ECL-2339	13.022313	-72.768279	SMC	0	0.72884	1.69788	2.32956	x	x	14,15	1.016	15123.2
OGLE SMC-ECL-2417	13.079155	-72.664622	SMC	0	7.53885	7.07905	1.06495	x	x	15	1.640	
OGLE SMC-ECL-2529	13.179320	-72.706830	SMC	0	1.07455	6.54472	6.09066	x	x	1, 3	0.968	19677.2
OGLE SMC-ECL-2541	13.186091	-71.833580	SMC	0	0.89364	0.87241	1.02433	x	x	15	1.140	19664.1
TIC 266017643	13.195519	9.803461	Gal	0	6	164.24	27.37333	x	x	10	0.859	5126.6
OGLE SMC-ECL-2586	13.221010	-73.186750	SMC	0	1.25169	1.51224	1.20816	x	x	1, 3	2.556	19973.7
OGLE SMC-ECL-2715	13.347010	-72.624820	SMC	0	0.76321	1.02086	1.33759	4:3	0.32	1, 3	0.957	15405.9
OGLE SMC-ECL-2896	13.512170	-72.543890	SMC	0	0.65978	1.18166	1.79099	x	x	1, 3	1.088	14340.5
OGLE SMC-ECL-3284	13.928850	-73.593630	SMC	0	1.01122	2.4348	2.40778	x	x	1, 3	1.076	12453.6
Gaia DR3 5237028901745954 56	13.938753	62.946494	Gal	0	0.620434	0.766964	1.23617	x	x	13	0.988	4659.0
V0736 And	14.378659	37.638616	Gal	0	0.3596225	0.3069135	1.17174	x	x	15		
Gaia DR3 3779678079281675 52	14.457916	46.742013	Gal	0	1.557556	0.569134	2.73671	x	x	13	1.073	5575.7
TIC 307119043	14.827524	51.221643	Gal	0	2.492484	4.742467	1.90271	x	x	6	1.349	7388.4
TIC 182294086	14.860828	-72.164975	SMC	0	19.266	96.56	5.01194	x	x	10	0.957	27013.4
CzeV1435	14.920380	61.187590	Gal	0	1.7731144	0.3908587	4.53646	x	x	9	6.572	7394.7
OGLE SMC-ECL-4418	15.464790	-72.096970	SMC	0	0.71821	3.26509	4.54615	x	x	1, 3	1.036	15361.9
OGLE SMC-ECL-4569	15.692934	-72.412363	SMC	0	1.97115	1.98509	1.00707	1:1	0.71	15	1.025	24010.4
OGLE SMC-ECL-4595	15.723242	-72.062588	SMC	0	1.58289	7.9655	5.03225	x	x	15	1.072	29744.8
OGLE SMC-ECL-4731	15.884400	-72.039780	SMC	0	0.73811	0.61356	1.203	x	x	1, 3	1.038	12805.4
OGLE SMC-ECL-4908	16.147250	-72.128080	SMC	0	2.55792	2.8518	1.11489	x	x	1, 3	0.988	15224.5
Gaia DR3 4012234108651761 92	16.230989	47.037637	Gal	0	1059.387	2.863	370.02689	x	x	10	5.205	
OGLE SMC-ECL-5015	16.335960	-72.062250	SMC	0	0.76283	1.15616	1.51562	3:2	1.04	1, 3	1.044	24039.2
TIC 196595710	16.956453	46.842117	Gal	0	1551	4.6104	336.41333	x	x	10	1.648	
TIC 52856877	17.334288	61.041245	Gal	0	5.186818	18.58641	3.58339	x	x	6	2.190	
Gaia DR3 5224452550307059 20	17.516555	60.901287	Gal	0	0.357662	0.653228	1.82638	x	x	13	0.964	5179.7
TIC 183596242	18.367299	-38.350866	Gal	0	0.4456	0.475	1.06598	x	x	10		
Gaia DR3 4134465442008808 96	18.801672	57.606248	Gal	0	0.951178	7.547427	7.93482	x	x	13	0.978	6136.9
OGLE SMC-ECL-5925	19.320340	-73.166989	SMC	0	2.90892	8.8216	3.0326	3:1	1.09	15		
Gaia DR3 4139303593703843 84	20.433859	58.575703	Gal	0	1.745764	74.595949	42.72969	x	x	13	0.984	5180.3
OGLE SMC-ECL-6093	21.103715	-73.223717	SMC	1	0.90193	2.03034	2.25111	x	x	14,15	1.026	17815.4
OGLE SMC-ECL-8061	22.239010	-73.277896	SMC	0	1.26659	1.77833	1.40403	x	x	15	1.028	16888.5
OGLE SMC-ECL-8098	22.845297	-73.388140	SMC	0	1.23385	1.06091	1.16301	x	x	15	0.920	16181.0
WISE J013310.8+613507	23.295420	61.585290	Gal	0	2.5670368	2.7303226	1.06361	x	x	9		
Gaia DR3 3994647076562549 76	23.839866	48.216903	Gal	0	6.934429	8.655612	1.24821	x	x	13	1.328	6346.6
Gaia DR3 5115721845431651 84	24.594285	62.368258	Gal	0	1.111992	0.893415	1.24465	x	x	13	1.373	
TIC 26766810	25.326565	25.745713	Gal	0	4.4344	1.4353	3.08953	x	x	10		
Gaia DR3 4053437619705363 20	25.469780	48.453185	Gal	0	3.214925	0.475366	6.76305	x	x	13	1.125	5518.7
Gaia DR3 5058543761787060 48	26.105725	57.363963	Gal	0	0.395542	0.613647	1.55141	x	x	13	0.989	4789.9
Gaia DR3 5063820086203083 52	26.998330	58.484187	Gal	0	0.469946	1.607418	3.42043	x	x	13	1.317	6823.7
Gaia DR3 4076103021128529 92	27.345582	51.957608	Gal	0	0.27613	4.742124	17.17352	x	x	13	0.957	5661.7
Gaia DR3 5111202954794627 072	27.478311	61.054208	Gal	0	2.522958	2.118876	1.19071	x	x	13	2.069	8822.9
Gaia DR3 4078496176902881 28	27.619643	53.266914	Gal	0	1.388514	1.842243	1.32677	4:3	0.49	13	1.154	6253.3
Gaia DR3 3304424872641419 52	29.369827	36.938288	Gal	0	2.165996	3.201325	1.47799	3:2	1.47	13	1.008	5132.5
ASASSN-V J020306.68+624315.4	30.777830	62.720950	Gal	0	3.2867	36.7607	11.18468	x	x	9		
TIC 232087348	30.996867	-70.737328	Gal	0	2.614296	9.648651	3.69073	x	x	6	1.070	6231.4
TIC 285681367	31.557025	64.580199	Gal	0	2.366008	3.970279	1.67805	5:3	0.68	6	3.211	15064.8
CY Tri	31.667300	33.724600	Gal	1	0.33343	0.5373	1.61143	x	x	3		
TIC 292318612	31.769613	42.338435	Gal	0	1.665448	1.733857	1.04108	x	x	6	1.222	4092.3
UCAC4 592-005224	32.099648	28.310789	Gal	0	208.3	87.754	2.37368	x	x	10		
TIC 285910268	32.189323	65.037423	Gal	0	2.5132	122	48.54369	x	x	10	1.874	
Gaia DR3 4570459598124115 20	32.660282	56.361212	Gal	0	2.907525	1.766785	1.64566	5:3	1.26	13	1.056	4761.0
ZTF J022105.82+595516.9	35.274250	59.921360	Gal	0	1.111972	2.36685	2.12852	x	x	9	2.041	9469.8
Gaia DR3 5143358413791343 36	35.979435	63.411351	Gal	0	1.718536	1.220503	1.40806	x	x	13	1.677	5564.5

Table A.1 (continued)

Name	RA [°]	DEC [°]	Loc.	Conf.	P_A [days]	P_B [days]	R	Res.	C [%]	Ref.	RUWE	T_{eff} [K]
Gaia DR3 514291963992396928	36.881203	63.214977	Gal	0	3.006382	0.212537	14.14522	x	x	13	0.999	9636.5
Gaia DR3 513987498047116544	38.031578	62.343023	Gal	0	1.019208	0.948252	1.07483	x	x	13	0.970	5399.5
ASASSN-V J023220.92+620149.3	38.087160	62.030370	Gal	0	0.3009191	7.927991	26.34592	x	x	15	48.575	
Gaia DR3 465028723463664384	38.292867	59.484742	Gal	0	3.460204	0.92533	3.73943	x	x	13	1.010	10007.6
Gaia DR3 465274395594682240	39.195205	60.984813	Gal	0	3.887904	1.896361	2.05019	x	x	13	1.432	5142.3
TIC 22874790	39.252181	24.647214	Gal	0	1.1095	335.1	302.02794	x	x	10		
TIC 50198590	40.093100	64.083217	Gal	0	2.7157	3.164	1.16508	x	x	12	23.388	
ASASSN-V J024221.82+625403.6	40.590920	62.901010	Gal	0	5.7615	11.5503	2.00474	2:1	0.24	9	1.123	22323.6
Gaia DR3 454774403147619840	41.812000	56.760000	Gal	1	0.352537	0.309863	1.13772	x	x	5	0.889	5805.7
Gaia DR3 461012963401936256	42.417307	58.265701	Gal	0	1.060832	10.593118	9.98567	x	x	13	1.069	18570.4
Gaia DR3 20743528104252928	42.468259	8.939651	Gal	0	1.706	0.3799	4.49066	x	x	10	1.624	5930.5
TIC 328181241	43.153958	3.347882	Gal	0	22.625534	26.418506	1.16764	x	x	6	4.675	5457.0
V1361 Cas	43.252000	57.542720	Gal	0	2.2367206	1.225857	1.82462	x	x	9	1.133	
TIC 207137124	43.702325	-56.810784	Gal	0	0.995134	32.155225	32.31246	x	x	6	3.918	5379.0
Gaia DR3 461553472144934656	44.301404	59.454303	Gal	0	0.270063	1.385304	5.12956	x	x	13	1.048	
TIC 286470992	45.330717	60.572294	Gal	0	3.110381	4.128543	1.32734	4:3	0.45	6	1.176	25709.8
ZTF J030300.04+551243.7	45.750210	55.212160	Gal	0	7.7787461	1.012515	7.6826	x	x	9	0.981	
ASASSN-V J030536.60+685727.5	46.402500	68.957640	Gal	0	0.602218	2.166085	3.59685	x	x	9	5.197	5968.4
ASASSN-V J030750.25+540358.2	46.959380	54.066160	Gal	0	1.525	2.4076967	1.57882	x	x	9	6.956	7315.2
TIC 384735219	48.409405	55.623714	Gal	0	8.3658	8.9405	1.0687	x	x	12	1.088	9315.4
Gaia DR3 5166225811703486464	49.178341	-10.308834	Gal	0	0.275808	2.432133	8.81821	x	x	13	1.036	5428.8
ZTF J032329.99+500030.20	50.874960	50.008390	Gal	0	19.0003	1.0102	18.80845	x	x	9	6.861	10450.9
TIC 31928452	53.969191	-66.936899	Gal	0	2.8823	7.829944	2.71656	x	x	6	30.842	5287.1
TIC 311092804	54.197043	0.587762	Gal	0	2.8377	1152	405.96258	x	x	10		
Gaia DR3 244408588611828096	54.711333	44.047482	Gal	0	0.178865	0.243028	1.35872	4:3	1.90	13	3.524	4940.7
TIC 392229331	54.767927	61.064204	Gal	0	1.822309	2.255905	1.23794	x	x	6	0.992	
TIC 38542448	56.265606	-6.779597	Gal	0	2.3077	7.0988	3.07614	x	x	12	1.397	6011.1
TIC 440681316	56.851724	23.914674	Gal	0	7.345	767.04	104.43022	x	x	10	1.001	10295.4
WISE J034823.6-814029	57.098500	-81.674790	Gal	0	0.3533253	6.0790202	17.20517	x	x	15	27.029	
Gaia DR3 445534966419218560	57.458651	56.117922	Gal	0	1.292364	1.088451	1.18734	x	x	13	1.026	8564.2
ZTF J035635.15+524229.8	59.146455	52.708268	Gal	0	0.2745782	0.256279	1.0714	x	x	15	1.084	
V1095 Per	59.271930	32.376531	Gal	0	0.3115635	0.3094544	1.00682	1:1	0.68	15		
TIC 265684107	59.446276	52.905947	Gal	0	2.6259	9.9669	3.79561	x	x	12	1.033	9007.9
Gaia DR3 469545650369412864	59.624908	56.534336	Gal	0	0.224785	1.551227	6.90094	x	x	13	1.018	6378.2
TIC 266395331	60.882924	48.564234	Gal	0	3.049	5.2396	1.71847	x	x	12	2.099	7946.7
TIC 266771301	61.462323	52.245283	Gal	0	3.479611	3.833457	1.10169	x	x	6	32.443	7007.2
CzeV1254	62.781040	56.375830	Gal	0	0.7154189	0.3625926	1.97307	2:1	1.35	9	2.542	5731.3
TIC 168789840	63.520209	-31.922876	Gal	1	1.305883	1.570013	1.20226	x	x	6	10.450	
TIC 56627600	63.699957	27.876176	Gal	0	12.9418	4.0676	3.18168	x	x	10		
V482 Per	63.922215	47.422170	Gal	0	2.4467526	6.001749	2.45294	5:2	1.88	3	1.430	
ZTF J041640.53+501904.4	64.168890	50.317900	Gal	0	1.1227787	1.4028162	1.24941	x	x	15	1.162	9342.0
TIC 454140642	64.773473	0.900042	Gal	1	10.3928	13.6239	1.3109	4:3	1.68	6	1.299	6131.6
TIC 470397849	65.422339	51.995456	Gal	0	2.6516	4.8728	1.83768	x	x	12		
TIC 139650665	65.602471	-18.916383	Gal	0	2.091887	10.631474	5.08224	x	x	6	5.750	5376.2
TIC 58539786	65.834021	29.142749	Gal	0	2.4611	29.2378	11.87997	x	x	12	1.094	6032.6
ASASSN-V J042738.92+463240.1	66.912200	46.544460	Gal	0	0.234402	0.265333	1.13196	x	x	15		
Gaia DR3 228205115816360832	67.213782	42.115243	Gal	0	1.125492	2.201828	1.95632	x	x	13	1.061	9734.7
Gaia DR3 258090121033397248	67.217417	48.572915	Gal	0	5.48996	25.643685	4.67101	x	x	13	1.414	9267.4
Gaia DR3 257683439171736576	68.629624	48.698441	Gal	0	0.81849	4.499209	5.49696	x	x	13	1.061	11184.3
TIC 178953404	69.096433	-25.587820	Gal	0	3.182144	28.005157	8.80072	x	x	6	3.992	5613.0
TIC 9493888	69.510209	55.731524	Gal	1	2.098992	2.706156	1.28926	x	x	6	2.070	5271.3
TIC 274481742	69.551889	50.057788	Gal	0	1.011	1.7686	1.74936	x	x	12	44.405	
ASASSN-V J043825.68-445216.2	69.607000	-44.871160	Gal	0	0.3658042	1.2458661	3.40583	x	x	15	1.635	6207.2
Gaia DR3 158123726424621824	69.925315	29.134575	Gal	0	1.58676	13.783777	8.68674	x	x	13	0.997	
ASASSN-V J044413.26+220945.5	71.055240	22.162640	Gal	0	2.766615	16.1053924	5.82133	x	x	15	0.984	11075.3
TIC 459959916	71.489665	4.829619	Gal	0	1.054483	8.768239	8.3152	x	x	6	1.634	6298.7
OGLE LMC-ECL-00728	71.555000	-69.064220	LMC	0	1.7705911	1.0937835	1.61878	x	x	3	1.014	

Table A.1 (continued)

Name	RA [°]	DEC [°]	Loc.	Conf.	P_A [days]	P_B [days]	R	Res.	C [%]	Ref.	RUWE	T_{eff} [K]
TIC 391620600	71.640389	44.753662	Gal	0	3.381354	6.47346	1.91446	x	x	6	1.594	5858.9
OGLE LMC-ECL-01050	72.165380	-68.458560	LMC	0	1.6707882	26.4766	15.84677	x	x	3	1.023	18407.2
Gaia DR3 2609451060523432 96	72.308262	52.265466	Gal	0	3.070683	37.120622	12.08872	x	x	13	1.010	9676.4
WISE J045225.6+453204	73.106760	45.534590	Gal	0	1.1678424	0.7159533	1.63117	x	x	15	10.857	
OGLE LMC-ECL-02156	73.281190	-70.195470	LMC	1	4.517236	1.2614425	3.58101	x	x	3	1.025	16178.6
OGLE LMC-ECL-02310	73.408250	-69.228480	LMC	1	1.0463484	16.06224	15.35076	x	x	3	0.944	
OGLE LMC-ECL-02903	73.803430	-68.873490	LMC	1	2.0799677	6.5669915	3.15726	x	x	3	0.967	21329.4
TIC 120911334	73.862103	38.312956	Gal	0	2.0005	2.4536	1.22649	x	x	12		
OGLE LMC-ECL-03611	74.251610	-69.511930	LMC	0	2.119573	1.39688	1.51736	3:2	1.16	3	0.872	16213.3
OGLE LMC-ECL-03906	74.415260	-69.131370	LMC	0	9.9285502	10.63576	1.07123	x	x	3	0.964	15875.7
OGLE LMC-ECL-04236	74.619230	-70.236480	LMC	1	2.4074806	2.4602955	1.02194	x	x	3	6.758	14009.8
TIC 43472931	74.681967	-10.755805	Gal	0	1.3613	1.4851	1.09094	x	x	12	1.457	
NSVS 2176810	74.735670	67.782120	Gal	0	3.6620862	0.4536163	8.07309	x	x	9	3.743	10623.8
TIC 244279814	74.762502	-2.111039	Gal	0	8.4245	9.1205	1.08262	x	x	12	1.865	5877.7
OGLE LMC-ECL-04465	74.791580	-68.647030	LMC	0	1.4105797	143.735	101.89782	x	x	3	1.056	9916.6
OGLE LMC-ECL-04623	74.910300	-69.423010	LMC	1	1.6422711	10.646813	6.48298	x	x	3	1.306	19679.0
TIC 121511673	74.971948	40.402072	Gal	0	2.159	3.7872	1.75415	x	x	12	0.925	11890.6
TIC 146435300	75.327853	-23.772725	Gal	0	3.1842	7.7056	2.41995	x	x	12	4.213	
TIC 13021681	75.534801	-24.061641	Gal	0	0.5406	11.0651	20.46818	x	x	12	2.484	4172.5
OGLE LMC-ECL-06179	75.905630	-68.939640	LMC	0	1.5127562	1.22769	1.2322	x	x	3	0.993	8281.0
OGLE LMC-ECL-06331	75.990480	-70.272930	LMC	0	1.033603	1.212532	1.17311	x	x	3	1.221	22358.6
Gaia DR3 2022016013928 51072	76.053644	42.807356	Gal	0	0.624014	14.132366	22.64751	x	x	13	1.454	
OGLE LMC-ECL-06538	76.119120	-68.627390	LMC	0	0.7434252	0.590837	1.25826	x	x	3	0.973	12431.4
OGLE LMC-ECL-06595	76.148870	-69.592190	LMC	0	1.1313483	1.188998	1.05096	x	x	3	0.966	15383.4
OGLE LMC-ECL-07329	76.536880	-67.887700	LMC	0	1.7172776	206.43	120.20771	x	x	3	1.126	5641.2
OGLE LMC-ECL-07485	76.626420	-68.580920	LMC	0	8.0282937	1.4757278	5.44023	x	x	3		
OGLE LMC-ECL-08902	77.462080	-68.875750	LMC	0	2.3378256	25.663	10.97729	x	x	3	1.105	
OGLE LMC-ECL-08914	77.468380	-69.395890	LMC	0	2.4548301	3.9438804	1.60658	x	x	3	1.078	17371.5
OGLE LMC-ECL-08957	77.493310	-70.471850	LMC	0	1.3388693	135.515	101.216	x	x	3	1.764	19658.2
OGLE LMC-ECL-09257	77.668320	-67.161210	LMC	0	0.9324693	3.59443	3.85474	x	x	3, 15	0.952	16208.3
OGLE LMC-ECL-09464	77.797920	-67.164150	LMC	0	1.2895788	3.69721	2.86699	x	x	3		
Gaia DR3 2627798817229 35424	77.972018	51.672042	Gal	0	1.637614	2.266959	1.38431	x	x	13	1.121	
ASAS J051200-0205.3	77.998500	-2.088000	Gal	0	0.3130401	0.4846737	1.54828	x	x	15	1.078	5726.8
HD 34377	78.284645	-59.982988	Gal	0	1430.3	7.943	180.0705	x	x	10	15.015	5593.9
V0417 Aur	78.382420	35.653060	Gal	0	1.86553	0.4182123	4.46072	x	x	9	0.996	10326.1
OGLE LMC-ECL-10429	78.429360	-69.310260	LMC	0	3.5779357	5.3666155	1.49992	3:2	0.01	3	0.887	23997.0
OGLE LMC-ECL-11224	78.913290	-70.096530	LMC	0	1.9450169	3.2025101	1.64652	5:3	1.21	3	0.980	19717.1
OGLE LMC-ECL-12807	79.891620	-68.273420	LMC	0	1.7252223	4.85997	2.81701	x	x	3	2.894	
ZTF J051938.88+540827.7	79.912014	54.141055	Gal	0	0.770718	0.5946131	1.29617	x	x	15	1.010	5823.3
OGLE LMC-ECL-12857	79.930080	-68.646880	LMC	0	2.0826965	1.825429	1.14094	x	x	3	3.726	7999.9
OGLE LMC-ECL-13221	80.161290	-68.873970	LMC	0	1.416421	0.7325898	1.93344	x	x	3	1.005	16181.7
CzeV1493	80.338540	34.634760	Gal	0	1.9126763	0.2712981	7.05009	x	x	9	0.995	6251.9
Gaia DR3 1844682311865163 52	80.461508	37.370170	Gal	0	2.345842	6.86879	2.92807	x	x	13	1.200	9365.0
OGLE LMC-ECL-13737	80.478970	-67.905750	LMC	0	1.2743786	6.06765	4.76126	x	x	3	1.238	19984.0
TIC 47279366	80.673720	16.905248	Gal	0	3.4075	42.1844	12.37987	x	x	12		
Gaia DR3 1844975701077352 96	80.679986	37.664808	Gal	0	2.3771	2.839768	1.19464	x	x	13	1.046	9894.7
OGLE LMC-ECL-14370	80.814500	-69.909360	LMC	0	1.0593788	1.903334	1.79665	x	x	3	1.026	12955.8
OGLE LMC-ECL-14375	80.817830	-70.168620	LMC	0	1.0711547	73.5596	68.67318	x	x	3	1.444	6112.8
TIC 24700485	81.204640	-7.592358	Gal	0	0.7398	10.6723	14.42593	x	x	12	4.936	5661.9
OGLE LMC-ECL-15301	81.380380	-69.437080	LMC	0	0.7373025	4.89865	6.64402	x	x	3	1.224	18193.4
OGLE LMC-ECL-15607	81.562750	-69.082690	LMC	1	1.0479561	0.4341706	2.4137	x	x	3	1.365	15072.7
OGLE LMC-ECL-15674	81.595710	-68.824190	LMC	0	1.433233	1.3875757	1.0329	x	x	3	1.190	19748.2
OGLE LMC-ECL-15742	81.638000	-69.153840	LMC	0	0.8584714	2.1258373	2.47631	5:2	0.95	3	0.980	16105.2
TIC 285853156	81.892808	28.552816	Gal	0	1.7661	10.0259	5.67686	x	x	12	3.181	5674.5
OGLE LMC-ECL-16532	82.028010	-69.019910	LMC	1	0.74377	77.91193	104.75272	x	x	3	3.416	24513.7
OGLE LMC-ECL-16539	82.036430	-70.353230	LMC	0	12.1675847	4.539704	2.68026	x	x	3	1.075	13787.4
OGLE LMC-ECL-16549	82.039210	-69.757940	LMC	0	164.78964	0.8180397	201.44455	x	x	3	1.239	7007.1

Table A.1 (continued)

Name	RA [°]	DEC [°]	Loc.	Conf.	P_A [days]	P_B [days]	R	Res.	C [%]	Ref.	RUWE	T_{eff} [K]
OGLE LMC-ECL-16831	82.169690	-68.693560	LMC	0	2.1848709	918.83	420.54201	x	x	3	1.008	19699.9
OGLE LMC-ECL-16988	82.251630	-68.909670	LMC	0	9.818468	1.4832487	6.61957	x	x	3		
OGLE LMC-ECL-17182	82.345400	-68.747290	LMC	1	2.237257	2.4707908	1.10438	x	x	3	1.141	22690.3
TIC 3311888	82.427702	35.375027	Gal	0	4.002	20.46	5.11244	x	x	10	2.280	29993.5
OGLE LMC-ECL-17347	82.436460	-68.480330	LMC	0	1.9224015	445.85	231.92346	x	x	3	8.336	
OGLE LMC-ECL-17637	82.583370	-69.772440	LMC	0	1.5995666	0.805298	1.9863	2:1	0.68	3	1.054	
OGLE LMC-ECL-17913	82.723260	-71.132920	LMC	1	1.318497	2.2143375	1.67944	5:3	0.77	3	0.980	25984.3
Gaia DR3 2079432854757612 80	82.738969	44.803406	Gal	0	52.829036	1.184305	44.60763	x	x	13	0.905	
OGLE LMC-ECL-17996	82.766860	-69.158070	LMC	0	1.5497505	1.7005157	1.09728	x	x	3	3.463	16186.2
TIC 302824830	83.058922	17.058138	Gal	0	715.03	152.39	4.69211	x	x	10	1.180	
OGLE LMC-ECL-18618	83.083830	-69.001730	LMC	0	3.6435437	1.6271319	2.23924	x	x	3	1.047	16202.9
OGLE LMC-ECL-18860	83.235210	-67.922530	LMC	0	2.8344662	10.64775	3.75653	x	x	3	1.010	15039.0
OGLE LMC-ECL-18966	83.289720	-69.455500	LMC	0	2.8618781	1.2371204	2.31334	x	x	3	1.125	18281.2
CzeV1759	83.537330	35.297250	Gal	0	0.9456281	3.4288	3.62595	x	x	9		
OGLE LMC-ECL-19771	83.764700	-68.817090	LMC	0	2.2344535	13.05004	5.84037	x	x	3	5.228	
OGLE LMC-ECL-19852	83.807500	-69.037830	LMC	0	2.0754453	1.8847946	1.10115	x	x	3	1.128	
OGLE LMC-ECL-19896	83.833040	-69.345420	LMC	0	1.4449138	1.3599	1.06251	x	x	3	1.065	17702.2
Gaia DR3 3448886540015107584	83.858615	33.004921	Gal	0	2.989964	0.52143	5.73416	x	x	13	0.972	9437.4
OGLE LMC-ECL-19942	83.863410	-69.687130	LMC	0	4.8175154	1.8836875	2.55749	x	x	3	1.032	24378.0
OGLE LMC-ECL-20145	83.967600	-69.378880	LMC	0	6.1196213	3.7219806	1.64418	5:3	1.35	3	1.032	19993.1
OGLE LMC-ECL-20147	83.970280	-68.913620	LMC	0	2.7578408	2.6993979	1.02165	x	x	3	14.688	27313.4
OGLE LMC-ECL-20382	84.084130	-69.208920	LMC	0	1.8146366	2.46648	1.35921	4:3	1.94	3	6.757	
SSS J053628.7-524202	84.119840	-52.700480	Gal	0	0.3442385	0.2679614	1.28466	x	x	15	5.984	6044.7
OGLE LMC-ECL-20901	84.370730	-69.392880	LMC	0	1.554462	6.602784	4.24763	x	x	3	2.765	26859.5
OGLE LMC-ECL-20903	84.371710	-69.144890	LMC	0	1.6831082	4.2565168	2.52896	5:2	1.16	3		
OGLE LMC-ECL-20932	84.388680	-69.406940	LMC	1	3.8304229	1.4679165	2.60943	x	x	3	0.966	24483.1
TIC 74919381	84.420643	24.878532	Gal	0	1.7527	4.5012	2.56815	x	x	12	3.288	7880.0
OGLE LMC-ECL-21094	84.477460	-69.679810	LMC	1	3.0101772	1.0141844	2.96808	3:1	1.06	3	3.276	19974.3
OGLE LMC-ECL-21456	84.684000	-69.095060	LMC	0	1.0817076	2.6574721	2.45674	5:2	1.73	3	10.105	9998.5
ASASSN-V J053844.30+304320.1	84.684600	30.722250	Gal	0	4.0916767	25.0218297	6.1153	x	x	15	1.047	6320.8
OGLE LMC-ECL-21569	84.743300	-69.076450	LMC	1	1.9815435	2.9328514	1.48008	3:2	1.33	3	0.889	
OGLE LMC-ECL-21603	84.770390	-69.493830	LMC	0	1.7811269	7.11817	3.99644	4:1	0.09	3	0.960	22541.2
OGLE LMC-ECL-21991	85.024580	-69.751390	LMC	0	10.32812	18.2655	1.76852	x	x	3	1.082	
OGLE LMC-ECL-21994	85.026420	-70.112190	LMC	1	7.4112146	6.0404463	1.22693	x	x	3	1.295	
OGLE LMC-ECL-22148	85.123960	-70.083310	LMC	0	1.8267531	2.7147783	1.48612	3:2	0.93	3	1.005	9967.0
OGLE LMC-ECL-22159	85.130200	-69.192490	LMC	0	2.9884068	3.4084378	1.14055	x	x	3	1.042	6798.2
OGLE LMC-ECL-22281	85.206460	-69.218260	LMC	0	2.8675292	1.503588	1.90712	x	x	3	1.068	19779.6
OGLE LMC-ECL-22434	85.299310	-70.866760	LMC	0	1.5813927	1.4755317	1.07174	x	x	3	5.603	7599.3
OGLE LMC-ECL-22891	85.565690	-69.081960	LMC	0	0.8755663	0.8546343	1.02449	x	x	3	7.835	
OGLE LMC-ECL-23000	85.654350	-69.070080	LMC	1	1.8998605	1.2455112	1.52537	3:2	1.69	3	3.296	24457.8
OGLE LMC-ECL-23469	86.005170	-69.282250	LMC	0	1.3995586	1.4808157	1.05806	x	x	3	1.439	7116.2
OGLE LMC-ECL-23823	86.365660	-69.772910	LMC	0	1.184466	204.424	172.58748	x	x	3		
Gaia DR3 3443402279093860352	86.591414	28.923839	Gal	0	0.53534	0.541528	1.01156	1:1	1.16	13	1.062	4299.5
TIC 93373156	86.750396	-20.903570	Gal	0	5.2804	8.5562	1.62037	x	x	12	0.969	5775.5
TIC 200094011	86.782967	0.298943	Gal	0	2.135567	2.437293	1.14129	x	x	6	4.057	
TIC 239761283	86.850133	30.756252	Gal	0	0.75	10	13.33333	x	x	10	0.995	
CzeV343	87.100050	30.950990	Gal	0	1.209364	0.806869	1.49884	3:2	0.08	3	1.617	10793.3
ASASSN-V J054904.04+083516.2	87.266830	8.587820	Gal	0	3.627496	1.4772221	2.45562	5:2	1.78	9	1.304	
NSVS 2209083	87.276130	60.177270	Gal	0	2.6801419	0.5517664	4.85739	x	x	9	21.054	
TIC 239872462	87.514177	34.417596	Gal	0	0.935825	2.961924	3.16504	x	x	6	1.301	15516.3
Gaia DR3 3400120484904001536	87.528200	21.330875	Gal	0	3.572446	1.759766	2.03007	2:1	1.50	13	0.954	
Gaia DR3 3335190578070549504	88.008860	8.805691	Gal	0	0.36877	1.890454	5.12638	x	x	13	1.050	
TIC 91600053	88.366603	16.891741	Gal	0	11.9077	35.0205	2.941	3:1	1.97	12	0.966	6980.4
V1793 Ori	88.512460	1.672720	Gal	0	3.5524	3.3475421	1.0612	x	x	9	7.727	
TIC 78333248	88.730875	26.354792	Gal	0	7.552	11.3808	1.50699	3:2	0.47	12	0.986	
KELT KC04C006546	89.356580	25.749730	Gal	0	2.6600008	0.8761122	3.03614	3:1	1.20	15	2.246	
TIC 309262405	89.424588	34.988493	Gal	0	4.198947	6.908918	1.64539	5:3	1.28	6	1.601	10758.2

Table A.1 (continued)

Name	RA [°]	DEC [°]	Loc.	Conf.	P_A [days]	P_B [days]	R	Res.	C [%]	Ref.	RUWE	T_{eff} [K]
TIC 219152539	89.956876	-48.239691	Gal	0	963	1.328	725.1506	x	x	10	6.166	
OGLE LMC-ECL-25635	90.321930	-69.051420	LMC	0	5.225498	610.933	116.91383	x	x	3	1.002	15478.3
TIC 140601757	90.595820	9.647273	Gal	0	4.4476	4.7835	1.07552	x	x	10		
TIC 238558210	91.091266	20.534238	Gal	0	0.9724	5.3377	5.4892	x	x	12	1.202	11063.6
TIC 80893927	91.577014	28.671038	Gal	0	1.7458	3.8647	2.21371	x	x	12	21.016	
CzeV1640	91.826630	28.123640	Gal	0	0.554234	0.842581	1.52026	3:2	1.35	3		
TIC 336882813	92.390615	14.628986	Gal	0	2.625028	6.422862	2.44678	x	x	6	11.642	6003.4
TIC 153406662	93.228955	9.035800	Gal	0	2.5213	8.8631	3.51529	7:2	0.44	12	1.393	15051.8
WISEJ061413.8-070754	93.557710	-7.131710	Gal	0	1.1867892	35.6518913	30.04063	x	x	9	3.184	7975.2
ASASSN-V J061439.02+220138.8	93.662560	22.027450	Gal	0	2.0268708	32.0472538	15.8112	x	x	15	13.299	10159.7
TIC 429901945	94.729255	20.598720	Gal	0	1.5166	4.4103	2.90802	x	x	12	9.994	15633.9
EPIC 202088178	95.779241	18.470816	Gal	0	2.3717092	0.9895017	2.39687	x	x	15	1.001	6230.4
ZTF J062316.07+160529.4	95.817000	16.091510	Gal	0	0.6360014	7.5366804	11.8501	x	x	9	4.566	6407.6
TIC 438226195	96.502751	15.216367	Gal	0	5.442645	11.697926	2.14931	x	x	6	15.595	
TIC 60584909	96.619265	-22.184408	Gal	0	5.9507	25.9813	4.36609	x	x	12	0.995	5986.3
Gaia DR3 3376140681762631168	96.842245	21.721270	Gal	0	0.39992	0.842531	2.10675	x	x	13	1.183	
TIC 306903715	98.004532	16.585394	Gal	0	4.86821	6.516885	1.33866	4:3	0.40	6		
TIC 54577663	98.161129	21.766208	Gal	0	3.4644	10.327	2.98089	3:1	0.64	12	1.343	9535.6
SSS J063336.1-334922	98.400180	-33.823180	Gal	0	0.2558717	0.1917377	1.33449	4:3	0.09	15	1.034	4792.9
Gaia DR2 3382211880029670272	98.432736	22.305026	Gal	0	0.468255	1.94163	4.14652	x	x	15	1.102	
Gaia DR3 3325963098535865856	98.587002	7.745466	Gal	0	0.584642	0.6136	1.04953	x	x	13	6.998	6139.4
TIC 53158069	99.698191	-1.050109	Gal	0	9.1129	14.4956	1.59067	x	x	12	1.124	8652.1
TIC 375036945	99.807090	-65.760744	Gal	0	1.5898	1.76	1.10706	x	x	12	1.037	3674.2
ASASSN-V J064048.28-224659.0	100.201170	-22.783050	Gal	0	2.8505583	6.6412165	2.3298	x	x	9	0.972	
CoRoT 223993566	100.454860	10.122060	Gal	0	1.18067	0.934856	1.26294	x	x	3	10.028	11086.0
ZTF J064411.43+105836.7	101.047625	10.976896	Gal	0	0.2568214	0.793966	3.09151	x	x	15	17.405	
ASASSN-V J064539.57+143349.6	101.414880	14.563760	Gal	0	2.646248	4.8951198	1.84983	x	x	9	3.228	7626.7
Gaia DR3 3113400013097881600	101.872246	-0.444575	Gal	0	0.86539	2.182992	2.52255	5:2	0.90	13	2.203	10478.4
TIC 36439758	102.235133	-0.464714	Gal	0	1.4156	8.2137	5.80227	x	x	12	1.005	7717.2
CoRoT 110829335	102.270254	-5.858710	Gal	0	8.9304	50.3075	5.63329	x	x	3	1.690	9675.8
BEST-II lra2a_00811	102.652920	-3.691750	Gal	0	1.8162916	0.3981756	4.56153	x	x	9	2.209	6887.1
TIC 78568780	102.848953	-22.167204	Gal	0	2.88838	23.903	8.27557	x	x	6	13.041	
Gaia DR3 3112366227355971584	103.057739	-1.125556	Gal	0	0.948312	0.632336	1.4997	3:2	0.02	13	1.817	8401.1
CRTS J065302.9+381408	103.262700	38.235700	Gal	1	1.8664	1.24652	1.49729	3:2	0.18	3	1.052	6586.8
TIC 79140936	103.846452	-22.623862	Gal	0	3.54389	30.913745	8.72311	x	x	6	1.662	9427.2
ZTFJ065616.65+154832.5	104.069420	15.809040	Gal	0	1.2513289	1.0600426	1.18045	x	x	9	1.197	7973.2
TIC 237816747	104.490886	2.292214	Gal	0	6.7663	4.4813	1.5099	3:2	0.66	10	1.039	
TIC 32945664	104.625374	-0.478507	Gal	0	1.0146	3.131	3.08595	x	x	12	1.196	
NSVS 7197656	105.184608	32.479577	Gal	0	0.2639961	3.1441296	11.90976	x	x	15	1.750	5024.2
Gaia DR3 2935716391431248384	105.242128	-16.522209	Gal	0	0.424388	7.412474	17.46627	x	x	13	1.010	10609.8
ASASSN-V J070251.10+050147.6	105.712920	5.029900	Gal	0	3.6133	1.4197927	2.54495	5:2	1.80	9	1.620	4841.9
TIC 125583594	105.847680	-6.869937	Gal	0	3.0367	5.5975	1.84328	x	x	12	3.342	17068.1
TIC 261940513	106.031230	6.342095	Gal	0	2.8909	3.402	1.1768	x	x	12	1.089	8995.6
TIC 80914862	106.116464	-20.563763	Gal	0	1.967319	18.666628	9.48836	x	x	6	4.621	7479.1
TIC 97356407	106.502031	-30.655710	Gal	0	1.533535	8.098533	5.28096	x	x	6	1.546	15508.9
GDS J0706058-030026	106.524500	-3.007380	Gal	0	1.4228503	1.737956	1.22146	x	x	9	8.670	13812.8
ASASSN-V J070838.27-171952.9	107.159500	-17.331370	Gal	0	4.3005671	3.7672138	1.14158	x	x	9	1.103	9389.7
ASASSN-V J071131.63-153341.3	107.881790	-15.561460	Gal	0	2.611144	1.7289645	1.51024	3:2	0.68	9	1.622	9488.4
TIC 262755078	108.045171	10.351860	Gal	0	2.2664	26.7636	11.80886	x	x	12	1.127	6347.2
TIC 278142612	108.558874	-80.058615	Gal	0	2.5061	4.8923	1.95216	x	x	12	4.344	
TIC 59453672	108.569920	20.273133	Gal	0	7.5126	8.3576	1.11248	x	x	12	1.055	5851.2
Gaia DR3 3111928351141425664	109.571295	1.765508	Gal	0	0.274758	0.144463	1.90193	x	x	13	0.955	4494.5
Gaia DR3 3047190824491991040	109.612639	-10.149447	Gal	0	0.45911	0.25037	1.83373	x	x	13	1.064	
ZTF J071917.56+232008.7	109.823180	23.335770	Gal	0	1.1566429	0.460891	2.50958	5:2	0.38	15	1.047	6334.5
TIC 409682934	110.371789	-15.436972	Gal	0	4.7742	13.4943	2.8265	x	x	12	8.293	9937.7
TIC 317863971	110.567508	3.031925	Gal	0	3.526276	3.733625	1.0588	x	x	6	1.398	9845.7
ASASSN-V J072304.90-110043.5	110.770420	-11.012090	Gal	0	2.553083	2.2011469	1.15989	x	x	9	1.281	12603.7

Table A.1 (continued)

Name	RA [°]	DEC [°]	Loc.	Conf.	P_A [days]	P_B [days]	R	Res.	C [%]	Ref.	RUWE	T_{eff} [K]
Gaia DR3 3061770932787038208	111.089388	-2.032067	Gal	0	0.422212	0.966995	2.29031	x	x	13	4.342	6037.4
Gaia DR3 2930398740886024192	111.474350	-19.281677	Gal	0	0.347152	2.294894	6.61063	x	x	13	1.170	5862.8
TIC 300446218	111.594902	-66.281066	Gal	0	5.557302	7.862233	1.41476	x	x	6	13.838	
CSS J072829.7+255437	112.123842	25.910388	Gal	0	0.488156	0.294211	1.6592	5:3	0.45	15	10.655	7563.3
ASAS J073054-1840.7	112.726040	-18.678440	Gal	0	2.068435	1.7285119	1.19666	x	x	9	6.029	21788.8
TIC 456737763	112.787827	-22.095222	Gal	0	0.7994	0.9492	1.18739	x	x	12	1.574	9574.0
BESTII F20a_01769	113.320080	-33.236410	Gal	0	2.6519588	0.2897737	9.15183	x	x	9	0.978	6093.2
ZTF J073417.15+200529.9	113.571496	20.091603	Gal	0	0.3353884	0.2595961	1.29196	x	x	15	3.173	7725.6
ASASSN-V J073451.49-070610.2	113.714540	-7.102840	Gal	0	5.5879951	1.683838	3.31861	x	x	9	1.010	8774.6
TIC 405114468	113.807000	-17.203648	Gal	0	2.7407	12.5098	4.56445	x	x	12	8.810	16526.8
ASASSN-V J073515.34-384551.0	113.813920	-38.764160	Gal	0	0.9473	1.174181	1.2395	x	x	9		
ASASSN-V J073836.07-254110.7	114.650290	-25.686300	Gal	0	6.3604401	1.5345683	4.14477	x	x	9	1.033	9601.0
TIC 125787704	115.159669	-27.319573	Gal	0	6.5593	7.6917	1.17264	x	x	12	1.110	7967.6
WISE J074104.5+020838	115.268770	2.144070	Gal	0	0.3766151	3.6876188	9.79148	x	x	15	33.207	
TIC 125952257	115.426817	-27.582624	Gal	0	2.161915	2.898585	1.34075	4:3	0.56	6	5.233	15826.1
TIC 140328928	115.821697	-23.639557	Gal	0	2.3	2.6959	1.17213	x	x	12	1.678	13211.0
2MASS J07450662+4446506	116.277574	44.780803	Gal	0	0.8605426	0.2946809	2.92025	x	x	15	42.590	
V0674 Pup	116.403880	-31.158890	Gal	0	0.6029032	6.5245459	10.82188	x	x	9	2.042	6819.8
TIC 127011022	116.506091	-25.471756	Gal	0	2.2689	2.8549	1.25827	x	x	12	1.056	
WISE J074616.9+124313	116.570600	12.720350	Gal	0	0.4389155	1.4468374	3.29639	x	x	15	1.332	6100.1
ASASSN-V J074844.43-374960.0	117.185170	-37.833320	Gal	0	0.5055883	1.9735046	3.90338	x	x	9	40.836	
ASAS J074939-3037.0	117.412170	-30.615060	Gal	0	0.441707	0.2648523	1.66775	5:3	0.06	15	1.339	6281.3
Gaia DR3 875709132614498560	117.697495	28.467895	Gal	0	0.442358	1.466414	3.31499	x	x	13	1.008	
Gaia DR3 3044312990239139840	118.096034	-5.697484	Gal	0	1.452632	1.779009	1.22468	x	x	13	0.995	4943.4
TIC 128802666	118.418216	-27.662181	Gal	0	1.6932	4.8618	2.87137	x	x	12	4.160	10915.9
ASASSN-V J075356.71-491144.1	118.486280	-49.195590	Gal	0	1.3816161	0.7337604	1.88293	x	x	15	3.253	
TIC 266657256	119.266500	4.186727	Gal	0	4.919396	6.870338	1.39658	x	x	6	0.953	5548.3
TIC 271204362	119.524572	7.213528	Gal	0	2.9375	3.2558	1.10836	x	x	10	0.845	10173.4
WISE J075848.7-374315	119.702920	-37.720980	Gal	0	0.395653	0.3093777	1.27887	x	x	9	1.114	5779.2
TIC 130276377	119.825676	-28.378980	Gal	0	2.757776	6.457989	2.34174	x	x	6	2.701	19885.5
TIC 130533284	120.122757	-27.531303	Gal	0	2.5066	3.1045	1.23853	x	x	12	1.028	15006.5
TIC 73296637	121.017527	-3.380218	Gal	0	1.483742	1.844061	1.24284	x	x	6	1.178	7497.6
TIC 144475902	121.339546	-34.049985	Gal	0	2.2991	3.4287	1.49132	3:2	0.58	12	1.020	
LZ Lyn	121.407540	52.353000	Gal	0	0.906131	0.3956921	2.28999	x	x	9	3.153	
TIC 443862276	121.618495	7.254959	Gal	0	3.073838	7.040997	2.29062	x	x	6	0.932	6198.0
TIC 144686626	121.661306	-33.115235	Gal	0	2.0281	16.7099	8.23919	x	x	12		
TIC 348651800	121.724336	-12.435678	Gal	0	2.077867	3.836246	1.84624	x	x	6	13.841	8180.0
TIC 134744873	122.643434	-37.750415	Gal	0	1.4405	28.4349	19.7396	x	x	12	1.113	12516.2
ASASSN- VJ081048.48+133402.0	122.702000	13.567220	Gal	1	2.12274	4.0133499	1.89065	x	x	9, 15	0.986	6293.5
ASASSN-V J081549.78-360750.1	123.957420	-36.130580	Gal	0	0.7775968	5.0107097	6.44384	x	x	9	0.995	17879.5
ASASSN -VJ081749.20+585421.7	124.455010	58.906040	Gal	0	0.2532754	3.8148775	15.06217	x	x	15	1.002	5805.9
NSVS 10096434	124.525178	16.271963	Gal	0	2.7856207	1.1681003	2.38474	x	x	15	2.794	6475.4
TIC 82818966	124.931906	-47.096644	Gal	0	2.417501	4.930024	2.03931	2:1	1.97	6	0.972	5722.6
TIC 409692211	126.002870	-15.797150	Gal	0	25.416	963.1	37.89345	x	x	10	1.639	6400.5
ASASSN-V J082616.93-675427.2	126.570540	-67.907570	Gal	0	1.4428125	0.3665626	3.93606	4:1	1.60	9	14.648	6274.9
TIC 140241924	126.771527	-50.765831	Gal	0	1.8035	4.3829	2.43022	x	x	12	1.087	5746.0
TIC 139944266	127.035827	-44.334557	Gal	0	1.443586	27.065312	18.74867	x	x	6	1.023	9037.8
TIC 231595025	127.800427	-24.467880	Gal	0	10.3896	19.6682	1.89307	x	x	12	1.033	7463.1
TIC 140593601	128.193380	-44.571091	Gal	0	3.3602	4.635	1.37938	x	x	12	1.690	
ASASSN-V J083557.21-325946.4	128.988380	-32.996220	Gal	0	0.3001982	1.8509248	6.16568	x	x	15	16.760	
TIC 461614217	129.293558	-43.823310	Gal	0	2.288076	9.365512	4.09318	x	x	6	8.005	15024.7
TIC 141733685	129.855041	-47.360673	Gal	1	5.290886	7.372395	1.39341	x	x	6	0.954	10537.9
WISE J084601.4-370223	131.505920	-37.039820	Gal	0	0.315164	0.383816	1.21783	x	x	9	0.945	6381.5
TIC 271186951	132.355842	-46.868040	Gal	0	1.731754	2.094425	1.20942	x	x	6	0.881	11426.1
CPD-34 3002	132.464210	-34.759400	Gal	0	2.318566	2.7375104	1.18069	x	x	9	1.125	9766.5
NSVS 15567664	132.604380	-9.515970	Gal	0	0.5898351	0.3810852	1.54778	x	x	9, 15	1.665	
TIC 29046597	132.628993	-47.587217	Gal	0	2.231	3.0951	1.38732	x	x	12	1.077	

Table A.1 (continued)

Name	RA [°]	DEC [°]	Loc.	Conf.	P_A [days]	P_B [days]	R	Res.	C [%]	Ref.	RUWE	T_{eff} [K]
TIC 437039270	132.836631	11.890602	Gal	0	1.0678	1188.5	1113.0361	x	x	10		
TIC 459056725	133.068337	8.062853	Gal	0	10.2485	10.2481	1.00004	1:1	0.00	10	1.159	
GSC 01949-01700	133.812000	29.615840	Gal	0	0.2405869	0.7583237	3.15197	x	x	14	4.332	4883.6
ASASSN-V J085631.48-401412.6	134.131170	-40.236830	Gal	0	1.3179	0.9182636	1.43521	x	x	9	1.664	8328.4
Gaia DR3 5323588396924782464	134.709000	-52.683000	Gal	1	0.313123	0.229048	1.36706	x	x	5	0.843	5803.6
TIC 37376063	134.747687	-29.182578	Gal	1	3.9561	14.5341	3.67385	x	x	12	6.611	5957.7
TIC 95928255	136.380566	-10.058331	Gal	0	2.36543	4.426586	1.87137	x	x	6	1.836	4366.3
TIC 357810643	138.466380	-61.279782	Gal	0	3.120829	20.528963	6.57805	x	x	6	2.449	8000.0
TIC 75740921	139.330597	-45.038900	Gal	0	0.93308	0.986341	1.05708	x	x	6	12.747	
TIC 293442412	139.357752	-52.325771	Gal	0	1.7852	2.876	1.61102	x	x	12	0.986	
TIC 386414884	139.424165	-54.286912	Gal	0	1.6408	1.7374	1.05887	x	x	12	41.849	
TIC 434452777	139.740446	-20.557157	Gal	0	0.449904	8.040997	17.8727	x	x	6	2.932	7251.9
ASASSN-V J091951.17-593306.9	139.963210	-59.551920	Gal	0	2.6686687	14.33574	5.37187	x	x	9	0.977	5783.1
ASASSN-V J092031.34-542438.1	140.130580	-54.410580	Gal	0	4.268089	6.1442495	1.43958	x	x	9	1.284	10449.5
TIC 414969157	141.176162	22.200757	Gal	0	4.630508	6.928951	1.49637	3:2	0.24	6	2.022	4935.4
1SWASP J093010.78+533859.5	142.545464	53.649490	Gal	1	1.3055472	0.2277142	5.73327	x	x	3	1.080	
TIC 370440624	143.232035	-68.681123	Gal	0	2.235057	8.70498	3.89475	x	x	6	1.902	6606.5
TIC 439511833	143.595968	-56.106778	Gal	0	6.594526	11.048213	1.67536	5:3	0.52	6	1.142	10612.0
TIC 33721975	145.622770	-47.507261	Gal	0	1.3589	6.5647	4.83089	x	x	12	1.015	6585.7
TIC 442333487	145.929223	-54.468346	Gal	0	0.6214	3.5479	5.70953	x	x	12	1.138	9872.4
TIC 45160946	147.614561	-36.191917	Gal	1	3.516299	7.8462	2.23138	x	x	6	26.331	5898.0
ASASSN-V J095041.07-344046.4	147.671120	-34.679570	Gal	0	0.39362	1.9085659	4.84875	x	x	15	5.175	5905.6
ASASSN-V J095454.54-720436.1	148.724330	-72.076920	Gal	0	0.7465108	0.3634727	2.05383	x	x	9	2.191	5854.3
TIC 274791367	149.395501	-57.049303	Gal	0	1.207163	14.311675	11.85563	x	x	6	2.233	17147.8
TIC 358713471	150.418404	17.409056	Gal	0	0.8047	0.2841	2.83245	x	x	10	20.966	
TIC 309025182	151.007452	-27.707244	Gal	0	1.401379	1.680424	1.19912	x	x	6	2.563	
TIC 462322817	151.061119	-58.968755	Gal	0	4.438139	7.2784	1.63997	5:3	1.60	6	1.087	6898.4
TIC 139621206	151.716866	-51.077723	Gal	0	3.8147	34.1729	8.95821	x	x	12	0.893	
WISE J100820.0-731554	152.083500	-73.265000	Gal	0	0.3683176	7.9453491	21.572	x	x	9	1.126	
ASASSN-V J101521.33-595651.9	153.838880	-59.947750	Gal	1	0.69329	0.69271	1.00084	1:1	0.08	15	0.844	5202.5
WISE J102135.0-613536	155.395900	-61.593450	Gal	0	0.3413826	12.3164019	36.078	x	x	15	1.140	7010.3
TIC 95436068	155.428350	21.393741	Gal	0	61.9981	2303.6001	37.15598	x	x	10	1.861	6498.7
ASASSN-V J102911.57-522413.6	157.298210	-52.403770	Gal	1	0.5727205	3.7902466	6.61797	x	x	9, 11	1.678	6267.6
ASAS J103449-6013.1	158.702290	-60.217750	Gal	0	7.59371	3.182093	2.38639	x	x	9	5.275	15618.9
TIC 458108996	159.190164	-59.834261	Gal	0	1.1821	1.4659	1.24008	x	x	12	4.254	
OGLE GD-ECL-00259	159.359900	-62.483390	Gal	0	1.1423587	0.6449106	1.77134	x	x	3	10.112	6791.7
TIC 458606169	160.433085	-56.491067	Gal	0	1.4421	3.1812	2.20595	x	x	12	2.078	7092.4
V0432 Vel	160.527000	-42.877970	Gal	0	1.46857	0.5449716	2.69476	x	x	9	10.211	
TIC 458740670	160.808111	-57.895051	Gal	0	6.2628	7.0207	1.12102	x	x	6	0.944	7986.4
WISE J104839.2-690956	162.163620	-69.165650	Gal	0	0.3557778	0.4463116	1.25447	x	x	15	1.541	5284.8
TIC 459333241	162.311407	-59.781248	Gal	0	3.9182	3.9886	1.01797	1:1	1.80	12	1.202	
TIC 167800999	162.328271	-21.422818	Gal	0	0.7928	9.8272	12.39556	x	x	12	10.972	
OGLE GD-ECL-03436	162.408090	-61.994590	Gal	0	1.6798563	3.1251724	1.86038	x	x	3	1.034	4226.4
TIC 459400252	162.552438	-56.449916	Gal	0	5.5037	8.4146	1.5289	3:2	1.93	12	1.195	6669.4
ASASSN-V J105224.11-554746.7	163.100460	-55.796300	Gal	0	1.4961114	53.1092318	35.49818	x	x	9		
OGLE GD-ECL-04406	163.399937	-61.548214	Gal	0	1.5728462	1.6757585	1.06543	x	x	3	0.973	10507.7
TIC 459705607	163.436465	-57.642881	Gal	0	1.376	1.4132	1.02703	x	x	12	0.948	9585.0
TIC 399492452	163.985711	-69.196354	Gal	0	1.75514	9.152187	5.21451	x	x	6	4.953	
ASASSN-V J105635.71-593913.2	164.148780	-59.653670	Gal	0	0.7139141	0.9063433	1.26954	x	x	15	0.999	10629.3
OGLE GD-ECL-05310	164.162752	-60.383570	Gal	0	3.336091	1.8336427	1.81938	x	x	3	3.429	6031.3
OGLE GD-ECL-05390	164.240832	-60.794400	Gal	0	1.75067	4.250057	2.42767	x	x	3	0.997	
OGLE GD-ECL-05656	164.461825	-61.630340	Gal	0	2.1541808	1.2867213	1.67416	5:3	0.45	3	1.150	9331.5
ASASSN-V J105824.33-611347.6	164.601380	-61.229880	Gal	0	12.9954333	2.3307278	5.5757	x	x	9	1.026	
TIC 466187603	165.271485	-63.854045	Gal	0	2.216	3.8214	1.72446	x	x	12	1.005	8771.7
TIC 166647000	165.716290	30.415195	Gal	0	0.4775	7.9306	16.60859	x	x	10	3.658	6532.6
OGLE GD-ECL-07057	166.643370	-61.169250	Gal	0	1.1605585	1.9234148	1.65732	5:3	0.56	3	1.153	
OGLE GD-ECL-07157	166.937750	-61.348880	Gal	1	0.8128751	2.6694423	3.28395	x	x	3	1.175	3829.0

Table A.1 (continued)

Name	RA [°]	DEC [°]	Loc.	Conf.	P_A [days]	P_B [days]	R	Res.	C [%]	Ref.	RUWE	T_{eff} [K]
ASAS J112157+0343.0	170.486130	3.715801	Gal	0	0.4113617	4.963508	12.06604	x	x	15	1.818	5800.3
TIC 97815168	170.522246	-24.777639	Gal	0	264.51	314.86	1.19035	x	x	10		
ASASSN-V J112601.23-661128.8	171.505130	-66.191320	Gal	0	2.805398	1.1937377	2.3501	x	x	9	1.113	10194.6
OGLE GD-ECL-07443	172.771267	-60.698850	Gal	0	1.7501509	1.4512089	1.206	x	x	3	0.971	9020.8
ASAS J113426-6320.0	173.609170	-63.333890	Gal	0	1.7172011	5.0107072	2.91795	x	x	9		
V0871 Cen	174.584830	-63.372750	Gal	0	2.090704	2.817	1.34739	4:3	1.05	9		
TIC 320233974	174.672596	-62.818712	Gal	0	3.2857	5.3016	1.61354	x	x	12	0.893	
V0384 Cen	174.822130	-62.174780	Gal	0	12.635401	3.6402566	3.47102	7:2	0.83	9	8.364	6743.3
TIC 320855910	174.873192	-65.397805	Gal	0	61.43	2.755	22.29764	x	x	10	5.747	5954.6
TIC 321474625	175.420727	-62.607413	Gal	0	1.3171	2.9414	2.23324	x	x	12	27.609	19568.3
TIC 321471064	175.527634	-62.267268	Gal	0	0.342094	1.557273	4.55218	x	x	6	1.866	7153.8
WISE J115225.7-665754	178.107210	-66.965060	Gal	0	2.0461214	3.3214941	1.62331	x	x	9	5.206	6281.8
CSS J120146.1+245254	180.442148	24.882071	Gal	0	0.3468923	0.7002585	2.01866	2:1	0.93	15	1.393	5837.8
TIC 311838200	181.861947	-70.489362	Gal	0	2.13397	2.49618	1.16974	x	x	6		
KELT KS38C016096	183.870920	-62.657960	Gal	0	2.791493	31.57253	11.31027	x	x	9	5.405	15580.5
TIC 314802266	184.932193	-71.498860	Gal	0	1.694052	13.069676	7.71504	x	x	6	44.710	6782.5
TIC 204698586	185.551846	-24.224846	Gal	0	0.84381	11.006707	13.04406	x	x	6	4.818	6440.9
TIC 321452145	188.311243	38.750870	Gal	0	7.898	133.374	16.88706	x	x	10	1.106	5014.1
ASASSN-V J124203.23-644513.2	190.513460	-64.753650	Gal	0	2.0725413	1.4122993	1.46749	x	x	9	14.850	7860.6
TIC 329089161	191.387399	-71.221330	Gal	0	1.1271	2.5373	2.25118	x	x	12	1.143	9637.4
ASASSN-V J125427.31-653437.7	193.613790	-65.577130	Gal	0	1.8401023	1.8893375	1.02676	x	x	9	1.256	8845.1
WISE J130824.1-555716	197.100730	-55.954700	Gal	0	0.3530785	0.4134506	1.17099	x	x	15	13.071	5887.0
V0700 Vir	199.428846	-0.562399	Gal	0	0.3985121	9.5365559	23.9304	x	x	15	1.711	
OGLE GD-ECL-10263	201.597010	-65.093620	Gal	0	0.4208822	0.378791	1.11112	x	x	3	1.184	
Gaia DR3 1663741485747221248	202.102553	61.876817	Gal	0	2.770754	8.163296	2.94624	3:1	1.79	13	1.055	6306.9
OGLE GD-ECL-11021	203.235727	-64.164070	Gal	0	1.1601455	3.0600241	2.63762	x	x	3	1.228	6102.9
ASASSN-V J134357.79-535409.5	205.990790	-53.902640	Gal	0	0.3701653	5.0985109	13.77361	x	x	15	9.341	5771.4
TIC 392909786	206.528159	5.115610	Gal	0	32.45	0.407	79.72973	x	x	10	1.133	
ASASSN-V J134743.51-512416.7	206.931290	-51.404650	Gal	0	0.5774803	0.4939062	1.16921	x	x	9	5.922	
TIC 111880742	208.302239	-31.927621	Gal	0	6.93	4.839	1.43211	x	x	10	1.284	13389.2
EPIC 212651213	208.930950	-9.418370	Gal	0	5.07655	13.1947	2.59915	x	x	3	20.767	5684.3
ASASSN-V J140754.66+354456.0	211.977750	35.748910	Gal	0	1.0129093	8.2610749	8.15579	x	x	9	7.566	5088.3
TIC 242328834	212.671920	-47.768998	Gal	0	0.394	175.9	446.4467	x	x	10	1.016	5734.7
TIC 408147984	213.482501	-59.643098	Gal	0	1.072756	3.804398	3.54638	7:2	1.33	6	6.150	7250.1
ASASSN-V J143536.01-721459.4	218.900040	-72.249850	Gal	0	7.3536094	6.36881	1.15463	x	x	9	1.346	
HD 128523	220.351710	-71.048110	Gal	0	2.45106	3.3045126	1.3482	4:3	1.11	9	11.522	10426.6
TIC 219006972	221.202871	66.378673	Gal	1	8.2325	13.6389	1.65671	x	x	12	1.012	5651.5
TIC 250119205	221.669507	-53.195218	Gal	0	2.426677	5.097049	2.10042	x	x	6	1.836	10038.8
TIC 308731030	222.829877	-49.723451	Gal	0	8.2186	11.167	1.35875	4:3	1.91	12	2.114	
TIC 161043618	223.425163	52.715848	Gal	1	1.350249	1.488497	1.10239	x	x	6, 15	23.997	6181.8
TIC 414475823	224.211179	-57.685879	Gal	0	3.478022	3.65741	1.05158	x	x	6	1.032	
TIC 310004006	224.834676	46.817665	Gal	0	0.645	31.521	48.86977	x	x	10		
TIC 257023157	225.248724	73.053188	Gal	0	0.416	31.188	74.97115	x	x	10		
TZ Boo	227.038063	39.970240	Gal	0	0.2971604	9.4776254	31.89397	x	x	15	6.135	5789.3
BV Dra, BW Dra	227.960000	61.860000	Gal	1	0.35007	0.29216	1.19821	x	x	3, 5		
TIC 285655079	233.992493	-57.122535	Gal	0	2.456281	6.691905	2.72441	x	x	6	3.974	6599.7
ASASSN-V J154012.48-723446.0	235.052000	-72.579440	Gal	0	1.054818	0.4812192	2.19197	x	x	9		
ASASSN-V J154043.29-494808.4	235.180370	-49.802320	Gal	0	2.6953877	0.5670568	4.75329	x	x	9	28.714	
TIC 348160530	235.258012	-14.823242	Gal	0	6.9518	208.918	30.05236	x	x	10	1.082	6325.8
TIC 459416198	235.505791	0.457083	Gal	0	10.88	15.77	1.44945	x	x	10		
TIC 459278502	235.991364	22.339806	Gal	0	15.888	13.561	1.1716	x	x	10		
TIC 274862252	237.426543	-53.506278	Gal	0	2.3437	2.9531	1.26002	x	x	12	1.081	7286.6
ASASSN-V J154958.67-494817.6	237.494460	-49.804890	Gal	0	6.068392	0.3874346	15.66301	x	x	9	1.129	
ASASSN-V J155157.55-430547.7	237.989790	-43.096590	Gal	0	2.92193	8.931	3.05654	3:1	1.88	9	2.769	
TIC 255532033	240.549599	-44.712993	Gal	0	4.173996	12.927714	3.0972	x	x	6	6.440	10018.4
TIC 219469945	241.047908	43.030301	Gal	0	2.717596	14.965529	5.5069	x	x	4, 6	1.091	
Gaia DR3 1323756753679794176	242.649013	34.621080	Gal	0	7.041158	0.128904	54.62327	x	x	13	2.462	7335.1

Table A.1 (continued)

Name	RA [°]	DEC [°]	Loc.	Conf.	P_A [days]	P_B [days]	R	Res.	C [%]	Ref.	RUWE	T_{eff} [K]
ASASSN-V J161601.84-424533.0	244.007670	-42.759180	Gal	0	3.2005508	0.3638294	8.79684	x	x	9	1.183	6482.0
WISE J161811.8-402805	244.549290	-40.468070	Gal	0	0.3770954	2.308219	6.12105	x	x	15	5.001	
ASASSN-V J162133.01-675919.1	245.387500	-67.988630	Gal	0	2.3832433	0.4278364	5.57045	x	x	9	0.987	7663.3
V0398 Nor	245.487420	-49.156800	Gal	0	1.58895	1.5410346	1.03109	x	x	9	1.838	11847.3
ASASSN-V J162738.80-432923.7	246.911670	-43.489910	Gal	0	0.5375934	0.4115693	1.3062	x	x	9	10.067	6419.6
WISE J163047.5+545403	247.698080	54.901170	Gal	0	0.2912781	3.226198	11.07601	x	x	15	7.136	5750.3
TIC 1337279468	252.514389	-44.034898	Gal	1	4.446303	5.939225	1.33577	4:3	0.18	6	12.825	
TIC 170146066	252.630189	-55.320633	Gal	0	5.4287	18.2741	3.3662	x	x	12	1.284	5771.4
V1037 Her	254.237290	29.318470	Gal	1	0.7875805	5.803712	7.36904	x	x	9, 11	4.306	5623.7
Gaia DR3 1414515322519168512	257.277242	49.948796	Gal	0	0.301544	0.231617	1.30191	x	x	13	0.944	4782.1
ASASSN-V J171020.36-794023.0	257.584830	-79.673050	Gal	0	0.5197554	1.456689	2.80264	x	x	9	1.237	7279.4
ZTF J171602.61+273606.5	259.010905	27.601883	Gal	0	0.3600118	4.5155344	12.54274	x	x	14	2.334	5960.1
Gaia DR3 4115999620890628096	259.250732	-20.297582	Gal	0	0.621141	0.773402	1.24513	x	x	13	0.962	
TIC 356318101	260.821333	22.308281	Gal	0	1.6848	3.2578	1.93364	x	x	12	1.648	
ASASSN-V J172557.86-702516.0	261.491080	-70.421120	Gal	0	4.3982343	0.324594	13.54996	x	x	9	24.997	
OGLE BLG-ECL-018877	262.171770	-29.463350	Gal	1	0.6008759	1.5565025	2.59039	x	x	3	1.033	
OGLE BLG-ECL-019637	262.255060	-29.496700	Gal	0	0.40113	0.368949	1.08722	x	x	3	1.089	
OGLE BLG-ECL-030128	263.342440	-33.796650	Gal	1	2.2742881	1.9120361	1.18946	x	x	3	1.011	7656.7
ASASSN-V J173344.14-363037.8	263.433920	-36.510500	Gal	0	5.4788615	2.6152141	2.095	x	x	9	1.282	
TIC 441794509	263.598849	74.472259	Gal	0	4.668622	14.785724	3.16704	x	x	6	1.144	6053.6
Gaia DR3 1343353448205456384	263.775976	38.311866	Gal	0	3.048348	11.792556	3.86851	x	x	13	0.968	5266.1
OGLE BLG-ECL-061232	265.101890	-27.717490	Gal	1	0.3791298	1.4676043	3.87098	x	x	3	1.067	4598.1
OGLE BLG-ECL-088871	266.248670	-23.712610	Gal	1	3.8779159	5.6508216	1.45718	x	x	3	1.206	15033.5
OGLE BLG-ECL-089724	266.278910	-23.831050	Gal	0	3.4925576	0.343487	10.16795	x	x	3	1.885	4451.6
OGLE BLG-ECL-093829	266.416820	-22.647150	Gal	0	3.7452992	0.5210858	7.18749	x	x	3	1.077	4147.7
OGLE BLG-ECL-100363	266.637710	-20.891720	Gal	0	4.3521616	0.5749267	7.56994	x	x	3	2.892	
OGLE BLG-ECL-103591	266.749460	-36.516420	Gal	1	2.2321488	2.2833714	1.02295	x	x	3	1.025	4110.6
OGLE BLG-ECL-104219	266.771400	-35.034830	Gal	0	0.4683403	0.457687	1.02328	x	x	3		
TIC 256158466	266.899180	-79.379329	Gal	0	5.774547	7.454373	1.2909	x	x	6	0.962	4464.8
ASASSN-V J175000.12-415247.9	267.500500	52.811470	Gal	0	3.2902183	3.7108779	1.12785	x	x	9		
OGLE BLG-ECL-133521	267.728280	-21.567020	Gal	0	1.0472674	1.0388721	1.00808	1:1	0.81	3	2.266	8974.1
TIC 444816203	267.901758	-32.033706	Gal	0	0.7536	2.5163	3.33904	x	x	12	2.385	6236.7
OGLE BLG-ECL-145467	268.023280	-29.328730	Gal	1	3.3049105	4.9097045	1.48558	3:2	0.96	3	0.970	8008.8
OGLE BLG-ECL-165082	268.441400	-29.216520	Gal	0	0.9599463	1.092108	1.13768	x	x	3	1.472	
OGLE BLG-ECL-187370	268.909340	-28.263800	Gal	0	11.9634963	87	7.27212	x	x	3	0.982	6005.2
OGLE BLG-ECL-190427	268.974610	-22.997510	Gal	1	0.9449826	2.5137669	2.66012	x	x	3	4.440	
OGLE BLG-ECL-197015	269.113620	-27.789690	Gal	0	0.3759299	6.53287	17.37789	x	x	3	2.630	6630.2
OGLE BLG-ECL-200747	269.191650	-31.233110	Gal	0	42.76521	0.287215	148.89616	x	x	3	3.963	4918.2
WISE J175944.9-502122	269.937330	-50.356340	Gal	0	0.374864	1.0160054	2.71033	x	x	9	12.655	4650.6
Gaia DR3 6724245225761139456	270.087000	-43.477000	Gal	1	0.314403	0.378357	1.20341	x	x	5	0.938	5785.2
OGLE BLG-ECL-246147	270.180740	-26.389080	Gal	0	2.0615552	2.1689469	1.05209	x	x	3	0.990	3736.9
OGLE BLG-ECL-250817	270.281070	-28.808760	Gal	0	9.2515062	0.4396163	21.0445	x	x	3	1.029	
OGLE BLG-ECL-251128	270.288540	-27.712380	Gal	0	0.3786368	0.406083	1.07249	x	x	3	5.775	
TIC 337346017	270.458748	-50.943783	Gal	0	4.3717	5.7395	1.31288	4:3	1.53	12	1.199	4608.0
TIC 462707324	270.596041	20.833625	Gal	0	12.4573	0.63	19.77349	x	x	10	2.227	
OGLE BLG-ECL-272587	270.787830	-28.921390	Gal	0	1.1199022	3.378545	3.01682	3:1	0.56	3		
OGLE BLG-ECL-274234	270.825150	-28.232950	Gal	0	6.5352552	91.39	13.98415	x	x	3	1.352	
OGLE BLG-ECL-277539	270.900470	-28.128210	Gal	0	0.3753292	0.5779823	1.53993	x	x	3		
OGLE BLG-ECL-282858	271.021460	-32.339170	Gal	0	0.3992092	0.539641	1.35177	4:3	1.38	3	1.412	
ASASSN-V J180818.54-684329.4	272.077230	-68.724830	Gal	0	0.3391935	6.6467632	19.59579	x	x	15		
OGLE BLG-ECL-335648	272.352160	-27.905910	Gal	1	4.6922359	2.720131	1.725	x	x	3	1.137	5255.0
OGLE BLG-ECL-352722	272.846670	-28.983380	Gal	0	0.5866713	3.28423	5.59808	x	x	3	1.256	
Gaia DR3 2109307852667550464	273.743299	39.207529	Gal	0	2.205617	4.373204	1.98276	2:1	0.86	13	0.968	4743.4
OGLE BLG-ECL-394187	274.210290	-28.725200	Gal	0	5.5976216	1.134909	4.93222	x	x	3	2.064	4343.0
OGLE BLG-ECL-398110	274.361010	-26.505740	Gal	1	1.1164591	8.2388401	7.37944	x	x	3	1.056	4381.2
OGLE BLG-ECL-403022	274.581350	-24.749370	Gal	0	2.6422384	1.1806143	2.23802	x	x	3	0.997	4517.3
OGLE BLG-ECL-406204	274.735900	-28.010320	Gal	0	0.5740634	1.7556268	3.05825	3:1	1.94	3	0.865	

Table A.1 (continued)

Name	RA [°]	DEC [°]	Loc.	Conf.	P_A [days]	P_B [days]	R	Res.	C [%]	Ref.	RUWE	T_{eff} [K]
WISE J181904.2+241243	274.767660	24.212040	Gal	1	0.3671285	0.4194289	1.14246	x	x	11, 15	1.483	5593.9
Gaia DR3 4477905552460741504	275.054107	7.264466	Gal	0	7.737	0.235	32.9234	x	x	10	0.973	5658.8
V0833 Lyr	275.426226	39.255868	Gal	0	0.3694649	0.3605839	1.02463	x	x	15	12.612	
ASASSN-V J182400.66-354210.9	276.002750	42.185370	Gal	0	3.3017214	0.3722	8.87083	x	x	9		
Gaia DR3 4161007815803012096	276.008132	-5.774128	Gal	0	3.070536	1.371504	2.23881	x	x	13	1.019	
V994 Her	276.941220	24.697410	Gal	1	2.0832658	1.4200395	1.46705	x	x	3	3.680	11999.0
WISEJ182934.1-395010	277.392420	-39.836360	Gal	0	0.5913301	0.5383272	1.09846	x	x	9	1.438	6973.7
CoRoT 310266512	277.832240	-5.831840	Gal	0	7.421	3.266	2.2722	x	x	3		
Gaia DR3 2147458221793949184	278.026086	54.402996	Gal	0	3.109478	1.853905	1.67726	5:3	0.64	13	0.938	3575.1
CoRoT 310284765	278.463600	-5.656530	Gal	0	2.371125	1.8754	1.26433	x	x	3	1.077	9004.5
Gaia DR3 4156431820198005248	279.117985	-8.525243	Gal	0	1.407928	1.331908	1.05708	x	x	13	5.135	5527.5
TIC 123098844	279.572843	44.698600	Gal	0	1.730707	11.210254	6.47727	x	x	6	1.335	6392.8
Gaia DR3 4508288602094505984	279.719282	13.163625	Gal	0	0.399492	1.528379	3.82581	x	x	13	5.732	7424.7
ASASSN-V J184117.47-414037.4	280.322790	-41.677288	Gal	0	2.124815	0.4845352	4.38526	x	x	9		
ASASSN-V J184212.96-775807.0	280.554000	-77.968620	Gal	0	0.5412306	0.3405923	1.58909	x	x	9	12.333	6258.1
Gaia DR3 4256607950976483840	280.635591	-5.252461	Gal	0	1.907376	0.903688	2.11066	x	x	13	1.710	8661.9
Gaia DR3 4505600296166989312	280.635808	13.120684	Gal	0	4.870614	4.70215	1.03583	x	x	13	0.951	4949.2
Gaia DR3 2091761983553949696	280.713417	34.654670	Gal	0	0.271486	0.372731	1.37293	x	x	13	1.012	5118.2
Gaia DR3 4504043245957168640	281.121588	11.135930	Gal	0	10.015578	1.042907	9.60352	x	x	13	1.910	5658.1
ASASSN-V J184700.16-492255.5	281.750670	-49.382080	Gal	0	4.1765513	3.2577395	1.28204	x	x	9	1.114	5784.9
Gaia DR3 2041659197183314432	282.145741	30.399305	Gal	0	0.283664	55.568657	195.89605	x	x	13	1.016	5134.4
Gaia DR3 4505497904155845120	282.312661	13.469479	Gal	0	0.28221	3.150768	11.16462	x	x	13	1.155	4700.1
Gaia DR3 2040256804464235520	283.996449	28.282368	Gal	0	5.739774	0.139815	41.05263	x	x	13	0.959	7174.9
Gaia DR3 4201927347951103488	284.492451	-11.193995	Gal	0	0.513114	0.453093	1.13247	x	x	13	1.083	5581.4
EPIC 219217635	284.752608	-17.265870	Gal	0	3.59486	0.61815	5.81551	x	x	3	1.227	5766.7
Gaia DR3 4517289341731165696	285.268359	18.064422	Gal	0	1.056042	0.545708	1.93518	x	x	13	1.128	6592.3
KID 03832716	285.394040	38.904910	Gal	1	1.141877	2.170274	1.90062	x	x	2, 15	3.174	6195.5
CoRoT 211625668	285.461470	3.307980	Gal	0	1.771922	5.257641	2.9672	3:1	1.09	3	2.755	
TIC 377192659	285.914758	57.457184	Gal	0	1.8172	8.4508	4.65045	x	x	10	0.936	8612.5
WISE J190356.0-333742	285.983680	-33.628600	Gal	0	0.4169934	0.4169902	1.00001	1:1	0.00	15	0.932	5029.6
CoRoT 211659387	286.003800	3.055000	Gal	0	0.39396	4.0005	10.15458	x	x	3		
Gaia DR3 4269211034315304832	286.003864	3.508937	Gal	0	1.772	5.258	2.96727	3:1	1.09	10	0.994	5439.2
Gaia DR3 4513882917294832640	286.391765	16.558561	Gal	0	0.875846	2.838248	3.24058	x	x	13	0.939	6841.2
TIC 384410712	286.694357	23.156756	Gal	0	2.6044	2.9768	1.14299	x	x	12	2.722	6201.8
Gaia DR3 4204113619406564352	286.904493	-9.457319	Gal	0	0.33327	0.867417	2.60275	x	x	13	6.128	5643.4
Gaia DR3 4204326997705570304	287.114664	-8.543055	Gal	0	0.272314	0.170204	1.59993	x	x	13	1.151	
KIC 4247791	287.164829	39.376900	Gal	0	4.100871	4.049732	1.01263	1:1	1.26	3	4.569	6233.7
Gaia DR3 4516377056329377792	287.445354	19.597742	Gal	0	1.035768	6.325886	6.10744	x	x	13	7.707	6375.0
ASASSN-V J191022.62+164303.2	287.594250	3.897550	Gal	0	1.20379	1.381573	1.14769	x	x	9	1.080	
Gaia DR3 4513263857861420544	287.648865	16.355321	Gal	0	0.45636	2.129335	4.66591	x	x	13	1.014	
Gaia DR3 2130268255146656256	287.884621	46.028573	Gal	0	0.422266	1.029215	2.43736	x	x	13	1.207	5617.6
Gaia DR3 4521240642906912256	288.026347	23.298684	Gal	0	3.00593	1.616295	1.85977	x	x	13	1.022	6396.4
Gaia DR3 4264206469687918592	288.248394	0.080909	Gal	0	3.166976	1.852653	1.70943	x	x	13	1.174	6885.2
Gaia DR3 4263034768239285760	288.471817	-1.094539	Gal	0	1.862082	0.592354	3.14353	x	x	13	0.939	5707.1
Gaia DR3 4520164564651727872	288.648651	22.157332	Gal	0	0.355088	0.32902	1.07923	x	x	13	1.032	4373.9
Gaia DR3 4293109022582320640	288.825262	4.312846	Gal	0	0.390062	0.164066	2.37747	x	x	13	0.982	
TIC 211637075	289.263190	9.338769	Gal	0	3.391	180.483	53.22412	x	x	10	2.559	5009.7
SSS J191726.4-543540	289.360670	-54.594220	Gal	0	0.3128593	2.8178337	9.00671	x	x	15		
Gaia DR3 4320727174167431168	289.517888	15.160579	Gal	0	2.163692	1.607176	1.34627	4:3	0.97	13	1.053	
HD 181469	289.742534	39.267130	Gal	0	8.653	94.226	10.8894	x	x	3	3.977	6979.6
KELT KC11C034703	289.962960	34.970900	Gal	0	2.1919011	9.3813864	4.28002	x	x	9	1.343	
TIC 300987891	289.968039	16.663800	Gal	0	5.541	5.6329	1.01659	1:1	1.66	12	1.018	6899.3
Gaia DR3 2038100043701450240	290.184501	28.541396	Gal	0	0.325552	79.87107	245.34044	x	x	13	0.980	5092.1
CzeV3436	290.353580	36.133030	Gal	0	0.6836872	0.3833927	1.78326	x	x	8	2.259	6914.0
CzeV2708	290.597670	36.294170	Gal	0	1.24205	0.272633	4.55576	x	x	9	1.451	6055.8
Gaia DR3 4308597705466532352	290.604938	9.668160	Gal	0	5.097978	1.412602	3.60893	x	x	13	0.994	5265.0
Gaia DR3 2050141310916611584	290.991691	35.958626	Gal	0	3.877374	4.766349	1.22927	x	x	13	1.629	7724.3

Table A.1 (continued)

Name	RA [°]	DEC [°]	Loc.	Conf.	P_A [days]	P_B [days]	R	Res.	C [%]	Ref.	RUWE	T_{eff} [K]
TYC 3929-724-1	291.232700	57.069000	Gal	1	4.10846	4.67547	1.13801	x	x	3	1.826	
Gaia DR3 4292639977810529280	291.640789	4.331223	Gal	0	1.64215	1.061804	1.54657	x	x	13	1.346	9640.4
Gaia DR3 4323257219102940160	291.714347	18.228635	Gal	0	1.588804	2.302579	1.44925	x	x	13	1.210	8123.3
Gaia DR3 2049954600104034304	291.820676	35.975820	Gal	0	4.030792	14.062535	3.48878	7:2	0.32	13	1.027	5771.6
Gaia DR3 1825483906846429184	293.462031	19.846805	Gal	0	6.45557	2.467705	2.61602	x	x	13	0.990	
Gaia DR3 2025279046615280640	293.504188	27.432478	Gal	0	2.759184	0.863998	3.19351	x	x	13	1.010	9635.5
Gaia DR3 4314657904341880832	293.592507	11.006839	Gal	0	3.349092	1.32064	2.53596	5:2	1.44	13	1.153	5981.8
Gaia DR3 1825578567909317632	293.657387	19.881442	Gal	0	4.770348	2.118271	2.252	x	x	13	1.455	9280.5
Gaia DR3 2021549301357843456	293.823697	25.752582	Gal	0	0.417266	0.182446	2.28707	x	x	13	1.255	
Gaia DR3 4318042922678224896	294.156333	14.316215	Gal	0	1.840298	0.915486	2.01019	2:1	0.51	13	1.082	4442.6
Gaia DR3 2025146250574308352	294.332664	27.158424	Gal	0	0.430934	0.698726	1.62142	x	x	13	1.017	5583.8
Gaia DR3 4207090654517833216	294.518815	-7.404433	Gal	0	3.426032	0.315937	10.84404	x	x	13	1.287	4598.4
Gaia DR3 2025081478136260608	294.832597	26.871716	Gal	0	3.072568	2.212912	1.38847	x	x	13	0.972	23303.8
Gaia DR3 2048268017993738752	294.839444	35.975154	Gal	0	0.234828	4.944031	21.05384	x	x	13	2.289	5046.8
Gaia DR3 1825745006505361920	294.933937	20.202009	Gal	0	7.807304	3.649778	2.13912	x	x	13	1.039	
Gaia DR3 2077913565886105344	295.309706	42.822037	Gal	0	0.373692	0.322663	1.15815	x	x	13	4.303	4529.1
Gaia DR3 2047323949824485376	295.479516	34.635703	Gal	0	2.346872	2.481432	1.05734	x	x	13	1.003	
Gaia DR3 1827708802964917760	295.527859	22.054362	Gal	0	0.545902	0.96728	1.77189	x	x	13	21.040	
ASASSN-V J194302.90+294814.1	295.762080	29.803910	Gal	0	1.6314193	3.3814447	2.0727	x	x	9	0.869	6093.9
ZTF J194331.02+255254.0	295.879290	25.881670	Gal	0	1.3572871	2.0934434	1.54237	x	x	15	1.033	9472.0
Gaia DR3 2031977619399032320	296.235173	29.583425	Gal	0	8.147016	8.083514	1.00786	1:1	0.79	13	0.892	
Gaia DR3 2020056405032433152	296.585034	23.395937	Gal	0	0.812118	0.753871	1.07726	x	x	13	1.586	
Gaia DR3 2020970648976206336	296.895517	25.636448	Gal	0	3.187571	107.735965	33.7988	x	x	13	1.195	
Gaia DR3 2032118077650924544	296.955946	30.241753	Gal	0	171.076078	2.335024	73.26523	x	x	13	1.008	7188.3
Gaia DR3 2020490437267187712	297.006120	24.058537	Gal	0	1.35866	1.729201	1.27273	x	x	13	1.088	9306.7
Gaia DR3 2031925182082532608	297.034812	30.088060	Gal	0	3.590404	0.789163	4.54964	x	x	13	1.013	
Gaia DR3 2026976864358731776	297.056926	25.787105	Gal	0	1.425158	0.89166	1.59832	x	x	13	1.013	
ZTF J194856.47+360309.2	297.235330	36.052570	Gal	0	0.6413882	0.8664298	1.35087	4:3	1.31	9		
Gaia DR3 2033828574151981056	298.002327	31.866931	Gal	0	1.768354	0.571495	3.09426	x	x	13	0.990	5109.9
Gaia DR3 2027154955201119488	298.172845	26.864218	Gal	0	1.647592	1.191313	1.38301	x	x	13	3.293	
Gaia DR3 1834469768675202560	298.530047	24.682368	Gal	0	2.881026	4.353022	1.51093	3:2	0.73	13	1.460	8483.8
Gaia DR3 2033656156987971840	298.820248	32.014540	Gal	0	7.548416	0.159107	47.44239	x	x	13	0.959	
Gaia DR3 2030312580776346112	298.881534	29.891560	Gal	0	0.462184	7.651529	16.55516	x	x	13	1.703	
Gaia DR3 2034277144881784832	298.908525	32.746538	Gal	0	2.452324	0.558699	4.38935	x	x	13	31.821	
V1356 Cyg	299.164210	29.991440	Gal	0	1.9566675	7.5682323	3.86792	x	x	9	2.444	17374.9
TIC 282005870	299.316193	27.313177	Gal	0	0.6811	1.7891	2.62678	x	x	12	1.781	10288.8
ZTF J195756.55+271912.8	299.485620	27.320240	Gal	0	2.8367388	3.5676917	1.25767	x	x	9	3.789	
Gaia DR3 2027512262117411072	299.485653	27.320224	Gal	0	2.837	3.568	1.25767	x	x	10	3.789	
Gaia DR3 2030426861313716224	299.522067	30.246542	Gal	0	1.305256	1.607371	1.23146	x	x	13	1.257	15840.5
Gaia DR3 2034419218049672704	299.620393	33.527522	Gal	0	1.411226	1.614413	1.14398	x	x	13	1.250	5065.7
Gaia DR3 2030212490900354048	299.976835	29.839710	Gal	0	1.189566	3.314311	2.78615	x	x	13	1.189	9990.1
ZTF J200018.70+390309.8	300.077963	39.052782	Gal	0	0.4525771	0.5595318	1.23632	x	x	15	0.910	6018.2
ZTF J200052.75+305205.6	300.219790	30.868240	Gal	0	19.9998494	3.4183586	5.85072	x	x	9	1.052	6697.6
TIC 104909909	300.606349	35.669853	Gal	1	2.5743422	1.3057949	1.97148	2:1	1.43	10, 11	1.295	13893.1
V0346 Sge	300.871983	21.086656	Gal	0	0.4662684	0.3092951	1.50752	3:2	0.50	15	6.154	
TIC 89278612	301.219498	32.643051	Gal	0	2.557052	3.641763	1.4242	x	x	6	12.229	9125.5
Gaia DR3 2058617549147113728	301.355473	34.989363	Gal	0	2.08353	15.704131	7.53727	x	x	13	1.271	
Gaia DR3 2059117002318116096	301.378990	35.972060	Gal	0	1.741608	1.064947	1.63539	5:3	1.88	13	1.057	9078.9
Gaia DR3 2074882590295669248	301.391172	42.318524	Gal	0	1.127028	2.46579	2.18787	x	x	13	1.013	6595.5
Brh V154	301.677210	24.989090	Gal	0	0.5549471	1.94456111	3.50405	7:2	0.12	9, 15	10.354	6337.7
Gaia DR3 1829670778385777920	302.250175	21.436492	Gal	0	5.414028	3.970943	1.36341	x	x	13	1.016	5451.2
Gaia DR3 2061735248734886400	302.637062	38.400325	Gal	0	1.079346	0.468297	2.30483	x	x	13	1.026	8066.6
Gaia DR3 2059178162649303808	302.983340	36.463072	Gal	0	5.993378	0.563785	10.63061	x	x	13	1.073	7093.7
ASASSN-V J201221.36+213400.7	303.088990	21.566870	Gal	0	0.3561	0.3343574	1.06503	x	x	15	59.610	
Gaia DR3 1836995514370597120	303.229266	27.908953	Gal	0	0.374674	3.126105	8.34353	x	x	13	1.054	6603.9
CzeV2647	303.523150	38.382910	Gal	1	0.5723295	0.9637074	1.68383	5:3	1.03	8	1.936	6318.9
ASASSN-V J201545.10+373555.2	303.937920	37.598660	Gal	0	2.75347	2.8234774	1.02543	x	x	9	1.111	8768.2

Table A.1 (continued)

Name	RA [°]	DEC [°]	Loc.	Conf.	P_A [days]	P_B [days]	R	Res.	C [%]	Ref.	RUWE	T_{eff} [K]
Gaia DR3 2068658632915468800	304.151811	41.930677	Gal	0	4.363316	1.242846	3.51075	7:2	0.31	13	0.965	
TIC 304713857	304.203364	18.576200	Gal	0	4.7272	9.0828	1.92139	x	x	12	5.861	5760.8
TIC 11917056	304.357294	39.293513	Gal	1	1.7936849	0.7679373	2.33572	x	x	10, 11	1.884	19881.3
CzeV4315	304.417950	39.243090	Gal	0	0.9193147	6.7389724	7.33043	x	x	15	0.918	13307.7
ZTF J201742.81+362821.2	304.428380	36.472570	Gal	0	1.1787963	0.6853393	1.72002	x	x	9	1.006	
TIC 382182610	304.472082	-36.204657	Gal	0	8.5928	11.7809	1.37102	x	x	12	0.939	
Gaia DR3 2061050802729418496	304.756649	37.920034	Gal	0	1.325726	0.813421	1.62982	x	x	13	1.098	
Gaia DR3 1861612037845705728	304.795015	30.560399	Gal	0	5.302642	0.323736	16.37953	x	x	13	1.191	8499.9
WISE J202244.1+325218	305.683920	32.871860	Gal	0	3.4272801	21.47198	6.26502	x	x	9	2.454	
V498 Cyg	305.795120	39.162310	Gal	0	3.484806	1.438457	2.4226	x	x	7	1.519	
Gaia DR3 2058085351143518464	306.408352	37.894974	Gal	0	1.152476	85.498447	74.18675	x	x	13	1.221	
TYC 2693-926-1	306.682633	35.341700	Gal	0	1.350447	1.099203	1.22857	x	x	3	3.398	5412.1
TIC 278352276	307.503640	48.607056	Gal	1	12.403102	18.810761	1.51662	3:2	1.11	6	0.845	
TIC 63459761	308.525065	41.135869	Gal	0	4.244072	4.362293	1.02786	x	x	6	1.260	
Gaia DR3 2167733048719069184	308.681181	48.208470	Gal	0	2.17693	0.584749	3.72285	x	x	13	1.105	4567.3
Gaia DR3 2056704914305732096	308.779214	35.826622	Gal	0	5.152764	0.910183	5.66124	x	x	13	1.190	7856.1
Gaia DR3 1817286807102270336	309.177000	20.120000	Gal	1	0.268858	0.232892	1.15443	x	x	5	0.970	
Gaia DR3 1862347439319475200	309.435623	30.852742	Gal	0	0.920364	1.417808	1.54049	x	x	13	0.993	4926.8
TIC 387288959	309.583230	69.362300	Gal	0	2.6963	83.0963	30.81864	x	x	12	4.805	
ASASSN-V J203821.68+300951.4	309.590320	30.164280	Gal	0	1.9584802	0.4393769	4.4574	x	x	15	0.988	8819.7
TIC 322727163	309.716625	50.466821	Gal	0	1.156328	1.640142	1.41841	x	x	6	20.922	
Gaia DR3 1859824197571796736	311.551340	31.682545	Gal	0	0.283018	0.394832	1.39508	x	x	13	1.017	5442.8
Gaia DR3 1869489385821202944	311.979230	34.771038	Gal	0	0.488582	2.110629	4.31991	x	x	13	0.970	4949.1
Gaia DR3 1760943570684334080	312.564502	12.412033	Gal	0	3.047312	15.580245	5.11278	x	x	13	0.985	5511.2
Gaia DR3 2166511040319614208	312.603366	47.202077	Gal	0	0.38052	1.264149	3.32216	x	x	13	1.011	3659.8
NSVS 5871089	313.102290	38.171750	Gal	0	0.7480267	0.5378686	1.39072	x	x	9		
ZTF J205229.71+473345.9	313.123830	47.562760	Gal	0	1.9223369	1.153058	1.66716	5:3	0.03	9	5.220	
Gaia DR3 1872913471188045312	313.727051	39.848684	Gal	0	2.26941	0.678956	3.3425	x	x	13	1.272	8153.6
Gaia DR3 2245787855903677952	314.203035	66.204173	Gal	0	1.313048	1.250967	1.04963	x	x	13	1.041	3930.3
WISE J210230.8+610816	315.628670	61.137960	Gal	1	1.8432444	0.5715872	3.22478	x	x	9, 11	2.027	9012.3
TIC 375325607	315.793095	55.469314	Gal	0	1.311984	9.223201	7.02996	x	x	6	29.305	
Gaia DR3 2165439879783209472	315.998617	47.984506	Gal	0	3.822778	2.650119	1.44249	x	x	13	1.816	8919.4
ZTF J210445.64+495005.8	316.190170	49.834970	Gal	0	1.2773286	3.4406492	2.69363	x	x	9	0.977	9257.6
TIC 273919067	316.241965	43.796242	Gal	0	2.1394	3.1915	1.49177	3:2	0.55	12	3.601	
Gaia DR3 1868409321799840768	316.499668	36.761395	Gal	0	0.543036	0.725643	1.33627	4:3	0.22	13	0.941	7303.0
SSS J210617.9-453858	316.574770	-45.649640	Gal	0	0.6100092	0.6415804	1.05176	x	x	15	1.071	9825.7
UCAC4 644-103150	316.607580	38.980122	Gal	0	0.3368955	3.0756614	9.12942	x	x	15		
Gaia DR3 2165141946503725056	316.935639	47.047120	Gal	0	1.272084	3.086064	2.42599	x	x	13	1.086	15007.5
ZTF J210808.00+452951.5	317.033370	45.497640	Gal	0	2.4372263	0.4552749	5.35331	x	x	15	3.783	5593.1
Gaia DR3 6897094092939104256	317.167097	-8.177796	Gal	0	0.111996	0.622656	5.5596	x	x	13	1.076	7180.5
TIC 358422952	317.232893	52.098012	Gal	0	3.0536	3.0757	1.00724	1:1	0.72	12	2.057	5148.7
Gaia DR3 2176903937763785216	317.354427	55.485175	Gal	0	3.446506	3.158925	1.09104	x	x	13	1.058	4166.7
WISE J210935.8+390501	317.399540	39.083800	Gal	0	0.33228	3.5157922	10.58081	x	x	15	1.420	5499.1
TIC 79225651	317.844939	-52.339240	Gal	0	1.7855	6	3.3604	x	x	10	1.833	
TIC 344541836	317.850729	57.620410	Gal	0	2.409932	2.755276	1.1433	x	x	6	14.346	18632.3
UCAC4 645-103963	318.063330	38.693927	Gal	0	0.3457637	3.4485185	9.97363	x	x	15	1.077	6074.2
Gaia DR3 2177329891137900032	318.209090	56.260390	Gal	0	0.90333	0.515231	1.75325	x	x	13	0.969	
Gaia DR3 2166229226047556096	318.442107	51.071054	Gal	0	15.0598	3.180452	4.73511	x	x	13	0.986	
WISE J211411.4+585336	318.547750	58.893400	Gal	0	0.3976895	1.1715113	2.94579	3:1	1.81	15	2.573	6598.6
Gaia DR3 6898893306278386688	319.184000	-6.562000	Gal	1	0.290062	0.292613	1.00879	1:1	0.88	5	0.939	5346.4
ZTF J212128.80+514855.6	320.370040	51.815450	Gal	0	2.195314	1.6280104	1.34846	4:3	1.13	9	7.995	7021.9
WISE J212247.5+735527	320.698070	73.924320	Gal	0	0.3032693	0.4100439	1.35208	4:3	1.41	15	0.971	5779.4
TIC 427092089	321.112009	64.380683	Gal	0	2.00191	2.086	1.042	x	x	6	1.969	9469.2
Gaia DR3 2170863908089217280	321.274386	49.322575	Gal	0	3.714414	2.643588	1.40507	x	x	13	0.993	6548.7
TIC 240256832	322.296887	44.033327	Gal	0	2.6484	3.6378	1.37358	x	x	12	9.061	7622.1
Gaia DR3 1952168090372267008	322.785455	37.809557	Gal	0	1.158128	1.25026	1.07955	x	x	13	1.015	6017.3
Gaia DR3 1967117802081173504	322.795044	41.616730	Gal	0	4.672324	3.584245	1.30357	x	x	13	1.022	5527.4

Table A.1 (continued)

Name	RA [°]	DEC [°]	Loc.	Conf.	P_A [days]	P_B [days]	R	Res.	C [%]	Ref.	RUWE	T_{eff} [K]
TIC 160514618	322.895561	34.402516	Gal	0	2.5281	6.9486	2.74855	x	x	12	1.108	
TIC 264402353	323.090421	78.695151	Gal	0	1.697811	8.096013	4.7685	x	x	6	0.986	6129.3
Gaia DR3 1966045232784781824	324.064461	40.289056	Gal	0	0.264192	0.779663	2.95112	3:1	1.63	13	1.052	4422.1
ZTF J213637.17+360500.8	324.154973	36.083545	Gal	0	0.2833991	1.8586832	6.55854	x	x	15	21.073	6072.1
ASASSN-V J213804.77+281007.8	324.519880	28.168830	Gal	0	0.747245	2.083481	2.78822	x	x	9	6.929	6124.1
TIC 278465736	324.800505	51.346631	Gal	0	0.6142	3.9063	6.35998	x	x	12		
Gaia DR3 2178057359827382272	325.003123	56.109079	Gal	0	3.296832	1.291317	2.55308	x	x	13	0.966	9833.2
Gaia DR3 1978029359778789888	325.081161	48.445380	Gal	0	0.678389	0.746095	1.0998	x	x	13	1.019	9113.1
Gaia DR3 1953928099249228032	325.126003	39.737305	Gal	0	1.068532	1.123977	1.05189	x	x	13	13.389	6145.1
Gaia DR3 2178581380197081088	325.523023	58.222165	Gal	0	1.810504	0.707697	2.5583	x	x	13	1.011	
Gaia DR3 1800509737128120320	325.791627	27.217748	Gal	0	0.85369	3.215801	3.76694	x	x	13	0.997	4402.5
Gaia DR3 1978958103506727424	326.593483	49.781513	Gal	0	0.421342	1.667499	3.95759	4:1	1.06	13	1.190	
TIC 139914081	326.971651	-49.037832	Gal	0	0.8471	15.7964	18.64762	x	x	12	2.025	5572.7
Gaia DR3 2216420454386370048	327.020592	62.789850	Gal	0	2.14556	0.404213	5.30799	x	x	13	4.203	
Gaia DR3 2202597664775578112	327.271647	58.943552	Gal	0	1.06056	2.05528	1.93792	x	x	13	1.205	6079.7
Gaia DR3 2199284050276697088	328.521806	57.784601	Gal	0	0.433052	1.459645	3.3706	x	x	13	1.386	5628.5
Gaia DR3 1981103972253288960	329.000459	52.050747	Gal	0	0.685961	0.739756	1.07842	x	x	13	1.022	
Gaia DR3 1973338392191011584	329.356711	45.001855	Gal	0	0.397442	6.522002	16.40995	x	x	13	2.299	5469.3
TIC 229804573	329.625330	-59.012145	Gal	0	1.464	0.53	2.76226	x	x	10	23.316	6175.8
Gaia DR3 1961000256819235328	329.904956	43.718061	Gal	0	0.473181	0.964035	2.03735	2:1	1.87	13	1.023	5257.3
Gaia DR3 2199104211409698816	330.104590	57.341933	Gal	0	0.979846	0.443703	2.20834	x	x	13	0.960	5014.7
Gaia DR3 2198180415480756224	330.629145	55.984692	Gal	0	1.328192	22.393498	16.86014	x	x	13	0.998	7572.9
ZTF J220417.14+552607.2	331.071420	55.435360	Gal	0	1.772187	1.4225802	1.24576	x	x	9	1.673	8728.5
ZTF J220518.78+592642.1	331.328250	59.445030	Gal	1	2.7956986	3.3460783	1.19687	x	x	9, 11	0.968	16695.3
ZTF J220853.42+493316.6	332.222610	49.554620	Gal	0	0.7383393	0.2084567	3.54193	7:2	1.20	15	1.012	5834.7
Gaia DR3 2197966251234148352	332.366702	56.166443	Gal	0	2.705704	2.822163	1.04304	x	x	13	1.017	7170.3
Gaia DR3 2199925099913441792	332.720979	59.647230	Gal	0	2.15344	1.57226	1.36965	x	x	13	1.087	7914.2
Gaia DR3 2005474711889658624	332.943294	54.420990	Gal	0	3.234134	0.617324	5.23896	x	x	13	1.036	4159.1
TIC 430745185	333.690287	49.255911	Gal	0	10.1586	10.714	1.05467	x	x	12	0.957	
Gaia DR3 2004590532743751424	333.801196	53.749768	Gal	0	0.340078	2.522543	7.41754	x	x	13	0.987	5758.4
Gaia DR3 2005911802117956096	334.655366	55.538438	Gal	0	1.508362	0.947192	1.59246	x	x	13	1.026	5250.5
ZTF J221845.49+500608.5	334.689560	50.102370	Gal	0	2.8501242	1.9758957	1.44245	x	x	15	1.018	6313.9
TIC 421782795	334.690025	56.126083	Gal	0	6.6884	3.469	1.92805	x	x	10	0.991	16336.3
Gaia DR3 1905994992912248320	335.103223	36.014911	Gal	0	0.834723	0.422142	1.97735	2:1	1.13	13	1.961	6328.2
Gaia DR3 1878929101147587072	335.115083	24.563415	Gal	0	2.107929	2.068346	1.01914	1:1	1.91	13	1.039	4719.7
TIC 414026507	336.837717	56.740362	Gal	0	4.229981	6.455288	1.52608	3:2	1.74	6	2.093	17953.0
Gaia DR3 2001849763802035712	337.436575	54.279883	Gal	0	2.263908	0.545817	4.14774	x	x	13	1.097	6026.4
Gaia DR3 2201723866572302848	337.832153	60.857037	Gal	0	2.627162	101.237102	38.53478	x	x	13	0.996	
NSVS 154567	337.924938	68.772890	Gal	0	11.4838	2.93956	3.90664	x	x	3		
Gaia DR3 1986716807300365824	339.088072	47.538959	Gal	0	6.451769	0.164641	39.18689	x	x	13	0.955	7326.7
TIC 262039241	339.690027	-20.621157	Gal	0	4.0832	1.795	2.27476	x	x	10		
ZTF J224132.79+582517.4	340.386630	58.421500	Gal	0	1.1628068	119.7988	103.02554	x	x	9	30.805	
Gaia DR3 2007240188275431936	340.921211	57.261299	Gal	0	1.625996	1.379002	1.17911	x	x	13	1.434	
Gaia DR3 2003907912126462464	341.302946	56.012542	Gal	0	0.404544	2.944626	7.27888	x	x	13	1.020	6091.8
Gaia DR3 2002122850696945664	341.422596	53.230019	Gal	0	3.484958	2.227952	1.5642	x	x	13	1.043	
Gaia DR3 2007474143733297152	342.740000	58.714103	Gal	0	1.63917	1.617598	1.01334	1:1	1.33	13	1.023	5552.7
TIC 371583423	343.115418	55.433045	Gal	0	1.765	2.0536	1.16351	x	x	12	9.644	6030.5
ZTF J225427.56+544055.9	343.614787	54.682178	Gal	0	0.385235	1.0061713	2.61184	x	x	15	31.466	
Gaia DR3 1984790600366568448	344.803515	48.306854	Gal	0	0.699564	1.513966	2.16416	x	x	13	1.028	7405.9
TIC 139188326	345.011534	-46.492162	Gal	0	12.33	0.59	20.89831	x	x	10	1.039	6630.6
WISEJ230200.8+405840	345.503670	40.977830	Gal	0	0.996781	0.3065449	3.25166	x	x	9	15.548	6702.8
V0597 And	346.516920	48.590250	Gal	0	0.4677073	0.3524904	1.32687	4:3	0.49	14	7.941	
ZTF J231009.99+561201.8	347.541654	56.200510	Gal	0	3.4262274	6.6604283	1.94395	x	x	15	1.086	7181.7
Gaia DR3 2208692193312331776	347.564145	65.090617	Gal	0	5.095412	1.198208	4.25253	x	x	13	1.663	
Gaia DR3 2210495392378660864	349.093506	66.228219	Gal	0	2.568998	285.579588	111.1638	x	x	13	1.030	8412.9
TIC 301138089	349.849905	-5.124351	Gal	0	21.2387	659.9	31.07064	x	x	10		
Gaia DR3 1997226175657082368	350.559020	56.248535	Gal	0	0.351738	1.855745	5.27593	x	x	13	1.278	4728.9

Table A.1 (continued)

Name	RA [°]	DEC [°]	Loc.	Conf.	P_A [days]	P_B [days]	R	Res.	C [%]	Ref.	RUWE	T_{eff} [K]
CzeV1645	350.883830	60.886940	Gal	0	1.0944876	1.6594636	1.5162	3:2	1.08	8		
Gaia DR3 2010769070836151296	351.050509	59.819433	Gal	0	1.312382	0.89549	1.46555	x	x	13	1.197	
Gaia DR3 1998851258144250112	352.521122	57.484618	Gal	0	0.280512	1.619602	5.77374	x	x	13	1.043	4911.9
Gaia DR3 1942119756681849344	352.593979	48.961381	Gal	0	4.303021	0.149352	28.81127	x	x	13	1.042	7567.8
TIC 25818450	352.743444	53.069150	Gal	0	10.132402	17.101657	1.68782	5:3	1.27	6	4.791	
ASASSN-V J233336.79+615012.0	353.403290	61.836680	Gal	1	3.3427872	1.2667572	2.63885	x	x	9, 15	1.797	5850.0
Gaia DR3 1918839728265382912	353.524226	36.870485	Gal	0	0.366704	4.201864	11.45846	x	x	13	1.086	5189.4
WISE J233926.8+534940	354.861770	53.827900	Gal	0	0.4484249	1.6138747	3.59899	x	x	15	15.339	7568.8
TIC 417752064	356.147418	74.173107	Gal	0	10.0118	15.0798	1.5062	3:2	0.41	12	8.158	6938.0
TIC 346000664	356.855009	57.360644	Gal	0	1.8298	7.0909	3.87523	x	x	12	1.196	11152.2
TIC 343943213	357.154981	18.230233	Gal	0	216.427	7.82	27.67609	x	x	10	1.612	
Gaia DR3 1940569067331012736	357.182000	48.820000	Gal	1	0.269075	0.372554	1.38457	x	x	5		
TIC 470710327	357.329052	61.962787	Gal	0	1.104686	19.950922	18.06027	x	x	6	11.938	
TIC 265274458	357.694256	73.156742	Gal	0	2.997813	57.3338	19.12521	x	x	6	1.160	9090.6
Gaia DR3 2012994482376100864	358.069196	62.459358	Gal	0	1.950456	34.404796	17.63936	x	x	13	7.237	7985.2
Gaia DR3 2012695312133566208	358.221987	61.525403	Gal	0	3.21884	2.533716	1.2704	x	x	13	0.927	9296.0